THÈSE

En vue de l'obtention du

DOCTORAT DE L'UNIVERSITÉ DE TOULOUSE

Délivré par : *l'Université Toulouse 3 Paul Sabatier (UT3 Paul Sabatier)*

Présentée et soutenue le *07/11/2016* **par :**

SNISARENKO Dmytro

Medium sized molecules clearance through artificial kidneys

JURY

CURCIO Efrem	Docteur, Institute on Membrane Techology	Rapporteur
SALMON Jean-Baptiste	Docteur, Université de Bordeaux	Rapporteur
STAMATIALIS Dimitrios	Professeur, University of Twente	Examinateur
BACCHIN Patrice	Professeur,Université de Toulouse	Invité
AIMAR Pierre	Professeur,Université de Toulouse	Invité
CAUSSERAND Christel	Professeur,Université de Toulouse	Directrice de thèse

---

École doctorale et spécialité :
MEGEP : Génie des procédés et de l'Environnement
Unité de Recherche :
Laboratoire de Génie Chimique de Toulouse
Directeur(s) de Thèse :
CAUSSERAND Christel
Rapporteurs :
CURCIO Efrem et *SALMON Jean-Baptiste*

Acknowledgements

Doctorate school for me has been a great experience and a wonderful opportunity for academic and personal growth.

During the realization of this project, I have communicated with a great number of wonderful people whose contribution I would like to acknowledge. Firstly, I want to express my sincere gratitude to my supervisors and co-supervisors, Prof. Christel Causserand, Prof. Patrice Bacchin and Prof. Pierre Aimar, for their constant involvement in fruitful discussions and their willing to provide required assistance throughout the entire duration of the present project. I cannot omit mentioning Dr. Sebastien Teychene and Dr. Nhat Pham, whose experience and advice helped me a lot during the development and fabrication of microfluidics devices. Some technical ideas presented in this work have come from them.

I would like to thank all members of the defense committee, Dr. Jean-Baptiste Salmon, Dr. Efrem Curcio and Prof. Dimitrios Stamatialis for accepting our invitation to be in the jury and their critical evaluation of the present thesis. It was a great opportunity to discuss our scientific discoveries and their interpretations with experts in the respective domains during the thesis defense.

I have been lucky of having great colleagues in the lab. I thank Emelyne, Lucia, Ioannis, Arthur, Le, Yandi, Zenamarkos and Alessio for being available to help me any time. Because of them the atmosphere in the lab was always friendly and cooperative. I feel really fortunate to have such friends. I have great memories of two stays at the University of Twente in a Biomaterials Science and Technology (BST) group. My warmest gratitude to Denys, Kasia, Ilaria, Odyl and Natalia for their help and contribution during those months of working together.

I would also like to thank my parents, who always encouraged me and believed in my success. The special thank deserves my beloved wife Nataliia for her constant support and her cheerful sacrifices of time to organize this manuscript in LaTex. The last, but not least, I would like to thank for the financial support from FP7 Marie Curie Initial Training Network, without it the realization of this project would not be possible.

Résumé

Malgré une longue histoire de développement, l hémodialyse (rein artificiel) possède encore quelques limitations, telles que la perte des propriétés initiales de la membrane en cours de traitement à cause du colmatage et la mauvaise élimination des toxines urémiques de taille moyenne.

La présente étude fait partie d un projet européen nommé BioArt dont le but est d apporter des solutions à ces limites. Dans cet objectif, l un des partenaires du projet a proposé le développement d un nouveau concept de membrane double couche au sein de laquelle sont incorporées des particules adsorbantes. Une caractérisation complète de cette nouvelle membrane était alors nécessaire, plus précisément l impact de la matrice mixte sur l élimination des toxines urémiques de divers groupes devait être évalué, ainsi que la propension du matériau membranaire à se colmater.

Les études des phénomènes de colmatage sont classiquement menées à l échelle macroscopique (faisceau de fibres creuses) sans analyse à l échelle d une fibre isolée. Le but premier de la présente thèse a alors été de proposer un dispositif permettant une étude du colmatage membranaire induit par la protéine à l échelle microscopique. Un dispositif microfluidique transparent dans lequel la membrane polymère est insérée a été élaboré et mis en œuvre pour la filtration des protéines modèles : l albumine de sérum bovin (BSA) et l α-lactalbumine. Grâce au couplage avec la microscopie de fluorescence, différents modes d adsorption des protéines sur la surface de la membrane ont été observés et liés aux variations des conditions hydrodynamiques à l intérieur de la puce. Il a été constaté, sous certaines conditions, une différence dans l accumulation de protéines entre l entrée, le centre et la sortie du canal tandis que dans d autres conditions cet effet s annule. En outre, un phénomène inattendu, l agrégation de l α-lactalbumine, a été observé au cours de la filtration. La localisation dans le canal et la forme des agrégats dépendent également des conditions hydrodynamiques et de la pression transmembranaire appliquée.

Dans le but d optimiser la conception de la membrane vis à vis de son aptitude à éliminer des molécules de taille moyenne de la circulation sanguine, un modèle mathématique a été proposé. L objectif du modèle était, en prenant en compte la présence de particules adsorbantes à l intérieur de la membrane double couche, de rendre compte de la combinaison des trois mécanismes d élimination du soluté : la

convection, la diffusion et l adsorption. Le modèle permet de prédire l influence de divers paramètres tels que la diffusivité de la molécule, l épaisseur de la membrane, la présence de la convection, la charge en particules adsorbantes, sur l intensification des flux à travers la membrane. Le modèle semble être un outil utile pouvant être appliqué à l optimisation de membranes pour l élimination des toxines.

Mots-clés: Hémodialyse, Dispositif Microfluidique, Colmatage de la Membrane, L adsorption de la protéine, Modèle de transfert de la masse.

Abstract

Despite a long history of development, the hemodialysis procedure (artificial kidney) still possesses some limitations, such as loss of the initial properties of the membrane due to fouling and poor removal of the middle sized uremic toxins.

The present study is part of an European project named BioArt the aim of which was to overcome these limitations. In that objective, one of the partners of BioArt project reported on the development of the novel promising concept of double layer membrane with embedded adsorptive particles. A thorough characterization of the new membrane was then necessary, more precisely the extent to which mixed matrix layer can improve the removal of the uremic toxins from various groups needed to be evaluated, as well as the propensity of the membrane material to become fouled.

The studies of the fouling phenomena are conventionally performed at the macro scale (bundle of hollow fibers) without insights of what is happening at the scale of an isolated fiber. Therefore, the primary aim of the present Thesis was to transfer the research of the protein-induced membrane fouling from the macro to the micro scale. A novel transparent microfluidics device with the polymeric membrane inside has been developed and applied for the filtration of model proteins: bovine serum albumin (BSA) and α-lactalbumin. Thanks to the coupling of the microchip with the fluorescent microscopy, different patterns of protein deposition on the membrane surface were observed and related to the variations in the hydrodynamic conditions inside the microchip. It was found that at certain conditions one may observe the difference in protein accumulation in the inlet, the middle, and the outlet of the channel while at other conditions this effect vanishes. Additionally, the unexpected phenomena of α-lactalbumin aggregation was observed over the course of filtration. The location and shape of the aggregates were also dependent on the hydrodynamic conditions and the applied transmembrane pressure.

Aiming to address the problem of membrane design optimization for the enhancement of the middle molecules elimination from the bloodstream, a mathematical model, which accounts for the presence of adsorptive particles inside the complex double-layer membrane, has been proposed. The objective of the model was to understand the interplay of three solute removal mechanisms: convection, diffusion, and adsorption. The model allows predicting the influence of various parameters such as molecule diffusivity, membrane thickness, the presence of

convection, content of adsorptive particles on the flux intensification across the membrane. The developed model seems to be a useful tool, which may be applied to design optimized membranes for the removal of toxins.

Keywords: Hemodialysis, Microfluidics Device, Membrane Fouling, Protein Adsorption, Mass Transfer Model.

Contents

List of Figures

List of Tables

General introduction to the PhD thesis

Background and motivation

The prevalence of end stage renal disease (ESRD) is increasing steadily over last decades. As of 2012, only in US around 571 000 people were suffering from ESRD (and more than one million people worldwide), with the annual mortality related to the kidney failure of more than 87 000 people [1].

The kidney failure is leading to the partial or complete loss of its natural functions and as a result the human body starts to accumulate various compounds (uremic toxins). In such case, the blood of patient needs to be purified through artificial kidney (hemodialysis). This diffusion-governed therapy allows the sufficient removal of small molecular weight toxins (<500 Da), while middle size ones (500 Da – 60 kDa) are retained in the patient [2]. The relation between the accumulation of middle size uremic retention solutes and morbidity and mortality was demonstrated by several studies [3, 4]. Twenty two middle uremic solutes with clinically significant toxicity were found, and under the condition of the kidney failure their concentration in the blood may raise from roughly 3-fold (retinol-binding protein (21.2 kDa)) to 40 or even 60-fold (β_2-microglobulin) (11.8 kDa) [3, 5]. Specifically, the accumulation of β_2-microglobulin was found to be related to the main long term complication, dialysis related amyloidosis (DRA) [6]. Thus, in order to postpose the appearance of this disease the improvement of the middle solutes removal techniques is an indispensable task. From the practical point of view, assuming that β_2-microglobulin production rate is in the range 150-300 mg day^{-1} and kidney is not contributing to its catabolism, the ideal replacement therapy should provide the daily removal of 150-300 mg (1050- 2100 mg week^{-1}). Since, the majority of patients undergo three hemodialysis sessions per week, its removal per session should be of 350-700 mg [6], which is not fulfilled by conventional hemodialysis.

One alternative to hemodialysis is the hemodiafiltration, which allows combining a diffusive and a convective mass transfer mechanisms and, as a result, gives a possibility to remove the major part of both small and middle molecular weight toxins as well as the excess of water [7]. According to Tang *et al.* [8], one of the main disadvantages of hemodiafiltration is its cost, which is 2-fold higher than the price of conventional dialysis. It is possible to deduct 30% of the expenses per session by reuse of the dialyzer 30 times; however, the process of dialyzer cleaning is still not well-established and the optimal reprocessing agents are not standardized. In addition, even hemodiafiltration with highly permeable dialysis membranes (so

called high-flux membranes) is not able to provide the required middle toxin removal per session [6].

Adsorption technique (hemoperfusion) can greatly contribute to the middle molecules removal. Two commercially available adsorption columns (Lixelle and BetaSorb) for selective β_2-microglobulin removal were developed and demonstrated high efficiency. Unlike membrane-based techniques, they are not able to provide removal of the excessive water and sufficient elimination of the small molecular weight toxins. Thus, the combination of advantages of hemodialysis and specific adsorption seems to be wise and even demonstrated promising results when adsorption column and hemodialyser were used in series [3, 9]. On the other hand, the addition of adsorption column to the extracorporeal blood circuit leads to the increase of the blood volume taken from body, which may result in adverse effects, like temporary hypotension. Thus, the compaction of the system without the reduction of clearance performance is desired.

Recently, the new concept of double-layer hollow-fiber membrane (standard geometry of the modern dialyzers) combining the particle-free and adsorbent loaded layers was introduced. This approach allows combination of the toxin removal by means of the membrane filtration and adsorption in one step by using a mixed matrix membrane, where the adsorbent is incorporated in the polymer matrix. In principle, the inner (particle-free layer) prevents the blood from contacting the adsorptive particles, which are dispersed in the outer layer. As so, the aim of particle-free layer is to provide sufficient biocompatibility and prevent direct contact between biological fluid and sorbent, while the presence of the adsorbent in the second layer improves the overall toxin removal [10]. In other words, the toxin firstly has to pass through the particle-free layer and only then be adsorbed inside the layer with adsorbent. The viability of this concept was proven for creatinine and some protein-bound toxins [7], which opened a new perspective in the optimization of the blood purification technique.

However, it is still important to evaluate the validity and the efficiency of this concept in terms of removal of the compounds belonging to the group of middle solutes, mainly including small proteins and cytokines [5]. In addition, the extent to which mixed matrix layer can improve the removal of the uremic toxins from various groups remains uncertain and the optimal membrane design are still need to be determined.

Aiming at the further advancement in the field of artificial organs the BioArt project

(grant no.316 690, EU-FP7-PEOPLE-ITN-2012) was launched in December 2012. It gathered 11 PhD students and 5 Post-doc researchers from 11 universities, research institutes and companies located in 5 countries (the Netherlands, France, Italy, Belgium, and Germany). The main objective of this project was to develop innovative artificial and bio-artificial devices for the treatment of kidney and liver failures. For this, all participants were split in three teams to work on so called work packages dealing with either artificial kidney or bio-artificial kidney or bio-artificial liver.

The present PhD thesis is a part of work package 1, the aim of which is to investigate the solutions to achieve prolonged and complete removal of uremic toxins. This particular thesis is focused on the approaches to control the removal and adsorption of the middle sized uremic toxins.

On one hand, almost immediately after a synthetic membrane is brought to the contact with blood, the protein adsorption on the surface of material starts to occur. The impact and the extent of this process are dependent on the properties of material, such as chemical composition, charge, morphology etc [11, 12]. Adsorption of the protein on the surface of membrane may lead to some issues with material biocompatibility such as blood coagulation, complement activation, blood cells adhesion [13-16] as well as to the decrease of permeation flux and changes of selectivity due to formation of protein semi-permeable layer on the top of the membrane [12]. Therefore, even though the adsorption of middle molecules on dialysis membrane can be viewed as additional mechanism of their removal from the blood stream [17], there is a need of precise control of this phenomena. In other words, the ideal case for the blood purification with use of highlighted double-layer membranes is to avoid an excessive protein adsorption on the surface of particle-free layer, which faces the blood stream and to achieve a sufficient adsorption inside the layer with adsorbent.

The studies of the fouling phenomena are normally performed based on the macro approaches, such as the permeate flux measurements or/and control of the transmembrane pressure [18]. These techniques are providing information about fouling at a macroscale (entire system), while no information is available concerning the microlevel (small part of the membrane surface). Besides, considering the module composed of a bundle of hollow fibers, these techniques only enable the analysis of a cumulative performance of all fibers, without insights of what is happening in different regions of the module or at the scale of an isolated

fiber. Thus, there is a definite need for the approaches employing direct observation of the fouling development in time, in order to get deeper insights in the solute-surface interactions at the microscale leading to the deterioration of the membrane properties.

Aiming at tackling this objective, novel microfluidics device was developed. This device enables the direct real-time observation of the fouling build-up at conditions close to ones of the natural kidney filtration unit. Chapter 3 of the present work discusses the characterization of the developed microfluidics device and its application in the preliminary studies of membrane fouling during the filtration of protein (Bovine Serum Albumin) solution. Then, Chapter 4 is dedicated to the analysis of membrane fouling at different hydrodynamic and pressure conditions applied for the filtration of solution of fluorescently labelled small size protein.

Secondly, aiming at advancing the concept of double-layer membrane, a specific effort was done in development of the mathematical model, which provides a description of the interplay of three toxin removal mechanisms involved in such complex membrane. Chapter 5 describes the steps of the model development and its validation by comparison of experimental and theoretical results.

Finally, Chapter 6 summarizes the main conclusions developed in the present project and highlights the perspectives for the further research.

1 Bibliography

Introduction

In this chapter, the literature review concerning the state-of-the-art in the domain of artificial kidneys is presented. Firstly, the functions of human kidney and the reasons for its failure are discussed. The kidney malfunctioning leads to the accumulation of various metabolism wastes, the classification and clinical importance of which are also addressed. Due to a great shortage of available donor s organs for transplantation, the different blood purification techniques may be applied in order to remove harmful wastes from the blood stream of the patient. These techniques are based on usage of semi-permeable barriers (membranes) or/and adsorbents. The pros and cons of these procedures are discussed in details. Finally, the key issues, which are still to be resolved, are highlighted along with our vision and strategy of their tackling.

1 Renal functions and uremic solutes

1.1 Natural kidney: structure, functions, reasons for failure

Blood contains the particles of various sizes and types, including cells, proteins, dissolved ions and products of metabolism. Some of these particles are essential for the body, while other has to be removed (i.e. urea). The body may control the chemical composition of the blood by various means, but the largest contribution to this process falls to the kidneys [19].

Normally, people have two kidneys of about $11\ \mathrm{cm}$ long and of about $160\ \mathrm{g}$ weight each [20] and are located behind the peritoneum against the posterior abdominal wall [21]. Each kidney contains around 1.2 million filtration unit (Figure 1.1), called nephrons [19, 22]. Each nephron has several functional regions: a cluster of blood vessels called glomerulus, which is surrounded by *Bowman s capsule* connected to *renal tubules (proximal tubule, loops of Henle, distal tubule)* that is ending in a *collecting duct*. The bundle of collecting ducts from nephrons are connected to the *bladder*. Inside the nephron, three separation mechanisms are taking place: filtration (in glomerulus and *Bowman s capsule*), reabsorption and secretion (both in renal tubules) [19, 23].

In the process of blood purification, blood passes through the membrane-lined tubules of the kidney and some solutes are removed by diffusion and subsequently

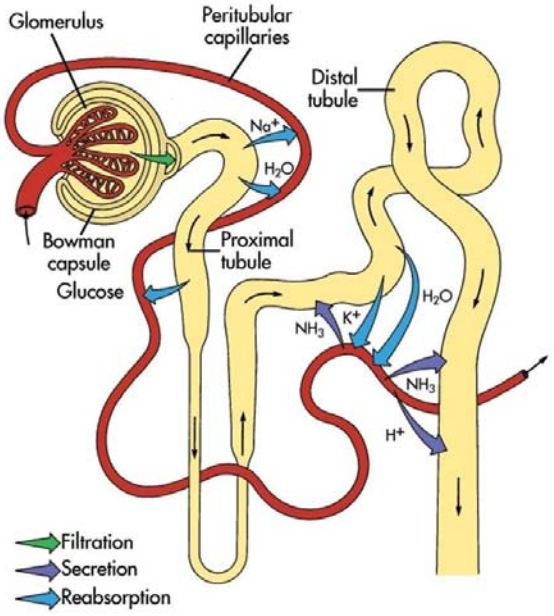

Figure 1.1: Structure of the nephron [24].

excreted [19]. Generally, kidneys perform several functions [21, 22]:

- Elimination of the water-soluble nitrogenous end-products of the protein metabolism;
- Regulation of the electrolyte balance in the body fluids;
- Maintenance of the acid-base balance;
- Production and secretion of hormones.

The condition when natural kidney becomes unable to function properly is called as *kidney failure*. It results in accumulation of harmful wastes and excess fluid in the body, which leads to *uremia* [19, 21]. The most common causes of which are [20, 25, 26]:

- High blood pressure (hypertension);
- High blood sugar (diabetes);
- Kidney diseases and infections, such as polycystic kidney disease, pyelonephritis etc;
- A narrowed or blocked renal artery;
- Long-term use of medications.

Normally, human can live with the kidneys which have at least 10% of properly working functional units [19]. However, sometimes their performance may drop below this level. Based on the duration, the renal function losses may be classified as: acute (short period), subacute and chronic (long period); and only the first one is often reversible. As the kidney disease progresses the filtration rate is steadily falling down, ultimately leading to the *end-stage renal disease* (ESRD) [23]. As soon as ESRD is diagnosed, the renal replacement therapy should be started and it can be provided in two manners: transplantation of the donor s organ or with use of an artificial substituent, which is called artificial kidney or hemodialysis. Definitely, the former approach is the optimal one; however, the main problem is the great mismatch between the required and the available donor organs. According to US statistics as of January 2014, the number of available organs may cover only around 10% of the needed quantity ($14\,029$ transplanted in 2013, against $120\,990$ currently required) [27]. Moreover, the essential requirement for the successful kidney transplantation is the genetic compatibility between donor and recipient, which brings an additional complication to immediate realization of this ESRD treatment [23]. It is for these reasons the need of implementation of the artificial function substituent emerges aiming at the removal of the potentially harmful metabolic compounds.

1.2 Uremic toxins

Uremic solutes, which are excreted by a healthy kidney and are getting retained and accumulated in the body of patients with uremia, are called *uremic retention solutes*. Some of these solutes may negatively interact with normal biological functions of organism causing adverse effects; they are referred as *uremic toxins* [5, 28]. Uremic retention solutes are subdivided into three groups: small molecules (<500 Da) without protein binding, middle solutes (>500 Da and up to 60 kDa), and solutes capable of protein binding [5].

The small uremic solutes are the most common and are found in the human body in higher concentration. Urea (Molecular weight (MW) = 60 Da) and creatinine (MW = 113 Da) are the main representatives of this group. These two solutes are typically used as markers for evaluation of the kidney functionality [5]. Not all the compounds belonging to this group are toxic [29]; however, the evidences of toxicity of some compounds was demonstrated. For instance, the guanidines were initially considered

to be neurotoxic [30], but more recent research also revealed their impact on vascular damage [31].

The class of the middle molecular weight solutes includes mainly peptides and cytokines [5]. In some studies, it was demonstrated that several compounds, which belong to this category, have a negative effect on the different types of cells. For instance, β_2-microglobulin ($\sim$12 kDa) may affect leukocytes, endothelial cells, smooth muscle cells [29] and was proven to be related to mortality of patients with kidney disorders [32-34]. In addition, it was found out that such solutes as Ig-light chain and advanced glycation end product of β_2-microglobulin have a negative influence on leukocytes [29]. The general toxicity of middle solutes and methods of their removal are discussed in more details in the following section.

The solutes capable of protein binding are typically called *protein-bound toxins*. These molecules tend to associate with high molecular weight proteins like albumin ($\sim$66 kDa) and, depending on the affinity between solute and protein, different ratios of their free fraction to the bound one may be detected in the human blood [35]. Some of the protein-bound toxins were reported to be associated with cardiovascular and chronic kidney diseases [36, 37]. For example, it was demonstrated that indoxyl sulfate is likely to affect cardiac cells [38] and lead to the leukocyte adhesion [39]. One of the proposed methods to decrease the serum levels of some of protein-bound toxins is dietary changes or consumption of specific sorbents [40]. However, the greater attention in the field of the blood purification and blood toxin removal was attracted by the membrane-based techniques.

1.3 Importance of removal and clinical toxicity of middle size uremic toxins

1.3.1 Middle size uremic toxins in ESRD

The mortality and morbidity are still issues of high importance in ESRD. Number of studies demonstrated the relation between these problems and the accumulation of the middle size uremic retention solutes by conventional hemodialysis treatment [6, 9, 41, 42]. Recently, twenty two middle uremic solutes with clinically significant toxicity (Table 1.1) were identified [5, 43]. While the level of these compounds in healthy people is controlled by catabolism in the renal tubules [3], their concentration in the serum of patients with ESRD may increase from roughly 3-fold (retinol-binding protein) to 40 or even 60-fold (β_2-microglobulin) [3, 9, 43].

Table 1.1: List of middle size uremic toxins in ESRD [43].

Interleukin-1β (32 kDa)	Complement factor D (23.7 kDa)	Adrenomedullin (5.7 kDa)
Cystatin C (13.3 kDa)	Atrial natriuretic peptide (3 kDa)	Neuropeptide Y (4.2 kDa)
Leptin (16 kDa)	Degranulation inhibiting protein (14.1 kDa)	λ-Ig and κ-Ig light chains (25 kDa each)
β-endorphin (3.4 kDa)	Delta-sleep inducing peptide (848 Da)	Tumor necrosis factor-α (26 kDa)
Cholecystokinin (3.8 kDa)	Methionine-enkephalin (555 Da)	β_2-microglobulin (11.8 kDa)
Endothelin (4.2 kDa)	Retinol-binding protein (21.2 kDa)	Clara Cell Protein (15.8 kDa)
Interleukin-6 (24.5 kDa)	Parathyroid hormone (9.2 kDa)	Hyaluronic acid (25 kDa)

For example, the elevated concentration of leptin is related to malnutrition [44] and it was demonstrated that there is an inverse dependency of its concentration and protein catabolic rate [4]. Some of other compounds were found to interfere with specific cell functions [45-47]. Thus, there is an evidence of clinical toxicity of the middle size compounds, which implies the need to control their concentration in the patients, who undergo renal replacement therapies. Due to the simplicity in the detection and clinical relevance, the most studied toxin from the category is β_2-microglobulin [6, 48]. Currently The European Best Practice Guidelines considers β_2-microglobulin as the best marker of middle molecules for the hemodialysis dose quantification [49].

1.3.2 Beta$_2$-microglobulin as a key marker of middle molecules removal

Beta$_2$-microglobulin (β_2m) is a poly peptide of 99 amino acids and has molecular weight of 11 729 Da and pI=5.5. It is present on the surface of most nucleated cells

and biological fluids (serum, urine, and synovial fluid). Its elimination occurs in the kidney via glomerular filtration with subsequent tubular catabolism; however, kidney failure leads to the accumulation of β_2-microglobulin in the body of patient. While the normal serum β_2-microglobulin concentration is 1.5-3 $\mathrm{mg\,L^{-1}}$, under condition of ESRD it can raise up to 20-50 $\mathrm{mg\,L^{-1}}$ [6, 50]. Additionally, for the patients with kidney failure, β_2-microglobulin is not just retained in the blood stream, but is also accumulated in the tissue, where it undergoes some chemical and conformational transformations, and is polymerized to form amyloids. First amyloids may be observed after two years of the hemodialysis ESRD treatment [51], however, the main long term complication, dialysis related amyloidosis (DRA), is diagnosed for patients treated with hemodialysis only after 6-10 years [6]. DRA is characterized by joint stiffness, joint osteoarthropathy, pain, swelling etc. Patients often present carpal tunnel syndrome (CTS), shoulder pain, and flexor tenosynovitis in hands [9]. Advanced glycation end-products were also identified in β_2m amyloids, meaning that they contribute to the disease progression and that they should also be precisely controlled in ESRD patients [9, 52].

2 Membrane technology for blood purification

2.1 Basics of membrane technology

Membrane is defined as the semi-permeable barrier that controls the permeation of chemical species by favoring the transport of ones, while hampering the penetration of others. Due to the versatility of properties and the possibility of their control, membranes are occupying an important place in the area of chemical technology and are being used in numerous applications [53, 54].

In principle, all membranes can be classified according to the size of the pores on ones for: reverse osmosis, ultrafiltration and microfiltration. The range of pore sizes determining the application of a membrane as well as their comparison with conventional filtration are depicted in Figure 1.2.

As it could be initially concluded, the reverse osmosis membranes possess pores of the size smaller than 2 nm (20 Å), however in real membranes no pores could be observed (membrane is dense) and the transport occurs through the free volume areas, while ultrafiltration and microfiltration membranes possess pores of the ranges 2 – 100 nm and 100 nm – 10 $\mu\mathrm{m}$, respectively [55].

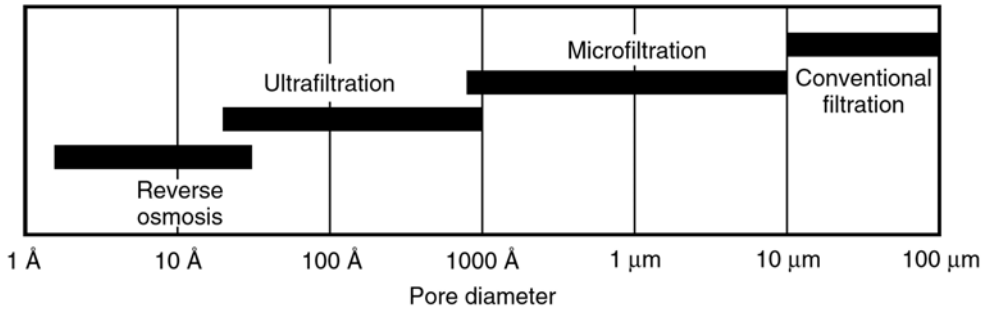

Figure 1.2: Membrane classification basing on the pore size and their comparison with conventional filtration [54].

During the separation process by means of membrane, the permeation of the chemical compounds is governed by difference in chemical potential between the both sides of the membrane. The driving force may be generated by the gradients of temperature, pressure, concentration (dialysis) or/and electrical potential. In addition, the transport across the membrane may be characterized by the different mechanisms depending on membrane morphology (dense or porous). For dense membranes, the generally accepted theory describing the solute transport is "solution-diffusion model". With respect to this model, the permeability P of a certain molecule is defined as a product of its diffusivity D and solubility S (Equation 1.1) in the membrane material [53, 54].

$$P = DS \tag{1.1}$$

Both solubility and diffusivity are the inherent properties of pair molecule-material, meaning that a certain molecule is interacting in a different manner with different material and vice versa. Consequently, the permeability of every chemical compound is strongly related to the properties of the membrane material.

In contrary, the transport through the porous membranes occurs mainly by means of pores. This implies that the permeability is not dependent solely on the membrane material (although the molecule-material interactions are still playing a significant role), but mostly on the pore sizes, pore size distribution, and general membrane porosity. For such transport description, the model of liquid flow through the set of capillary pores of diameter d is used (Equation 1.2):

$$J = \frac{\Delta p \varepsilon}{32 \mu l} d^2 \tag{1.2}$$

where J is flux through the membrane, Δp is transmembrane pressure (TMP), ε is the membrane porosity, μ is the viscosity of the permeating fluid, l and d are the pore length and diameter, respectively [54]. Characterization of the porous membranes is conventionally done by such parameters as retention R towards certain compound and molecular weight cut-off (MWCO). The retention represents the extent to which the compound may be rejected by the membrane. This parameter may vary in the range from 0 (no retention and solute freely passes through) to 1 (compound is fully retained) and is defined by Equation 1.3:

$$R = 1 - \frac{c_{perm}}{c_{feed}} \tag{1.3}$$

where c_{perm} and c_{feed} are the concentrations of compound in the permeate (fluid, which crossed the membrane) and in feed solution, respectively. The membrane retention is directly related to the sieving coefficient, which represents the fraction of compound permeated through the membrane and is defined as (1 - R). The MWCO parameter shows the molecular weight of compound, 90% of which is retained by the membrane. For the determination of this parameter such compounds as polyethylene glycol, dextrans or proteins are used. Practically, the method of MWCO is not standardized and sometimes may differ among industrial manufacturers. However, knowing the retention and MWCO of particular membrane, one can estimate its separation performance [53].

The measurements of the membrane permeability with use of molecules of different molecular weight provides the rejection versus molecular weight curve (Figure 1.3).

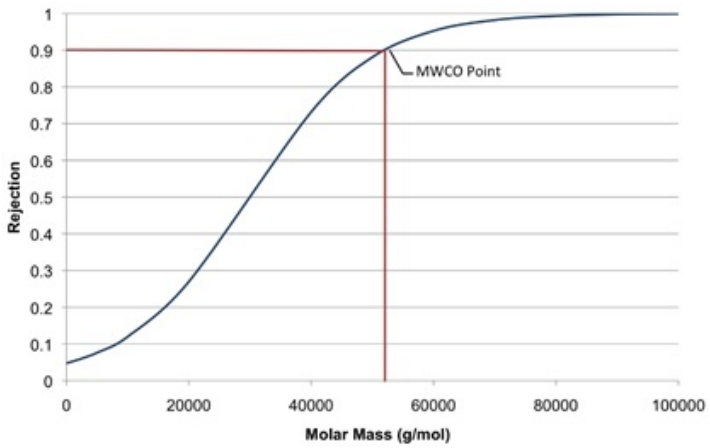

Figure 1.3: Schematic representation of the rejection versus molecular weight curve [56].

It has to be point out that the MWCO serves as one of parameters of a membrane quality. In fact, the sharper the curve is, the better separation of compounds with similar molecular weight it provides. Therefore, one of objectives in the membrane optimization is the obtainment of a curve, which is as sharp as possible. It should be also emphasized that the shape of this curve is dependent on the operational conditions (temperature, pressure, cross-flow velocity) used during the membrane characterization [56].

2.2 Membrane geometry and operation conditions

From the fabrication point of view, all membranes may be categorized as flat and tubular. Flat membranes are then assembled in the plate-and-frame or spiral-wound modules. The plate-and-frame module normally contains 20–30 plates arranged in stack. A typical height of feed channel is in the range of 0.5–$1.0\ \mathrm{mm}$, and the system is operated in high-shear conditions. The family of the tubular membranes includes [55]:

- hollow fiber membranes (diameter: <$0.5\ \mathrm{mm}$);
- capillary membranes (diameter: 0.5 – $5\ \mathrm{mm}$) ;
- tubular membranes (diameter: >$5\ \mathrm{mm}$).

Depending on the application and a particular case each of these module types may provide some advantages and disadvantages. For example, tubular and plate-and-frame modules are used for the filtration of highly fouling solutions. The plate-and-frame modules can withstand higher pressures than tubular or capillary modules. In contrary, the high cost limits the usage of tubular and plate-and-frame modules in case of relatively non-fouling applications (filtration of solutions with lower concentration), where the use of spiral-wound and capillary modules is more cost-effective. Spiral-wound and capillary modules are often selected in some food applications, such as ultrafiltration of cheese whey and clarification of apple juice [54].

Hollow fiber modules were introduced in the early 1970s. A typical module contains several thousands of fibers and is around $30\ \mathrm{cm}$ long and several cm in diameter. Each module has a membrane area of 2–$10\ \mathrm{m}^2$, meaning that the hollow fiber geometry provides the best filtration area-to-volume ratio. For these modules, operating pressures are quite low and normally do not exceed $2\ \mathrm{bar}$ in order to avoid

the breaking of the fibers, which may be considered as a disadvantage for the processes where higher pressures are required. Nevertheless, under mild pressure conditions hollow fiber modules allow the achievement of good throughputs with many solutions [54]. As blood purification does not require high pressures, the hollow fiber membranes are widely used for this application. In addition, good area-to-volume ratio inside the module allows to minimize the priming volume of blood that is crucial in hemodialysis (details in the following section).

The filtration process with use of membranes may be performed in dead-end and cross flow modes (Figure 1.4).

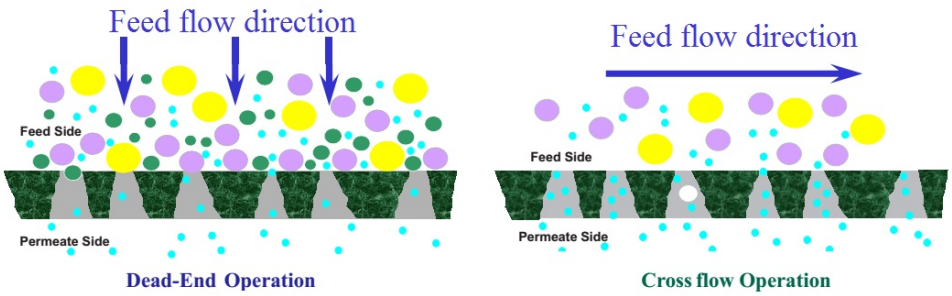

Figure 1.4: Schematic representation of dead-end and cross flow filtration [57].

As it can be understood from Figure 1.4, in the dead-end filtration, the flow of liquid to be filtered is directed perpendicularly to the membrane surface. This approach is more effective for the filtration of solutions with low concentration. However, in case of feed with high concentration, dead-end becomes less effective as filtered solutes accumulate on the membrane surface, which leads to a reduction of filtration rate. Therefore, cross flow filtration is more applicable in such cases, because the flow directed tangentially to the membrane surface creates a sweeping effect, which allows to keep more stable filtration rate [57].

Cross flow filtration process can be also modified in the way that the tangential movement in the permeate side is initiated. In this case, two different modes are distinguished: co-current, when the feed and the permeate flow in the same direction along the membrane and counter-current, when feed and permeate flow in the opposite directions along the membrane.

2.3 Membrane materials for medical applications

Membranes for medical application occupy the huge part of the membrane market. Their production is at least equivalent to the production of membranes for all other applications combined and is much larger in terms of dollar value [54]. Membranes for medical purposes differ in chemical composition, transport properties and biocompatibility. An ideal blood-contacting membrane should be highly biocompatible (not be recognized as foreign object the by organism of the patient), allow the transfer of the uremic toxins of different sizes and be resistant to all chemical and sterilizing agents applied [58].

Today, there are several commercially available hemodialysis membranes of different materials (Table 1.2).

Table 1.2: List of commercial synthetic hemodialysis membranes [59].

Material	**Manufacturer**
Polyacrylonitrile (PAN)	Pan-DX Asahi, PAN AN69 Hospal, SPAN Akzo
Polysulfone (PS)	Asahi, Fresenius, Helbio, Minntech, Toray
Polyester polymer alloy	Nikkiso
Polyarylethersulfone (Arylane®)	Gambro-Hospal
Polyethersulfone (Diapes®)	Membrana
Polyamide (PA)	Gambro
Polymethylmethacrylate (PMMA)	Toray
Ethylene vinyl-alcohol copolymer	Kuraray
Polycarbonate polyether copolymer (PPC Gambrane®)	Gambro

It is clear that the separation performance of hemodialysis membranes should mimic the one of natural kidney. Figure 1.5 demonstrates the schematic sieving curves of low-flux (conventional dialysis) and high-flux membranes in relation to the one of a natural kidney. The detailed information about properties and advantages of these membrane types are discussed in the subsequent section.

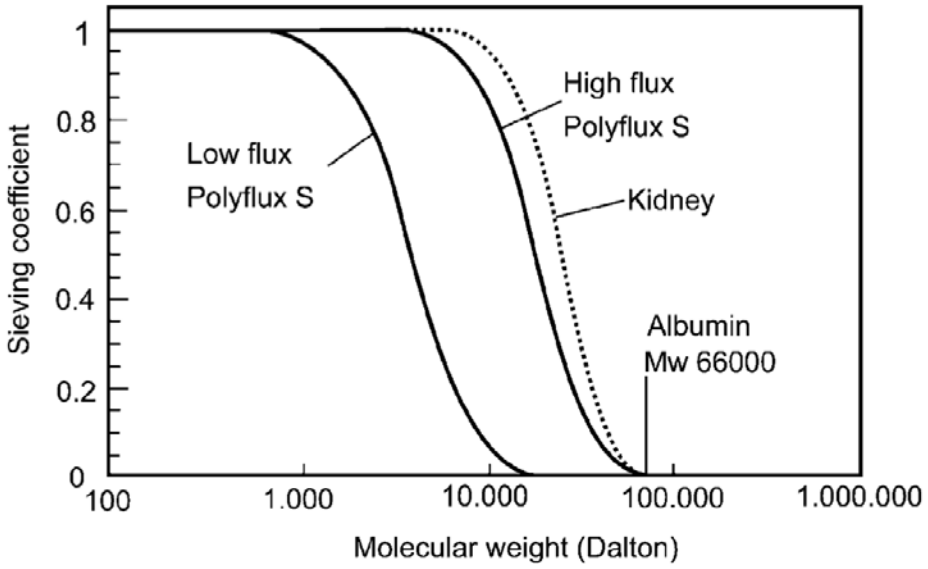

Figure 1.5: Comparison of sieving coefficients of two types of dialysis membranes and natural kidney [60].

As it can be concluded from the curves presented in Figure 1.5, the low-flux membrane allow the free passage only of the molecules with the molecular weight up to 1000 Da, while the compounds with molecular weight from 1000 Da to 10 kDa are only partially transmittable. The larger molecules are fully retained. In parallel, the sieving curve of high-flux membranes is much closer to the one of a kidney. Apart from small molecules, the compound with molecular weight up to 60 kDa can be removed at least partially.

The hemodialysis membrane or more precisely hemodialysis module (dialyzer) is conventionally operated at counter-current mode. This means that the blood (feed) and the solution called dialysate flow in the opposite direction on the different sides of the membrane (this process is discussed in more details in the Section 2.6.1).

2.4 Mass transfer mechanisms in membrane filtration

The membrane for hemodialysis contains pores that allow the passage of small molecules as water, urea, creatinine etc., while larger blood components as white cells, red cells and majority of plasma proteins are retained. The driving force for the permeation of uremic toxins through the dialyzer membrane may be generated by solely diffusion (hemodialysis) or convection (hemofiltration) or by both mechanisms in the same time (hemodiafiltration) [20].

2.4.1 Diffusion

Diffusion is the mechanism of solute transport across the membrane, which is driven by the solute concentration difference between two compartments. This transfer will continue until the moment when the concentration of solutes, which are able to permeate, is equalized. The schematic representation of diffusion is depicted in Figure 1.6.

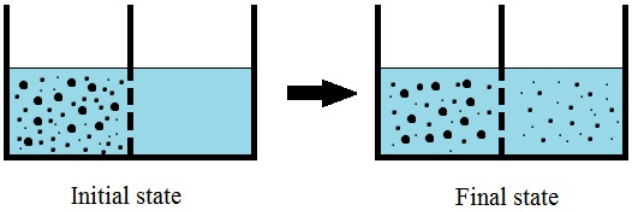

Figure 1.6: Schematic representation of diffusive transport. Initial state (left): the mixture of solutes is present only in one compartment. Final state (right): the equilibrium concentration is achieved only for smaller solutes, due to their ability to permeate through the membrane.

The flux of a solute across the membrane is governed by the Fick s law (Equation 1.4):

$$J_{diff} = -D\frac{dC}{dx} \tag{1.4}$$

Where J_{diff} is the solute flux driven by the diffusion (in $\mathrm{mol\,m^{-2}\,s^{-1}}$), D stands for diffusivity of solute inside the membrane (in $\mathrm{m^2\,s^{-1}}$), $\frac{dC}{dx}$ is the solute concentration gradient across the membrane. The sign minus is demonstrating that solute transport occurs from the zone with higher concentration to the one with lower concentration. The integration of Equation 1.4 with boundary layers set at blood and dialysate sides of the membrane leads to the standard form of solute flux driven by diffusion (Equation 1.5):

$$J_{diff} = \frac{D}{l}(C_b - C_d) \tag{1.5}$$

where l is the thickness of membrane, C_b and C_d are concentrations of the permeating solute in the blood and dialysate side, respectively.

Due to the fact that diffusion coefficient decreases with the increase of the compound molecular weight [61], this mechanism is more significant for the removal of small

solutes as urea and creatinine. Thus, the separation of larger compounds (i.e, small proteins) by diffusion is hampered and requires application of another mechanism, convection.

2.4.2 Convection

The convective transport through the membrane results from the presence of the pressure gradient across the membrane. By applying the excessive pressure from one side, the transport of water and solutes of sizes inferior to the membrane pore size starts to occur (Figure 1.7).

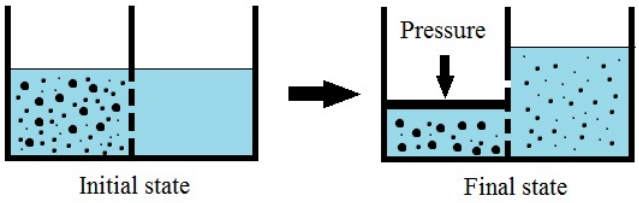

Figure 1.7: Schematic representation of convective transport.

In case, when a certain concentration of solutes is present in both blood and dialysate sides, the transmembrane pressure (TMP) is defined as the difference between the hydrostatic pressure and the oncotic pressure ($\Delta\Pi$) as in Equation 1.6 [23]:

$$\Delta p = \frac{P_{b_{in}} - P_{b_{out}}}{2} - \frac{P_{d_{in}} - P_{d_{in}}}{2} - \Delta\Pi \tag{1.6}$$

Where $P_{b_{in}}$, $P_{b_{out}}$, $P_{d_{in}}$, $P_{d_{out}}$ are the pressures in the inlet and outlet of the blood and dialysate sides, respectively.

In order to explain the concept of the oncotic pressure, it is important to point out that the concentration of the large solutes with sizes superior to the size of the membrane pores increases from the "initial" to the "final" state depicted in Figure 1.7. Keeping in mind that water tends to move from the less concentrated region to a more concentrated one to make them equilibrated, in the "final" state it "prefers" to move from the right-hand to the left-hands side across the semi-permeable barrier. Consequently, the applied hydrostatic pressure is partially counter-balanced by the pressure generated by water in the right-hand side, which is known as oncotic pressure. In principle, oncotic pressure is also called colloid osmotic pressure, which indicates that this pressure has a similar nature with

osmotic one, but is generated by the species of different nature. Particularly, the term "osmotic pressure" is used for solutions of salts, while the term "oncotic pressure" is applicable for solutions of the proteins or colloidal matter.

The solute flux J_s across the membrane is directly proportional to its local concentration C_s, the flux of solvent J_v and Staverman reflection coefficient σ (Equation 1.7) [20]:

$$J_s = \big(1 - \sigma\big) J_v C_s \tag{1.7}$$

Where $(1 - \sigma)$ term represents the fraction of J_v permeating through the membrane in pores large enough to allow passage of a given solute [62]. Thus, for small solutes like urea this term is close to 1, meaning that all pores contributing to the transfer of solvent participating in the transport of solute as well. In contrary, for larger molecules like proteins this term is approaching 0 due to steric hindrances.

In order to characterize the performance of hemodialyzer the parameter called ultrafiltration coefficient K_{UF} in units of $\mathrm{mL\,h^{-1}\,mbar^{-1}}$ is used and is defined as in Equation 1.8:

$$K_{UF} = \frac{J_v A}{TMP} \tag{1.8}$$

Where A is the total surface area of membrane inside the dialyzer. According to the Equation 1.8 the relation between $J_v A$ and TMP is linear; however, it s valid only at relatively low values of TMP and is changing at higher values due to the deposition of protein and fibrin on the membrane in the blood side of the hemodialyser [23].

2.4.3 Clearance and dialysance

The clearance and dialysance are two parameters which demonstrate how much blood in mL was purified from particular substance per unit of time. In order to describe these parameters let us consider the dialyzer as shown in Figure 1.8.

Where Q stands for the flow rate in $\mathrm{mL\,h^{-1}}$ or $\mathrm{mL\,min^{-1}}$ and C is concentration in $\mathrm{mg\,mL^{-1}}$, subscripts b and d represent blood and dialysate sides, while in and out refer to inlet and outlet, respectively.

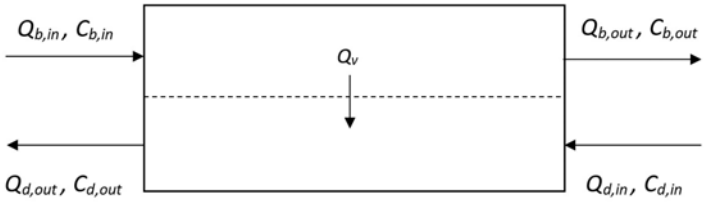

Figure 1.8: Schematic representation of flows inside the hemodialyser.

Now, let us write a mass balance for the dialyzer Equation 1.9:

$$Q_{b,in}C_{b,in} + Q_{d,in}C_{d,in} = Q_{b,out}C_{b,out} + Q_{d,out}C_{d,out} \tag{1.9}$$

Assuming that the mass transfer occurs both by diffusion and convection, and, logically, some part of solution is transferred from the blood to the dialysate with the flow rate Q_v, one may substitute $Q_{b,out}$ and $Q_{d,out}$ as $Q_{b,out}$=$Q_{b,in}$–Q_v and $Q_{d,out}$=$Q_{d,in}$+Q_v to get mass balance in a new form (Equation 1.10):

$$Q_{b,in}C_{b,in} + Q_{d,in}C_{d,in} = \big(Q_{b,in} - Q_v\big)C_{b,out} + \big(Q_{d,in} + Q_v\big)C_{d,out} \tag{1.10}$$

After rearrangement of Equation 1.10:

$$Q_{b,in}\big(C_{b,in} - C_{b,out}\big) + Q_vC_{b,out} = Q_{d,in}\big(C_{d,out} - C_{d,in}\big) + Q_vC_{d,out} \tag{1.11}$$

In such form of the mass balance, the left part is describing the amount of solute leaving from the blood, while the right side expresses the quantity of solute transferred to dialysate. In addition, the first term in each side represents the diffusive contribution to the transfer, while the right term is the convective component [33].

The dialysance Dl expresses the amount of solute leaving from the blood or appearing in the dialysate over the concentration driving force Equation 1.12:

$$Dl = \frac{Q_{b,in}C_{b,in} - Q_{b,out}C_{b,out}}{C_{b,in} - C_{d,in}} \tag{1.12}$$

By application of a condition that the concentration of toxin in the dialysate before entering the dialyzer is equal to 0 ($C_{d,in} = 0$) the definition of clearance K is obtained (Equation 1.13):

$$K = \frac{Q_{b,in}C_{b,in} - Q_{b,out}C_{b,out}}{C_{b,in}} \tag{1.13}$$

Moreover, in case when convection is not involved in the solute transfer ($Q_v = 0$), meaning that the flow rate in the inlet and outlet of each compartment is the same, the expressions of clearance and dialysance are reduced and are turned into diffusive forms:

$$K_{diff} = \frac{Q_{b,in}\big(C_{b,in} - C_{b,out}\big)}{C_{b,in}} \tag{1.14}$$

$$Dl_{diff} = \frac{Q_{b,in}\big(C_{b,in} - C_{b,out}\big)}{C_{b,in} - C_{d,in}} \tag{1.15}$$

Thus, the general forms of dialysance and clearance with separated convective and diffusive terms are (Equation 1.16 and Equation 1.17):

$$K = \frac{Q_{b,in}\big(C_{b,in} - C_{b,out}\big)}{C_{b,in}} + Q_v\frac{C_{b,out}}{C_{b,in}} \tag{1.16}$$

$$Dl = \frac{Q_{b,in}\big(C_{b,in} - C_{b,out}\big)}{C_{b,in} - C_{d,in}} + Q_v\frac{C_{b,out}}{C_{b,in} - C_{d,in}} \tag{1.17}$$

Where the first term in both equations reflects the diffusive part and the second term expresses the convective component. Finally, the clearance of dialyzer is normally defined only by its diffusive component and with use of such components as urea, creatinine, phosphate, and vitamin B_{12} [23].

2.5 Concentration polarization

As the filtration process progresses, the components of the feed solution start to move towards the membrane. However, since the permeation of solute with sizes close or greater than the size of membrane pore is hindered, concentration gradients form in the proximity of the membrane surface (Figure 1.9).

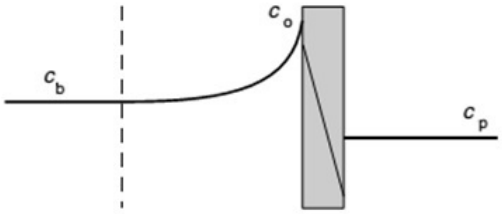

Figure 1.9: Schematic representation of concentration polarization. (C_b and C_p stand for the solute concentrations in the bulk solution and the permeate, C_0 – solute concentration in the proximity to the membrane) [54].

As it can be seen from Figure 1.9, the concentration polarization is located only in the feed side. However, if the membrane module is operated in co- or counter-current mode, the variation of concentration from membrane surface to bulk solution may be also observed in the permeate side.

One of approaches to describe the effect of concentration polarization is to model this phenomenon by using an assumption that a thin layer of unmixed fluid, with thickness δ, exists between the membrane surface and the well-mixed bulk solution [54]. The thickness of this layer is dependent on the different parameters such as properties of the solution (viscosity, concentration), intensity of flows towards and along the membrane, dimensions of the filtration module etc. In order to quantify the thickness of this boundary layer the specific hydrodynamic correlation collected in textbooks should be used. Finally, aiming at reducing the concentration polarization, different strategies may be applied, the main of which is the increase of the fluid flow velocity along the membrane surface.

2.6 Concept of membrane- and adsorbent-based renal replacement therapies

2.6.1 Hemodialysis

Hemodialysis is the most wide-spread membrane-based treatment for ESRD, and only in 2011 it was provided for about 1.9 million patients worldwide [63]. Hemodialysis procedure comprises the pumping of blood through the extracorporeal dialyzer, where its purification occurs. Modern dialyzer (Figure 1.10) contains hollow fiber membranes of different quantity (up to 15 000) and total filtration area

(up to 2.5 m^2) [20, 64] and the blood priming volume ranges from 75 mL to 200 mL [65].

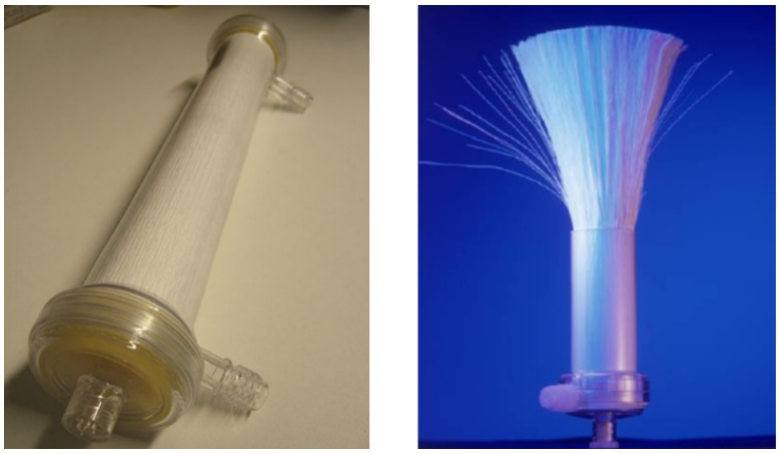

Figure 1.10: Modern hemodialyser [20].

Inside the dialyzer the blood is conventionally flowing inside the fiber, while the dialysate solution is passing in the shell side in the counter-current direction (Figure 1.11).

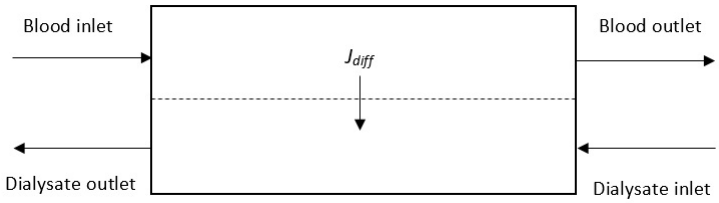

Figure 1.11: Schematic representation of flows in hemodialysis.

The composition of the dialysate is similar to the normal body fluid in terms of electrolyte composition, but is completely toxin-free. As so, the diffusive transport of toxins across the membrane is generated by the difference in their concentrations. Such approach allows the removal of toxins, and prevention of changes in the salts content in the blood stream [20].

As it was already discussed, at counter-current operation mode, the concentration polarization takes place on both sides of the membrane. In order to partially overcome its influence, the augmentation of the mass transfer is achieved by the increase of the dialysate flow rate up to 2 times higher value than that of the blood flow [66]. During hemodialysis the hollow fiber membrane plays the role of a barrier for some species, while allowing the passage of other ones. Which blood

components and to which extent are able to be removed is mainly dependent on the molecular weight of solute: the higher molecular weight is, the lower propensity to be transferred. Additionally, the type of membrane is a second key factor in the blood purification process. Dialysis membranes are categorized as: *low- ux* (LF) with water permeability in the range 0.03-$0.09\ \mathrm{mL\,h^{-1}\,m^{-2}\,Pa^{-1}}$ and *high- ux* (HFl) with water permeability higher than $0.15\ \mathrm{mL\,h^{-1}\,m^{-2}\,Pa^{-1}}$. Membranes belonging to the former type possess smaller pores, thus allowing passage of small solutes, while the latter ones have larger pores, which results in possibility to remove some part of larger compounds (middle size uremic toxins) [20]. Some research groups reported that high-flux membranes may contribute to such undesired side effect, as albumin loss [67]. Thus, the basic requirement for membranes of this type is narrow pore size distribution (sharp selectivity curve, see Figure 1.3), allowing the passage of middle solutes and retaining larger compounds. This property of dialysis membrane is still to be developed and optimized.

Apart from larger pores size feature of HFl membrane, the second important parameter is the *internal ltration rate*. Since there is no convection in dialysis, the volume of the blood and the dialysate compartment remain unchanged, meaning that the net filtration rate is 0. However, due to pressure drop along the fibers and, consequently, pressure gradient across the membrane, the local internal filtration occurs. Some part of water with some toxins may be transferred from blood and then permeate back (backfiltration) from the dialysate side (Figure 1.12).

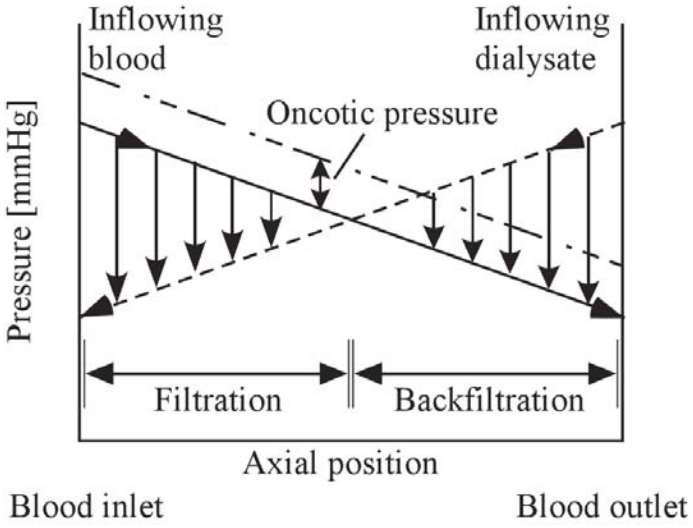

Figure 1.12: Schematic representation of internal filtration inside the dialyzer [68].

As it can be seen from Figure 1.12 at the beginning of dialyzer (blood inlet), the blood pressure is superior to the pressure in the dialysate compartment. Thus, the local convective transfer from the blood to the dialysate occurs in this region. In contrary, as blood moving forward along the dialyzer the pressure inside this compartment reduces, while the pressure in the dialysate side increases as we get closer to the dialysate inlet. Hence, at some point along the length of the dialyzer the pressures in both compartments equalize and then the pressure in dialysate start to dominate over the one in the blood side. As so, the local convective backflow starts to take place and it compensates the blood volume reduced at the beginning of the dialyzer. Consequently, in order to preclude a blood contamination by backflowing liquid, the specific additional requirements to the dialysate composition and purity should be met (details in the following section).

HFl dialysis seems to be advantageous to the low-flux dialysis in terms of the possibility to remove some part of middle molecules; however, their removal is still limited by much smaller diffusivity in comparison to small uremic retention solutes [48]. Thus, in addition to diffusion-based dialysis, the artificial kidney may be operated in two other modes: hemofiltration and hemodiafiltration, the most important feature of which is the presence of convective term in the mass transfer. Thus, these procedures are also referred as *convective therapies*.

2.6.2 Hemofiltration

In hemofiltration (HF) the movement of solutes across a semi-permeable membrane is governed solely by convection (Figure 1.13), generated by hydrostatic pressure difference, because no dialysate is used, and consequently, there is no concentration gradient across the membrane [20].

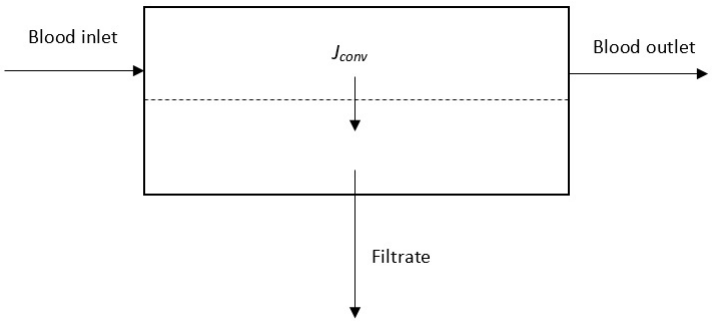

Figure 1.13: Schematic representation of flows in hemofiltration.

Due to the convection, solutes of different sizes, but smaller than the membrane pore size, are dragged through the membrane along with the flow of water. While the blood components with sizes larger than the membrane pores remain inside the blood and their concentration increases as water is removed through the membrane. To maintain the flux and to avoid excessive rise of blood viscosity, the replacement fluid should be injected, before or after the filtration unit, in the quantity equal to removed water volume minus its desired removal. Normally, solutes of the molecular weight up to $15\ \mathrm{kDa}$ can be removed from the blood by HF, meaning that larger important blood components as cells and large proteins are retained. The small toxins in this case are able to pass freely through the membrane pores, while only some part of middle sized molecules is able to be filtered out [69]. Thus, the application of convection provides a better solution for poor removal of the middle-sized solutes compared to the hemodialysis. However, it still does not allow the complete elimination of these toxins. On the other hand, hemofiltration offers less effective removal of small molecular weight toxins, because of the limitations in the maximal volume of water, which can be removed from the blood [33]. Thus, it seems to be beneficial and reasonable to combine the positive features of hemodialysis that is sufficient removal of small toxins together with the strength of hemofiltration, namely facilitated elimination of the middle-sized uremic retention solutes.

2.6.3 Hemodiafiltration

Practically, hemodiafiltration (HDF) is the combination of hemodialysis and hemofiltration, because both diffusion and convection contribute to the uremic retention solutes removal (Figure 1.14) [33].

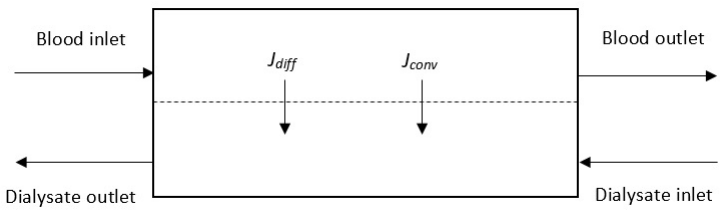

Figure 1.14: Schematic representation of flows in hemodiafiltration.

During HDF a toxin-free dialysate is passing in the shell side of dialyzer counter currently to the blood stream, which results in the generation of the concentration gradient responsible for the diffusive component of the mass transfer, which is of

higher importance for smaller molecules. On the other hand, the difference in hydrostatic pressure applied (up to 0.4 bar [70]) between the blood and dialysate side governs the convective transport (ultrafiltration), which contributes to the removal of excessive water and solutes with higher molecular weights [71, 72]. Normally, the amount of removed water is far greater than it is required; hence, an external fluid infusion is an important aspect. The substitute fluid should be ultrapure with the content of bacteria and endotoxins lower than 0.1 colony forming units per mL and 0.05 endotoxin unit per mL, respectively [72]. Initially, the substitution fluid was supplied in the costly disposable plastic bags, which limited the available volume (around 4 L) per session of treatment called conventional HDF. But then, the new approach of the infusion fluid preparation was developed. The dialysis machine was equipped with a purification unit, which allows to purify the spent dialysate and use it again for the water replacement. This approach allowed the commencement of so called online-HDF [48], which may be performed in one out of two generally-accepted manners of the substitution fluid infusion: before and after dialyzer. The former technique is called predilution HDF, while the latter is referred as postdilution HDF. In some cases, both techniques are combined, resulting in mixed-dilution HDF [73]. Theoretically, the predilution hemodialysis seems to be advantageous from the point of view that it prevents the critical increase of the blood viscosity and, consequently, clotting inside the dialyzer. On the other hand, the predilution results in the reduction of toxins concentration just before the entrance of dialyzer resulting in the decrease of their clearances that, in turn, reduces the efficiency of the overall process [74]. Numerous studies were conducted in order to compare pre- and postdilution HDF modes with each other [75-78], as well as with low-flux dialysis (LFD) and high-flux dialysis (HFD) [79], and demonstrated the better outcomes of HDF.

However, there are still some limitations remaining in all blood purification techniques. The main of which is necessity of constant quantification of endotoxins present in the system, while this analysis is regularly performed by the external laboratories [80].

2.6.4 Hemoperfusion

Hemoperfusion is an alternative blood purification technique, in which the column filled with adsorbent capable of toxin removal is used instead of the semi-permeable membrane. There are two types of sorbents, which may be used: sorbents with

hydrophobic properties (activated carbon, nonionic resins), and those that remove molecules by chemical affinity (ion exchange resins) [81]. In 1964 Yatzidis [82] has demonstrated that the effective removal of various toxins is possible by using uncoated activated carbon. However, such approach possesses several threats, as platelet depletion, hemolysis, hypertension, possible release of the particles to the blood stream [81, 83, 84]. One possible way to overcome these issues introduced by Chang [85] is to cover sorbent with the layer of coating material. However, this leads to the decrease of the filtration efficiency due to the presence of an additional barrier which has to be passed by the toxin before it reaches the adsorbent [43]. Moreover, unlike convective therapies hemoperfusion is not able to remove excess of water and provide balancing of the blood composition. Thus, some researchers suggested to apply the principles of hemoperfusion together with other blood purification techniques [84, 86, 87].

3 Middle molecules removal by renal replacement therapies

As it was already discussed, β_2-microglobulin is responsible for the undesired side effect as dialysis related amyloidosis and is currently considered as the best marker for middle molecules for dialysis dose quantification. Due to such undesired side effects of dialysis treatment, the great effort in development of other blood purification techniques, which would allow the simultaneous removal of small and middle uremic toxins (especially, β_2-microglobulin) was done. As it was discussed in the Section 2.6, based on the manner of the toxin elimination applied, these techniques are categorized as *membrane-based* and *adsorbent-based* strategies. Therefore, Section 3 is devoted to the analysis and comparison of the clinical efficiencies of the various methods.

3.1 Membrane-based techniques

Number of old and recent studies revealed that the low-flux dialysis (LFD) membranes do not enable the removal of middle solutes to a significant extent. Beta$_2$-microglobulin accumulation progresses in patients treated with such membranes [2, 88, 89]. Thus, the one part of research was redirected to the high-flux dialysis (HFD), which showed promising results even for patients

switched from LFD [90-92]. The effect of HFD use on the risks of CTS and mortality were evaluated by Koda *et al*. [93] based on the results collected during 26 years from 819 patients. Shifting from LFD to HFD reduced these risks to 0.503 and to 0.613, respectively. Within the frame of another clinical study [94] the comparison of HFD with LFD demonstrated that former technique provides 42% lower CTS risks and almost 28% reduction of plasma β_2m concentration.

The second alternative to LFD is hemofiltration (HF), where solutes are exclusively removed by means of convection, generated by the pressure difference. High blood flow rates and high-flux membranes with high hydraulic permeability are essential for this treatment strategy. However, due to aforementioned reasons, there are very few reports about its clinical trials [48, 79]. For example, Kramer *et al*. [95] studied the clearances of various compounds (including β_2m) using three different membranes. These membranes exhibited different sieving properties, which is reflected by the sieving coefficients for β_2m: 0.5 (AN69®), 0.54 (Polysulfone), and 0.35 (Polyamide), while all three membrane allowed the free passage of creatinine. As so, the clearance of creatinine was $90\ \mathrm{mL\,min^{-1}}$ for AN69®, and $105\ \mathrm{mL\,min^{-1}}$ for Polysulfone and Polyamide membranes. The average β_2m clearances were $33\ \mathrm{mL\,min^{-1}}$ for polyamide, $44\ \mathrm{mL\,min^{-1}}$ for AN69® and $54\ \mathrm{mL\,min^{-1}}$ for polysulfone membrane. Santoro with coworkers [92] clinically compared online-HF with LFD by monitoring the conditions of 64 patients, equally separated for each treatment type. Significant improvement in survival in HF (78%) in comparison to LFD (57%) was observed. In the same time, HF provided superior to LFD removal of β_2m, leading to its blood levels of $24\ \mathrm{mg\,dL^{-1}}$ versus $37\ \mathrm{mg\,dL^{-1}}$.

Hemodiafiltration is the process in which high flux membrane efficiency is additionally improved by the presence of convection (ultrafiltration). As a result, the maximal clearance for both small and middle size molecules is achieved [96, 97]. The important role in the HDF outcome plays the place of replacement fluid infusion, before or after the filtration unit (pre- or post-dilution). Ahrenholz *et al*. [98] demonstrated that postdilution mode is more efficient than predilution. This finding was attributed to the observed thicker protein boundary layer in case of postdilution, which was formed because the convective forces were applied to the blood with the relatively higher proteins concentration [43].

The volume of substitution fluid provided per session of treatment is also of high importance. The shift from conventional HDF to online-HDF enable use of larger

quantities of replacement solution and, as a result, improves the outcomes of the treatment. Maduell *et al.* [99] compared the β_2m reduction ratio achieved by both conventional and online-HDF. The increase of substitution volume from 4 to 22.5 L per session resulted in augmentation of β_2m reduction ratio from 56.1 to 71.1 %.

Number of studies demonstrated superior removal characteristics provided by HDF in comparison to other renal replacement strategies [8, 100]. Ward *et al.* [101] analyzed the difference between 21 L substitution volume HDF and HFD in terms of removal of both small (urea and creatinine) and middle (β_2-microglobulin and complement factor D) uremic retention solutes and came to conclusion that the removals of all analyzed compounds were greater for HDF. Recently, Cornelis *et al.* [102] investigated the influence of treatment duration on the outcome of the conventional dialysis and hemodiafiltration. The results revealed that removal of small molecules (urea, creatinine, uric acid and phosphate) were equally increased in prolonged HD and HDF treatments. In the same time, the increased removal of middle molecules (β_2-microglobulin and fibroblast growth factor 23) was also observed for both extended modalities, but in this case, the extent of improvement was more significant for HDF. The positive influence of the treatment duration on the removal of β_2-microglobulin may be attributed to its intracellular distribution in the organism during ESRD [103]. This implies that before removal from organism, β_2m has to transfer into the intravascular compartment across the capillary wall, which is not rapid (transcapillary transfer rate is approximately $100\ \mathrm{mL\,min^{-1}}$), which, in turn, provides an explanation for the frequently observed β_2-microglobulin concentration rebound after the end of treatment [104].

Despite all the discussed advantages of the convective renal replacement therapies, the financial constrain is still crucial limiting factor, which prevents their spreading and extensive use [89]. According to Tang *et al.* [8], the cost of one treatment session by HDF is slightly higher than that of HFD and 2-fold higher than the price of the low-flux dialysis. Authors also emphasized that it is possible to deduct 30% of the expenses per session by reuse of the dialysis module 30 times. However, the process of dialyzer cleaning is still not well-established and optimal reprocessing agents are not standardized.

3.2 Adsorbent-based techniques

Hemoperfusion (HP), unlike convective therapies does not enable removal of the excess of water and balancing of blood composition. In contrary, HP may increase the middle solutes removal capacity when it is used in combination with membrane-based techniques. Several commercially available adsorbent columns were developed (Lixelle and BetaSorb) and other were tested in small scale [9, 43].

One of the main adsorbents tested for the blood purification is activated carbon (charcoal). Its high adsorptive capacity is achieved by a specifically designed surface porosity and large surface areas. Optimal size of pores aiming at the removal of middle uremic retention solutes should be in the range of 2-20 nm (mesopores) [105]. In these pores solutes are trapped by means of physical Van der Waals forces, and this adsorption is frequently described by Langmuir or Freundlich isotherms [9].

The therapeutic column Lixelle was developed by Japanese company Kaneka Corporation for a selective adsorption of β_2m. The column is filled with biocompatible cellulose beads with the average diameter of 460 µm and with covalently bound hexadecyl groups, as hydrophobic ligands for hydrophobic compounds removal. The beads porosity was designed in the manner that allowed adsorption of the small proteins (middle solutes) and exclusion of larger protein albumin. Two sizes of Lixelle column are available: larger S-35 with volume of 350 mL and smaller S-15 of 150 mL. These single-use columns are used in combination with dialyzer (Figure 1.15) and allows blood flow rates up to $250\,\mathrm{mL\,min^{-1}}$ [3].

It was found that the β_2m adsorption capacity is more than 1 mg per 1 mL of beads [106]. In addition, the total β_2m removal by Lixelle in combination with a dialyzer is in the range 200- 300 mg, which resulted in great reduction of β_2m post-treatment level [107]. Other studies demonstrated that not just β_2m is adsorbed by Lixelle, but also other proteins, including such molecules as retinol-binding protein, interleukin-1β, and interleukin-6, which also have to be removed from the blood stream [108, 109].

BetaSorb is a second commercially available adsorption column intended to improve the poor performance of conventional dialysis in middle solutes elimination. The device contains tissue-compatible small beads of hypercrosslinked polymer [110].

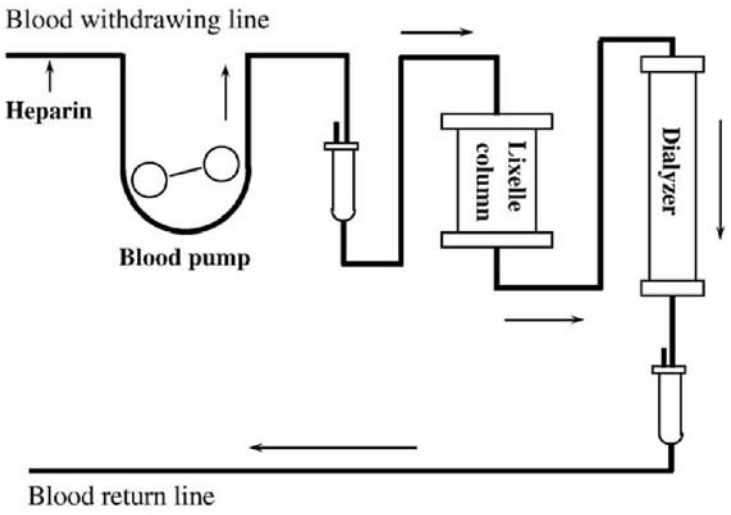

Figure 1.15: Schematic representation of dialysis line with integrated Lixelle column [3].

As Lixelle column, BetaSorb is also used in combination with a dialyzer. In one of studies HFD was compared with combined HFD/BetaSorb treatment. The removal of several middle molecules (β_2m, angiogenin, interleukin-18, retinol-binding protein, leptin) was significantly higher in the combined therapy. For example, combination of two strategies enable β_2m removal of around $400\ \mathrm{mg}$ per session [9]. Despite the highlighted advantages, there are also some significant drawbacks. One of which, the combination of two methods results in the increase of blood priming volume, which may lead to adverse effects as temporary hypotension.

3.3 Novel approach in combination of membrane- and adsorption-based techniques

Aiming to overcome the aforementioned complication, the new elegant concept of a double-layer membrane combining the particle-free and adsorbent loaded layers was proposed (Figure 1.16).

The aim of the particle-free top layer is to provide sufficient biocompatibility and prevent direct contact between biological fluid and sorbent (this need was discussed in Section 2.6.4), while the presence of adsorbent in the second layer improves the overall toxin removal [11]. Hence, this approach allows the toxin removal by means of membrane filtration and adsorption in one step. It was demonstrated that such membrane design provides perfect adsorbent particles distribution without cluster formation and their sufficient accessibility for the toxins. Moreover, the viability of

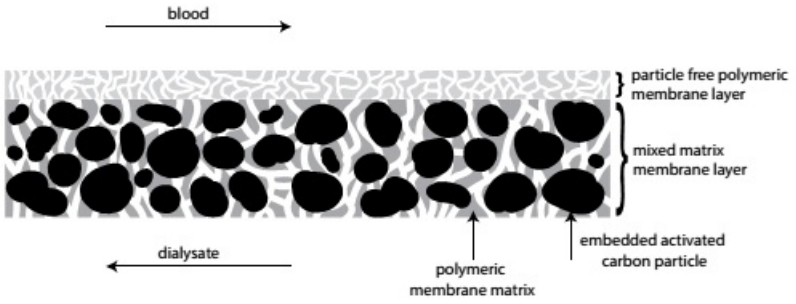

Figure 1.16: Schematic representation of double-layer mixed matrix membrane for blood purification [10].

this concept was proven for creatinine and some protein-bound toxins under both convective and diffusive experiments [7].

Nevertheless, the extent to which mixed matrix layer can elevate the elimination of the uremic toxins from various groups remains uncertain and the optimal membrane design still has to be determined. Therefore, there is a need of the mathematical model, which would provide the description of the interplay of three toxin removal mechanisms involved in such complex membrane. Which, in turn, would serve as a tool for the membrane design and for the prediction of its performance.

4 Protein-related fouling of blood-contacting membranes

Almost immediately after a synthetic membrane is brought in contact with blood, the protein adsorption on the surface of material starts to occur. The extent of this process is dependent on the properties of the membrane material, such as chemical composition, charge, morphology, roughness etc [11, 12]. Besides, the membrane for the blood purification application is intended to allow removal of the toxins of defined molecular weight range and provide a minimal harmful effect on the patient. However, adsorption of protein may lead to some issues with material biocompatibility such as blood coagulation, complement activation, blood cells adhesion [13-16]. In addition, the accumulation of the protein on the membrane surface leads to a formation of a deposit layer, which alters the selective properties of the virgin membrane. Besides, the formation of such layer creates an additional resistance to a transfer of toxins through the membrane, which leads to a decrease of the overall efficiency of the blood purification [12].

Taking into account that the patient s blood is contacting large surface areas of

membranes during around 150 blood purification treatments per year, the investigation of hemodialysis material in terms of its propensity to protein adsorption is essential [111]. Some researches were performed to analyze the total protein adsorption on different membrane materials. Mares *et al.* [112] evaluated the total protein adsorption on the hemodialysis polysulfone membranes after the clinical treatment of 5 patients. In the probes of eluate 153 proteins were detected, 84 of which were common for all the patients and 57 of them were identified by mass spectrometry. Moreover, authors found out that the molecular weights of 95% of detected proteins were in the range of 18-85 kDa. In addition, Bonomini *et al.* [42] performed the laboratory study of total protein adsorption on two commercially available dialysis membranes made of cellulose diacetate (CDA) and ethylenevinyl alcohol (EVAL). For both membranes the number of detected proteins was almost the same, 284 and 280, respectively. However, the mass of proteins eluted by 1 mL of specific buffer was significantly higher in case of CDA membrane: 1.2 mg vs 2.4 mg, which clearly justifies the impact of the membrane material on the protein-surface interaction.

The one of generally accepted strategies to reduce the protein adsorption is balancing of hydrophilic and hydrophobic polymer regions distribution on the surface. Two approaches are used to combine hydrophilic and hydrophobic properties in one material: copolymerization of monomers with different properties and blending of hydrophilic polymer with the hydrophobic one [111, 113-115]. For instance, Ward *et al.* [116] fabricated membranes from the blend of polysulfone (PS) and polyvinyl pyrrolidone (PVP) dissolved in dimethylacetamide. The resulting membrane was more hydrophilic in comparison to simple PS based, which resulted in a lower protein adsorption, which in turn resulted in the improved biocompatibility. In another research, Su *et al.* [117] performed an in vitro and in vivo characterization of hollow-fiber polyethersulfone (PES)/PVP blend membrane. Fabricated membrane demonstrated promising results in terms of urea, creatinine and β_2-microglobulin removals without visible changes in blood biochemistry and only with a small loss of albumin.

Despite the negative effects of protein adsorption, it also can have the beneficial function. Since the class of middle uremic toxins is mainly represented by proteins, their adsorption on dialysis membrane can be viewed as additional mechanism of removal from the blood stream [17]. The effect of membrane type and charge on the amount of adsorbed small proteins, especially β_2-microglobulin, was investigated by some research groups [118-120]. It was demonstrated that for some materials,

like polysulfone or acrylonitrile/methallyl sulphonate copolymer, this phenomena is less significant, while in case of some other materials (polyacrylonitrile, polymethylmetacrylate), small protein adsorption can provide an important improvement in total removal capacity [119, 121]. On the other hand, even though the protein adsorption may be considered beneficial in some regard, it should be closely controlled in order to reduce the possibility of various side effects occurrence (blood coagulation, complement activation, blood cells adhesion etc).

Optical methods of protein fouling analysis are the most straightforward non-invasive techniques, which allow "truly real-time" and sensitive observation of phenomena taking place on the membrane surface. The fluorescence labeling provides an important improvement in terms of contrast enhancement [122]. There are a lot of fluorophores which may be used for the protein labeling. Some of the most common ones are: fluorescein (FITC-green), tetramethyl rhodamine (TRITC-red), sulphorhodamine sulphonylchloride (Texas Red) and Rhodamine B (RITC-red). In case of multi-labeling experiments (more than one compound is stained), the selection of dyes should avoid the overlapping of excitation/emission wavelengths [123]. For instance, Crespo *et al*. [124] performed the experiment with FITC and Texas Red dyes for staining of three different proteins (BSA, β-lactoglobulin and γ-globulin) and experimentally proved the absence of emission spectra overlapping. As an alternative approach, the fluorescent image acquisition should be made separately for each component of mixture with subsequent superimposition in order to gather the signals from all proteins in a single picture [125].

5 Microfluidics – as a tool to shift research from macro to a microscale

Recently, a lot of scientific effort was devoted to the miniaturization of devices used in the field of chemistry, biology, engineering etc [126, 127]. Over last decades, the significant interest was attracted by the microfluidics devices, due to the fact that in comparison to the conventional engineering facilities they provide several advantages, such as ease in portability, integration of process and instrumentation, micro quantities of reactants, shortened processing time, better control and reliability, reduced energy demand etc [128]. Moreover, it was demonstrated that

there is a possibility of integration of the membrane functionality into a microfluidic devices [129, 130] or even placement of the membrane itself in the microchip [131, 132]. Both these approaches were used to down-scale standard membrane function, such as separation, purification, dialysis, sample pre-treatment [53]. As so, it became possible to perform membrane-based separation at the micro scale. In particular, it was demonstrated that such devices can be successfully used for the extraction of sulfide from water and oil [132], glucose recovery [133] and other biomedical applications [131, 134, 135].

The main representative of materials used for the fabrication of the microchips is polydimethylsiloxane (PDMS), due to its relatively low price, optical transparency, chemical inertness, non-toxicity and because it is easily molded [136-138]. However, despite these advantages, PDMS possesses significant drawbacks which limits its use in some conditions and applications. Firstly, PDMS is a hydrophobic material, which means that to work with aqueous solutions the additional pumping system is required or the complex hydrophilization procedures have to be applied to overcome this limitation [136]. Secondly, PDMS absorbs small molecules into its matrix and is gas permeable [139], which means that PDMS itself possesses the properties of a membrane. Finally, PDMS is easily deformable which can become an issue for application requiring elevated pressures, because it may lead to the changes in device geometry [139] and/or integrity [135]. Therefore, other materials with properties allowing to overcome highlighted limitations were proposed. One of such materials is Norland Optical Adhesive (NOA), which is optically transparent, inherently hydrophilic [140], and possesses greater Young s modulus than one of PDMS [136]. It means that NOA has a better mechanical strength and is less prone to the deformations under the applied pressure. Moreover, several studies revealed the superior long-term biocompatibility of NOA compared to PDMS [139], which makes this material more attractive from the biomedical viewpoint. Finally, Bartolo *et al*. [141] demonstrated the 4 times smaller autofluorescence of NOA than of PDMS, indicating that NOA is a suitable material for application where the fluorescence-based detection is used.

One of aforementioned advantages provided by the microfluidic devices over the conventional macroscale devices is better control (possibility of a rapid sample collection and analysis), which may be achieved by coupling of a microchip with other analytical tools. For example, Gao *et al*. [142] connected the microchip with electrospray ionization mass spectrometry (ESI-MS) aiming at protein identification from the mixture obtained in the microreactor. In another study, Perozziello *et al*.

[143] integrated the microchip with Raman spectroscopy in order to detect small peptides filtered out from the mixture with larger proteins. In order to perform the direct real-time observation of the fouling build-up on the membrane surface, Ngene *et al*. [18] coupled the microchip, made of microstructured membrane, with the camera attached to magnifying lenses. All these examples indicate that coupling of microfluidics devices with other tools is extensively used for the in-depth investigation of membrane processes at the microscale.

In the view of aforementioned reasons and aiming at transferring the research of the membrane-protein interactions from a macro to a micro scale, there is an interest in development of microchip, which would:

1. Be made of NOA material;
2. Consist of two different, but perfectly aligned, systems of microchannels (retentate and permeate sides);
3. Allow easy and direct placement of the polymeric membrane between the systems of microchannels;
4. Enable the integration of fluorescent microscopy for the real-time observation of membrane fouling.

6 Bottlenecks and selected strategy of their resolution

The first blood treatment issue which has to be addressed is absence of a precise control over protein adsorption on the membrane surface. Aiming at tackling this bottleneck it was decided to develop a method of real-time microscopic observation of the membrane surface during its contact with protein solution. For this, the investigation of the membrane-based protein filtration should be transferred from the macroscale (Amicon cell/module of hollow fibers) to the microscale. Hence, Chapter 3 of this work is dedicated to the development and characterization of a novel microfluidics device, with membrane inside. In principle, this device resembles the micro cross flow filtration unit, which, in combination with fluorescent microscopy, allows not only the real-time observation of the protein accumulation on the membrane surface, but it also provides a possibility to transfer the membrane-based filtration from the macro to the microscale. Then, Chapter 4 discusses the membrane fouling induced by a fluorescently labelled small size

protein at the different hydrodynamic conditions and applied transmembrane pressures.

The second problem, which hinders the further efficient development of the double layer membrane concept for the blood purification is the absence of a tool to optimize the membrane design and the process conditions. Hence, Chapter 5 of present thesis is dealing with the development and validation of a mathematical model, which accounts for the presence of three solute removal mechanisms: diffusion, convection, and adsorption. This model allows to predict the influence of various parameters such as molecule diffusivity, membrane thickness, presence of convection, content of adsorptive particles on the flux intensification across the membrane.

7 References

1. NxStage, Medical, End Stage Renal Disease (ESRD): Key Facts and Statistics and Information Regarding Home Hemodialysis Therapy. 2012: http://www.nxstage.com/download/file/fid/419.

2. Ronco, C., A. Heifetz, K. Fox, C. Curtin, A. Brendolan, F. Gastaldon, C. Crepaldi, A. Fortunato, G. Pietribasi, A. Caberlotto, A. Brunello, S.M. Manani, M. Zanella, and G. LaGreca, Beta 2-microglobulin removal by synthetic dialysis membranes. Mechanisms and kinetics of the molecule. *International Journal of Arti cial Organs*, 1997. 20(3): p. 136-143.

3. Kutsuki, H., beta(2)-Microglobulin-selective direct hemoperfusion column for the treatment of dialysis-related amyloidosis. *Biochim Biophys Acta*, 2005. 1753(1): p. 141-5.

4. Johansen, K.L., K. Mulligan, V. Tai, and M. Schambelan, Leptin, body composition, and indices of malnutrition in patients on dialysis. *Journal of the American Society of Nephrology*, 1998. 9(6): p. 1080-1084.

5. Vanholder, R., R. De Smet, G. Glorieux, A. Argiles, U. Baurmeister, P. Brunet, W. Clark, G. Cohen, P.P. De Deyn, R. Deppisch, B. Descamps-Latscha, T. Henle, A. Jorres, H.D. Lemke, Z.A. Massy, J. Passlick-Deetjen, M. Rodriguez, B. Stegmayr, P. Stenvinkel, C. Tetta, C. Wanner, and W. Zidek, Review on uremic toxins: Classification, concentration, and interindividual variability. *Kidney Int*, 2003. 63(5): p. 1934-1943.

6. Drueke, T.B. and Z.A. Massy, Beta2-microglobulin. *Semin Dial*, 2009. 22(4): p. 378-80.

7. Tijink, M.S., M. Wester, G. Glorieux, K.G. Gerritsen, J. Sun, P.C. Swart, Z. Borneman, M. Wessling, R. Vanholder, J.A. Joles, and D. Stamatialis, Mixed matrix hollow fiber membranes for removal of protein-bound toxins from human plasma. *Biomaterials*, 2013. 34(32): p. 7819-28.

8. Tang, H.-L., W.-K. Tsang, K.-S. Fung, C. Tang, H.W.-H. Chan, and K.-L. Tong, On-line hemodiafiltration and high-flux hemodialysis: comparison of efficiency and cost analysis. Hong Kong J *Nephrol* 2001;3(1):21-, 2001. 3(1): p. 21-26.

9. Winchester, J.F., J.A. Salsberg, and N.W. Levin, Beta-2 Microglobulin in ESRD: An In-Depth Review. *Advances in Renal Replacement Therapy*, 2003. 10(4): p. 279-309.

10. Tijink, M.S., M. Wester, J. Sun, A. Saris, L.A. Bolhuis-Versteeg, S. Saiful, J.A. Joles, Z. Borneman, M. Wessling, and D.F. Stamatialis, A novel approach for blood purification: mixed-matrix membranes combining diffusion and adsorption in one step. *Acta Biomater*, 2012. 8(6): p. 2279-87.

11. Werner, C. and H.J. Jacobasch, Surface characterization of polymers for medical devices. International Journal of *Arti cial Organs*, 1999. 22(3): p. 160-176.

12. Sun, S., Y. Yue, X. Huang, and D. Meng, Protein adsorption on blood-contact membranes. *Journal of Membrane Science*, 2003. 222(1-2): p. 3-18.

13. Frank, R.D., J. Weber, H. Dresbach, H. Thelen, C. Weiss, and J. Floege, Role of contact system activation in hemodialyzer-induced thrombogenicity. *Kidney International*, 2001. 60(5): p. 1972-1981.

14. Fujimori, A., H. Naito, and T. Miyazaki, Adsorption of Complement, Cytokines, and Proteins by Different Dialysis Membrane Materials: Evaluation by Confocal Laser Scanning Fluorescence Microscopy. *Arti cial Organs*, 1998. 22(12): p. 1014-1017.

15. Johnson, R.J., Complement activation during extracorporeal therapy - biochemistry, cell biology and clinical relevance. *Nephrology Dialysis Transplantation*, 1994. 9: p. 36-45.

16. Swinford, R.D., S. Baid, and M. Pascual, Dialysis Membrane Adsorption During CRRT. *American Journal of Kidney Diseases*, 1997. 30(5): p. S32-S37.

17. Cheung, A.K., Biocompatibility of Hemodialysis Membranes. *J. Am. Soc. Nephrol.*, 1990. 1: p. 150-161.

18. Ngene, I.S., R.G.H. Lammertink, M. Wessling, and W. van der Meer, A microfluidic membrane chip for in situ fouling characterization. *Journal of Membrane Science*, 2010. 346(1): p. 202-207.

19. Casiday, R. and R. Frey. Maintaining the Body s Chemistry: Dialysis in the Kidneys. 1999; Available from: `http://www.chemistry.wustl.`

edu/~edudev/LabTutorials/Dialysis/Kidneys.html.

20. Stamatialis, D.F., B.J. Papenburg, M. Girones, S. Saiful, S.N.M. Bettahalli, S. Schmitmeier, and M. Wessling, Medical applications of membranes: Drug delivery, artificial organs and tissue engineering. *Journal of Membrane Science*, 2008. 308(1-2): p. 1-34.

21. Bronzino, J.D., *The Biomedical Engineering Handbook, Third Edition* - 3 Volume Set: Tissue Engineering and Artificial Organs. 2006: CRC Press.

22. Levy, M., B. Koeppen, and B. Stanton, *Principles of Physiology*, 4th Edition. 2006: Mosby.

23. Morel, H.,*Equilibre acide-base lors de l hémodia ltration en ligne : modélisation, analyses in vitro et clinique des transferts de bicarbonate, in Laboratoire UMR6600 : BioMécanique et BioIngénierie (BMBI)*. 2009, Université de Technologie de Compiegne.

24. Gary A. Thibodeau and K.T. Patton, *Anatomy & Physiology*. 2002: Mosby; 5 edition.

25. Healthwise, Inc. *Chronic Kidney Disease*. Topic Overview. 2011.

26. Perin, L., S. Da Sacco, and R.E. De Filippo, Regenerative medicine of the kidney. *Adv Drug Deliv Rev*, 2011. 63(4-5): p. 379-87.

27. National, Kidney, Foundation. *Organ Donation and Transplantation Statistics*. 2014.

28. Vanholder, R., G. Glorieux, R. De Smet, N. Lameire, and Eutox, New insights in uremic toxins. *Kidney International*, 2003. 63: p. S6-S10.

29. Vanholder, R., S. Van Laecke, and G. Glorieux, What is new in uremic toxicity? *Pediatric Nephrology*, 2008. 23(8): p. 1211-1221.

30. D Hooge, R., G. Van de Vijver, P.P. Van Bogaert, B. Marescau, R. Vanholder, and P.P. De Deyn, Involvement of voltage- and ligand-gated Ca2+ channels in the neuroexcitatory and synergistic effects of putative uremic neurotoxins. *Kidney International*, 2003. 63(5): p. 1764-1775.

31. Glorieux, G.L., A.W. Dhondt, P. Jacobs, J. Van Langeraert, N.H. Lameire, P.P. De Deyn, and R.C. Vanholder, In vitro study of the potential role of guanidines in leukocyte functions related to atherogenesis and infection.

Kidney International, 2004. 65(6): p. 2184-2192.

32. Cheung, A.K., M.V. Rocco, G. Yan, J.K. Leypoldt, N.W. Levin, T. Greene, L. Agodoa, J. Bailey, G.J. Beck, W. Clark, A.S. Levey, D.B. Ornt, G. Schulman, S. Schwab, B. Teehan, G. Eknoyan, and H.S. Grp, Serum beta-2 microglobulin levels predict mortality in dialysis patients: Results of the HEMO study. *Journal of the American Society of Nephrology*, 2006. 17(2): p. 546-555.

33. Carpi, A., C. Donadio, and G. Tramonti, Progress in hemodialysis - from biotechnology to clinical practice. 2011, Croatia: InTech.

34. Randoux, C., P. Gillery, N. Georges, S. Lavaud, and J. Chanard, Filtration of native and glycated beta-2-microglobulin by charged and neutral dialysis membranes. *Kidney International*, 2001. 60(4): p. 1571-1577.

35. Patzer, J., Principles of Bound Solute Dialysis. *Therapeutic Apheresis and Dialysis*, 2006. 10(2): p. 118-124.

36. Lin, C.-J., C.-F. Pan, H.-L. Liu, C.-K. Chuang, T. Jayakumar, T.-J. Wang, H.-H. Chen, and C.-J. Wu, The role of protein-bound uremic toxins on peripheral artery disease and vascular access failure in patients on hemodialysis. *Atherosclerosis*, 2012. 225(1): p. 173-179.

37. Wu, I.W., K.-H. Hsu, C.-C. Lee, C.-Y. Sun, H.-J. Hsu, C.-J. Tsai, C.-Y. Tzen, Y.-C. Wang, C.-Y. Lin, and M.-S. Wu, p-Cresyl sulphate and indoxyl sulphate predict progression of chronic kidney disease. *Nephrology Dialysis Transplantation*, 2011. 26(3): p. 938-947.

38. Lekawanvijit, S., A. Adrahtas, D.J. Kelly, A.R. Kompa, B.H. Wang, and H. Krum, Does indoxyl sulfate, a uraemic toxin, have direct effects on cardiac fibroblasts and myocytes? *European Heart Journal*, 2010. 31(14): p. 1771-1779.

39. Ito, S., M. Osaka, Y. Higuchi, F. Nishijima, H. Ishii, and M. Yoshida, Indoxyl Sulfate Induces Leukocyte-Endothelial Interactions through Up-regulation of E-selectin. *Journal of Biological Chemistry*, 2010. 285(50): p. 38869-38875.

40. Jourde-Chiche, N., L. Dou, C. Cerini, F. Dignat-George, R. Vanholder, and P. Brunet, Protein-bound toxins–update 2009. *Semin Dial*, 2009. 22(4): p. 334-9.

41. Zhang, H., Microarray analysis reveals the involvement of beta-2

microglobulin (B2M) in human osteoarthritis. Osteoarthritis and Cartilage, 2002. 10(12): p. 950-960.

42. Bonomini, M., B. Pavone, V. Sirolli, F. Del Buono, M. Di Cesare, P. Del Boccio, L. Amoroso, C. Di Ilio, P. Sacchetta, G. Federici, and A. Urbani, Proteomics characterization of protein adsorption onto hemodialysis membranes. *J Proteome Res*, 2006. 5(10): p. 2666-74.

43. Clark, W.R. and J.F. Winchester, Middle Molecules and Small–Molecular-Weight Proteins in ESRD: Properties and Strategies for Their Removal. *Advances in Renal Replacement Therapy*, 2003. 10(4): p. 270-278.

44. Young, G.A., G. Woodrow, S. Kendall, B. Oldroyd, J.H. Turney, A.M. Brownjohn, and M.A. Smith, Increased plasma leptin/fat ratio in patients with chronic renal failure: a cause of malnutrition? *Nephrology Dialysis Transplantation*, 1997. 12(11): p. 2318-2323.

45. Balke, N., U. Holtkamp, W.H. Horl, and H. Tschesche, Inhibition of degranulation of human polymorphonuclear leukocytes by complement-factor-D *Febs Letters*, 1995. 371(3): p. 300-302.

46. Cohen, G., M. Rudnicki, and W.H. Horl, Isolation of modified ubiquitin as a neutrophil chemotaxis inhibitor from uremic patients. *Journal of the American Society of Nephrology*, 1998. 9(3): p. 451-456.

47. Haagweber, M., B. Mai, and W.H. Horl, Isolation of a granulocyte inhibitory protein from uremic patients with homology of beta-2-microglobulin.*Nephrology Dialysis Transplantation*, 1994. 9(4): p. 382-388.

48. Krieter, D.H., H.D. Lemke, B. Canaud, and C. Wanner, Beta(2)-microglobulin removal by extracorporeal renal replacement therapies. *Biochim Biophys Acta*, 2005. 1753(1): p. 146-53.

49. European, Renal Association, II.2 Haemodialysis dose quantification: middle molecules (MM). *Nephrology Dialysis Transplantation*, 2002. 17(suppl 7): p. 21-23.

50. Quaglia, M., C. Carazzone, S. Sabella, R. Colombo, S. Giorgetti, V. Bellotti, and E. De Lorenzi, Search of ligands for the amyloidogenic protein beta2-microglobulin by capillary electrophoresis and other techniques.

Electrophoresis, 2005. 26(21): p. 4055-63.

51. Brancaccio, D., M. Gallieni, T. Niwa, P. Braidotti, and G. Coggi, Ultrastructural localization of advanced glycation end products and beta2-microglobulin in dialysis amyloidosis. *J Nephrol*, 2000. 13(2): p. 129-36.

52. HOU, F.-F., Dialysis-related amyloidosis: role of advanced glycation end product-β_2-microglobulin in joint inflammation. *Hong Kong J Nephrol* 2002;4(2):73, 2002. 4(2): p. 73-77.

53. de Jong, J., R.G. Lammertink, and M. Wessling, Membranes and microfluidics: a review. *Lab on a Chip*, 2006. 6(9): p. 1125-39.

54. Baker, R.W., *Membrane Technology and Applications*. 2004: Wiley.

55. Mulder, M., *Basic Principles of Membrane Technology Second Edition*. 1996: Kluwer.

56. MemRE, The Membrane Research Environment. Molecular Weight Cut-Off. Available from: `$http://membranes.edu.au/wiki/index.php/Molecular_Weight_Cut-Off.$`

57. Systems, K.M. An overview of membrane technology and theory. 2012; Available from: `http://www.kochmembrane.com/PDFs/Application-Bulletins/KMS-Membrane-Theory.aspx.`

58. Bouré, T. and R. Vanholder, Which dialyser membrane to choose? *Nephrology Dialysis Transplantation*, 2004. 19(2): p. 293-296.

59. Hörl, W.H., K.M. Koch, R.M. Lindsay, C. Ronco, and J.F. Winchester, Replacement of Renal Function by Dialysis. 5th edition ed. 2004, *Kluwer Academic Publishers: Springer-Science+Business Media*, B.V. 1606.

60. Stamatialis, D.F., B.J. Papenburg, M. Gironés, S. Saiful, S.N.M. Bettahalli, S. Schmitmeier, and M. Wessling, Medical applications of membranes: Drug delivery, artificial organs and tissue engineering. *Journal of Membrane Science*, 2008. 308(1-2): p. 1-34.

61. Lakowicz, J.R., Principles of Fluorescence Spectroscopy. 2007: *Springer*.

62. Jaffrin, M.Y., Convective mass transfer in hemodialysis. *Artif Organs*, 1995. 19(11): p. 1162-71.

63. Fresenius, Medical Care AG & Co. ESRD Patients in 2011. A Global Perspective. 2011.

64. Fresenius, Medical Care North America. Fresenius Optiflux® Dialyzers. 2011.

65. Pal, S., Design of Artificial Human Joints & Organs. 1 ed. 2014: *Springer US*. 419.

66. Himmelfarb, J. and T.A. Ikizler, Hemodialysis. *New England Journal of Medicine*, 2010. 363(19): p. 1833-1845.

67. Pellicano, R., K.R. Polkinghorne, and P.G. Kerr, Reduction in beta2-microglobulin with super-flux versus high-flux dialysis membranes: results of a 6-week, randomized, double-blind, crossover trial. *Am J Kidney Dis*, 2008. 52(1): p. 93-101.

68. Yamamoto, K.-i., M. Hiwatari, F. Kohori, K. Sakai, M. Fukuda, and T. Hiyoshi, Membrane fouling and dialysate flow pattern in an internal filtration-enhancing dialyzer. *Journal of Arti cial Organs*, 2005. 8(3): p. 198-205.

69. Catapano, G. and J. Vienken, Biomedical Applications of Membranes, in Advanced Membrane Technology and Applications. 2008, John Wiley & Sons, Inc. p. 489-517.

70. Ronco, C., B. Canaud, and P. Aljama, Hemodiafiltration. Vol. 158. 2007: *Karger AG*. 237.

71. Ofsthun, N.J., S. Karoor, and M. Suzuki, Hemodialysis Membranes, in Advanced Membrane Technology and Applications. 2008, John Wiley & Sons, Inc. p. 519-539.

72. Fischbach, M., H. Fothergill, A. Zaloszyc, and L. Seuge, Hemodiafiltration: the addition of convective flow to hemodialysis. *Pediatr Nephrol*, 2012. 27(3): p. 351-6.

73. Pedrini, L.A., V. De Cristofaro, B. Pagliari, and F. Sama, Mixed predilution and postdilution online hemodiafiltration compared with the traditional infusion modes. *Kidney International*, 2000. 58(5): p. 2155-2165.

74. Tiranathanagul, K., P. Susantitaphong, C. Keomany, N. Mahatanan, K. Praditpornsilpa, and S. Eiam-Ong, Long-term efficacy of pre- and post-dilution online hemodiafiltration with dialyzer reuse. *J Med Assoc Thai*,

2012. 95(5): p. 650-6.

75. Meert, N., S. Eloot, M.-A. Waterloos, M. Van Landschoot, A. Dhondt, G. Glorieux, I. Ledebo, and R. Vanholder, Effective removal of protein-bound uraemic solutes by different convective strategies: a prospective trial. *Nephrology Dialysis Transplantation*, 2009. 24(2): p. 562-570.

76. Meert, N., M.A. Waterloos, M. Van Landschoot, A. Dhondt, I. Ledebo, G. Glorieux, J. Goeman, J. Van der Eycken, and R. Vanholder, Prospective evaluation of the change of predialysis protein-bound uremic solute concentration with postdilution online hemodiafiltration. *Artif Organs*, 2010. 34(7): p. 580-5.

77. Maduell, F., F. Moreso, M. Pons, R. Ramos, J. Mora-Macià, J. Carreras, J. Soler, F. Torres, J.M. Campistol, A. Martinez-Castelao, and f.t.E.S. Group, High-Efficiency Postdilution Online Hemodiafiltration Reduces All-Cause Mortality in Hemodialysis Patients. *Journal of the American Society of Nephrology*, 2013.

78. Czifra, A., A. Pall, J. Kulcsar, K. Barta, A. Kertesz, G. Paragh, I. Lorincz, Z. Jenei, A. Agarwal, A. Zarjou, J. Balla, and Z. Szabo, Hemodialysis and hemodiafiltration differently modulate left ventricular diastolic function. *Bmc Nephrology*, 2013. 14.

79. Nistor, I., S.C. Palmer, J.C. Craig, V. Saglimbene, M. Vecchio, A. Covic, and G.F. Strippoli, Convective Versus Diffusive Dialysis Therapies for Chronic Kidney Failure: An Updated Systematic Review of Randomized Controlled Trials. *Am J Kidney Dis*, 2014.

80. Krick G. and Ronco C., *On-Line Hemodia ltration: The Journey and the Vision* 2011.

81. Botella, J., P.M. Ghezzi, and C. Sanz-Moreno, Adsorption in hemodialysis. *Kidney Int*, 2000. 58(S76): p. S60-S65.

82. Yatzidis, H., A convenient haemoperfusion micro-apparatus for treatment of endegeneous and exogenous intoxicatons; its use as an effective artificial kidney. Proc. *Eur. Dial. Transplant. Assoc.*, 1964. 1: p. 83–87.

83. Mydlík, M., J. Bucek, K. Derzsiová, J. Jarcuška, and M. Takác, Influence of charcoal haemoperfusion on platelet count in acute poisoning and during regular dialysis treatment. *International Urology and Nephrology*, 1981.

13(4): p. 387-389.

84. Saiful, *Mixed Matrix Membrane Adsorbers for Protein and Blood Puri cation.* 2007: University of Twente [Host].

85. Chang, T.M.S., Sempermeable Aqueous Microcapsules ("Artificial Cells"): With Emphasis on Experiments in An Extracorporeal Shunt System. *ASAIO Journal*, 1966. 12(1): p. 13-19.

86. Davankov, V., L. Pavlova, M. Tsyurupa, J. Brady, M. Balsamo, and E. Yousha, Polymeric adsorbent for removing toxic proteins from blood of patients with kidney failure. *Journal of Chromatography B: Biomedical Sciences and Applications*, 2000. 739(1): p. 73-80.

87. Ronco, C., A. Brendolan, M. Dan, P. Piccinni, R. Bellomo, M.L. Wratten, P. Inguaggiato, and C. Tetta, *Use of sorbents in acute renal failure and sepsis. Dialysis, Dialyzers and Sorbents: Where Are We Going?*, 2001. 133: p. 180-193.

88. Diraimondo, C.R. and V.E. Pollak, Beta-2-microglobulin kinetics in maintenance hemodialysis- a comparison of conventional and high-flux dialyzers and the effects of dialyzer reuse.*American Journal of Kidney Diseases*, 1989. 13(5): p. 390-395.

89. Mumtaz, A., M. Anees, M. Bilal, and M. Ibrahim, *Beta-2 Microglobulin Levels in Hemodialysis Patients. Saudi J Kidney Dis Transplant*, 2010. 21(4): p. 701-706.

90. Al-Taee, I.K., J.J. Al-Safar, Y.S. Al-Falahi, and I.A. Al-Shamma, The Clinical Significance of β_2-microglobulin in End-Stage Renal Disease. *Saudi J Kidney Dis Transplant*, 2003. 14(4): p. 492-496.

91. El-Wakil, H.S., A.A. Abou-Zeid, I.E. El-Gohary, N.A. Abou El-Seoud, M.A. Abou El-Yazeed, and M.A. El-Leithy, Effect of high flux versus low flux hemodialysis on serum beta-2 microglobulin, advanced oxidation protein products and protein carbonyl. *Alexandria Journal of Medicine*, 2011. 47(1): p. 37-42.

92. Santoro, A., E. Mancini, R. Bolzani, R. Boggi, L. Cagnoli, A. Francioso, M. Fusaroli, V. Piazza, R. Rapana, and G.F. Strippoli, The effect of on-line high-flux hemofiltration versus low-flux hemodialysis on mortality in chronic kidney failure: a small randomized controlled trial. *Am J Kidney Dis*, 2008. 52(3): p.

507-18.

93. Koda, Y., S. Nishi, S. Miyazaki, S. Haginoshita, T. Sakurabayashi, M. Suzuki, S. Sakai, Y. Yuasa, Y. Hirasawa, and T. Nishi, Switch from conventional to high-flux membrane reduces the risk of carpal tunnel syndrome and mortality of hemodialysis patients. *Kidney International*, 1997. 52(4): p. 1096-1101.

94. Locatelli, F., D. Marcelli, F. Conte, A. Limido, F. Malberti, D. Spotti, and T. Registro Lombardo Dialisi, Comparison of mortality in ESRD patients on convective and diffusive extracorporeal treatments. *Kidney International*, 1999. 55(1): p. 286-293.

95. Kramer, B.K., A. Pickert, C. Hohmann, H.M. Liebich, G.A. Muller, M. Hablitzel, and T. Risler, In vivo clearance and elimination of 9 marker substances during hemofiltration with different membranes. *International Journal of Arti cial Organs*, 1992. 15(7): p. 408-412.

96. Lornoy, W., I. Becaus, J.M. Billiouw, L. Sierens, and P. van Malderen, Remarkable removal of beta-2-microglobulin by on-line hemodiafiltration. *American Journal of Nephrology*, 1998. 18(2): p. 105-108.

97. Wei, S.S., E.P. Paganini, M.D. Cressman, and E. Wright, Use of hemodiafiltration to enhance delivered dialysis. *ASAIO journal (American Society for Arti cial Internal Organs : 1992)*, 1994. 40(4): p. 977-80.

98. Ahrenholz, P., R.E. Winkler, W. Ramlow, M. Tiess, and W. Muller, On-line hemodiafiltration with pre- and postdilution: A comparison of efficacy. *International Journal of Arti cial Organs*, 1997. 20(2): p. 81-90.

99. Maduell, F., C. del Pozo, H. Garcia, L. Sanchez, J. Hdez-Jaras, M.D. Albero, C. Calvo, I. Torregrosa, and V. Navarro, Change from conventional haemodiafiltration to on-line haemodiafiltration. *Nephrology Dialysis Transplantation*, 1999. 14(5): p. 1202-1207.

100. Bammens, B., P. Evenepoel, K. Verbeke, and Y. Vanrenterghem, Removal of the protein-bound solute p-cresol by convective transport: A randomized crossover study. *American Journal of Kidney Diseases*, 2004. 44(2): p. 278-285.

101. Ward, R.A., S. Schmidt, J. Hullin, G.F. Hillebrand, and W. Samtleben, A comparison of on-line hemodiafiltration and high-flux hemodialysis: A prospective clinical study. *Journal of the American Society of Nephrology*,

2000. 11(12): p. 2344-2350.

102. Cornelis, T., F.M. van der Sande, S. Eloot, E. Cardinaels, O. Bekers, J. Damoiseaux, K.M. Leunissen, and J.P. Kooman, Acute Hemodynamic Response and Uremic Toxin Removal in Conventional and Extended Hemodialysis and Hemodiafiltration: A Randomized Crossover Study. *Am J Kidney Dis*, 2014.

103. Gura, V., A. Davenport, M. Beizai, C. Ezon, and C. Ronco, Beta2-microglobulin and phosphate clearances using a wearable artificial kidney: a pilot study. *Am J Kidney Dis*, 2009. 54(1): p. 104-11.

104. Tattersall, J., Clearance of beta-2-microglobulin and middle molecules in haemodiafiltration. *Contrib Nephrol*, 2007. 158: p. 201-9.

105. Cornelius, R.M., W.G. McClung, R.M.A. Richardson, C. Estridge, N. Plaskos, C.M. Yip, and J.L. Brash, Effects of Heat/Citric Acid Reprocessing on High-Flux Polysulfone Dialyzers. *ASAIO Journal*, 2002. 48(1): p. 45-56.

106. Furuyoshi, S., M. Tsunomori, S. Takata, and N. Tani, Newly developed adsorbent for direct hemoperfusion to remove beta-2-microglobulin. *Arti cial Organs*, 1992. 16(6): p. 646-647.

107. Gejyo, F., Y. Kawaguchi, S. Hara, R. Nakazawa, N. Azuma, H. Ogawa, Y. Koda, M. Suzuki, H. Kaneda, H. Kishimoto, M. Oda, K. Ei, R. Miyazaki, H. Maruyama, M. Arakawa, and M. Hara, Arresting dialysis-related amyloidosis: A prospective multicenter controlled trial of direct hemoperfusion with a beta(2)-Microglobulin adsorption column. *Arti cial Organs*, 2004. 28(4): p. 371-380.

108. Nakatani, M., S. Furuyoshi, S. Takata, and N. Tani, Adsorption characteristics of adsorbent column (Lixelle) for the treatment of dialysis-related amyloidosis. *Jpn. J. Artif. Organs*, 1998. 27: p. 571– 577.

109. Tsuchida, K., Y. Takemoto, T. Nakamura, O. Fu, C. Okada, S. Yamagami, and T. Kishimoto, Lixelle adsorbent to remove inflammatory cytokines. *Arti cial Organs*, 1998. 22(12): p. 1064-1067.

110. Cowgill, L.D., J.F. Winchester, J.A. Brady, N.W. Levin, and C.A. Davis, Biocompatibility of A Novel Adsorptive Polymer During in Vivo Hemoperfusion in Normal Dogs. *ASAIO Journal*, 2001. 47(2): p. 161.

111. Deppisch, R., M. Storr, R. Buck, and H. Gohl, Blood material interactions at the surfaces of membranes in medical applications. *Separation and Puri cation Technology*, 1998. 14: p. 241–254.

112. Mares, J., V. Thongboonkerd, Z. Tuma, J. Moravec, and M. Matejovic, Specific adsorption of some complement activation proteins to polysulfone dialysis membranes during hemodialysis. *Kidney Int*, 2009. 76(4): p. 404-13.

113. Higuchi, A., K. Sugiyama, B.O. Yoon, M. Sakurai, M. Hara, M. Sumita, S.-i. Sugawara, and T. Shirai, Serum protein adsorption and platelet adhesion on pluronic^{TM}-adsorbed polysulfone membranes. *Biomaterials*, 2003. 24(19): p. 3235-3245.

114. Li, L., C. Cheng, T. Xiang, M. Tang, W. Zhao, S. Sun, and C. Zhao, Modification of polyethersulfone hemodialysis membrane by blending citric acid grafted polyurethane and its anticoagulant activity. *Journal of Membrane Science*, 2012. 405-406: p. 261-274.

115. Hasegawa, T., Y. Iwasaki, and K. Ishihara, Preparation and performance of protein-adsorption-resistant asymmetric porous membrane composed of polysulfone/phospholipid polymer blend. *Biomaterials*, 2001. 22: p. 243-251.

116. Ward, R.A., E. Klein, G.B. Harding, and K.E. Murchison, Response of complement and neutrophils to hydrophilized synthetic membranes. *ASAIO transactions / American Society for Arti cial Internal Organs*, 1988. 34(3): p. 334-7.

117. Su, B.-h., P. Fu, Q. Li, Y. Tao, Z. Li, H.-s. Zao, and C.-s. Zhao, Evaluation of polyethersulfone highflux hemodialysis membrane in vitro and in vivo. *Journal of Materials Science: Materials in Medicine*, 2008. 19(2): p. 745-751.

118. Valette, P., M. Thomas, and P. Déjardin, Adsorption of low molecular weight proteins to hemodialysis membranes: experimental results and simulations. *Biomaterials*, 1999. 20(17): p. 1621-1634.

119. Moachon, N., C. Boullanger, S. Fraud, E. Vial, M. Thomas, and G. Quash, Influence of the charge of low molecular weight proteins on their efficacy of filtration and/or adsorption on dialysis membranes with different intrinsic properties. *Biomaterials*, 2002. 23(3): p. 651-658.

120. Malik, D.J., G.L. Warwick, M. Venturi, M. Streat, K. Hellgardt, N. Hoenich,

and J.A. Dale, Preparation of novel mesoporous carbons for the adsorption of an inflammatory cytokine (IL-1 beta). *Biomaterials*, 2004. 25(15): p. 2933-40.

121. Gejyo, F. and M. Arakawa, Dialysis amyloidosis: current disease concepts and new perspectives for its treatment. *Contrib Nephrol*, 1990. 78: p. 47-59; discussion 59-60.

122. Chen, V., Non-invasive observation of synthetic membrane processes ? a review of methods. *Journal of Membrane Science*, 2004. 241(1): p. 23-44.

123. Zator, M., M. Ferrando, F. López, and C. Güell, Membrane fouling characterization by confocal microscopy during filtration of BSA/dextran mixtures. *Journal of Membrane Science*, 2007. 301(1-2): p. 57-66.

124. Crespo, J.P.S.G., M. Trotinb, D. Houghc, and J.A. Howellb, Use of fluorescence labelling to monitor protein fractionation by ultrafiltration under controlled permeate flux. *Journal of Membrane Science*, 1999. 155: p. 209-230.

125. Chan, R. and V. Chen, Characterization of protein fouling on membranes: opportunities and challenges. *Journal of Membrane Science*, 2004. 242(1-2): p. 169-188.

126. Sato, K., A. Hibara, M. Tokeshi, H. Hisamoto, and T. Kitamori, Microchip-based chemical and biochemical analysis systems.*Advanced Drug Delivery Reviews*, 2003. 55(3): p. 379-391.

127. Erickson, D. and D.Q. Li, Integrated microfluidic devices. *Analytica Chimica Acta*, 2004. 507(1): p. 11-26.

128. Da Cunha, M.R., N. Perez, C. Negreira, R.M.R. Costa, M. Inês, and M.R. Gongora-Rubio, *Characterization of Passive and Active Micro uidic Devices Manufactured in LTCC Technology, in Ibersensor 2006*. 2006: Montevideo.

129. Cabodi, M., N.W. Choi, J.P. Gleghorn, C.S.D. Lee, L.J. Bonassar, and A.D. Stroock, A microfluidic biomaterial. *Journal of the American Chemical Society*, 2005. 127(40): p. 13788-13789.

130. Eijkel, J.C.T., J.G. Bomer, and A. van den Berg, Osmosis and pervaporation in polyimide submicron microfluidic channel structures. *Applied Physics Letters*, 2005. 87(11).

131. Neeves, K.B. and S.L. Diamond, A membrane-based microfluidic device for

controlling the flux of platelet agonists into flowing blood. *Lab Chip*, 2008. 8(5): p. 701-9.

132. Toda, K., Y. Ebisu, K. Hirota, and S. Ohira, Membrane-based microchannel device for continuous quantitative extraction of dissolved free sulfide from water and from oil. *Anal Chim Acta*, 2012. 741: p. 38-46.

133. Hsieh, Y.-C. and J.D. Zahn, Glucose recovery in a microfluidic microdialysis biochip. *Sensors and Actuators B: Chemical*, 2005. 107(2): p. 649-656.

134. Khademhosseini, A., J. Yeh, G. Eng, J. Karp, H. Kaji, J. Borenstein, O.C. Farokhzad, and R. Langer, Cell docking inside microwells within reversibly sealed microfluidic channels for fabricating multiphenotype cell arrays. *Lab Chip*, 2005. 5(12): p. 1380-6.

135. Ould-Dris, A., P. Paullier, L. Griscom, C. Legallais, and E. Leclerc, Analysis of the mass transfers in an artificial kidney microchip. *Journal of Membrane Science*, 2010. 352(1-2): p. 116-125.

136. Kim, S.H., Y. Yang, M. Kim, S.W. Nam, K.M. Lee, N.Y. Lee, Y.S. Kim, and S. Park, Simple Route to Hydrophilic Microfluidic Chip Fabrication Using an Ultraviolet (UV)-Cured Polymer. *Advanced Functional Materials*, 2007. 17(17): p. 3493-3498.

137. McDonald, J.C., D.C. Duffy, J.R. Anderson, D.T. Chiu, H. Wu, O.J. Schueller, and G.M. Whitesides, Fabrication of microfluidic systems in poly(dimethylsiloxane). *Electrophoresis*, 2000. 21(1): p. 27-40.

138. McDonald, J.C. and G.M. Whitesides, Poly(dimethylsiloxane) as a Material for Fabricating Microfluidic Devices. *Accounts of Chemical Research*, 2002. 35(7): p. 491-499.

139. Sollier, E., C. Murray, P. Maoddi, and D. Di Carlo, Rapid prototyping polymers for microfluidic devices and high pressure injections. *Lab Chip*, 2011. 11(22): p. 3752-65.

140. Dupont, E.P., R. Luisier, and M.A.M. Gijs, NOA 63 as a UV-curable material for fabrication of microfluidic channels with native hydrophilicity. *Microelectronic Engineering*, 2010. 87(5–8): p. 1253-1255.

141. Bartolo, D., G. Degre, P. Nghe, and V. Studer, Microfluidic stickers. *Lab on a Chip*, 2008. 8(2): p. 274-279.

142. Gao, J., J. Xu, L.E. Locascio, and C.S. Lee, Integrated Microfluidic System Enabling Protein Digestion, Peptide Separation, and Protein Identification. *Analytical Chemistry*, 2001. 73(11): p. 2648-2655.

143. Perozziello, G., P. Candeloro, F. Gentile, M.L. Coluccio, M. Tallerico, A. De Grazia, A. Nicastri, A.M. Perri, E. Parrotta, F. Pardeo, R. Catalano, G. Cuda, and E. Di Fabrizio, A microfluidic dialysis device for complex biological mixture SERS analysis. *Microelectronic Engineering*, 2015. 144: p. 37-41.

2 Materials and Methods

This chapter summarizes the materials and methods used in the present project. Firstly, the list of used solutions and membranes is presented with respective suppliers. Then, the microfluidics device development and fabrication are shown with essential details. After this, the microfluidics device characterization techniques as well as the filtration and image analysis protocols are summarized.

1 Solutions

1.1 Solutes and solvents

Phosphate buffer solution (PBS) was prepared from the concentrated 10x PBS bulk solution purchased from Fisher BioReagents, France. Ultrapure water used in the experiments was purified from the osmotic water obtained from an ELGA PURELAB Classic water purification system (final minimum resistivity of $18\ \mathrm{M\Omega\,cm}$).

Alpha-lactalbumin (LALBA) from bovine milk (Type III, calcium depleted), Atto 647N Protein Labeling Kit, Bovine Serum Albumin (BSA), and Bovine Serum Albumin–fluorescein isothiocyanate conjugate (BSA-FITC) were purchased from Sigma-Aldrich, France.

Cibanon green BF dye was purchased from CIBA Specialty Chemicals Inc, Basel, Switzerland and was used for the leakage testing of the microfluidics devices.

1.2 Protein-conjugate preparation

The commercially available α-lactalbumin was supposed to be used for the real-time observation of the membrane fouling. Since, the fluorescent microscopy was selected as a detection method, the protein needed to be labeled with a fluorescent tag.

1.2.1 Labeling procedure

The protein (α-lactalbumin) labeling procedure was performed according to the protocol, which was suggested by the supplier [1].

1. Protein was dissolved in sodium bicarbonate buffer solution to obtain the concentration of $10\ \mathrm{mg\,mL^{-1}}$.

2. The reactive dye was dissolved in 20 µL DMSO (present in the labeling kit). In order to minimize the chance for hydrolysis before coupling to the protein, this step was done right before the addition of the solution of native protein.
3. The protein solution was transferred to the vial containing the reactive dye.
4. The reaction mixture was incubated for 2 hours at gentle stirring.

1.2.2 Separation of protein-dye-conjugates from free dye

The gel filtration columns were used in order to achieve good separation of the protein-dye-conjugates from excess free dye (size exclusion limit: $5\ \mathrm{kDa}$). Solvent flow in the columns was achieved by gravity only, there s no need to apply pressure.

1. Before use, the column first was equilibrated with $10\ \mathrm{mL}$ water, then with $15\ \mathrm{mL}$ phosphate buffer.
2. The labeling mixture was added to the column and left for infiltration.
3. To start the elution, $5\ \mathrm{mL}$ of phosphate buffer was added.
4. The dye-protein conjugate (first band) was collected, the free dye (second band) was trapped inside the column.

1.2.3 Determination of dye/protein (D/P) ratio

The obtained solution of conjugate was characterized by calculations of dye to protein ratio (D/P) and the final protein concentration. For this, the absorbance of the conjugates at $280\ \mathrm{nm}$ and $647\ \mathrm{nm}$ was measured at a cuvette with $1\ \mathrm{cm}$ thickness and with use of Libra S12 UV Spectrophotometer (Biochrom, UK). Prior to the measurements the conjugate was diluted (10x), so that the maximum absorbance is in the range from 0.5 to 1.

The D/P molar ratio was calculated according to the formula provided by the supplier of the labeling kit [1]:

$$D/P = \frac{A_{647}\varepsilon_{protein}}{\left[A_{280} - 0.05A_{647}\right]\varepsilon_{dye}} \tag{2.1}$$

A_{647} – absorbance of the conjugate at $647\ \mathrm{nm}$;
A_{280} – absorbance of the conjugate at $280\ \mathrm{nm}$;
$\varepsilon_{protein}$ – molar extinction coefficient of protein ($27\,400\ \mathrm{cm^{-1}\,M^{-1}}$) at $280\ \mathrm{nm}$;
ε_{dye} – molar extinction coefficient of dye ($150\,000\ \mathrm{cm^{-1}\,M^{-1}}$) at $647\ \mathrm{nm}$;
0.05 – correction factor due to the fluorophore s absorbance at $280\ \mathrm{nm}$.

The final protein concentration was calculated with use of Equation 2.2:

$$c_{protein}[\mathrm{mg\,mL^{-1}}] = \frac{A_{280} - 0.05A_{647}}{\varepsilon_{protein}} MW_{protein} Dilution factor \qquad (2.2)$$

$MW_{protein}$ – molecular weight of the protein ($\mathrm{g\,mol^{-1}}$).
$Dilution factor$ – dilution of the labeled conjugate prior to measurement by spectrophotometer (we used 10).

The final conjugate solution was diluted with PBS in order to achieve a concentration of $50\ \mathrm{mg\,L^{-1}}$. This concentration is clinically relevant as it is very close to the mean/median uremic concentration of β_2-microglobulin [2].

2 Membranes

Two types of membranes were used. The commercially available polyethersulfone (PES) membrane (product code: 14 650-47-D) with $50\ \mathrm{kDa}$ cut-off and thickness of $120\ \mu\mathrm{m}$ was purchased from Sartorius AG, France. The homemade SlipSkin™ membrane with thickness of $75\ \mu\mathrm{m}$ and clean water permeability of $56\pm12\ \mathrm{L\,m^{-2}\,h^{-1}\,bar^{-1}}$ was fabricated by our partners in University of Twente and the fabrication procedure was presented elsewhere [3].

3 Microfluidics device

3.1 Materials

For the fabrication of the microfluidics device the following materials were used: dry film photoresist (WBR2100, DuPont, USA), hydrophobic agent Novec™ (3M, USA), NOA 68 (Norland Optical Adhesive 68, Norland Products, USA), Polydimethylsiloxane (PDMS, Sylgard® 184 silicone elastomer, Dow Corning, USA), HSW Fine-Ject hypodermic needles (Sigma-Aldrich, France), K_2CO_3 with

purity over 99% (Fisher Scientific, France). The connective Teflon tubings with internal diameter of 250 µm were purchased from Cluzeau Info Labo, France.

3.2 Development and fabrication: details, pitfalls, and tips.

3.2.1 Designing step

The primary step of a microfluidics device development is the creation of proper design. In the present study, the design of the microchip was dictated by the idea of constructing a transparent device composed of two systems (retentate and permeate) of microchannels with membrane sandwiched in between. For this, three schemes (Figure 2.1) were designed with use of CleWin4 software [4], which enables the drawing of high precision (up to 1 µm).

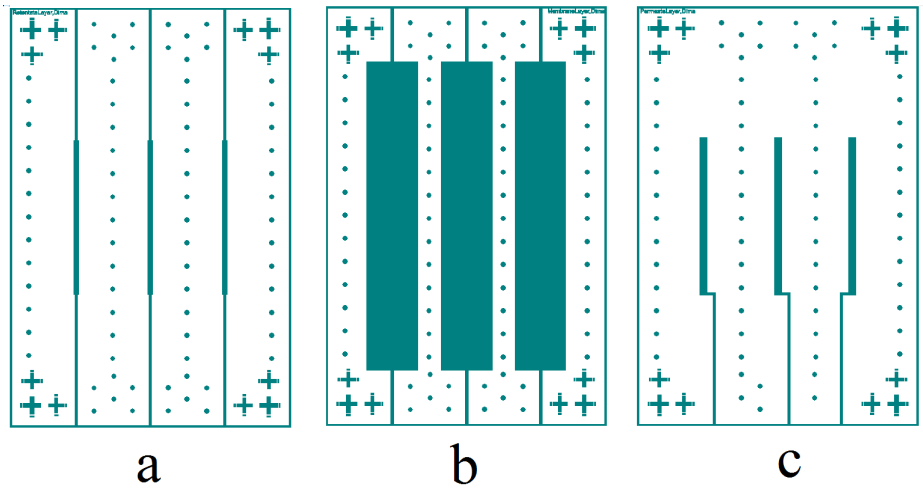

Figure 2.1: 2D structure of the retentate (a) and the permeate (c) microchannel systems along with membrane layer (b).

In the designs Figure 2.1 (a) and Figure 2.1 (c) one may distinguish two types of channels: three parallel wide ones (in the center) and narrow (at the top and the bottom). The wide channels will be further referred as “retentate windows” or “permeate windows” depending on whether they are in the retentate or the permeate microchannel system. Retentate and permeate layers are intended to be aligned with each other (Figure 2.2 (B)) so that “retentate windows” and “permeate windows” will overlap to form specific areas (“permeation windows” or simply “windows”) where permeation through the membrane may occur (Figure 2.2 (C)). Four sets of

crosses placed in the corners of each design are used for the alignment of the layers of the ultimate device (Figure 2.2 (A)).

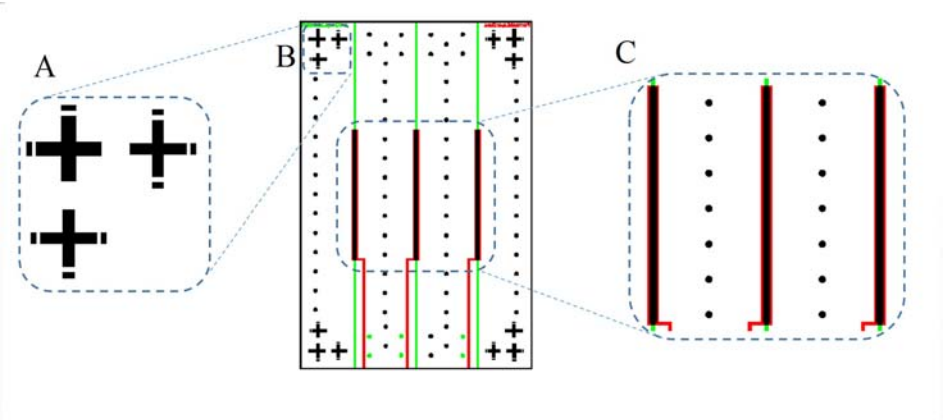

Figure 2.2: Schematic representation of the alignment of a retentate and a permeate sides. (A – the zoom of crosses for the alignment, B – aligned permeate and retentate sides of the chip, C – zoom of "permeation windows").

As it can be seen from Figure 2.2 (C) and Figure 2.1, the width and the length of the "permeate window" are slightly greater than the ones of the retentate. This is done in order to increase the chances of good manual alignment between the permeate and the retentate side, which would be almost impossible in case of the equality of their dimensions. Moreover, the sets of crosses are "equipped" with small rectangles (Figure 2.2 (A)), which serve as the limits of the alignment imperfection. In practice, the crosses of the permeate and the retentate sides may not be perfectly overlapped, but the edge of the cross in the retentate layer should not lay over the rectangle of the respective cross in the permeate layer and vice-versa.

The structure of retentate side (Figure 2.1 (a)) is designed to mimic the hydrodynamic conditions of an individual hollow-fiber membrane of the hemodialysis module inside the "retentate window". The parameter to evaluate similarity in conditions is Reynolds number (Equation 2.3).

$$Re = \frac{\rho \vartheta d_h}{\mu} \tag{2.3}$$

where ρ stands for the viscosity of the flowing liquid, ϑ is the mean velocity of the flow inside the fiber, d_h hydraulic diameter of the fiber (or the microchannel) and μ is the dynamic viscosity of the fluid.

The conventional commercially available hollow-fiber membranes for the hemodialysis have the internal diameter of approximately 200 μm and are gathered in the bundle of 7000-14 000 fibers to form a hemodialysis module [5]. Taking into account that the generally accepted optimal blood flow rate (Q_b) during dialysis is in the range 200-400 $\mathrm{mL\,min^{-1}}$ [6] and that the blood viscosity is around 3 to 4 times higher than that of water [7] it becomes possible to define the range of standard Re in the individual fiber in the module. All the data and results of calculations are presented in Table 2.1.

Table 2.1: Data used for the evaluation of Re in individual fiber in hemodialysis module.

Blood and ber properties			
d_h, [m]	ρ, [$\mathrm{kg\,m^{-3}}$]	η, [Pa s]	
0.0002	1060	0.003	
Hemodialysis conditions [4]			
Q, [$\mathrm{mL\,min^{-1}}$]	200	400	200	400
Q, [$\mathrm{cm^3\,s^{-1}}$]	3.33	6.67	3.33	6.67
Q, [$\mathrm{m^3\,s^{-1}}$]	3.33×10^{-6}	6.67×10^{-6}	3.33×10^{-6}	6.67×10^{-6}
Number of fibers	7000		14000	
Q, [$\mathrm{cm^3\,s^{-1}}$fiber^{-1}]	4.76×10^{-10}	9.52×10^{-10}	2.38×10^{-10}	4.76×10^{-10}
Re	1.1	2.1	0.5	1.1

According to the Table 2.1, the clinical hemodialysis treatment is performed at small Re (laminar conditions). Thus, the achievement of the similar conditions in a "retentate windows" of the microfluidic device is desired. Moreover, since it is planned to use the flat membrane in the microchip instead of the hollow-fiber, it was decided that the width of the filtration zone should be equal to the internal circumference of unfolded fiber (approximately 630 μm), while its length was restricted by the technical limitations of the chip fabrication and can be 2 cm at most. On the other hand, due to the aforediscussed reasons, the width of the "permeate window" is 930 μm, which allows a 150 μm deviation from the ideal alignment of the layers. Besides, the width of the small channels adjacent to the edge of the retentate and permeate designs is equal to 300 μm and they are used for the placement of a "world-to-chip" connectors.

In order to place the membrane inside the microchip the special cavity of the height approximately equal to the membrane thickness has to be introduced in the

microfluidic device design. For this purpose the additional 2D design for the membrane layer (Figure 2.1 (b)) was developed. Here, for the simplicity of fabrication, the width of the small channels is 400 µm, which allows a 50 µm deviation from the ideal alignment. The addition of the membrane layer to the structure of the ultimate microfluidics device is presented in Figure 2.3 "Retentate part fabrication".

Developed designs were printed on the transparent film with use of a high resolution printer (TecPhotoGravure, France).

3.2.2 Microfluidics device fabrication

Each microfluidics device consists of a permeate and a retentate side with a membrane in the middle, imitating a real cross flow membrane filtration system. The fabrication of such microchips involved several steps and use of the standard soft lithography procedure. The resulting microchip has a multilayer structure, where a membrane is sandwiched between two monoliths with embedded channels prepared from the novel UV-curable adhesive NOA 68. A schematic representation of the manufacturing process is shown in Figure 2.3.

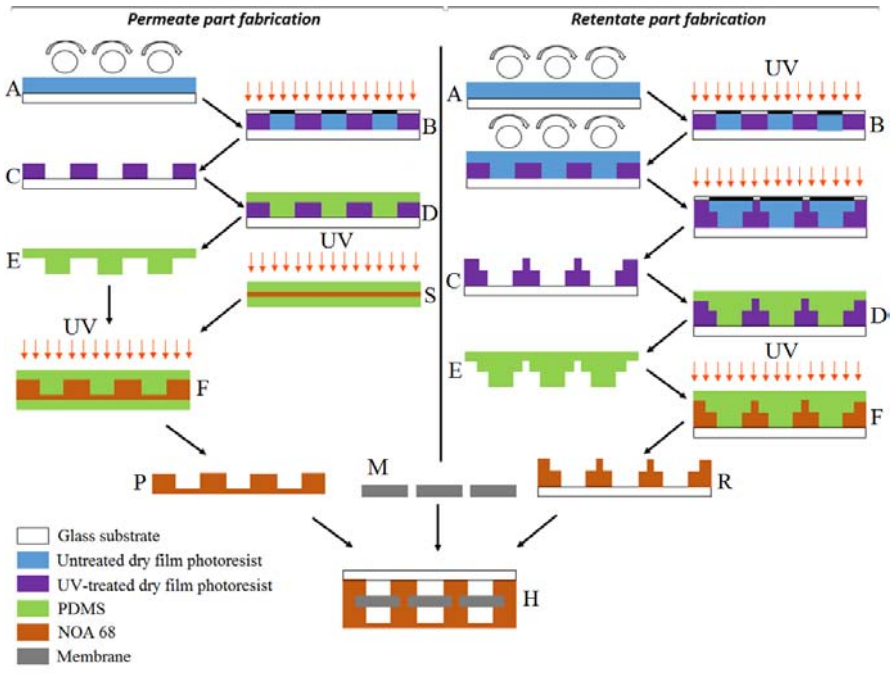

Figure 2.3: Schematic representation of microfluidic device fabrication process.

The fabrication starts with the lamination of the dry film photoresist at temperature of $85°C$ on the top of a glass slide with size of 80 x 50 mm (Figure 2.3 (A)), which was used as a substrate. Three dry film photoresist layers of 100 µm each were laminated one over another to obtain the final thickness of 300 µm. It is important to allow the substrate to cool down to the room temperature after the lamination of each layer. This approach leads to a better adhesion between the dry film material and the glass substrate, and reduces the occurrence of detachment of the laminated layers.

The structure of the microchannel system was patterned through the high-resolution printed mask under a continuous UV treatment for 30 s (Figure 2.3 (B)). A drop of water may be placed on the substrate in order to achieve a good contact with the mask. Figure 2.4 demonstrates the change of dry film appearance after the UV exposure. It is crucially important to make sure that there are no white objects in the UV chamber, as they reflect the light and may induce partial curing of dry film under the mask.

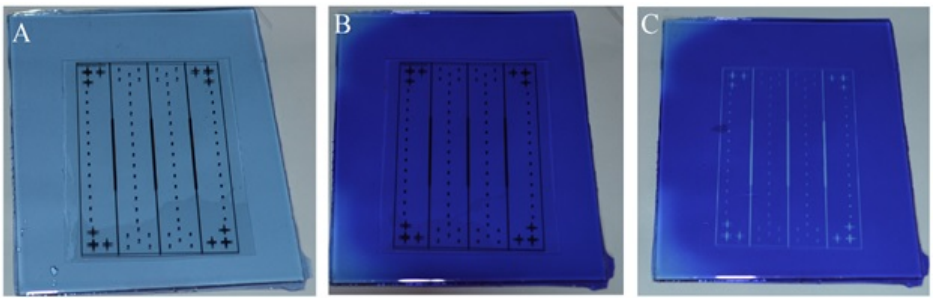

Figure 2.4: The changes of the dry film photoresist under the UV exposure. (Image A – untreated dry film photoresist, B – UV-treated with the mast of the retentate side, C – UV-treated without the mask).

The laminated and treated substrate was subjected to a 1 min baking at 100 °C on the hotplate to achieve better fixation between the glass and the laminate. The post-baking cooling has to be slow in order to give enough time for the relaxation of dry film material and to avoid cracking. For this, the substrate has to be places on surface with poor thermal conductivity. One of the ideal choices is wrapped sheet of paper, which, thanks to air between layers, enables moderate rate of the dry film cooling.

In case of the fabrication of the retentate side, the cooled down system, was used as new substrate. As so, it was subjected to the second lamination-treatment-fixation process aiming to the formation of a hierarchical structure with a cavity for the membrane placement. For this, one layer (100 µm) of the dry film photoresist was

laminated on top of UV-treated substrate (Figure 2.3(C)). The UV treatment of 10 s with use of the second mask (Figure 2.1 (B)) was then applied.

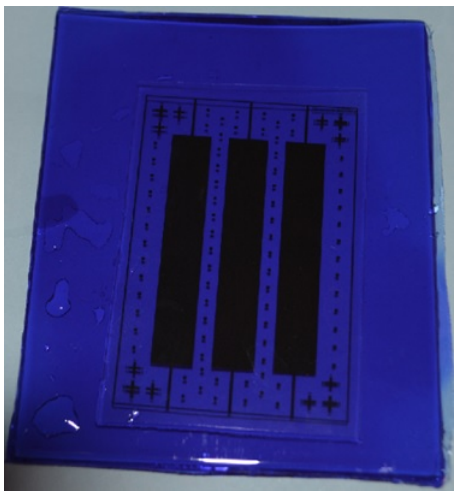

Figure 2.5: The membrane layer mask placed on top of the prepared substrate.

As it can be seen from Figure 2.5, the second mask is perfectly aligned with the substrate and covers all the untreated parts visible on Figure 2.3 (C). Therefore, there is no risk of undesirable exposure of the unprotected zones.

After UV exposure and backing, the cooled down single layer permeate and the double layer retentate systems were immersed in 1%wt KCO_3 at $28°C$ for 10 min to remove the untreated part of the dry film photoresist. The resulting systems with engraved channels were used as the dry film molds (Figure 2.3 (C)).

Then, a 10:1 wt mixture of polydimethylsiloxane (PDMS) prepolymer and curing agent was used to get a replica of the mold. Prior to pouring of the prepolymer, the mold was silanized by immersion in Novec^{TM} for 20 min and dried overnight in order to ensure an easier PDMS detachment. The prepolymer-agent mixture was poured on the dry film master mold and degassed under vacuum for 45 min, and then it was heat-cured for 4h at $80°C$ (Figure 2.3 (D)). After PDMS replica (Figure 2.3 (E)) is ready, it was again slowly cooled down to the room temperature, peeled off from the mold, and placed under vacuum for degassing before further use.

In order to ensure a good adhesion between layers on the step of the final assembling of the device, different substrates were used for fabrication of retentate and permeate side layers. The retentate layer was prepared on the glass slide, while for the fabrication of the permeate layer the flat film of NOA 68 (S) was used. For this, approximately 2 g of NOA 68 were placed between two flat degassed PDMS

forms and cured for 3 min under the UV light. Then, the respective substrate was used for permeate and retentate sides fabrication. At this step, liquid NOA 68 was poured on top of the substrate, covered by the degassed PDMS replica and kept for 30 min at room temperature, so that the trapped air bubbles would be absorbed by PDMS.

The degassed permeate system was exposed to UV light for 12 s to achieve partial solidification of NOA 68, after which the PDMS replica could be safely peeled off (F). The metal capillaries with external diameter of 300 µm and internal one of 150 µm were placed inside the small channels. These capillaries were obtained by dissolving of HSW Fine-Ject hypodermic needles in laboratory grade chloroform (Fisher Scientific, France). Since the capillaries are circular in a cross section and the channels are squire, the remaining space has to be filled in order to achieve leak-free system. For this the small drops of NOA 68 were added in the locations, where the membrane, the metal capillary and NOA 68 housing would be in contact (indicated by dashed ovals in Figure 2.6). In order to achieve a better fixation of the capillaries inside the channels, the additional 2 s UV treatment was applied. The resulting permeate side is presented on Figure 2.7.

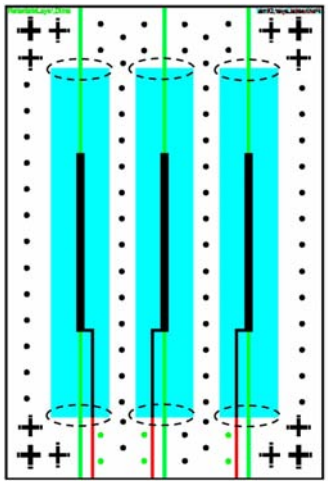

Figure 2.6: Schematic representation of location, where the additional reinforcement of metal/membrane/NOA68 connection is required.

Besides, the degassed retentate system was UV treated for 14 s. At this condition, it is possible to achieve the state of NOA 68, which is solid enough to keep the shape and is still sufficiently sticky to provide a fair adhesion to a membrane material.

Then, the membrane (Figure 2.3 (M)) was placed in the designed cavity in the retentate side of the microchannel system. The metal capillaries were inserted under

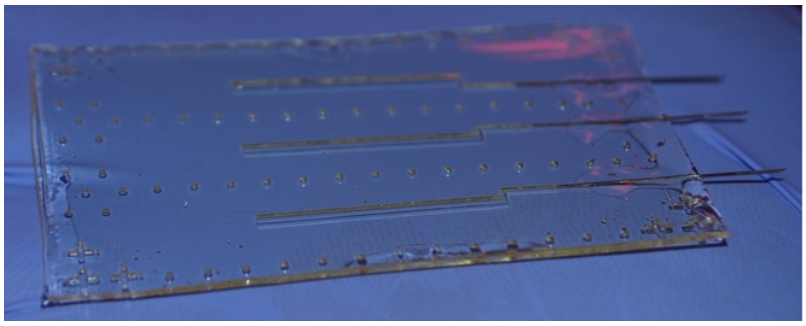

Figure 2.7: Appearance of the permeate system of microchannels with the metal capillaries.

the membrane and served as a world-to-chip connection (Figure 2.8).

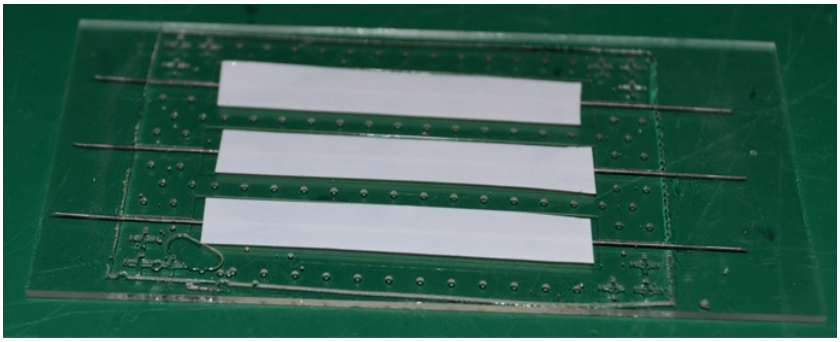

Figure 2.8: Appearance of the retentate system of microchannels with the membrane inside and placed metal capillaries.

Finally, the retentate (Figure 2.3 (R)) and permeate (Figure 2.3 (P)) sides were brought into contact and manually aligned under the optical microscope. The assembled chip (Figure 2.3 (H)) was finally cured by a two steps procedure: 3 minute treatment under UV light, followed by 12 h baking at 45°C.

3.2.3 Integrity testing

On the stage of a microchip development and optimization one of the crucial parameters is the integrity of the device. To evaluate whether the microchip is leaking the solution of the Cibanon green BF dye was manually pumped through the retentate compartment of the device. Such testing was performed until several consecutive chips were found to be leak-free.

3.3 Microfluidics device characterization

In order to evaluate the internal characteristics of the microchip, the calculation of resistances for each stream (feed, retentate and permeate) and intermediate pressure (pressure in the retentate compartment inside the chip) are required. To obtain the values of resistances the set of experiments with different inlet and permeate pressures was conducted. Particularly, in different experiments the inlet pressure was set at $400\ \mathrm{mbar}$, $350\ \mathrm{mbar}$ or $250\ \mathrm{mbar}$, while the initial permeate pressure was selected to allow the minimal permeate flow. Then, each 10 min the permeate pressure was reduced by $10\ \mathrm{mbar}$ until it ultimately reaches $0\ \mathrm{mbar}$. Such approach allowed to follow the changes in the permeate flow rate. Each reduction of permeate pressure resulted in the increase of filtrate flux and combination of these experimental results along with Solver function in Microsoft Excel and the least square method, allowed us to determine the intermediate pressure (P_o) and three resistances. For this the following set of equations was used:

$$\frac{P_0 - P_{per}}{Q_{per}} = R_{per} \quad (2.4) \qquad \frac{P_0 - P_{ret}}{Q_{ret}} = R_{ret} \quad (2.5) \qquad \frac{P_{in} - P_0}{Q_{in}} = R_{in} \quad (2.6)$$

where Q is fluid flow rate, the subscripts ret, per and in stand for the retentate, the permeate and the inlet respectively.

In addition, since the developed chip has one entrance (inlet) and two outlets (retentate and permeate), from the mass balance one may calculate the intermediate pressure:

$$P_0 = \frac{R_{ret}R_{per}P_{in} + R_{ret}R_{in}P_{per} + R_{in}R_{per}P_{ret}}{R_{ret}R_{per} + R_{ret}R_{in} + R_{per}R_{in}} \quad (2.7)$$

Finally, knowing the intermediate pressure, one may calculate the transmembrane pressure (TMP) as:

$$TMP = P_0 - P_{per} \quad (2.8)$$

4 Filtration protocols

4.1 Protocol of a filtration at the macroscale (Amicon® cell)

The macroscale permeability of the commercial PES membrane was measured using conventional $50\ \mathrm{mL}$ Amicon® cell. For this, membrane was initially prepressurized at $1\ \mathrm{bar}$ until the stable permeate flux is reached and then tested at transmembrane pressures of $0.25\ \mathrm{bar}$, $0.5\ \mathrm{bar}$, $0.75\ \mathrm{bar}$ bar and $1\ \mathrm{bar}$, with ultrapure water. The mass of collected permeate was recorded each $30\ \mathrm{s}$.

The transfer of the native and the labeled α-lactalbumin through the commercial PES membrane were determined using small $10\ \mathrm{mL}$ Amicon®cell in order to reduce the required volume of feed solution. For this, $9\ \mathrm{mL}$ of protein solution with concentration of $50\ \mathrm{mg\,L^{-1}}$ were placed in the Amicon® cell and the pressure of $1\ \mathrm{bar}$ was applied. Three samples of permeate $1\ \mathrm{mL}$ each were separately collected one after another, meaning that the total withdrawn volume in each experiment was $3\ \mathrm{mL}$. The separate collection of sample also allowed to analyze whether the permeate composition varies over the filtration process. The duration of each experiment did not exceed $5\ \mathrm{min}$. After the filtration, the permeate samples along with the feed and the retentate were analyzed by Libra S12 UV Spectrophotometer (Biochrom, UK) at the wavelength range 200 – $800\ \mathrm{nm}$.

4.2 Protocol of a filtration at the microscale

4.2.1 Filtration without fluorescence

In order to evaluate the possibility to monitor the reduction of a membrane permeability inside the microchip, the filtration of $0.5\ \mathrm{g\,L^{-1}}$ BSA solution in phosphate buffer (PBS) was performed. The procedure was analogous to the one applied for the microchip characterization. The inlet pressure was set at $400\ \mathrm{mbar}$, while the initial permeate pressure was set in the way to allow minimal permeate flow. Then, each $10\ \mathrm{min}$ the permeate pressure was reduced by $10\ \mathrm{mbar}$. Obtained results were compared to the pure PBS filtration in order to quantify the membrane fouling at the microscale.

4.2.2 Filtration with the application of the fluorescent microscopy

The filtration experiments were followed with two systems: a Zeiss Axio Observer.Zlm inverted microscope equipped with a HXP 120C power supply, a filter set 38 (to be able to detect the fluorescence of used proteins: BSA-FITC and α-lactalbumin-Atto-647N), and an automated stage. The microscope is controlled by the Zeiss Axio Vision Software. The other used equipment was the Fluigent MFCS-Flex pressure controller, combined with a FLOWELL flow-controller. There are a total of 3 pressure and flow controllers. Two pressure controllers can supply a pressure of up to $1000\ \mathrm{mbar}$, while the other one goes up to $350\ \mathrm{mbar}$. As for the flow controllers, one can operate at a maximum flow of $7715\ \mathrm{nL\,min^{-1}}$, the other one at maximum flow of $55\ \mu\mathrm{L\,min^{-1}}$, and the last one at a maximum flow of $1100\ \mu\mathrm{L\,min^{-1}}$. The pressure-flow system is controlled by the MAESFLO software. The microfluidic chips are connected to the tubes of the pressure-flow controller and placed on the microscope stage to start the experimental protocol (Figure 2.9).

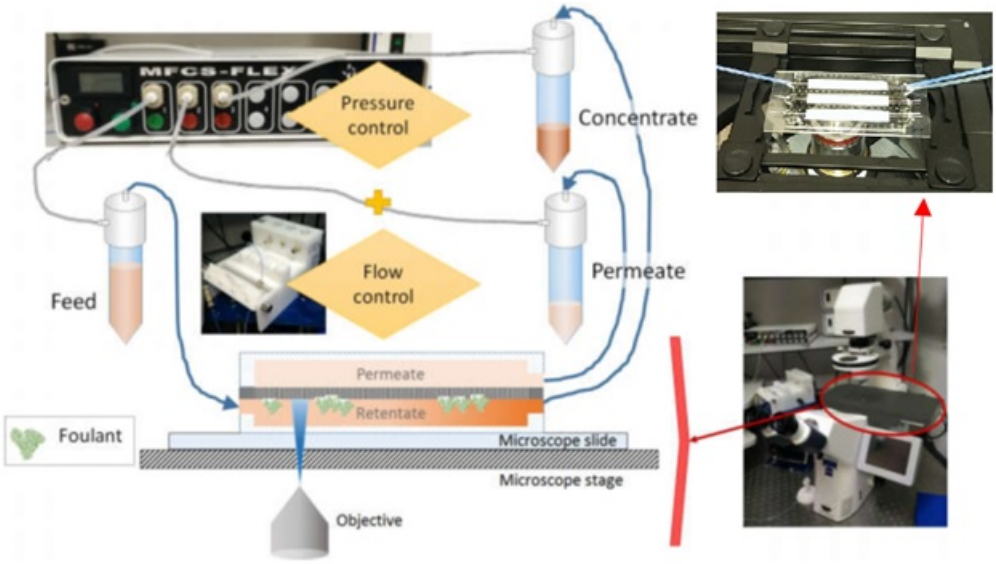

Figure 2.9: Schematic representation of the experimental set-up used combining the fluorescent microscopy and the microchip.

Before starting with the filtration process, the membrane was compacted for 1 hour. For this, the pure PBS was flown through the microchip at $130\ \mu\mathrm{L\,min^{-1}}$ and no pressure was applied from the permeate side (these conditions correspond to the TMP of $90\ \mathrm{mbar}$). In addition, in case of PES membrane, this step was used to remove the preservative (glycerol) from the pores of the membrane.

The filtration process inside the microchip was performed at a single pass mode, meaning that the feed solution after reaching the retentate reservoir was not resupplied to the system. The control over the cross flow velocity and transmembrane pressure was done by adjustment of the pressures at the inlet, the retentate, and the permeate reservoirs. Due to the limitations brought by flow controllers, only the inlet and permeate flow rates were constantly measured with data acquisition step of 10 s, while the retentate flow rate was calculated from the flow balance.

The fluorescence on the membrane surface at the retentate compartment of the microchip was also followed; images of the whole channel were acquired every 5 min with the GFP or Cy5 filter (depending on protein used). Since the length of analyzed channel is superior to the area, which can be captured by the camera, the camera was sliding along the channel to collect the set of images.

Then, the gray value as a unit of a fluorescence intensity was measured by the ImageJ software.

After the filtration procedure the pure PBS was again supplied to the system for at least 15 min in order to evaluate the permeability of a fouled membrane and the possible changes in the fluorescent signal.

The schematic protocol of the filtration procedure is summed up in Figure 2.10.

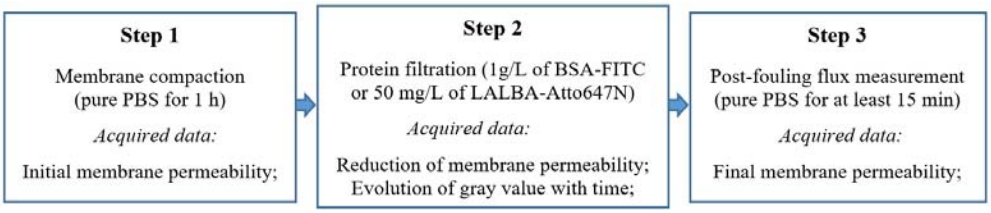

Figure 2.10: Schematic representation of different steps involved in the microfluidics device testing along with main data acquired on each step.

In case, the process was performed at transmembrane pressure (TMP) equal to zero, the post-fouling flux was compared to the clean water flux through a virgin membrane. For this a permeability reduction index (PRI) was introduced (Equation 2.9)

$$PRI = 1 - \frac{J_{post}}{J_0} \tag{2.9}$$

Where J_{post} and J_0 stand for the post-experimental and initial permeate fluxes.

4.2.3 Characterization of permeate flow reduction profile

For the analysis of experiments, where the permeate flow reduction was constantly monitored (TMP>0), the zones of its pattern are distinguished in the following manner. The first zone represents the steep linear decrease of the permeate flow and takes place in the beginning of the filtration process. The third zone is observed in the end the of the filtration experiment and is characterized by linear decline of the filtrate flow with the minimal slope. Consequently, the second ("transition") zone is located between the first and the third ones and may vary in duration and shape depending on the experimental conditions.

5 Image analysis protocol

The images obtained from the microscope were exported as .tiff files and analyzed using ImageJ software [8]. The fluorescence was measured in gray values, so that the greater fluorescence is reflected by the whiter pixel, which in turn results in the higher gray value. In order to evaluate the spatial distribution of fouling along the membrane, the analysis of gray values was performed at different positions in the channel: the inlet, the middle, and the outlet (Figure 2.11).

Figure 2.11: Different positions for the gray values measurements along the microchannel.

The software measures the gray value on each pixel along the vertical line (red line in Figure 2.11), yielding an average gray value with its respective standard deviation.

For the cases, when over the course of filtration the dark zones were formed against the bright background (as in Figure 2.13 (A)), the modified protocol was established. The analysis of the gray values at the inlet, the middle, and the outlet was performed not along the line, but inside the rectangular zone, as depicted in Figure 2.12.

Figure 2.12: Different positions for the gray values measurements along the microchannel, when dark zones were formed.

For each rectangular image the specific threshold gray value was applied to discriminate the bright background zones (gray value above the threshold) and the dark regions (gray value below the threshold). As the membrane fouling progressed during the experiment, for each individual image the intensity of background is different. Therefore, the threshold value was individually selected so that the most accurate separation of the bright and the dark regions would be achieved (Figure 2.13).

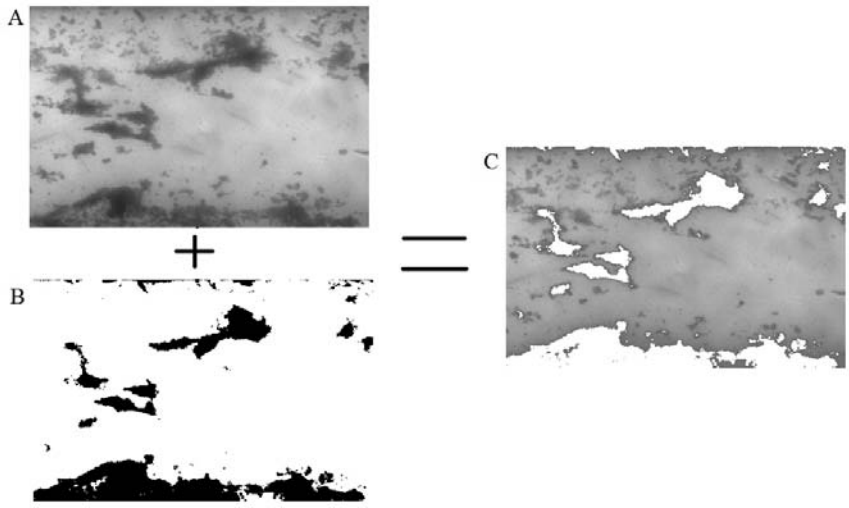

Figure 2.13: Image processing for the determination of the surface coverage by dark zones and evaluation of the fluorescent intensity of the background. (A – the original image, B – image converted into a binary system, C – result of subtraction of image B from A).

Once the threshold value is selected, the image is converted into the binary blank and white system, where the black parts represent the zones below the threshold and the white once – above the threshold. Using such approach, one may determine the percentage of the black regions. Then, the original (Figure 2.13 (A)) and the binary (Figure 2.13 (B)) images are superimposed in order to subtract the dark zone from

the original image. The resulting image (Figure 2.13 (C)) possesses the initial background with white zones (subtracted part), which provides a possibility to calculate the mean gray value of the background. However, ImageJ considers the white zones as maximal gray value (255) for the calculation, while in practice they should not be taken into account, and as a result, it provides an overestimated mean gray value. Practically, the equation used by ImageJ in such case may be presented as in Equation 2.10.

$$MeanGV_{initial} = MeanGV_{wsr}(1 - f) + 255f \tag{2.10}$$

where $MeanGV_{initial}$ is the mean gray value determined by ImageJ, f – fraction of surface covered by dark zones, and $MeanGV_{wsr}$ – the mean gray value without subtracted regions.

Thus, to eliminate the mean gray value of the area without subtracted parts the Equation 2.10 may be rearranged to obtain Equation 2.11:

$$MeanGV_{wsr} = \frac{MeanGV_{initial} - 255f}{1 - f} \tag{2.11}$$

Finally, since in the ImageJ software it is not possible to make calculations without considering the white zones, it becomes impossible to identify reasonable standard deviation. Therefore, the gray value measurement for the experiments, where dark zones were detected, are presented without error bars.

6 SEM imaging

The microfluidics device after the fouling experiment was dissected (separation of the glass substrate from the NOA68 part) and the part with membrane inside was dried at $40°\mathrm{C}$ overnight. Dry sample was gold spattered at $20\ \mathrm{mA}$ for $80\ \mathrm{s}$ by K550X Sputter Coater, (Quorum Technologies Ltd, UK) and analyzed using Phenom XL Scanning Electron Microscope (Fondis Bioritech, France).

Now that the used materials and methods are summarized, let us proceed with experimental part of the present project.

7 References

1. Sigma-Aldrich. *Atto 647N Protein Labeling Kit*. 2016; Available from: http://www.sigmaaldrich.com/content/dam/sigma-aldrich/docs/Sigma/Datasheet/6/76508dat.pdf.

2. Vanholder, R., R. De Smet, G. Glorieux, A. Argiles, U. Baurmeister, P. Brunet, W. Clark, G. Cohen, P.P. De Deyn, R. Deppisch, B. Descamps-Latscha, T. Henle, A. Jorres, H.D. Lemke, Z.A. Massy, J. Passlick-Deetjen, M. Rodriguez, B. Stegmayr, P. Stenvinkel, C. Tetta, C. Wanner, and W. Zidek, Review on uremic toxins: Classification, concentration, and interindividual variability. *Kidney Int*, 2003. 63(5): p. 1934-1943.

3. ter Beek, O., D. Pavlenko, D. Snisarenko, M.H. Suck, and D. Stamatialis, *Development of polyethersulfone and SlipSkin blend membranes for prolonged hemodialysis*. 2016, University of Twente.

4. Nurdin, L., A. Venancio-Marques, S. Rudiuk, M. Morel, and D. Baigl, High-throughput photocontrol of water drop generation, fusion, and mixing in a dual flow-focusing microfluidic device. *Comptes Rendus Chimie*, 2016. 19(1–2): p. 199-206.

5. Kawasumi Laboratories America, I. *Hollow Fiber Dialyzer for Hemodialysis*. 2011; Available from: http://www.kawasumiamerica.com/wp-content/uploads/2011/08/renak-brochure.pdf.

6. Himmelfarb, J. and T.A. Ikizler, Hemodialysis. *New England Journal of Medicine*, 2010. 363(19): p. 1833-1845.

7. Elert, G., *The Physics Hypertextbook*. 1998–2014, http://physics.info/viscosity/.

8. Schneider, C.A., W.S. Rasband, and K.W. Eliceiri, NIH Image to ImageJ: 25 years of image analysis. *Nat Meth*, 2012. 9(7): p. 671-675.

Characterization of microfluidics device and its coupling with fluorescent microscopy

3

Introduction

In this chapter, the characterization of a developed membrane-based microfluidics device (MMD) as well as its coupling with the fluorescent microscopy are presented.

Firstly, the hydrodynamic and the flow distribution inside the MMD are characterized. This is done in order to understand the flow conditions at which the filtration process occurs. Such information is valuable, because it provides a possibility to compare the filtration throughput at the macro scale (Amicon cell) and the micro scale (MMD). In addition, estimation of filtration conditions is important for the interpretation of the protein filtration process outcome.

A model to determine the pressure conditions inside the retentate compartment of a MMD is developed and used for the calculation of the transmembrane pressure. The set of resistances was evaluated in order to estimate the membrane permeability at the micro scale and to compare it to the macroscale one in order to check the good working of the MMD (absence of leakage).

In the second part, the main objective is to investigate how it is possible to combine the developed MMD with fluorescence microscopy. The influence of various operating parameters on the fluorescent measurements was investigated. Particularly, the position of focus, the exposure time, the noise fluorescent signal from the bulk solution and the upper wall of the microchannel were evaluated with respect to the potential of real-time observation of the membrane fouling.

In the third part, in order to have a first analysis of the membrane fouling by measuring fluorescence, the microscale cross flow filtration of the protein (Bovine Serum Albumin) solution was performed. Various hydrodynamic conditions along with different transmembrane pressures were tested to analyze their impact on the membrane fouling.

1 Membrane-based microfluidics device characterization and resistance modelling

Once the membrane-based microfluidics device (MMD) was developed and manufactured, the integrity testing was performed in order to demonstrate that the device is leak-free and is able to withstand elevated pressures, at which the

microchip is supposed to be used. For this the solution of dye (Cibanon green BF) was pumped through the microchannel. Figure 3.1 demonstrates the top view of the microchip after the leak-proof testing of channel 1 (upper part of the MMD), while two other channels remain virgin.

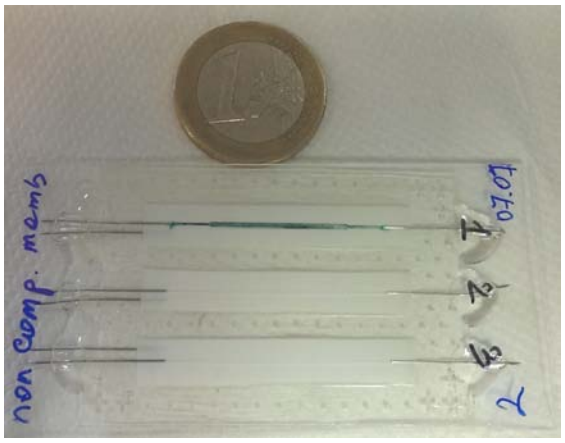

Figure 3.1: Photo of MMD after filtration of solution of dye in one of the microchannels.

As it can be seen from Figure 3.1, during the testing, the solution of dye was kept inside the designed channel without any apparent lateral spreading along the membrane. However, such integrity of the device and stability of flow was achieved only in case when the conditioning of the system with osmotic water was performed before the use of solution of dye. In other words, the membrane inside the MMD has first to be rinsed with water, so that all pores would be filled before the testing solution is supplied. Therefore, in order to insure that the solute would flow inside the microchannel without lateral permeation, the conditioning of the system is the primary measure.

Since during the use of the MMD the control of experimental conditions was realized by the remote pressure controller (the structure of the set-up is presented in Section 4.2.2 of Chapter 2), the determination of the pressure profile inside the MMD was required. For this, the set of pressure stepping experiments was conducted in order to monitor the influence of the inlet, the retentate, and the permeate pressures on the flow rates distribution inside the system. Figure 3.3 and Figure 3.4 demonstrate the experimentally obtained flow profiles inside the retentate and permeate compartments at constant inlet pressure of 350 mbar and varied permeate pressure (from 0 to 140 mbar). The outlet pressure (retentate) is the atmospheric pressure (Figure 3.2).

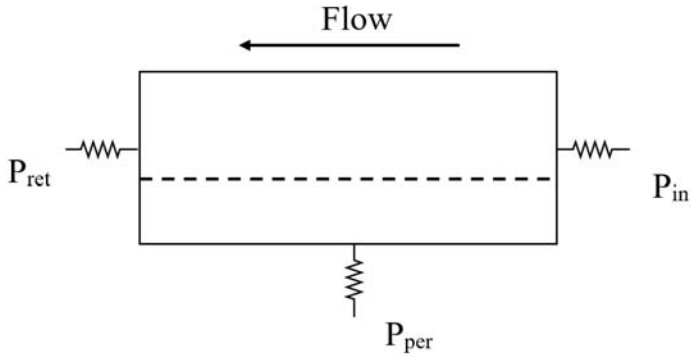

Figure 3.2: Schematic representation of controlled pressures during the use of MMD. (Dash line stands for the membrane placed inside the MMD).

It is worth-noting that the ΔP parameter on the secondary Y-axis of Figure 3.4 stands not for transmembrane pressure (TMP), but for the difference between the inlet and the permeate pressures. For example, the ΔP of 230 mbar means that the inlet and permeate pressures were set at 350 mbar and 120 mbar, respectively.

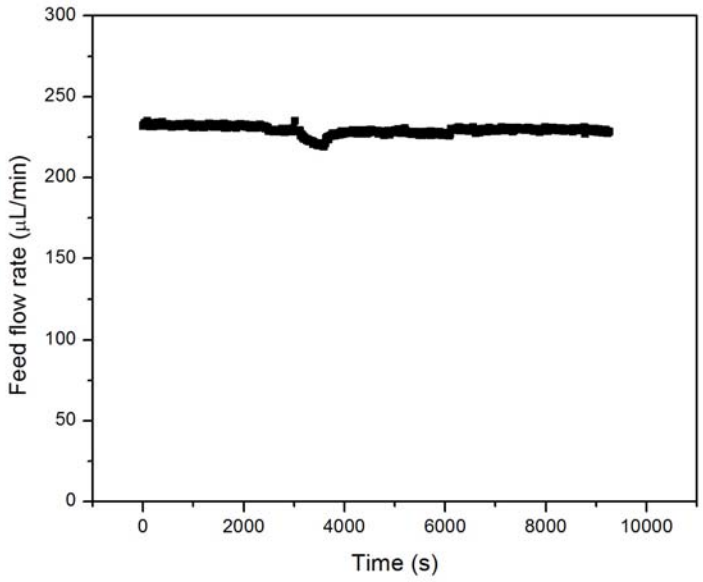

Figure 3.3: Feed flow profile at constant inlet pressure of 350 mbar.

According to Figure 3.3, the feed flow rate is stable throughout the entire experiment, while the permeate flow rate was demonstrating a step-like response to the changes in the permeate pressure (Figure 3.4). Based on observed responsiveness one can

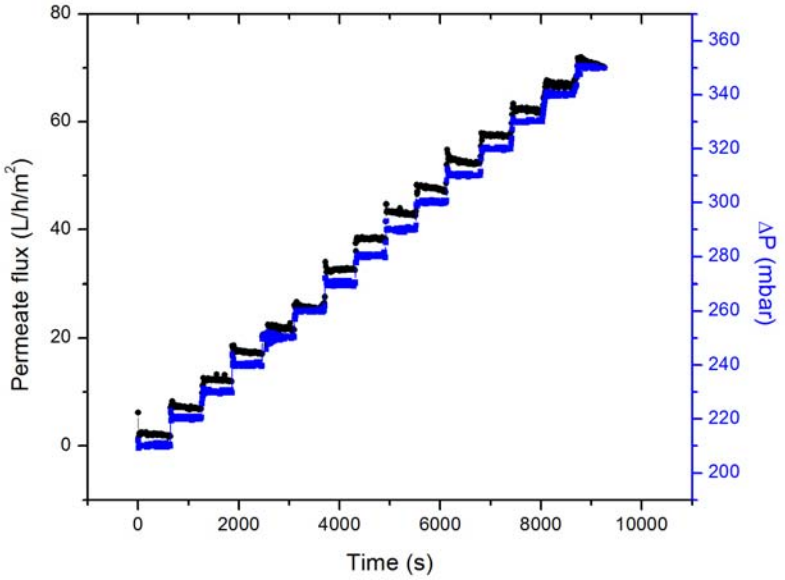

Figure 3.4: Pressure stepping for the MMD at constant inlet pressure of 350 mbar.

conclude that the developed MMD coupled with the pressure and flowrate monitor is sensitive even to the minor changes in experimental conditions. In addition to the experiment presented in Figure 3.3 and Figure 3.4, analogous procedures were performed at inlet pressures of $400\ \mathrm{mbar}$ and $250\ \mathrm{mbar}$ in order to have a set of data that could help to characterize the flow distribution in the MMD. The collected results were used to establish a model which allows to calculate the resistances of different parts (inlet, retentate and permeate) of the MMD with use of the following set of equations:

$$\frac{P_0 - P_{per}}{Q_{per}} = R_{per} \quad (3.1) \qquad \frac{P_0 - P_{ret}}{Q_{ret}} = R_{ret} \quad (3.2) \qquad \frac{P_{in} - P_0}{Q_{in}} = R_{in} \quad (3.3)$$

where Q is fluid flow rate, the subscripts ret, per and in stand for the retentate, the permeate and the inlet respectively.

Combined with the flow rate conservation ($Q_{in} = Q_{ret} + Q_{per}$), the solving of these equations allows to determine the set of resistances and the pressure, P_0, of the retentate inside the MMD. The solving is realized with a least square fitting of the

model on the whole experimental data set.

The schematic description of the system of resistances in the microfluidic device along with its calculated values are presented on Figure 3.5.

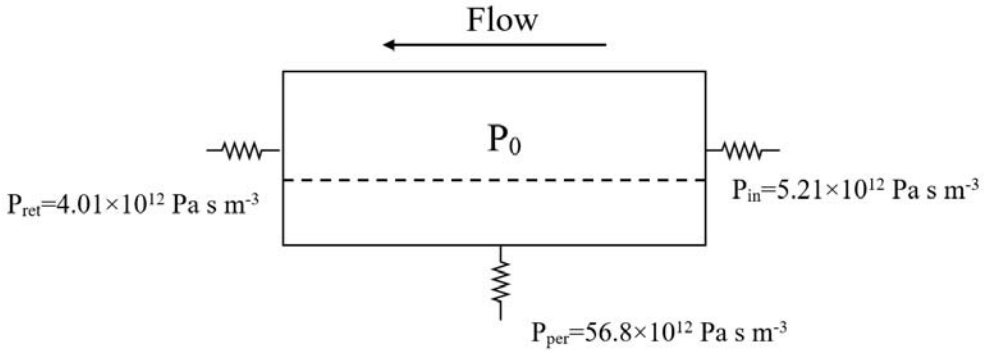

Figure 3.5: Schematic representation of the system of resistances in the MMD with modelled values.

According to Figure 3.5, the resistances of the inlet and the retentate (mainly due to the tubes and connections) are in the same order of magnitude: $5.21 \times 10^{12}\,\mathrm{Pa\,s\,m^{-3}}$ and $4.01 \times 10^{12}\,\mathrm{Pa\,s\,m^{-3}}$, respectively. Despite the symmetrical structure of the retentate side of the MMD small difference between obtained values for R_{ret} and R_{in} is attributed to the greater length of "inlet" tubing connecting MMD to the feed reservoir compared to the tubes used to collect the retentate. On the other hand, the resistance of the permeate side was found to be one order of magnitude greater than for inlet and retentate: $56.8 \times 10^{12}\,\mathrm{Pa\,s\,m^{-3}}$. This result is related to the contribution of the membrane resistance Equation 3.4.

$$R_{memb} = \frac{1}{L_p S} \tag{3.4}$$

Where L_p stands for the membrane permeability (value is presented on the next page) and S is the filtration area inside the MMD ($0.126\ \mathrm{cm^2}$).

Since the calculated membrane resistance is $52.9 \times 10^{12}\,\mathrm{Pa\,s\,m^{-3}}$, it can be stated that membrane provides 93% of the overall permeate resistance of the MMD.

The intermediate pressure P_0 can be determined (Equation 3.5) in order to define the theoretical transmembrane pressure (Equation 3.6) and respective permeate fluxes at

different conditions throughout the experiment.

$$P_0 = \frac{R_{ret}R_{per}P_{in} + R_{ret}R_{in}P_{per} + R_{in}R_{per}P_{ret}}{R_{ret}R_{per} + R_{ret}R_{in} + R_{per}R_{in}} \tag{3.5}$$

$$TMP = P_0 - P_{per} \tag{3.6}$$

To evaluate the precision of the model the comparison of the experimental and the modelled permeate fluxes is presented in Figure 3.6.

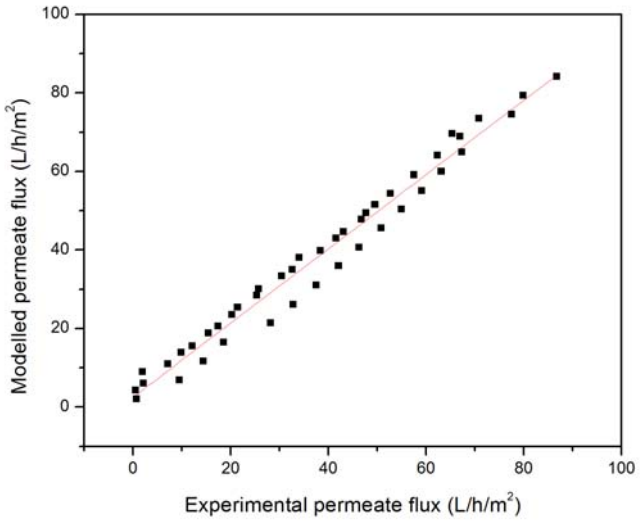

Figure 3.6: Comparison of modelled and experimental permeate flux.

According to Figure 3.6, the developed model provides rather precise theoretical prediction of the permeate flux, since the values of the modelled transmembrane pressures are close to the experimental ones (Figure 3.7). Thus, using the modelled values of TMP, the comparison between the membrane water permeability in the developed MMD and in conventional Amicon® cell can be performed. Based on the macro experiment (with use of Amicon® cell) the membrane permeability is $562 \pm 53\ \mathrm{L\,m^{-2}\,h^{-1}\,bar^{-1}}$, while at the microscale experiment it was determined to be $541 \pm 37\ \mathrm{L\,m^{-2}\,h^{-1}\,bar^{-1}}$, meaning that the membrane permeability measured at the macro and the microscale are very close to each other.

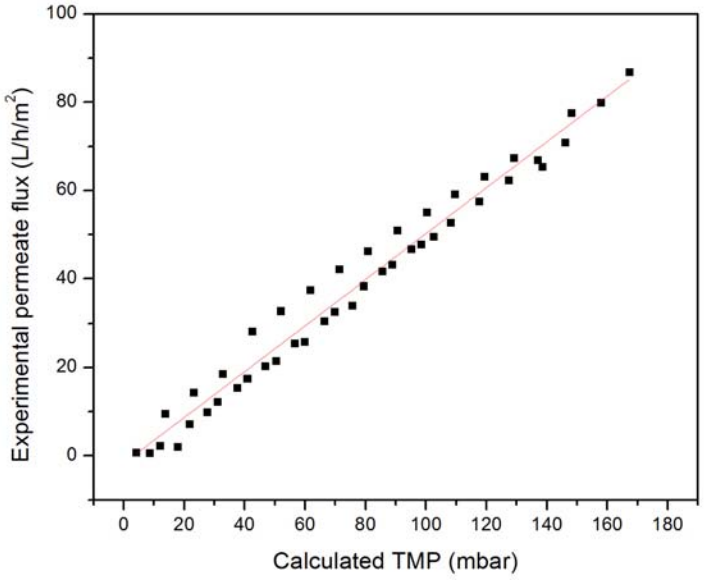

Figure 3.7: Permeate fluxes obtained at different TMPs calculated from the model.

From Figure 3.7 it can be seen that there is a linear correlation between the modelled TMP and the resulting permeate flux, which is similar to the outcome of conventional water permeability testing in Amicon® cell. Therefore, it can be stated that having the model to evaluate the pressure conditions inside the MMD, it is possible to perform membrane-based processes at the micro scale with precise control.

2 Preliminary testing of membrane-based microfluidics device performance during the protein filtration

Once the integrity of the MMD was demonstrated and hydrodynamic modelling was performed, the possibility to observe the permeate flow reduction due to membrane fouling was evaluated. For this purpose, the comparison of pure PBS permeability with the permeate flow pattern during the filtration of protein (BSA) solution (Figure 3.8) was performed. The BSA was chosen for this test in order to be sure to have the protein deposition on the membrane; the protein (MW=66 kDa) is totally retained by the membrane with molecular weight cut off 50 kDa.

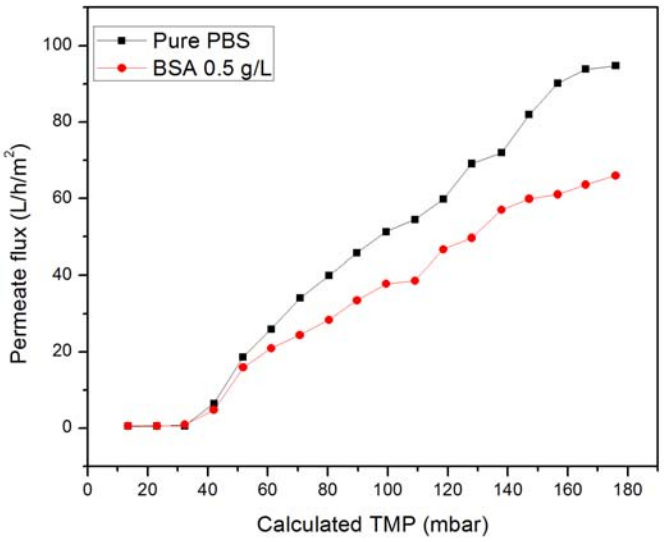

Figure 3.8: Comparison of pure PBS and BSA solution filtrations.

According to Figure 3.8, first three points on the permeate flux curve both for PBS and BSA filtration are not on the straight line with further measurements. The reason for such inaccuracy is that the developed model was not adjusted for every MMD. Even despite the established fabrication process of the MMD, there are still some parameters, which could bring a deviation from one MMD to another. For example, the internal diameter of the metal capillaries, which were used to connect the device to the experimental set-up, is not standard and deviates in the range of several micrometers. Moreover, the position of each capillary is not ideally controlled between different microdevices. It is due to this reason, there is a possibility of slight mismatch between resistances used in the model and the ones in every particular MMD.

The permeate flow during protein filtration (Figure 3.8) starts to deviate from the reference curve around TMP of $60\ \mathrm{mbar}$, which corresponds to the permeate flux of $20.94\ \mathrm{L\,h^{-1}\,m^{-2}}$. The reduced permeate flow during protein filtration may be attributed to different mechanisms of membrane/solute interactions (concentration polarization, pore clogging, formation of the protein deposit, gel formation etc). However, at this point, the main conclusion from Figure 3.8 is that the developed MMD allows to perform the membrane-based separation at the microscale and to observe the permeate flow reduction due to the fouling.

3 Coupling of the microfluidics device with the fluorescent microscopy

In order to obtain detailed information about fouling on the membrane surface throughout the experiment, the real-time observation may be employed. One of the approaches allowing the *in-situ* follow-up of the membrane fouling development is a coupling of the transparent MMD with the fluorescent microscopy. Aiming to optimize this procedure, the impact of different microscopy-related parameters on the experimental results has to be evaluated.

3.1 Effect of focusing on the fluorescence signal

One of parameters which may influence the result of measurement of the fluorescent signal is the position of the focus. Figure 3.9 demonstrates the appearance of the membrane surface (at perfect focus) with some protein adsorbed during the filtration process, which was performed inside the MMD. The term "perfect focus" stands for the position of the microscope objective at which the image of a membrane surface is the most sharply defined.

Figure 3.9: The appearance of the membrane surface at perfect focus after fouling with fluorescent BSA. (Positions 1, 2 and 3 are arbitrary selected at regions with visually different fluorescent intensity). Magnification: x50.

In order to estimate how the deviation of the focus position is influencing the measured fluorescent signal, the set of images at different positions along the Z-axis (normal to the membrane surface) with a step of $50\ \mu\mathrm{m}$ was acquired, and analyzed at three different positions (Figure 3.10) marked in Figure 3.9.

According to Figure 3.10, the fluorescent signal obtained from the zones with different intensity is almost independent on the position of focus. In particular, the gray value at the point 1 depending on the Z-position is varying in the range from 67 to 69. Similarly, the deviations ranges for points 2 and 3 are also rather narrow: from

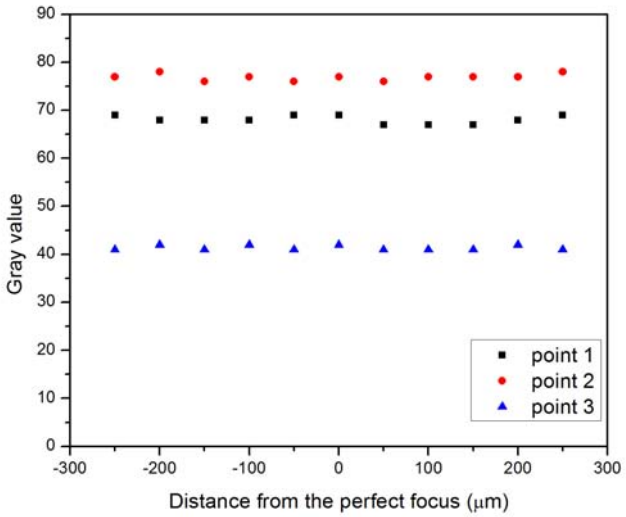

Figure 3.10: The influence of Z-position of focus on the acquired fluorescent signal. (The focus on membrane surface is set perfectly at the sixth position).

76 to 78, and from 41 to 42, respectively. Therefore, it can be concluded that even a significant misplacement (in the analyzed range of 250 μm) of the focus would not lead to noticeable changes in the recorded intensity of the fluorescent signal.

3.2 Exposure time during the image acquisition

Since the intensity of the fluorescent signal is serving as a visual indicator of the membrane fouling, the precision of its measurement is of high importance. Hence, the duration of the collection of light (exposure time) coming from the membrane by the camera has to be carefully adjusted. Such adaptation has to fulfil two limiting requirements. On one hand, the selected exposure time (ET) has to allow the clear observation of the evolution of fouling during the filtration of the fluorescent species. In other words, the exposure time should be long enough to capture the measurable signal coming from the surface. On the other hand, it is important to avoid the achievement of the overexposure, the condition when collected signal is equal to the maximal possible light intensity, which may be measured by the used camera. The main drawback of the overexposure is that even in case of further fouling build-up, the increasing fluorescent intensity would not be recorded. Therefore, the exposure time should be short enough, so that the continuously

intensifying fluorescent signal during the filtration process would not reach the maximal measurable intensity. Several examples of how the ET influences the fluorescent profile during the filtration of 0.1 g L PBS-based (pH=7.4) solution of BSA-FITC are shown in Figure 3.11. All experiments were conducted at feed flow rate of 250 µL min^{-1} and TMP of 180 mbar.

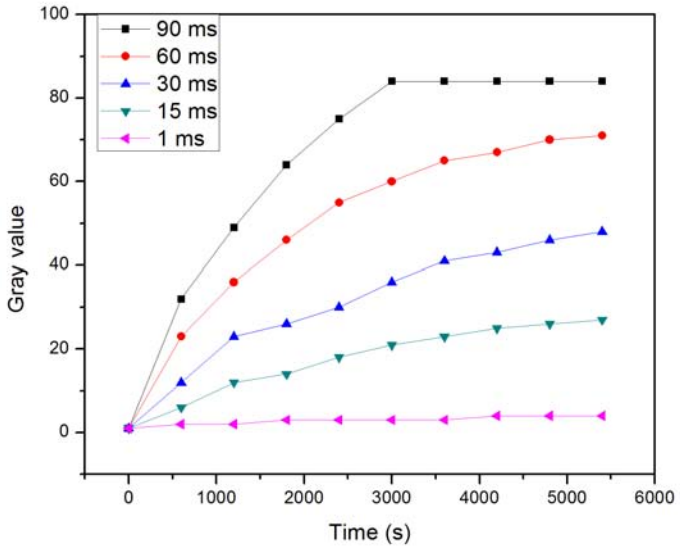

Figure 3.11: The schematic representation of possible gray value profiles depending on selected exposure time.

As it could be seen from Figure 3.11, depending on the selected exposure time, the obtained pattern of gray value evolution is different. Namely, the exposure time of 1 ms is not optimal, because with the obtained pattern it is hard to evaluate the extent of membrane fouling since the range of the fluorescent signal variation is too narrow. Similarly, the exposure time of 90 ms is not optimal, because the maximal gray value (overexposure) was reached after 3000 s and, therefore, any further increase in fluorescence cannot be monitored. On the other hand, three other exposure times are appropriate since they allow the clear visualization of the changes of the fluorescent signal from the beginning of the fouling build-up until the end, without reaching the overexposure. Hence, for the selected type and concentration of protein the exposure time has to be between 15 ms and 60 ms.

3.3 Influence of the optical structure of the microchip

The close examination of the optical structure of the MMD in combination with the fluorescent microscopy (Figure 3.12) would reveal that acquired fluorescent signal may come from various sources.

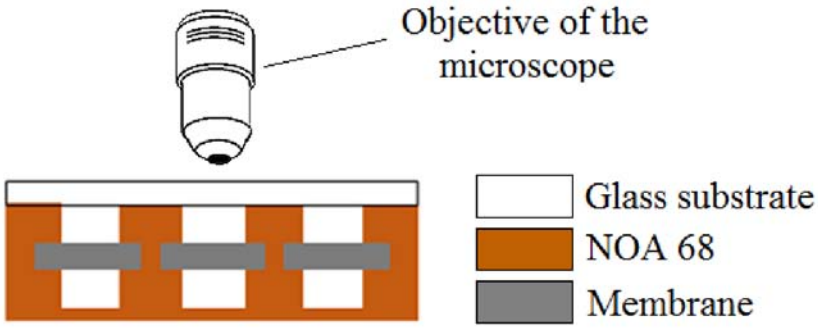

Figure 3.12: The schematic depiction of microscope objective position in relation to the MMD.

In principle, the resulting image is a sum of signals from the membrane surface, where fouling occurs, from the solution flowing inside the microchannel, where the labeled species are dissolved, and from the glass surface, where the adsorption is also possible, especially dealing with the protein solutions. Therefore, the contribution of each source has to be carefully evaluated.

3.3.1 Significance of protein adsorption on the glass surface

In order to evaluate how the protein adsorbed on the glass surface may contribute to the intensity of fluorescent signal from the whole system, the post experimental MMD «autopsy» was performed. It is important to point out that this test was performed after the filtration, which was conducted with used of more concentrated solution of BSA-FITC ($1\ \mathrm{g\,L^{-1}}$ vs $0.1\ \mathrm{g\,L^{-1}}$) compared to other tests presented in Section 3.

According to Figure 3.13, the images obtained from the glass surface exhibit no significant signal at selected exposure times. In contrary, even at the exposure time of $1\ \mathrm{ms}$, the membrane surface possesses measurable fluorescence. While at the exposure time of $30\ \mathrm{ms}$ the overexposure condition is achieved. Thus, it can be postulated that the protein adsorption on the glass surface at analyzed conditions

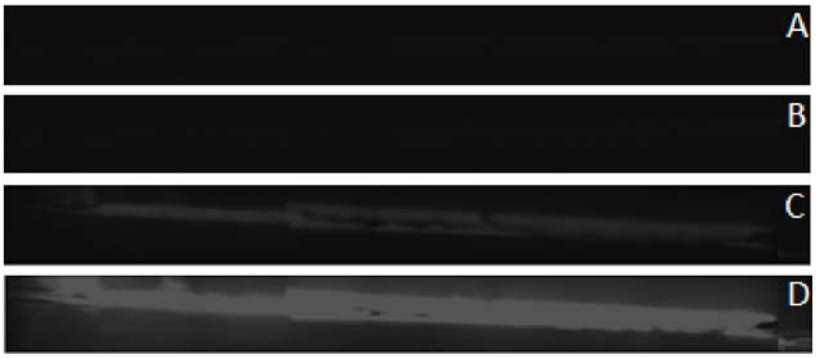

Figure 3.13: Comparison of fluorescence intensity of membrane and glass surfaces at different exposure times (A – glass surface at $1\ \mathrm{ms}$, B – glass surface at $30\ \mathrm{ms}$, C – membrane surface at $1\ \mathrm{ms}$, D – membrane surface at $30\ \mathrm{ms}$).

does not have a noticeable contribution to the overall fluorescence intensity and as a result we can neglect this value.

3.3.2 Influence of solution flowing inside the channel

Another possible source of error in the measurement of the fluorescence intensity is the solution of labeled species flowing inside the microchannel. Theoretically, in addition to fluorescent light coming from the membrane surface, the camera of the microscope may also capture some additional signal from the dissolved species. In order to determine the extent of their influence the two-step experiment was performed. Initially, the filtration of fluorescent BSA ($0.1\ \mathrm{g\,L^{-1}}$) was carried out for $60\ \mathrm{min}$ aiming to obtain a fouled membrane surface with significant fluorescent signal, and then, the channel was rinsed with pure buffer solution (PBS) during $40\ \mathrm{min}$ to compare the gray value before and after the rinsing (Figure 3.14). In addition, the fluorescent signal collection was performed at three different exposure times ($60\ \mathrm{ms}$, $30\ \mathrm{ms}$ and $15\ \mathrm{ms}$), which were found to be optimal in Section 3.2.

From Figure 3.14, the substitution of BSA-FITC solution inside the retentate compartment of the MMD with the pure PBS results in minor changes in in the gray values. Particularly, at the exposure time of $60\ \mathrm{ms}$, the switching from filtration to rinsing results in the slight reduction of gray value from 62.6 to 60.4. While, at $30\ \mathrm{ms}$ and $15\ \mathrm{ms}$, the effect was oppositely directed and induced an increase from 42.6 to 45.6 and from 20.9 to 21.7, respectively. Since these variations happened

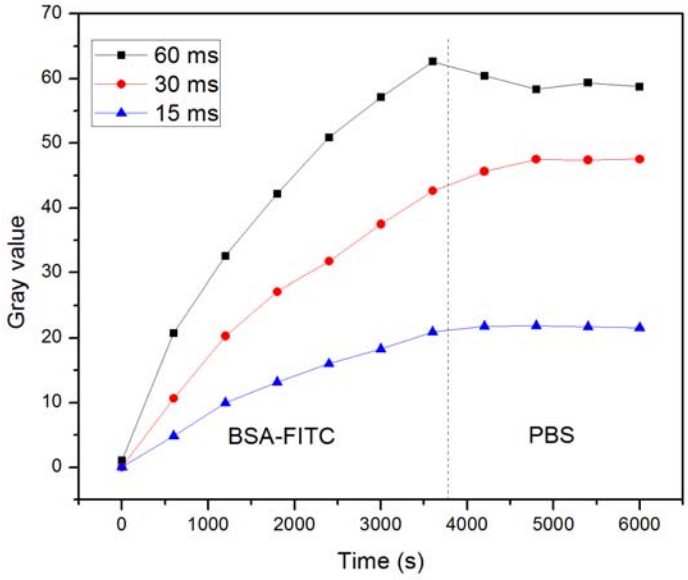

Figure 3.14: The effect of post experimental rinsing on the fluorescent signal intensity.

right after the beginning of the rinsing step and did not progress thereafter, it can be assumed that one of the sources of these changes is simply in the replacement of reservoirs with different solutions. Disconnection of one reservoir and its substitution with another one is regularly associated with formation of air bubble in the inlet tubing. As so, this air bubble passing through the MMD may induce partial detachment of protein from the fouled membrane surface, which would lead to a decrease of the fluorescent signal. In parallel, the air bubble may also initiate some rearrangements of the fouling layer (displacement of protein deposits, partial unfolding of adsorbed proteins), which may contribute to the increase of the fluorescent signal. In order to avoid such ambiguity in the discussion of the effect of the post-experimental rinsing, we would just conclude that the impact (if any) of the solution inside the microchannel on the recorded fluorescence is not exceeding 5%. Keeping in mind that all the following filtration processes are conducted at same exposure time and concentration of the solution, we may assume that this variation would be proportional and would not influence their comparison.

The continuous rinsing in all three cases was not inducing any reduction of fluorescent signal. Such finding suggests that once the protein solution is flushed away, the system, even when PBS is still flowing inside the channel, remains stable

and the fluorescence intensity is unchanged. These observations lead us to a major conclusion. The stability of the fluorescent signal during the rinsing may be attributed to the formation of stable deposit layer in opposition to the concentration polarization, which would have been removed during the protein solution washing out.

Finally, considering the latest discussions, it can be stated that neither solution inside the MMD nor the adsorption on the internal glass surface has a significant influence on the precision of the acquisition of signal from the membrane surface. Consequently, there is no need to take any measures to modify the collected images in order to obtain the pure intensity of light coming from the membrane surface.

4 Preliminary study. Investigation of BSA-mediated membrane fouling

Once the MMD was coupled with the fluorescent microscopy and the process-related parameters were optimized, the set of experimental investigations of the membrane fouling with the fluorescent protein (BSA-FITC) with concentration of $1\ \mathrm{g\,L^{-1}}$ was conducted. Both the influence of the cross-flow velocity and transmembrane pressure (TMP) on the fouling pattern were evaluated.

4.1 Influence of cross-flow velocity on membrane fouling

4.1.1 Experiments conducted at TMP≈0 mbar

The primary experiments were conducted at the condition where no transmembrane convection was involved. The pressure in the retentate side was counter balanced by application of the same pressure from the permeate side in order to minimize the net permeate flow (Figure 3.15).

From Figure 3.15, the permeate flow throughout both experiments was maintained at the low levels of around $0.5\ \mathrm{L\,h^{-1}\,m^{-2}}$. It was not exactly zero, due to poor precision of the flow meter at this range of flow rates. Nevertheless, such profiles indicate that the TMP was negligible, meaning that the “non-convective” regime was achieved. It should be pointed out that due to unknown reasons there was a slight reduction of

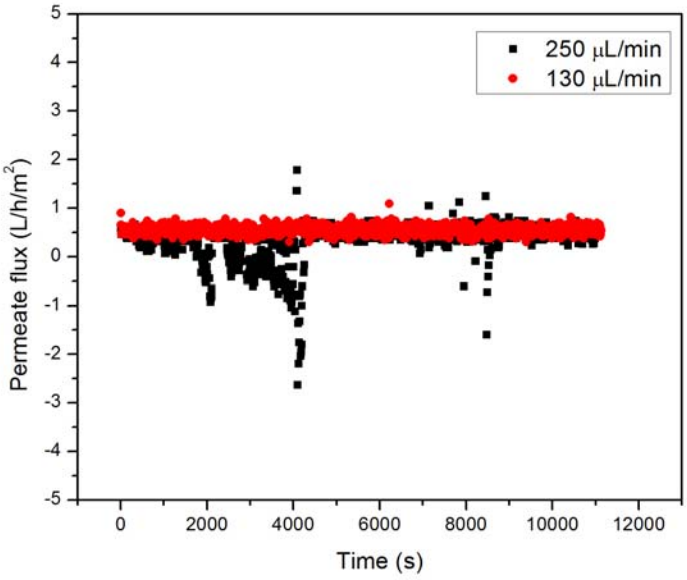

Figure 3.15: The permeate flow profiles during the experiments with TMP≈0 at two different cross flow velocities.

the permeate flow in case of the feed flow rate of $250\ \mu\mathrm{L\,min^{-1}}$. However, since the baseline of "non-convective regime" is around $0.5\ \mathrm{L\,h^{-1}\,m^{-2}}$ and not exactly zero, we would consider negligible the permeate reduction up to $-0.5\ \mathrm{L\,h^{-1}\,m^{-2}}$. In contrast, the drop of permeate flow below this range may influence the deposition of protein as the permeate backflow may hinder its transfer from bulk solution towards the membrane surface. However, such declines are observed only during the short periods of time (not longer than $2\ \mathrm{min}$). Hence, we may hypothesize that such short term deviations would not induce detectable differences in the outcome of the long process.

Therefore, it can be stated that highlighted experiments were conducted in similar conditions of TMP≈0. In addition to the flow control, the fluorescent images were collected every five minutes and the evolution of gray values is presented in Figure 3.16 and Figure 3.17 for feed flow rates of $130\ \mu\mathrm{L\,min^{-1}}$ and $250\ \mu\mathrm{L\,min^{-1}}$, respectively.

According to Figure 3.16 and Figure 3.17, in the obtained patterns it is possible to distinguish two main zones with different rate of fluorescent signal evolution.

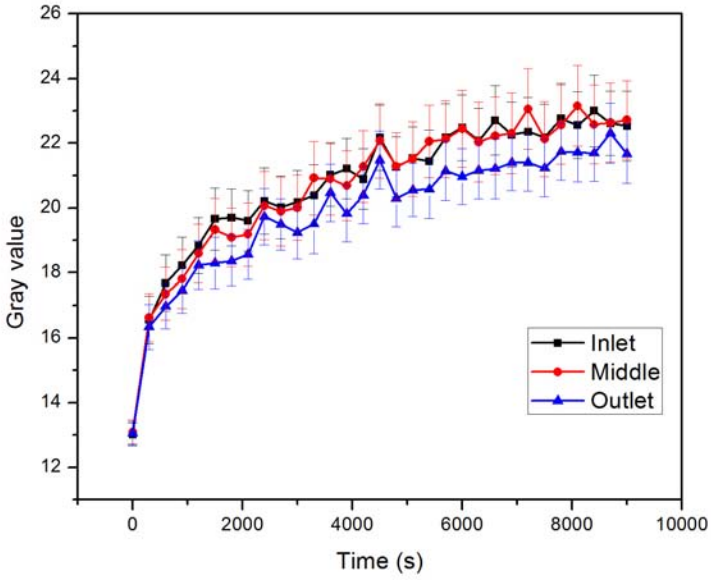

Figure 3.16: Evolution of fluorescent signal from the membrane surface at cross-flow velocity of 130 µL min^{-1} and TMP≈0.

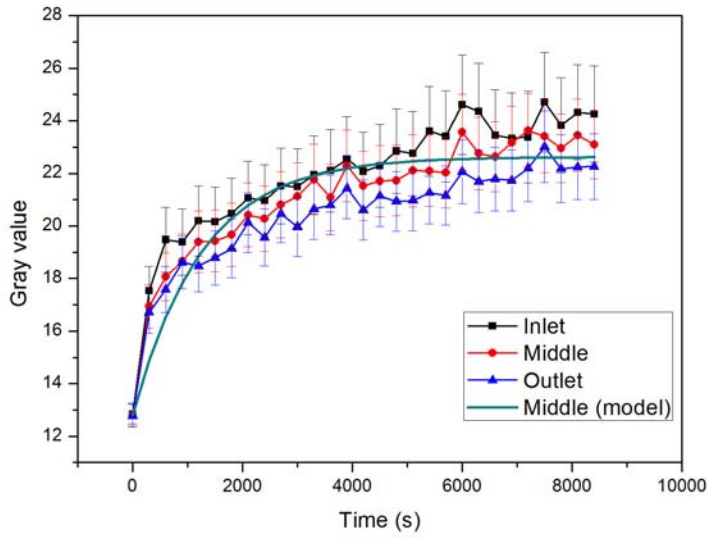

Figure 3.17: Evolution of fluorescent signal from the membrane surface at cross-flow velocity of 250 µL min^{-1} and TMP≈0.

The first zone spreads from the inception of the protein solution supply and during

the next 300 seconds and is characterized by a sharp rise of the fluorescent intensity which stands for the intense accumulation of protein chains. In principle, at this stage the initial contact between the membrane surface and the protein solution happens. Conventionally, this initial zone in case of TMP=0 is related to the rapid formation of protein monolayer on the membrane surface [1-3].

Both, for the flow rates of 250 $\mu L\,min^{-1}$ and 130 $\mu L\,min^{-1}$, during initial 300 s of the membrane/protein contact, the gray value increases up to 17, without apparent differences between the inlet, the middle, and the outlet of the channel (this analysis is discussed in Section 5 of Chapter 2). Such result suggests the uniform initial coverage of the membrane by the protein layer. Moreover, it also suggests that the process is not controlled by the cross flow velocity in this range of conditions. In other words, it is not controlled by the diffusion within the boundary layer. Hence, it seems that the process is reaction limited (heterogeneous reaction). These results are in agreement with the work of Jones and O Melia [4], who demonstrated that the BSA adsorption is reaction-limited and not diffusion-limited. In addition, the Langmuir s isotherm for reaction-controlled adsorption was proposed (Equation 3.7):

$$\Gamma(t) = \Gamma_e(1 - e^{-k_0 t}) \tag{3.7}$$

Where $\Gamma(t)$ and Γ_e stand for the mass of adsorbed BSA at time *t* and at equilibrium, k_0 (s^{-1}) is the overall reaction rate constant.

Since in the present study we use the fluorescent microscopy to quantify the BSA adsorption in the units of gray values (GV) in contrast to the adsorbed mass, we may modify the proposed Equation 3.7 to make it applicable for our case (Equation 3.8):

$$GV(t) = CV_e(1 - e^{-k_0 t}) \tag{3.8}$$

Using the fluorescent signal recorded from the middle of the channel during the process performed at 250 $\mu L\,min^{-1}$ and applying Equation 3.8 along with the least square method, the fitted parameters k_0 and GV_e were determined to be 7.9×10^{-4} s^{-1} and 22.63, respectively (resulting modelled curve is presented in Figure 3.17). The obtained result concerning the overall reaction rate constant (k_0) in our case is two orders of magnitude greater than the one determined by Jones and O Melia [4] that is 5.99×10^{-6} s^{-1} for non-fluorescent BSA at pH=10 and ionic

strength of 0.001 M . Such discrepancy is attributed to several differences in the methodology of two experiments. Firstly, the material of used membranes is different: we used polyethersulfone with cut off 50 kDa, while in the referenced publication the regenerated cellulose membrane with cut off 30 kDa was tested. Since the regenerated cellulose is a well-known material with anti-fouling properties, it is not surprising that this membrane demonstrated lower adsorption reaction rate. In addition, the method of adsorption quantification was not the same in both studies. In the present project the fluorescent signal was monitored (the signal is then relative to the accumulated protein at the membrane), while Jones and O Melia applied chemical desorption with sodium dodecyl sulphate. Finally, the conditions of experiments were different: we performed the fouling process at cross-flow (dynamic) conditions at pH=7.4, while in the referenced publication the static conditions and pH=10 were applied. The direct measurements that we realized in dynamic conditions (under the flow) with the fluorescence are then complementary to the data obtained by Jones and O Melia and, therefore, could help to improve the knowledge on protein adsorption on membrane surface.

The second zone of gray value evolution in Figure 3.16 and Figure 3.17 embraces the time span from end of first zone until the end of the experiment. This zone is characterized by the lower rate of fluorescence evolution compared to the initial stage of the process. This region may be attributed to the progression in the protein deposit formation on the membrane surface. The slow increase of the fluorescence intensity is clearly reflected by Figure 3.16 and Figure 3.17. In addition, one may notice that in this zone the difference between signals recorded from the inlet, the middle and the outlet parts of the channel becomes apparent. Particularly, within the second zone, at feed flow rate of 250 µL$\,\mathrm{min}^{-1}$ the gray value grows from 17 to 24.3 at the inlet part, to 23.1 at the middle and to 22.3 at the outlet. In parallel, in case of 130 µL$\,\mathrm{min}^{-1}$, the changes of fluorescence intensity are also noticeable: from 17 to 22.6 at the inlet and the middle, and from 17 to 21.7 at the outlet.

Such discrepancy between signals obtained at the different parts of the microchannel may be ascribed to the pressure drop which takes place inside the MMD (concept of the internal filtration). As so, although the net filtration rate inside the MMD remains close to zero, the local permeation at the inlet may happen and be balanced by the backflush occurring at the outlet part. In such case, the force which drags the protein solution through the membrane is superior at the inlet region and leads to the more significant fouling. In the same time, the backflushing flow at the outlet slightly hinders the movement of protein towards the membrane surface, and

therefore, the extent of its adsorption is notably lower. Finally, the differentiation between fouling degree at the inlet, the middle and the outlet is more obvious at the higher cross flow velocity. This observation is connected to the fact that according to Bernoulli s equation (Equation 3.9) the higher flow rate leads to the more significant local differences in the pressure drop between the inlet and the outlet of the microchannel.

$$\Delta P = \frac{32\rho l \vartheta^2}{Red_h} \tag{3.9}$$

where, ρ stands for the fluid density, l – length of the microchannel, ϑ – velocity of the fluid, Re – Reynolds number, d_h – hydraulic diameter.

The Equation 3.9 implies that at greater cross flow velocity results in the higher pressure drop along the microchannel (Table 3.1). In addition, in order to provide more complete characterization of MMD, the residence time (volume of MMD divided by the flow rate) of the fluid inside the retentate compartment is presented in Table 3.1.

Table 3.1: Dependence of the calculated pressure drop and residence time inside the microchannel on the feed flow rate.

Feed flow rate, $\mu L\,min^{-1}$	Re	Residence time, s	Δ P, Pa
250	8.96	1.1	85.4
130	4.65	2.1	44.42
75	2.69	3.7	25.63

4.1.2 Experiments conducted at TMP=180 mbar

The second set of experiments aiming to evaluate the influence of the cross flow velocity was performed with application of the transmembrane pressure of 180 mbar. This approach allows to monitor the fouling development in real-time not only by the observation of the fluorescent signal evolution, but also by controlling the intensity of the permeate flow during the entire experiment. For example, Figure 3.18 presents the changes in the permeate flow during the course of the protein filtration depending on the cross flow velocity, while Figure 3.19 and Figure 3.20 are demonstrating the

fouling associated increase of the fluorescence at different hydrodynamic conditions in the retentate side.

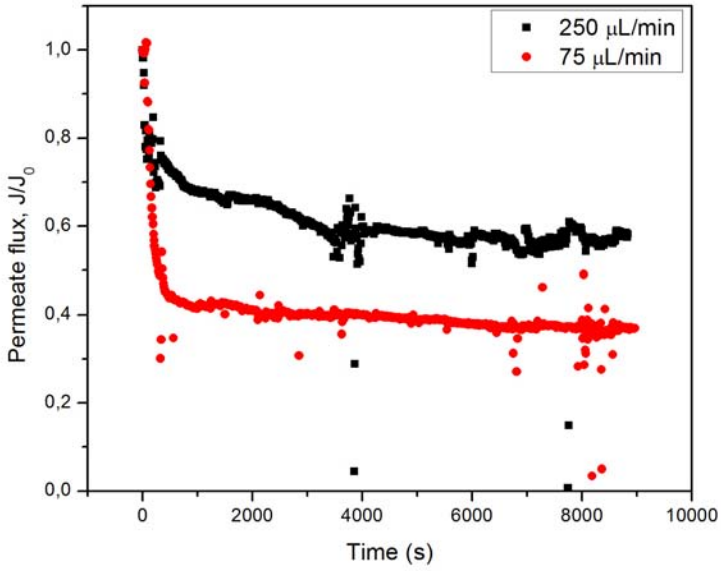

Figure 3.18: The influence of cross flow velocity on the permeate flow reductions.

Firstly, according to Figure 3.18 one may conclude that the applied technique and the developed MMD allows to perform continuous monitoring of permeate flow evolution at the constant TMP conditions.

Analyzing the obtained permeate flow profiles, it can be seen that in case of higher feed flow rate, it is possible to distinguish 3 zones, which are characterized by different rates of the transmembrane flow reduction. As it was mentioned in the "Materials and Methods" chapter, the zones of permeate flow decline are distinguished in the following manner. The first zone represents the steep linear decrease of the permeate flow and takes place in the beginning of the filtration process. The third zone is observed in the end the of the filtration experiment and is characterized by linear decline of the filtrate flow with the minimal slope. Consequently, the second ("transition") zone is located between the first and the third ones and may vary in duration and shape depending on the experimental conditions.

Practically, the primary contact between the membrane and the protein solution (Figure 3.18, "250 $\mu L\,min^{-1}$" case) results in the rapid (during first few minutes)

30% drop of the membrane permeability. Such effect is observed due to the membrane pore blockage either by the pre-existing protein aggregates [5, 6] or by protein adsorption from the supersaturated solution close to the mouths of pores [7]. While the subsequent reduction of the membrane permeability is associated with the "thickening" of the protein deposit on the surface either by the deposition of new protein layers or by the formation of the "gel" layer.

As so, immediately after the initial linear permeate flow decline the flow reduction start to occur at slower rate (second zone). During this period, which takes place until $3700\ \mathrm{s}$ the permeate flow is reduced by 15%. Once this time point is reached, it is possible to observe some perturbation of system, which is happening during around $300\ \mathrm{s}$. Such fluctuations may be related to the hypothesis that here some rearrangements/stabilization of the fouling layer occur. Once the system is stabilized the third zone starts to appear. It seems that this part of the filtration process has only minor impact on the overall decline of the membrane permeability.

In contrast, even though the profile permeability at $130\ \mu\mathrm{L\,min^{-1}}$ also exhibits three distinct zones of different fouling rates, the permeate flow reduction during the first zone is more significant and second zone is much shorter in time. During the first $360\ \mathrm{s}$, the membrane permeability undergoes a 50% reduction, which is almost twice as high as for the reduction found for the higher cross flow velocity. This effect was reported previously [8, 9] and is related to the different residence times of the protein solution inside the microchannel, or more precisely to the ratio between the axial convection and drag force which pulls the protein solution through the membrane. In case of the slower feed flow rate this ratio becomes smaller, meaning that the protein molecules are moving more intensively towards the membrane than in the direction of the outlet from the microchannel. In other words, the sweeping effect, which prevents protein from being adsorbed on the membrane surface is considerably smaller in case of smaller cross flow velocities. This leads to the enhanced transfer of protein from the bulk solution to the interface with the membrane and ultimately to the greater fouling.

In principle, the concept of ratio between two convections may be applied to explain the reason for the shortening of the second zone, which comprises the time range from $360\ \mathrm{s}$ up to $1000\ \mathrm{s}$. During this period, the membrane permeability reduces by 10%, which is comparable to the "transition" zone at the higher feed flow rate. Finally, since first two zones take place rapidly, the third zone becomes the longest: from $1000\ \mathrm{s}$ till the end of the filtration process. The membrane permeability at this stage

slightly reduces by approximately 5%, once again indicating its small contribution of the overall filtrate flow decline.

Besides, the obtained results may be explained by applying the generally accepted film theory. Mathematically, it can be represented by Equation 3.10:

$$Pe = \frac{J\delta}{D} = \ln \frac{c_m}{c_b} \tag{3.10}$$

where J is the permeate flux, δ is the thickness of boundary layer, D is diffusion coefficient of the dissolved specie (protein in our case), c_m and c_b stand for concentrations in the proximity of the membrane surface and in the bulk, and Pe is Peclet number.

As it can be analyzed through Equation 3.10, the increase of permeate flux and of the boundary layer thickness for a given compound (constant diffusion coefficient) leads to a greater concentration (c_m) and is reflected by greater Pe.

Considering the film theory, in the process conducted at 75 µL min^{-1} the concentration c_m and Pe are expected to be superior to the ones in "250 µL min^{-1}" case. In order to estimate Pe for both processes, the boundary layer thickness has been evaluated. For this, the Leveque correlation for rectangular channel (Equation 3.11) was applied:

$$Sh = 1.86(ReSc\frac{d_h}{l})^{0.33} \tag{3.11}$$

where d_h is hydraulic diameter and l is length of the microchannel.

Knowing the value of Sherwood number (Sh), one may estimate the thickness of the boundary layer by using Equation 3.12:

$$\delta = \frac{d_h}{Sh} \tag{3.12}$$

The results of Pe and δ estimations for all performed filtration experiments are presented in Table 3.2.

Table 3.2: Estimated values of Pe and boundary layer thickness.

Experiment	**Boundary layer thickness (δ)***	**Peclet number (Pe)****
75 µL min^{-1} + 180 mbar	23.2 µm	11.56
250 µL min^{-1} + 180 mbar	15.6 µm	6.75
130 µL min^{-1} + 90 mbar	19.3 µm	4.19

* - for evaluation of δ the diffusion coefficient of 6.1×10^{-11} $\mathrm{m}^2\,\mathrm{s}^{-1}$ [10] was used.

** - since the permeate flux (J) is changing with time, the initial permeate flux value was used for the calculation of Pe.

As it can be seen from Table 3.2, the boundary layer thickness and Pe are greater in 75 µL min^{-1} case. This implies that the c_m increases and, consequently, permeate flux reduction should be more significant in this case, which is corroborated by Figure 3.18.

Here, we have to point out that in Equation 3.10 a single average value of boundary layer thickness was used. While, the film theory dictates that the boundary layer thickness is not uniform along the membrane and progressively increases from the inlet towards the outlet of the system. In the view of this concept, we may expect that greater fouling would be observed at the outlet of the microchannel. The credibility of this prediction may be evaluated through the analysis of fluorescent signal evolution at different regions of MMD.

The presence of above discussed first zone can also be found in the profiles of the fluorescence obtained during the filtration experiments (Figure 3.19 and Figure 3.20), while the second and the third regions are hardly distinguishable in fluorescent profiles without comparison with permeate flow profiles.

From Figure 3.19, three zones with different rates of fluorescence evolution could be distinguished. Moreover, the location of these zones is in agreement with the ones observed for the respective curve in Figure 3.18. Particularly, the initial drop of the membrane permeability leads to the sharp rise of fluorescent signal up to 17. Then, during the second period the smooth growth of fouling is reflected by the increase of the gray values from 17 to 23.6 ± 0.3 at all the parts of the channel. Therefore, the comparison of changes of the fluorescence throughout the course of the filtration process with the variation of the membrane permeability demonstrates a sufficient

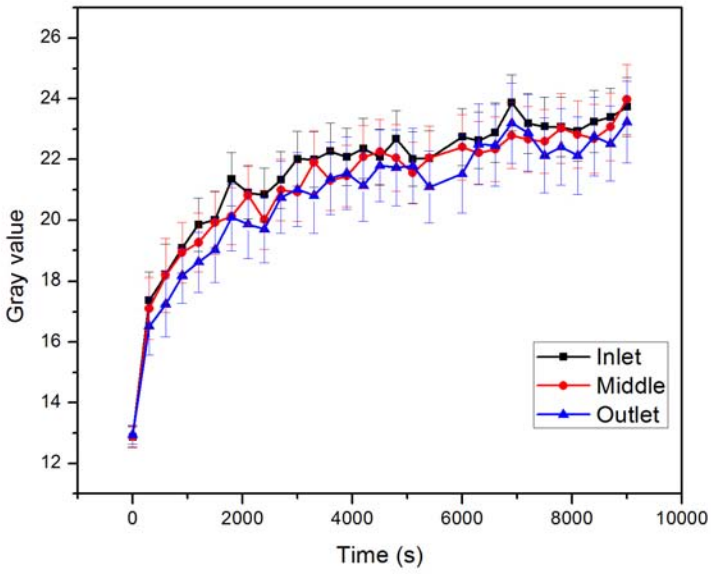

Figure 3.19: The changes on fluorescent signal from the membrane surface at the cross flow velocity of 250 µL min^{-1} and TMP=180 mbar.

correlation (more details are given later), meaning that the extent of fluorescence is a rather sensitive parameter in the evaluation of the fouling development. Finally, no visible difference between the inlet, the middle and the outlet regions of fouling is present on the fluorescent profile. This result suggests the uniform coverage of the membrane surface with the foulant.

As it can be seen from Figure 3.20, the main advancement of the fouling takes place within first 1000 s. During this time the fluorescence recorded at the inlet part rise up to 22.1, at the middle – up to 20.1, and at the outlet – up to 19.1. As of this moment, the subsequent increase of gray values is much slower and is in agreement with slow permeate flux decline in Figure 3.18. Consequently, at these conditions the evolution of the fluorescent signal is in agreement with fouling development observed by the monitoring of the permeate flows.

In the same time, unlike the fluorescence profile recorded at higher cross flow velocity, the one at 75 µL min^{-1} exhibits well-marked split between the inlet, the middle and the outlet regions of the microchannel. The inlet part exhibited the greatest gray value, while the outlet – the smallest. This result is counter intuitive in the view of the film theory and still is not well understood. Probably, it is related to

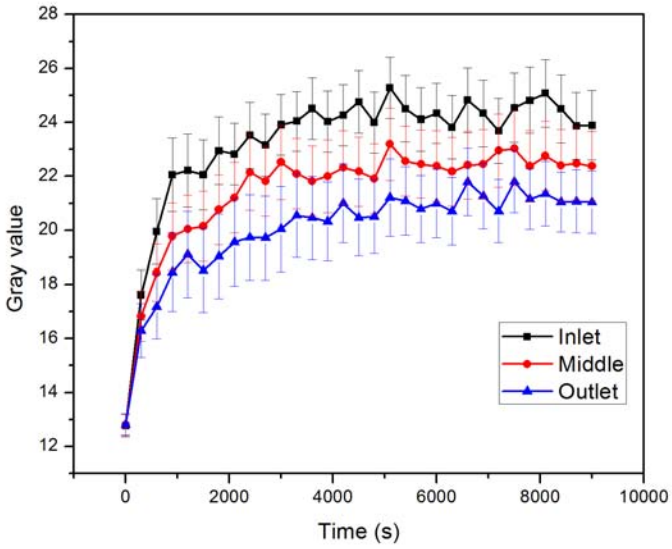

Figure 3.20: The changes on fluorescent signal from the membrane surface at the cross flow velocity of 75 µL min^{-1} and TMP=180 mbar.

the hypothesis that the protein undergoes some conformational changes at the inlet part of the microchannel and then it assumes the configuration, which is characterized by the reduced ability to adsorb. In any case, since no clear explanation for this result was found, the further analysis of this phenomena may be considered as an interesting perspective.

Besides, the previously discussed concept of internal filtration, responsible for the inequality of the fluorescent signal at the different parts of the microchannel, has to be disregarded in this case, as the applied TMP is three orders of magnitude greater than the pressure drop along the microchannel. This is corroborated by Figure 3.19, where no difference in gray values is observed, while the influence of the pressure drop has to be more apparent due to higher cross flow velocity.

4.2 Influence of transmembrane pressure on membrane fouling

One of crucial parameters determining the membrane fouling is the transmembrane pressure. Since, the permeate flux decline in case of dialysis mode (TMP=0) cannot be continuously monitored, the fluorescent microscopy may serve as a tool, to follow the fouling development in the real-time. Therefore, such approach allows

the comparison of the membrane fouling build-up during the processes with and without the transmembrane pressure employed. Figure 3.17 and Figure 3.19 present the fluorescence profiles recorded at the same feed flow rate and at different TMPs.

As it can be analyzed through Figure 3.19, the fluorescent signals obtained from the inlet, the middle and the outlet are almost identical and in the end of the filtration process all three gray values are equal to 23.6 ± 0.3. On the other hand, in Figure 3.17 one may recognize some mismatch between different parts of the microchannel. Thus, it leads to a conclusion that the presence of significant convective flow through the membrane levels the influence of the pressure drop along the membrane, which is apparent at close to zero TMP.

On the other hand, the comparison of total resulting fouling based on acquired fluorescence is rather problematic. Even though, the cumulative fluorescence (inlet+middle+outlet) at the end of experiment at no TMP is inferior to the one at the end of experiment conducted at TMP of 180 mbar: 68.9 vs 70.8, considering the size of error bars, it would be rather speculative to claim the greater protein accumulation on the membrane surface at the former condition.

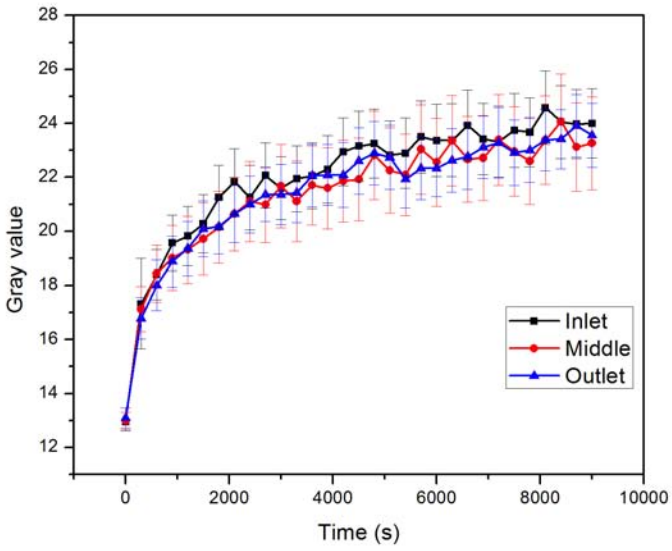

Figure 3.21: Evolution of fluorescent signal from the membrane surface at cross-flow velocity of 130 µL min^{-1} and TMP=90 mbar.

Similar conclusions can be drawn from the comparison of Figure 3.16 and Figure 3.21. Firstly, the fluorescence of the inlet and the middle parts of the microchannel recorded during the process with TMP=0 is visibly different from the outlet one. It means that at these conditions the pressure drop along the channel has an influence on the distribution of the fouling layer. In contrary, the fluorescence profile in case of the filtration experiment (Figure 3.21) possesses more homogeneous appearance. Here, the gray values of the inlet, the middle and the outlet are overlapped and exhibit the same signal at the end of the process. This observation is again related to the fact that the applied TMP is much greater than the pressure drop along the microchannel, meaning that the pressure drop does not have a noticeable effect on the fouling distribution. In addition, alike the processes performed at $250\ \mu\mathrm{L\,min^{-1}}$, the influence of TMP on the total fouling is also noticeable, but not leading to a clear conclusion on the extent of fouling.

Moreover, for the experiment conducted at $130\ \mu\mathrm{L\,min^{-1}}$ and TMP=$90\ \mathrm{mbar}$, the evolution of the fluorescent signal (average value of the inlet, the middle and the outlet ones) may be plotted as a function of the permeate flow reduction (Figure 3.22).

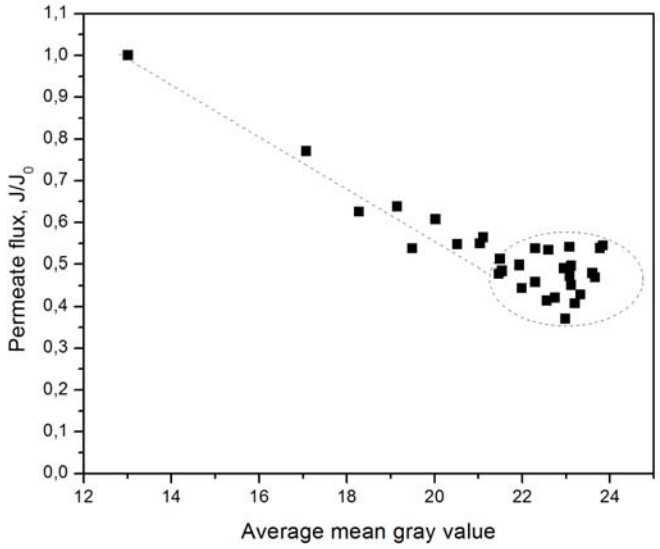

Figure 3.22: Correlation between the permeate flux reduction and the evolution of the fluorescence (average value of the inlet, the middle and the outlet) at the feed flow of $130\ \mu\mathrm{L\,min^{-1}}$ and TMP=$90\ \mathrm{mbar}$.

As it can be seen from Figure 3.22 the initial reduction of the permeate flow until around 50% of the starting value is a linear function of the gray value with the negative slope. This implies that at this region the fluorescent signal is a sensitive indicator of the extent of the permeate flux decline. However, once the gray value of around 21 is reached, there is no longer any clear correlation between gray value and flux value.

Another type of correlation between gray value and flux value may be observed in Figure 3.23 reporting the results obtained at 75 µL min^{-1} and TMP=180 mbar.

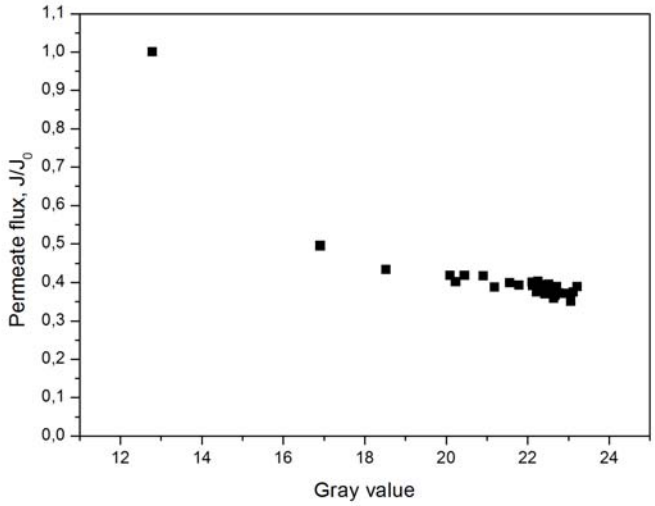

Figure 3.23: Correlation between the permeate flux reduction and the evolution of the average fluorescence along the microchannel at the feed flow of 75 µL min^{-1} and TMP=180 mbar.

According to Figure 3.23, there is no linear correlation between the permeate flux reduction and the intensity of the fluorescent signal. In the same time, Figure 3.24 demonstrates the dependence of gray values on the filtrate flux reduction during the filtration performed at the feed flow rate of 250 µL min^{-1} and TMP of 180 mbar.

All correlations presented in Figure 3.22, Figure 3.23 and Figure 3.24 are surprising as in all three cases almost stable permeate flux is accompanied by the increase of gray values. Indeed, we could a-priori think that the formation or the accumulation of gel layer at the surface could lead to a decrease in flux with a quasi-stable signal

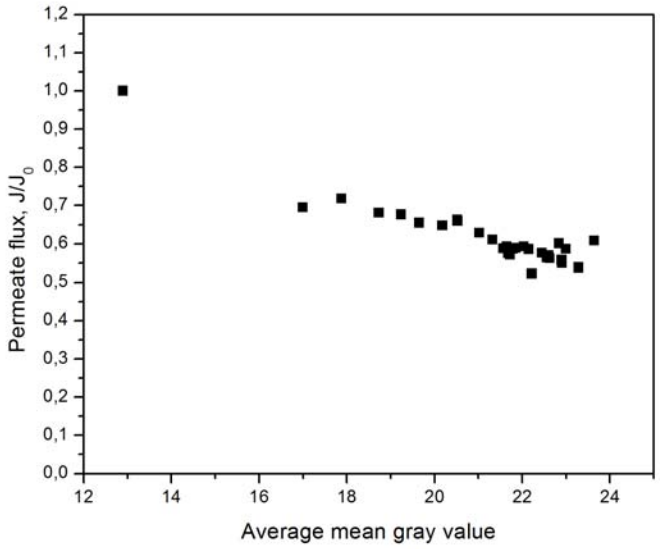

Figure 3.24: Correlation between the permeate flux reduction and the evolution of the average fluorescence along the microchannel at the feed flow rate of 250 µL min^{-1} and TMP=180 mbar.

of fluorescence (the fluorescence signal being relative to the surface concentration).

In contrast, our results suggest that the accumulation of new protein chains (increase of fluorescence) does not have an influence on the permeate flux, which is rather hard to imagine except if the accumulation leads to a protein restructuration (aggregates formation as it will be discussed in the next chapter). These aggregates are highly concentrated that would lead to an increase of the fluorescence signal with a negligible impact on the permeate flux, as aggregates of large sizes should not lead to a significant hydraulic resistance).

Trying to make a comparative analysis of obtained correlations, it can be stated that the correlation observed in Figure 3.24 seems to be intermediate between ones detected in Figure 3.22 and Figure 3.23. Probably, this finding may be related to the hydrodynamic conditions inside the retentate compartment. At the early stages of the filtration process the transmembrane convection is actively dragging the protein chains towards the surface, which leads to the deposit thickening. This leads to the reduction of the membrane permeability and is reflected by the augmentation of the gray values. The continuous increase of the thickness of the deposit layer leads to

the reduction of a slit, available for the passage of the protein solution towards the outlet of the channel. As so, probably at some point system reaches the condition when the sweeping effect of axial convection counter balances the transmembrane drag force. From here on, the deposit could stop to grow, which may result in rather stable membrane permeability. In parallel, some rearrangements of the deposit layer, which have no effect on the filtrate flux, may still go on, which is reflected by the variations in the gray values.

Aiming to summarize all the end data for the experiments where both the fluorescence and the permeate flow reduction were followed in time, we plotted Figure 3.25, which indicates the gray values at the end of the filtration process and the respective total reduction of the permeate flow rate.

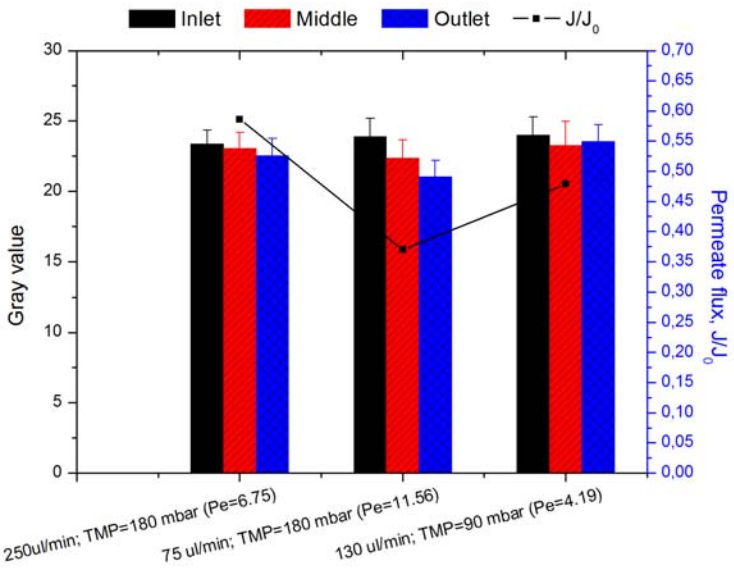

Figure 3.25: Comparison between the local fluorescent signals and the permeate flux reduction at different experimental conditions.

5 Conclusion

The main objectives of this chapter were to characterize the conditions inside the MMD, to optimize the coupling of the developed MMD with fluorescent microscopy and to use the obtained system for the preliminary testing of protein filtration at the microscale. Summarizing all the discussed results, the following conclusions can be drawn.

Developed MMD was characterized by building a model, which allows the determination of hydrodynamic and pressure conditions inside the MMD depending on applied pressures in the inlet, the retentate and the permeate. Application of this model allowed to demonstrate that the membrane permeability inside the MMD is very close to the one measured in conventional Amicon cell. This implies that the novel MMD provides a possibility to perform membrane-based filtration at the micro scale.

Coupling of MMD with fluorescent microscopy was successfully achieved, and the influence of various microscopy-related parameters on the image acquisition was evaluated. Therefore, other the course of filtration of fluorescently labelled species not only the permeate flux decline, but also the evolution of fluorescent signal may be continuously monitored.

The adsorption of BSA-FITC during the no convection process was found to be reaction-limited. It means that the diffusion towards the surface is significantly faster than the reaction on the surface. Therefore, the intensification of cross flow velocity, which leads to a reduction of boundary layer thickness has minor effect on the cumulative fluorescent signal from the inlet, the middle and the outlet of the microchannel. However, at higher tangential flow, the difference between fluorescence recorded at different parts of the membrane becomes more pronounced. This effect is probably related to the concept of local permeation induced by the pressure drop along the microchannel.

During the process where the transmembrane pressure was applied (filtration) the evolution of gray value seems to correlate with the permeate flux decline at the beginning of the experiment, where the primary contact between membrane and protein occurs. The analysis of correlation between the fluorescent signal and the permeate flux decline demonstrated that filtrate flux is not decreasing any more once the minimal value is reached, while the gray value continue to increase a bit. Possibly, this is related to some rearrangements of protein deposit that do not have influence on the transmembrane flux.

During filtration process, the most accumulation favoring conditions are the ones with highest Pe number. The increase in the fluorescent signal is more rapid in this case, which indicates the effect of the Pe on the accumulation rate. Moreover, in these conditions, some differences are noticed between the inlet and the outlet. However, surprisingly, the gray values are greater at the inlet and lower at the outlet while the opposite prediction could be made within the frame of film theory,

considering the boundary layer development along the membrane. Probably, due to the concentration at the inlet part of the microchannel the configuration of protein is changed and new configuration possesses reduced ability to adsorb on the latter part of the membrane.

Finally, the speculations about the phenomena governing the variations between the rates of the membrane permeability reduction and gray value increase are based only on some assumptions about protein configuration in solution and rearrangements in the fouling layer, which still has to be verified. In contrary, it also important to notice that nowhere in the discussion the possibility of the fluorescence quenching was addressed. Moreover, we did not consider the fact that most probably, the fluorescent signal indicates the state only of the top layer (or several top layers) of the protein deposit without information on the depth of the accumulated layer. Nevertheless, in order to address these points and verify their importance, the additional experimental studies are required and may be considered as an interesting perspective in the protein filtration at the microscale.

6 References

1. Robertson, B.C. and A.L. Zydney, Protein absorption in asymmetric ultrafiltration membranes with highly constricted pores. *Journal of Colloid and Interface Science*, 1990. 134(2): p. 563-575.

2. Huisman, I.H., P. Prádanos, and A. Hernández, The effect of protein–protein and protein–membrane interactions on membrane fouling in ultrafiltration. *Journal of Membrane Science*, 2000. 179(1–2): p. 79-90.

3. Bowen, W.R. and D.T. Hughes, Properties of microfiltration membranes. Part 2. Adsorption of bovine serum albumin at aluminium oxide membranes. *Journal of Membrane Science*, 1990. 51(1): p. 189-200.

4. Jones, K.L. and C.R. O Melia, Protein and humic acid adsorption onto hydrophilic membrane surfaces: effects of pH and ionic strength. *Journal of Membrane Science*, 2000. 165(1): p. 31-46.

5. Kelly, S.T., W.S. Opong, and A.L. Zydney, The influence of protein aggregates on the fouling of microfiltration membranes during stirred cell filtration. *Journal of Membrane Science*, 1993. 80(1-3): p. 175-187.

6. Kelly, S.T. and A.L. Zydney, Mechanisms for BSA fouling during microfiltration. *Journal of Membrane Science*, 1995. 107(1-2): p. 115-127.

7. Kim, K.J., A.G. Fane, C.J.D. Fell, and D.C. Joy, Fouling mechanisms of membranes during protein ultrafiltration. *Journal of Membrane Science*, 1992. 68(1-2): p. 79-91.

8. Field, R.W., D. Wu, J.A. Howell, and B.B. Gupta, Critical flux concept for microfiltration fouling. *Journal of Membrane Science*, 1995. 100(3): p. 259-272.

9. Howell, J.A., Sub-critical flux operation of microfiltration. *Journal of Membrane Science*, 1995. 107(1): p. 165-171.

10. Clark, W.R., W.L. Macias, B.A. Molitoris, and N.H. Wang, Plasma protein adsorption to highly permeable hemodialysis membranes. *Kidney Int*, 1995. 48(2): p. 481-8.

Membrane fouling induced by the middle molecule filtration

4

Introduction

In this chapter, the membrane fouling during the filtration of the fluorescently labeled α-lactalbumin is investigated.

Firstly, the membrane fouling at no convection conditions (no transmembrane pressure) is analyzed. Since at such conditions, the continuous monitoring of the membrane permeability reduction based on the flow measurements is not possible, the intensity of the fluorescent signal is used as a unit of the membrane fouling. Besides, the post-experimental membrane permeability is measured in order to find a correlation with the data on fluorescence.

In the second part, different transmembrane pressures and hydrodynamic conditions are applied to investigate the membrane fouling over the course of filtration. The spatial distribution of fouling is evaluated. The reduction of the membrane permeability is studied at the microscale and is accompanied by the real-time fluorescent image acquisition.

In the third part, the commercially available polyethersulfone membrane is compared with a novel home-made SlipSkin^{TM} membrane. Particularly, the influence of the cross flow velocity in the retentate side of the membrane-based microfluidics device (MMD) on the fouling pattern is studied for both membrane materials.

1 Fluorescent labeling of α-lactalbumin

The main objective of the present work is to analyze the protein/membrane interaction of medium sized proteins at pH≈7.4 (pH of blood [1]) during the membrane filtration. Since the key representative and the main marker of such molecules (β_2-microglobulin) is extremely expensive, α-lactalbumin was selected to perform the preliminary experiments as a model molecule. This choice was dictated by their similarity in size and isoelectric point (Table 4.1) and availability of α-lactalbumin.

Table 4.1: Properties of α-lactalbumin and β_2-microglobulin [2, 3].

Protein	**Molecular weight, [kDa]**	**Isoelectric point (pI)**
α-lactalbumin	14.2	4.5
β_2-microglobulin	11.8	5.7

According to Table 4.1, the molecular weight of α-lactalbumin is slightly greater than the one of β_2-microglobulin, while it is below the upper limit (60 kDa) of the molecular weight range of middle sized uremic toxins [4]. In parallel, the isoelectric point of α-lactalbumin is below 7.4, which implies that at chosen conditions the charge of both proteins is negative. Thus, the electrostatic interactions between each of these proteins and the membrane material are expected to be similar.

Aiming to follow the membrane fouling during the filtration of protein solution with use of the fluorescent microscopy, the labeling of α-lactalbumin with the fluorescent tag Atto647N was performed according to the protocol presented in Chapter 2. The common outcome of the labeling procedure in terms of D/P (Dye to Protein) ratio is 1.42 ± 0.36, which suggests that in average each molecule of protein bears approximately 1.5 fluorescent tags.

Comparison of labeled and native protein was done by their separate filtration on an Amicon cell and PES membrane. Table 4.2 summarizes the data on UV absorption at 280 nm of the feed, the retentate and the permeate of native and fluorescently labeled α-lactalbumin. Three samples of permeate 1 mL each were collected one after another during the same filtration. Hence, the total filtrate volume was equal to 3 mL.

Table 4.2: Comparison of feed, retentate and permeate absorbance of the labeled and native α-lactalbumin.

	Feed	**Retentate**	**Permeate 1**	**Permeate 2**	**Permeate 3**	**Rejection coef cient**
Labeled	0.138	0.146	0.03	0.04	0.038	71%
Native	0.083	0.088	0.058	0.068	0.068	23%

According to Table 4.2, it can be seen that the labeled α-lactalbumin is less transmitted through the selected membrane than the native one. Logically, such observation may be ascribed to the presence of the fluorescent tag or to the labeling procedure, which both may induce some changes of the protein properties (changes of configuration, increase in size etc.) or the nature of its interaction with the membrane material. Moreover, the analysis of UV absorbances of the feed (solution of labeled protein), the retentate and the permeates on the broad wavelength (200 nm – 800 nm) was performed (Figure 4.1).

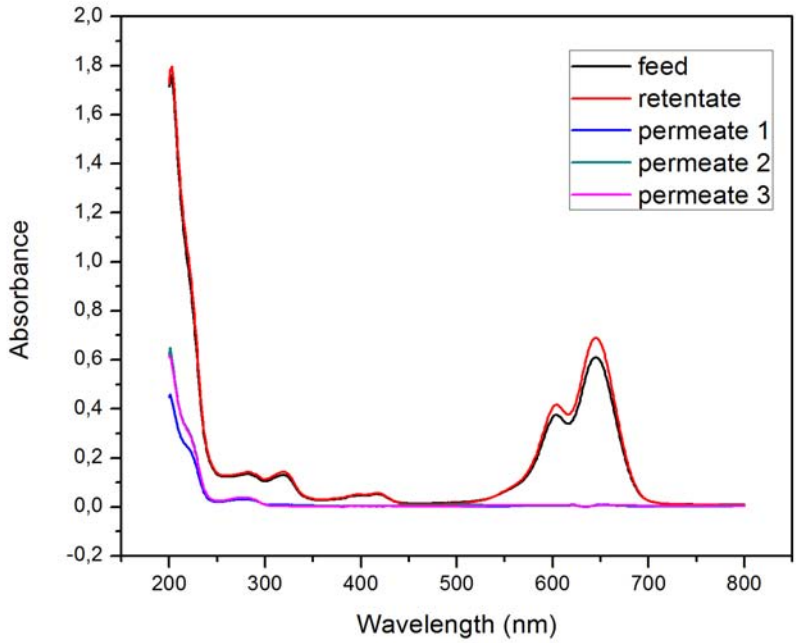

Figure 4.1: UV absorbance profiles for feed, retentate and permeate of the solution of labeled α-lactalbumin.

Figure 4.1 reveals that only the non-labeled residues may be detected in the permeate. All five profiles exhibit the absorbance band at $280\ \mathrm{nm}$ which stands for protein itself. However, the samples of the feed and the retentate possess the absorption maximum at $647\ \mathrm{nm}$, which is a characteristic band for the fluorescent tag (Atto-647N). Therefore, the presence of the label precludes the protein from permeation through the membrane and/or probably leads to the facilitated adsorption on the membrane surface. In fact, the discovery of possible changes in protein properties (molecular size and relative molecular charge) was done by Bingaman *et al.* [5], who performed the study with use of different proteins and fluorescent tags. Hence, our results are not surprising.

Nevertheless, taking into account that for the further studies of the membrane fouling, low concentration of α-lactalbumin ($50\ \mathrm{mg\,L^{-1}}$) is required, the selected tag seems to be appropriate due to the fact that it expresses one of the most intense fluorescent signals compared to other labels with red fluorescence [6].

2 Investigation of α-lactalbumin-mediated membrane fouling at TMP=0

The starting set of experiments with fluorescent α-lactalbumin was conducted in the absence of the convective flow through the membrane, meaning that there was no drag force pulling the solute towards the membrane surface. Over the course of filtration the homogeneous coverage (without apparent aggregates) was recorded (Figure 4.2).

Figure 4.2: The appearance of the membrane surface with adsorbed protein after the non-convection process at feed flow rate of 130 µL min^{-1}.

Figure 4.3, Figure 4.4 and Figure 4.5 depict the increase of the fluorescent signal from the different parts of the microchannel at different hydrodynamic conditions, while Figure 4.6 provides a comparison between the fluorescent signals at the inlet part of the MMD depending on the cross flow velocity.

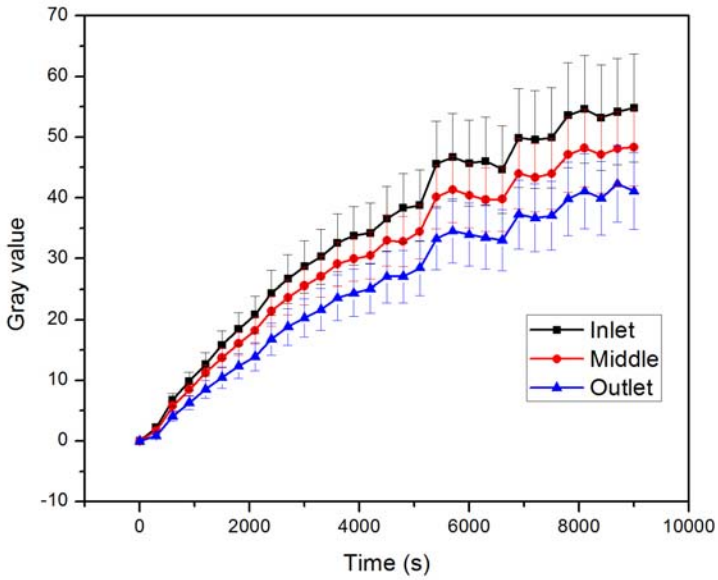

Figure 4.3: Evolution of gray value at the inlet, the middle, and the outlet of the microchannel at feed flow rate of 130 µL min^{-1}.

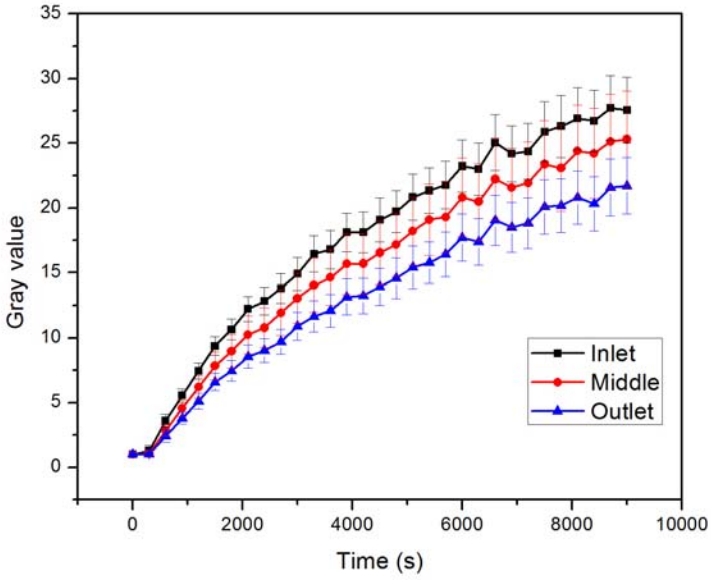

Figure 4.4: Evolution of gray value at the inlet, the middle, and the outlet of the microchannel at feed flow rate of 75 µL min^{-1}.

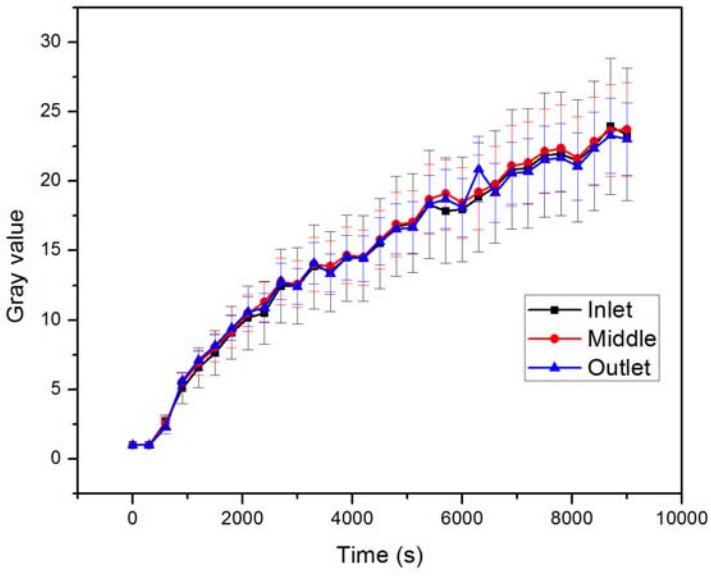

Figure 4.5: Evolution of gray value at the inlet, the middle, and the outlet of the microchannel at feed flow rate of 35 µL min^{-1}.

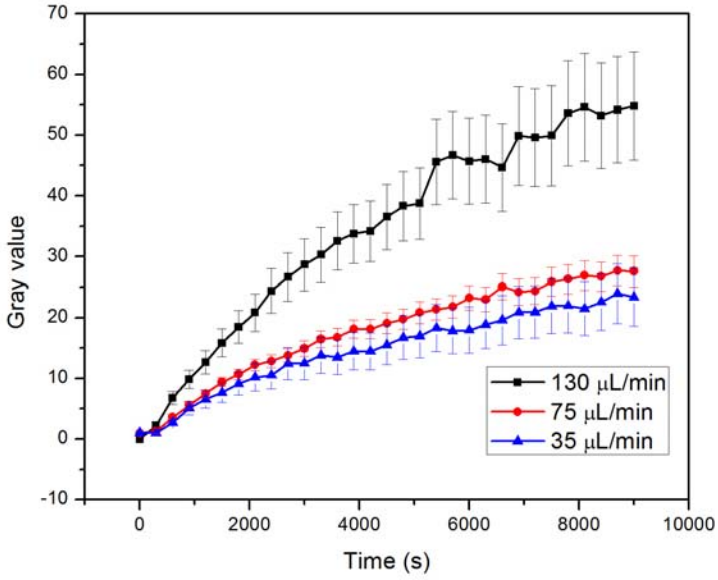

Figure 4.6: Evolution of gray value at the inlet of the microchannel at different cross flow velocities and TMP$\approx$0.

As it can be concluded from figures above, the flow rate of 130 µL min^{-1} results in the greatest fouling (the most intense fluorescence), while at two other cross flow velocities the gray values are similar. The final gray values at the inlet, the middle and the outlet of the microchannel obtained in the experiment with flow rate of 130 µL min^{-1} are almost twice greater than in 75 µL min^{-1} and 35 µL min^{-1} cases. For example, the gray values at the inlet of the MMD are 54.8 ± 8.9, 27.6 ± 2.5, and 23.4 ± 4.8 respectively. The tendency of greater protein accumulation at higher feed flow rate may be related to the sensitivity of α-lactalbumin to the hydrodynamic conditions. As it was reported in some studies, at greater velocity (higher shear stress) the protein has higher propensity to unfold [7, 8]. Such change of the conformation leads to the facilitated interaction between hydrophobic parts of the protein molecule adsorbed on the membrane surface with the one flowing in the solution. As a result, the greater degree of protein unfolding the greater fouling is observed, which is reflected in Figure 4.6. Moreover, based on the obtained results, this effect is more noticeable at feed flow rate above 75 µL min^{-1}. On the other hand, the obtained results could be explained under the assumption that the adsorption process is diffusion-limited. If this assumption is correct, the results in Figure 4.6 could be analyzed from the film theory viewpoint. As the fouling

processes were performed at no convection regime, according to the film theory the thinner boundary (shorter diffusion path) leads to a greater extent of adsorption. In order to estimate the boundary layer thickness during the conducted experiments, the Leveque correlation for rectangular channel (Equation 4.1) was used.

$$Sh = 1.86(ReSc\frac{d_h}{l})^{0.33} \tag{4.1}$$

After calculating the value of Sherwood number (Sh), it is possible to estimate the thickness of the boundary layer by applying Equation 4.2:

$$\delta = \frac{d_h}{Sh} \tag{4.2}$$

The estimation of boundary layer thickness using the α-lactalbumin diffusion coefficient of $1.07 \times 10^{-10}\ \mathrm{m^2\,s^{-1}}$ reveals that the decrease of feed flow rate from $130\ \mu\mathrm{L\,min^{-1}}$ to $35\ \mu\mathrm{L\,min^{-1}}$ results in δ increase from $23.2\ \mu\mathrm{m}$, to $27.9\ \mu\mathrm{m}$ (at $75\ \mu\mathrm{L\,min^{-1}}$) and $35.8\ \mu\mathrm{m}$. Hence, the main trend in obtained results is corroborated by the estimation of boundary layer thickness within the frame of film theory.

Besides, the cross flow velocity has an influence on the spatial distribution of fouling along the membrane. At greater flow rates (Figure 4.3 and Figure 4.4) one can clearly see the discrepancy between the gray values obtained at the inlet, the middle, and the outlet of the microchannel at every time point. This observation is ascribed to the presence of pressure drop (calculated value are presented in Table 4.3) along the membrane and the concept of internal filtration. The latter concept dictates that even if global transmembrane flux is close to zero, due to the pressure drop, the local pressure at the inlet of the channel is greater than the one at the outlet. Therefore, the local filtration occurs at the beginning of the channel and the backfiltration (permeation from the permeate side back to the retentate compartment) can possibly take place close to the end part of the membrane. Ultimately, such distribution of flows results in the gradual reduction of local gray value from the inlet towards the outlet, which is observed in Figure 4.3 and Figure 4.4. In parallel, no differences in gray values along the membrane are detected at the feed flow rate of $35\ \mu\mathrm{L\,min^{-1}}$. Such result suggests that below certain cross flow velocity, the pressure drop along the channel becomes too small to have a noticeable impact on the local transmembrane pressure conditions inside the MMD. Another important finding on fluorescent signal evolution is that at all three analyzed flow rates, the plateau of

gray values is not reached even after $9000\ \mathrm{s}$ of experiment. This implies that it takes more time than the selected duration of the process to achieve a maximal quantity of foulant on the membrane surface. Such result is slightly different compared to the one obtained for BSA-FITC at no convection conditions, where the plateau was reached within the duration of the experiment (see Chapter 3). This difference might be attributed to the significant difference in protein concentration: $1\ \mathrm{g\,L^{-1}}$ in case of BSA-FITC and only $50\ \mathrm{mg\,L^{-1}}$ in case of α-lactalbumin. Besides, we may consider the structural properties of these two proteins. According to Greene *et al.* [9] α-lactalbumin can easily assume an alternative conformation and is stable at partially denatured states. One the other hand, BSA is considered a relatively rigid or "hard" protein [10]. Based on these quotes, we may assume that BSA is less susceptible to conformational changes. Thus, it can be hypothesized that during the fouling development α-lactalbumin undergoes some conformational changes. These rearrangements may contribute to greater accumulation of protein molecules on the membrane surface, which is reflected by the continuous augmentation of gray values throughout the entire duration of the experiment.

In order to evaluate the influence of protein deposition at no convection conditions on the membrane permeability, the permeability reduction index (PRI) is presented in Table 4.3. The equation for calculation of PRI was given in Chapter 2 (Section 4.2.2).

Table 4.3: Permeability reduction index depending on the hydrodynamic conditions.

Feed ow rate	**Re**	**ΔP, [Pa]**	**PRI**
$130\ \mu\mathrm{L\,min^{-1}}$	4.65	44.4	0.36
$75\ \mu\mathrm{L\,min^{-1}}$	2.69	25.6	0.37
$35\ \mu\mathrm{L\,min^{-1}}$	1.26	12.0	0.33

Based on data shown in Table 4.3 the PRI is almost identical for higher Re numbers and is slightly smaller in $35\ \mu\mathrm{L\,min^{-1}}$ case. The lower permeability reduction in the latter case is again related to the reduced impact of hydrodynamic conditions, which was discussed previously. Moreover, according to Table 4.3, the lower cross flow velocity leads to smaller pressure drop along the microchannel, which, in turn, results in lower local filtrate flow. As so, the transmembrane drag force becomes negligible in such case.

Besides, the greater membrane permeability reduction in 75 µL min^{-1} case compared to 35 µL min^{-1} one is in the agreement with measurements of the fluorescent signals: the greater gray value is, the more significant PRI is. In contrary, the comparison of PRIs and gray values obtained for 75 µL min^{-1} and 130 µL min^{-1} demonstrates the absence of correlation. The reasons for this outcome are not yet well understood.

3 Influence of feed flow rate on α-lactalbumin-mediated membrane fouling at TMP=90 mbar

The second set of experiments aiming to evaluate the influence of the cross flow velocity on the membrane fouling was performed with application of the transmembrane pressure of 90 mbar (Figure 4.7).

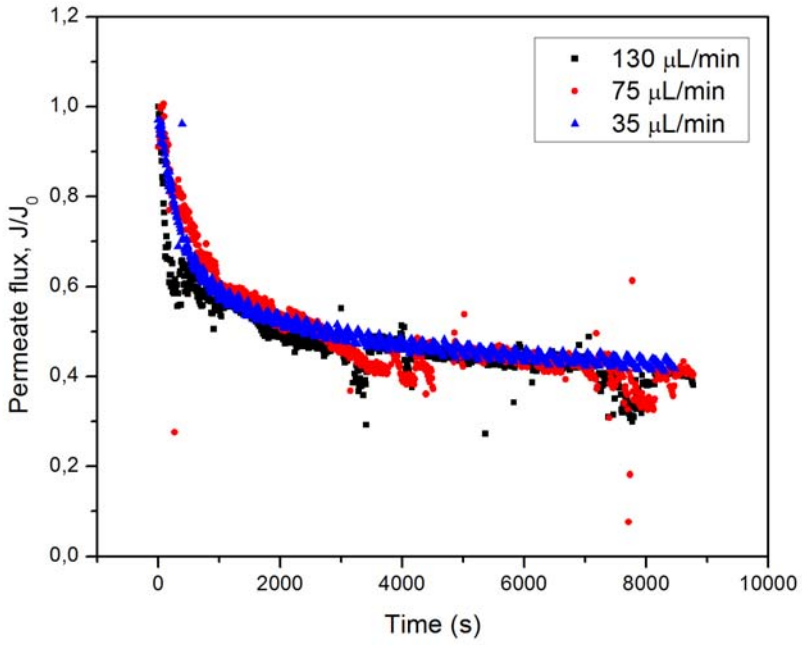

Figure 4.7: Permeate flow reduction profiles at different feed flow rates and TMP=90 mbar.

As it can be analyzed through Figure 4.7, at different feed flow rates the entire permeate flow reduction profile can be separated on three zones, which are characterized by unequal rates of filtrate flux decline. As in the previous chapter, the

zones of permeate flow decline are distinguishes in the following manner. The first zone represents the steep linear decrease of the permeate flow and takes place in the beginning of the filtration process. The third zone is observed in the end the of the filtration experiment and is characterized by linear decline of the filtrate flow with the minimal slope. Consequently, the second ("transition") zone is located between the first and the third ones and may vary in duration and shape depending on the experimental conditions. Presence of this "transition" zone between fast and slow fouling was reported by Pradanos *et al.* [11].

The permeability reduction profiles within the initial zone are more distinct than at the further stages of filtration. This region represents the primary contact between the protein solution and the membrane surface. The fastest linear permeability reduction of around 40% was achieved at 130 µL min^{-1} during first 600 s. The primary loss of the productivity is similar at 75 µL min^{-1} and at 35 µL min^{-1} cases. In the former case, the steep initial permeability drop of 40% is reached after 1000 s, while during the latter process the 35% decrease of filtrate flux is achieved after 600 s.

The second zone of the obtained profiles is located differently in time and is characterized by an intermediate rate of permeability reduction. From Figure 4.7 it can be seen that the greater feed flow rate results in more prolonged "transition" zone. Even though, the processes happening within this period of time are not well described, theoretically the prolonged duration of such transition may be ascribed to the presence of more significant sweeping effect. It prevents the system from reaching the state, which is characteristic for the commencement of the third zone with slowest fouling. Finally, the total permeate flow reduction index in the end of the process is almost the same: 0.62, 0.59 and 0.58 (in the order from the highest feed flow rate to the lowest). This means that after the filtration process the membrane exhibits the permeability only of 40% compared to the virgin state.

Along with constant measurements of the permeate flow rate, the fluorescent images of the whole membrane filtration area were also recorded. The most unexpected outcome was the observation that over the course of filtration some dark structures were formed on the membrane surface (Figure 4.8 and Figure 4.9). Such structures were not observed neither during BSA filtration (at all analyzed TMPs) nor during the non-convection experiments with α-lactalbumin.

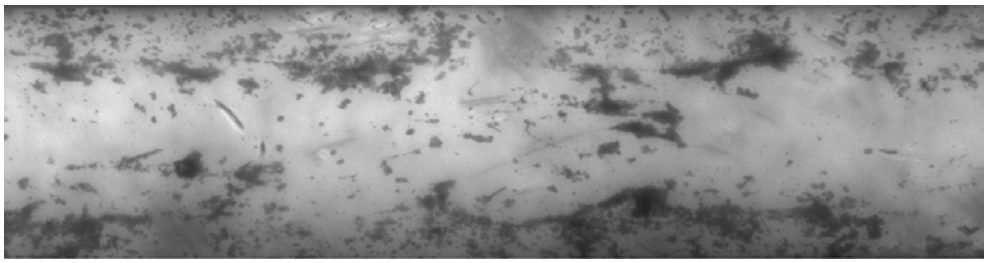

Figure 4.8: Fluorescent image of a part of microchannel during the experiment conducted at 130 µL min^{-1} and TMP=90 mbar. (The brightness of image was adjusted to obtain a better contrast between the dark zones and the bright background). Magnification: x50.

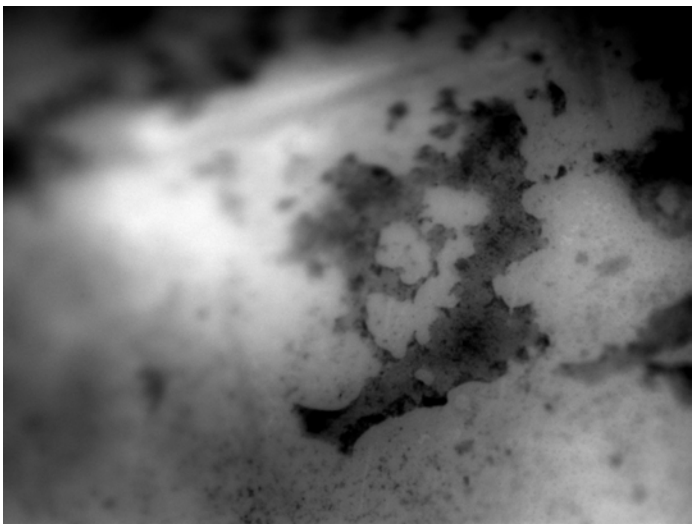

Figure 4.9: Fluorescent image of a part of microchannel during the experiment conducted at 130 µL min^{-1} and TMP=90 mbar. Magnification: x500.

As it can be seen from Figure 4.8 and Figure 4.9, during the course of filtration a lot of dark structures are formed. We believe that this observation may be explained by the phenomena called aggregation-caused fluorescence quenching (ACQ). Such phenomenon was reported in some publications [12, 13] and is explained by a specific intermolecular interaction of the fluorescent molecules. Briefly, in tightly packed state the fluorescent tags of the neighboring molecules may have π–π interactions, which in turn lead to the annihilation of their light emission [14]. Assuming that the formation of discussed dark zones is governed by ACQ, we would further denote these structures as aggregates.

The close examination of Figure 4.8 reveals that the formed aggregates are different in shape, size and location. Besides, in Figure 4.9 some small dark grains between large clusters can be seen and they may also be considered as aggregates which did

not grow to larger sizes. However, it is worth noting that the formed structures are not visible in scanning electron microscopy (SEM) image (Figure 4.10), which are acquired from post experimentally "dissected" MMD. Therefore, it may be postulated that the aggregates are indeed detectable only when the surrounding molecules emit the fluorescent light.

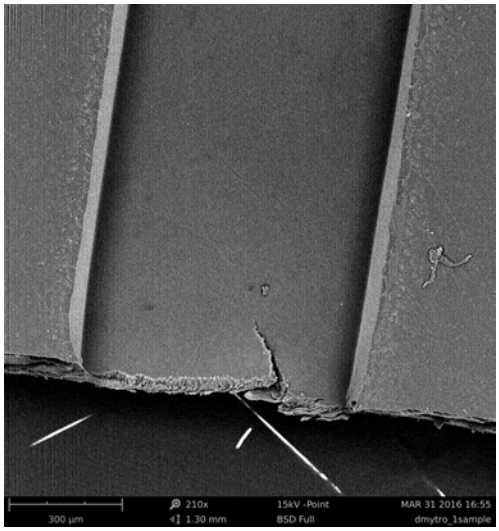

Figure 4.10: SEM image of dissected microchip after the filtration of fluorescent α-lactalbumin.

Aiming to perform the quantitative analysis of such aggregates formation depending on the transmembrane pressure applied and the hydrodynamic conditions inside the microchannel the specific image analysis was performed (Section 5 in Chapter 2). The application of this method allows to discriminate dark and bright zones by using the threshold gray value and then to analyze them separately. Therefore, in our study, for each experiment we determined the percentage of membrane surface covered with aggregates (percentage of surface with gray value below the threshold) and the evolution of fluorescent signal from the non-ACQ zones (gray value above the threshold). In order to evaluate the precision of the developed method, the error bars are shown in Figure 4.13 and Figure 4.14. For this, the estimation of the surface coverage was done at threshold gray values n+1 and n-1, where n stands for the initially selected threshold.

Figure 4.11 demonstrates the increase of the surface coverage with the formed aggregates at the inlet, the middle, and the outlet parts of the microchannel during the filtration process conducted at 130 µL$\,\mathrm{min}^{-1}$ and 90 mbar. To avoid cumbersome images, only the ones acquired at 25 min (upper left image), 50 min,

75 min, 100 min, 125 min, and 150 min (bottom right) are presented.

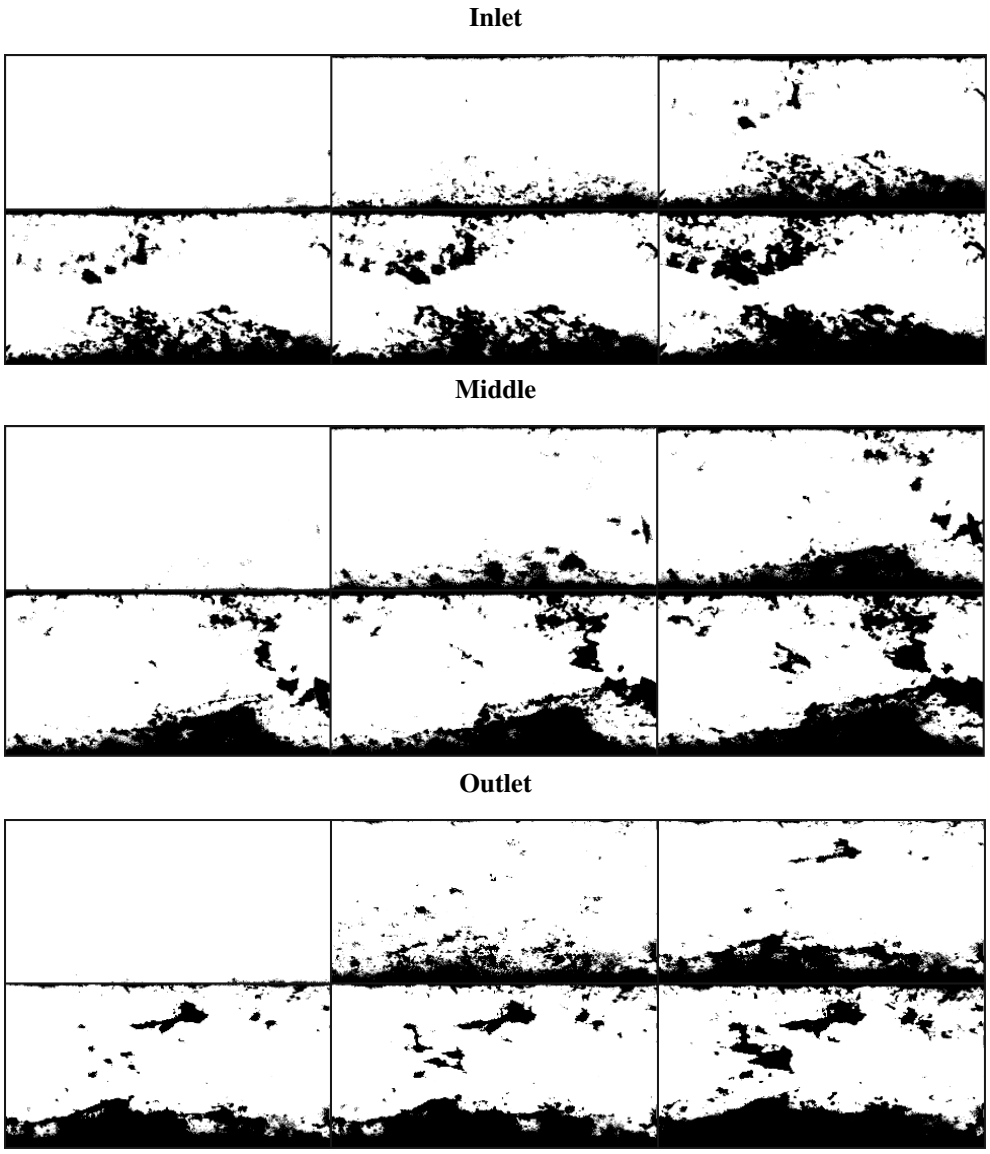

Figure 4.11: Qualitative evolution of ACQ zones during the experiment performed at 130 µL min^{-1} and 90 mbar (upper set of images represents the inlet of the microchannel, middle set – middle, and the bottom – outlet).

As it can be concluded from Figure 4.11, at analyzed experimental conditions the ultimate surface coverage is rather significant (numerical estimation and comparison are provided further). The upper left image of each set represents the state of the membrane surface after 25 min of protein filtration. At this point, in none of the parts of microchannel the aggregates are visible. However, the permeate flow reduction profile (Figure 4.7) indicates that the most severe fouling occurs within

this first part of filtration process. As so, no direct correlation between the permeate flux decline and the formation of aggregates is observed in the beginning of filtration process. Hence, the conclusion that the initial membrane permeability decline is associated with the pore blockage and/or the formation of thin deposit layer of the protein molecules can be drawn. On the other hand, it should also be mentioned that the fluorescent images were acquired at low magnification (x50), and probably, at this point formed aggregates are not large enough to be visible. Nevertheless, the upper middle images (after 50 min of filtration) show the presence of aggregates at all three analyzed regions of the MMD. The majority of detected ACQ zones are located close to the edge of the channel. This finding is most probably related to the flow conditions along the width of the channel: the maximal flow velocity is in the center, while the minimal one is the proximity of the channel s wall. As so, the residence time of the solution close to the edge is greater than in the center, while the transmembrane drag force is practically the same. Besides, according to Kim *et al.* [15] one of the factors responsible for the aggregation of proteins is supersaturation of solution close to the membrane pores. Hence, the part of solution flowing near the wall of the channel has longer residence time inside the microchannel and therefore has more chances to become supersaturated. As a result, the first aggregates are formed in such conditions. From here on, the surface coverage is steadily increasing at the inlet, the middle, and the outlet of the channel. Interestingly, one can see that the formation of large aggregate starts from the small nuclei which then grows in size. This real-time observation corroborates the fouling mechanism proposed previously [15, 16].

Aiming to analyze the correlation between the permeate flux reduction and the surface coverage with aggregates during the entire filtration process, Figure 4.12 was plotted.

As it may be concluded from Figure 4.12, the initial drop in membrane permeability is not associated with the formation of visible aggregates. The first ACQ zones are detected after membrane losses 45% of its initial productivity. However, from here on, almost linear dependence with negative slope is observed until the end of the experiment. The same trend was also observed for other filtration processes conducted in this study at another conditions. Besides, we have to point out again that the absence of correlation at the early stages may be related to the small magnification used during image acquisition. As so, an additional study with use of greater magnification can be considered as a perspective for the further investigation of the protein deposit formation during filtration at the microscale.

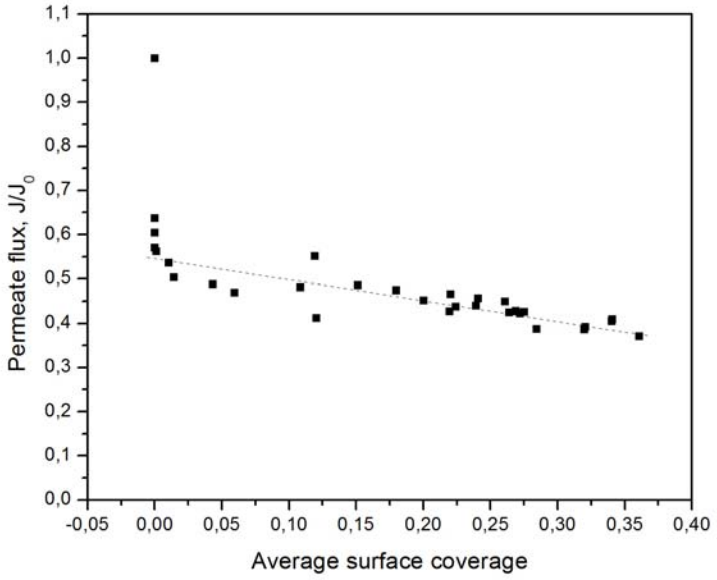

Figure 4.12: Correlation between the permeate flow reduction and the surface coverage with ACQ zones at 130 µL min^{-1} and 90 mbar.

The quantitative representation of changes in surface coverage with ACQ zones is presented in Figure 4.13, while Figure 4.14 demonstrates the evolution of mean gray value of non ACQ region.

According to Figure 4.13, the surface coverage with ACQ zones become apparent only after the initial delay, and is followed by continuous almost linear increase. The only exception from this trend is noticeable at time point of 5400 s, where the instant reduction of surface coverage is observed. Such occurrence is related to the presence of air bubble in the solution, captured on one of images (Figure 4.15 (C)). The shear stress created on the air/membrane interface was large enough to detach some part of deposits from all analyzed zones of the microchannel. After this momentary trend disruption, the subsequent aggregate expansion led to the ultimate surface coverage of 0.36 ± 0.02. This means that during the experiment performed at feed flow rate of 130 µL min^{-1} and TMP of 90 mbar, a bit more than one third of the surface of the membrane at the inlet, the middle, and the outlet of the microchannel is covered by the formed aggregates.

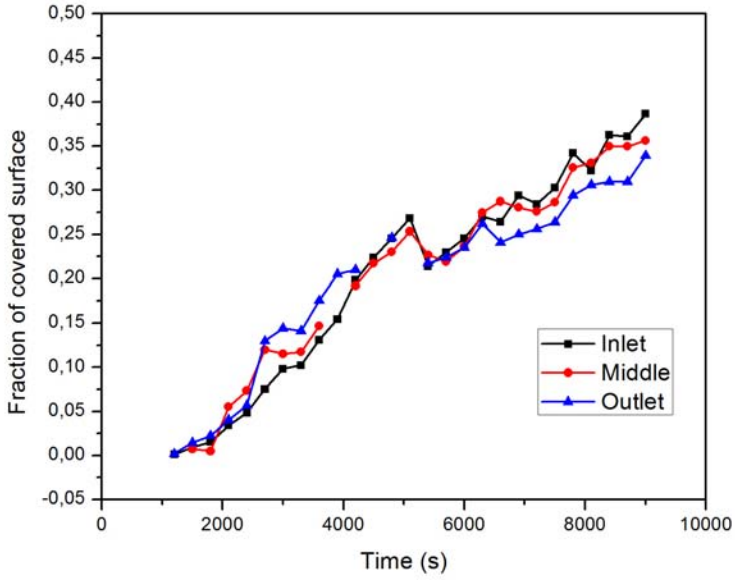

Figure 4.13: Changes in the percentage of membrane surface covered with aggregates at 130 µL min^{-1} and 90 mbar.

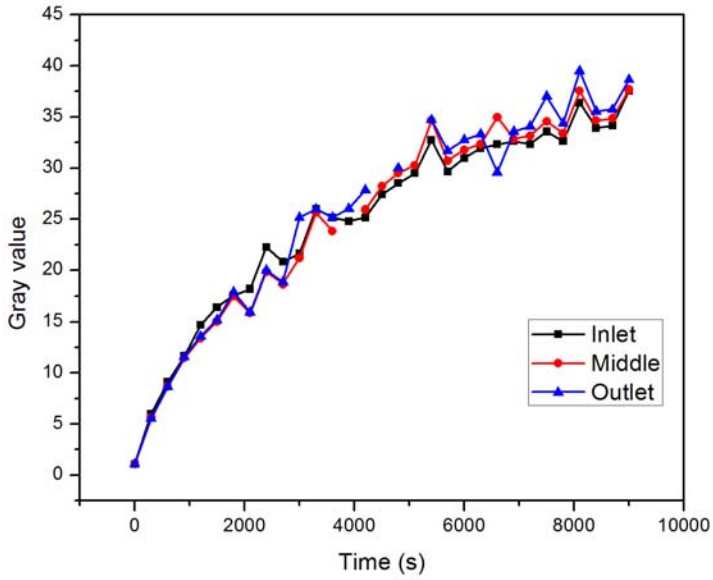

Figure 4.14: Evolution of mean gray value of non-ACQ zone during the experiment conducted at 130 µL min^{-1} and 90 mbar.

Besides, the size of error bars in Figure 4.13 and Figure 4.14 suggests that the developed method of image analysis is rather precise and allows the comparison of surface coverages obtained over different filtration processes with an adequate accuracy. On the other hand, the analysis is not automated and requires the processing of each image separately, therefore, the error bars are not calculated for other experiments.

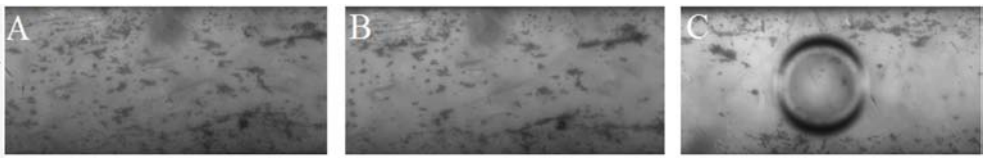

Figure 4.15: The state of membrane surface before (image A, time point 5100 s) and after (image B, time point 5400 s) the passage of air bubble captured in image C. Magnification: x50.

The ACQ zones expansion is accompanied by the increase of mean gray value of non-quenched region. The profile presented in Figure 4.14 is less linear and almost reaches a plateau at the late stages of the filtration experiment. This implies that application of transmembrane pressure of 90 mbar is sufficient to achieve almost steady state of fouling layer only after 9000 s of the filtration process. On the other hand, one can see that application of TMP erases the difference between the fluorescent signals at the inlet, the middle and the outlet of the microchannel. This indicates that here the pressure drop along the membrane is not influencing the spatial distribution of protein accumulation.

The comparison of Figure 4.14 and Figure 4.3 suggests that the fouling is lower during the process where transmembrane pressure is applied. Such conclusion would be misleading in the view of membrane permeability reductions obtained in the end of these processes. The mismatch may be attributed to the compressibility of the protein deposit. According to Ho and Zydney [16], the protein deposit on the membrane surface is more compressed at higher TMP. Therefore, tighter packing of protein molecules may also result in partial quenching of the fluorescent signal coming even from zones without visible aggregates. Besides, another explanation can be found in the formation of the aggregates. Since, they are not observed during "non-convective" regime, we may assume that in this case it is possible to quantify all the adsorbed protein. In parallel, in Figure 4.14 the gray values represent only the non-ACQ zones, while regions covered with aggregates may also have a considerable contribution to the overall decline of the membrane permeability.

Consequently, the comparison of gray values obtained at TMP of $90\ \mathrm{mbar}$ and "non-convective" regime is not straightforward in this case, and therefore the further results obtained at "non-convective" cases and with application of TMP are not compared with each other.

The evolution of surface coverages with ACQ zones obtained at different feed flow rates and transmembrane pressure of $90\ \mathrm{mbar}$ are presented in Figure 4.16 and Figure 4.17.

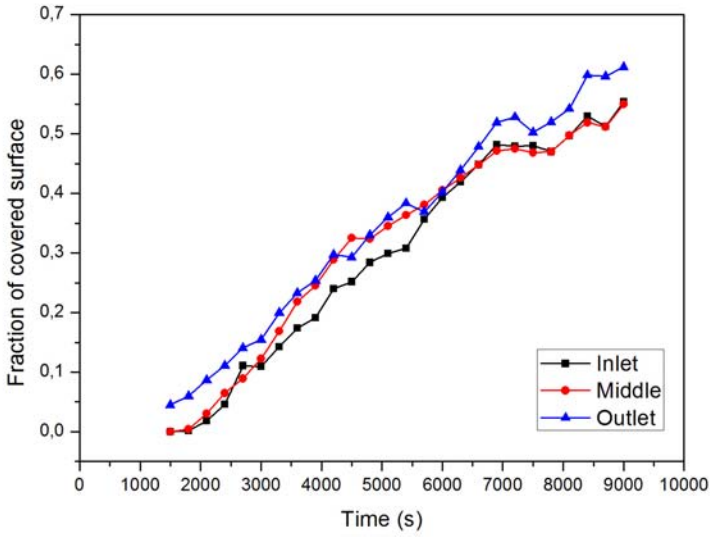

Figure 4.16: Changes in the percentage of membrane surface covered with aggregates at $75\ \mu\mathrm{L\,min^{-1}}$ and $90\ \mathrm{mbar}$.

Obtained results indicate that at different feed flow rates the augmentation of surface coverage with ACQ zones is linear. However, the time of detection of first aggregates and extent of final coverage are different. Over the course of filtration performed at $35\ \mu\mathrm{L\,min^{-1}}$ the first quenched zones are visible after $600\ \mathrm{s}$, while at greater cross flow velocities the initial delay is longer. This finding is related to a longer residence time of the protein solution inside the microchannel, which enables more rapid achievement of supersaturation. In principle, the same explanation is valid for the terminal extent of surface coverage. The decrease of feed flow rate (increase of residence time) results in the increased quantity of ACQ zones. Practically, the higher surface coverage of 0.68 ± 0.04 is achieved at the slowest flow rate in contrast to 0.57 ± 0.03 for the flow rate of $75\ \mu\mathrm{L\,min^{-1}}$ and 0.36 ± 0.02 observed in "$130\ \mu\mathrm{L\,min^{-1}}$" case.

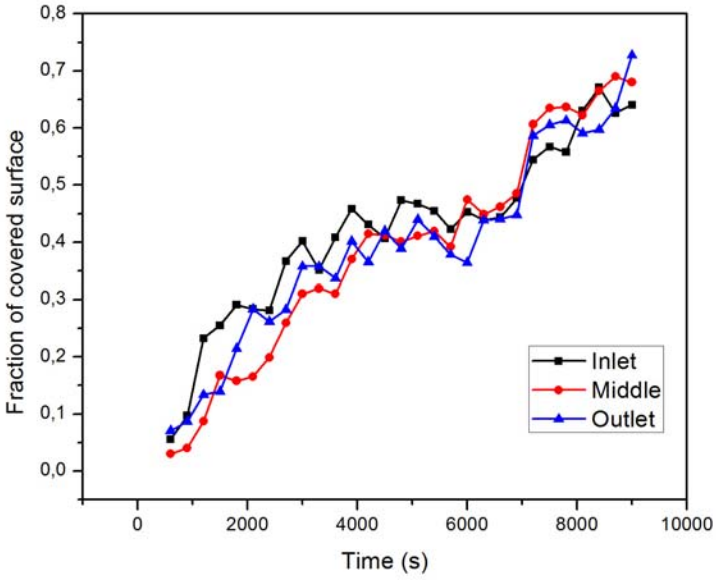

Figure 4.17: Changes in the percentage of membrane surface covered with aggregates at 35 µL min^{-1} and 90 mbar.

Obtained results may be also explained through the application of film theory. As it was discussed in Section 4.1 of Chapter 3, the mathematical expression of this theory is as in Equation 4.3:

$$Pe = \frac{J\delta}{D} = \ln \frac{c_m}{c_b} \tag{4.3}$$

According to Equation 4.3 the reduction of boundary layer thickness (δ) induced by augmentation of tangential flow leads to a smaller protein concentration in the proximity of the membrane (c_m). The estimated values of Peclet number (Pe) and boundary layer thickness for processes performed at different cross flow velocities and the TMP of 90 mbar are presented in Table 4.4.

As it can be seen from Table 4.4, the boundary layer thickness increases as the feed flow rate decreases. This leads to a greater accumulation of protein, which seems to correlate with surface coverage with ACQ zones.

The changes of mean gray values of non ACQ zones are summarized in Figure 4.18 and Figure 4.19.

Table 4.4: Estimated values of Pe and boundary layer thickness at the experiments conducted at different feed flow rates and TMP=$90\ \mathrm{mbar}$ along with surface coverages with ACQ zones in the end of filtration.

Experiment	**Boundary layer thickness (δ)***	**Peclet number (Pe)****	**Surface coverage with ACQ zones**
$130\ \mu\mathrm{L\,min^{-1}}$	$23.2\ \mu\mathrm{m}$	2.88	0.36 ± 0.02
$75\ \mu\mathrm{L\,min^{-1}}$	$27.9\ \mu\mathrm{m}$	3.45	0.57 ± 0.03
$35\ \mu\mathrm{L\,min^{-1}}$	$35.9\ \mu\mathrm{m}$	4.43	0.68 ± 0.04

* - for evaluation of δ the diffusion coefficient of $1.07 \times 10^{-10}\ \mathrm{m^2\,s^{-1}}$ was used.
** - since the permeate flux (J) is changing with time, the initial permeate flux value was used for the calculation of Pe.

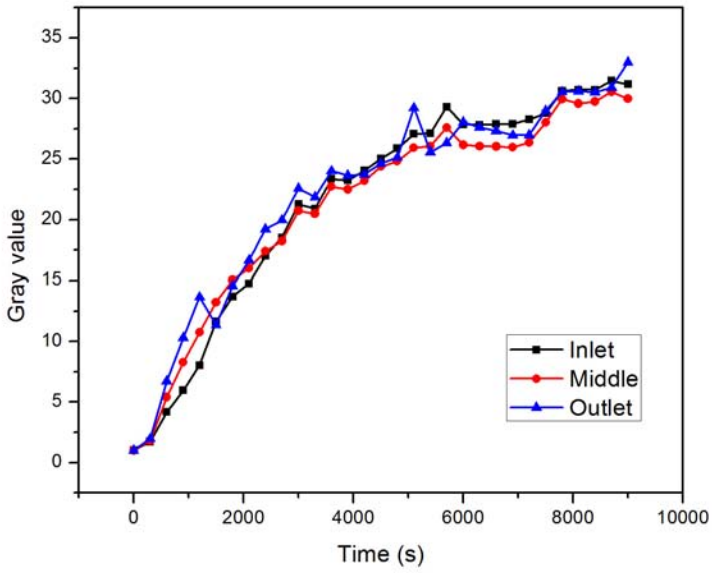

Figure 4.18: Evolution of mean gray value of non-ACQ zone during the experiment conducted at at $75\ \mu\mathrm{L\,min^{-1}}$ and $90\ \mathrm{mbar}$.

Comparison of Figure 4.14 with Figure 4.18 and Figure 4.19 reveals that there are two main trends in gray value variation depending on the feed flow rate. Firstly, the transition from the lower cross flow velocity to the higher one results in the increase of the fluorescent signal at the end of the experiment: 25.4 ± 1.5, 31.4 ± 1.6 and 37.7 ± 0.9. As in previous sections, such finding may be explained by the impact of

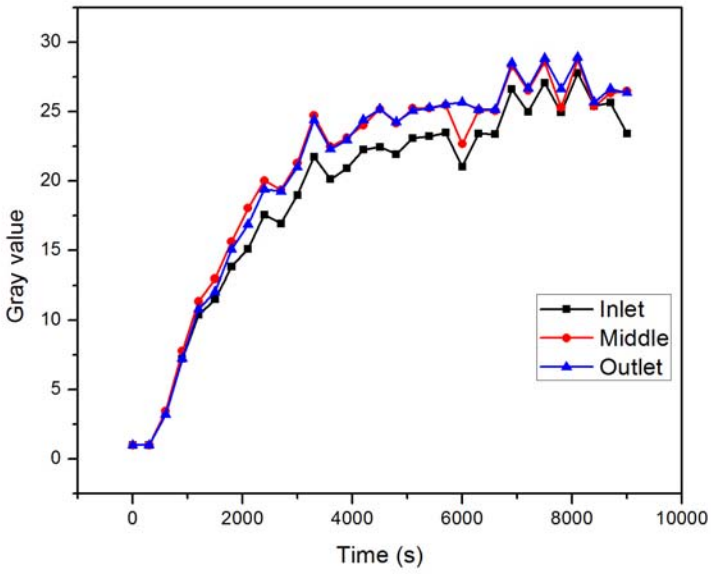

Figure 4.19: Evolution of mean gray value of non-ACQ zone during the experiment conducted at at 35 µL min^{-1} and 90 mbar.

hydrodynamic conditions on the protein unfolding. As so, the higher Re leads to greater unfolding, which in turn is reflected by the higher gray value. The second observed trend is the gradual shifting of gray value augmentation from almost linear (Figure 4.14) to a visible plateau (Figure 4.19). This effect is also related to the hydrodynamic conditions. At more gentle conditions, system is closer to an equilibrium state and, therefore, is less prone to such changes at the solution/membrane interface as protein unfolding, deposit displacement and other possible ways of deposit rearrangements. On the other hand, gentle conditions are expected to generate a higher accumulation of protein, which contradicts the gray value measurements. However, it seems that this effect is reflected by the higher surface coverage at lower cross flow velocities.

Summarizing the data related to the experiments performed at TMP of 90 mbar, one can see that despite the variations in surface coverage with ACQ zones and differences in gray values between experiments, the increase of one parameter is accompanied by the reduction of the other and vice versa (graphically it is shown later in Figure 4.31). In other words, if one process is characterized by higher gray value than the second one, it also exhibits lower surface coverage with the ACQ zones. Moreover, despite the differences in the appearance of the protein deposit,

the final membrane permeability is reduced to the same extent. This outcome suggests that the overall ultimate resistance of the protein deposit is similar in all three experiments. Therefore, it seems that the key parameter, which defines the filtration process throughput is the compactness (density) of the protein deposit, which theoretically has to be constant at the same TMP.

4 What is the effect of an intermediate TMP on the membrane fouling at $130\ \mu\mathrm{m\,min^{-1}}$?

Aiming to investigate the fouling process at intermediate conditions between no convection (TMP=0) and filtration ($90\ \mathrm{mbar}$), the experiment at the feed flow rate of $130\ \mu\mathrm{L\,min^{-1}}$ and transmembrane pressure of $45\ \mathrm{mbar}$ was performed. Expecting the similar results as for other two extreme cases, this process was extended up to $5.5\ \mathrm{h}$ ($19\,800\ \mathrm{s}$). Only the part of results, which is acquired within the same period of time as in other processes ($9000\ \mathrm{s}$), is used for comparisons with the outcomes of other filtrations. This approach is used to get better distinction between results at the region of interest.

The variation of the filtrate flux was matched to the one recorded during the "$130\ \mu\mathrm{L\,min^{-1}}$ + $90\ \mathrm{mbar}$" filtration process. The comparison is depicted in Figure 4.20.

The permeate flow reduction profiles exhibit similar appearance at both TMPs. At the end of the filtration process the PRI of membrane in $130\ \mu\mathrm{L\,min^{-1}}$ + $90\ \mathrm{mbar}$" case was 0.62, while in $130\ \mu\mathrm{L\,min^{-1}}$ + $45\ \mathrm{mbar}$" case it was 0.59. This finding suggests that at analyzed conditions the drop of membrane productivity is independent of the applied TMP. However, the comparison of permeate reduction index obtained at no convection regime (Table 4.3), at $45\ \mathrm{mbar}$ and $90\ \mathrm{mbar}$ (Figure 4.20) shows almost twice greater fouling at two latter case: 0.36 vs 0.59 and 0.62.

Besides, the difference in the appearance of protein deposit on the membrane surface depending on TMPs is significant. As it has already been pointed out, there are no visible aggregates on membrane surface during "non-convective" process. However, both filtration processes at $45\ \mathrm{mbar}$ (Figure 4.21) and $90\ \mathrm{mbar}$ (Figure 4.13) resulted in considerable surface coverages with ACQ zones.

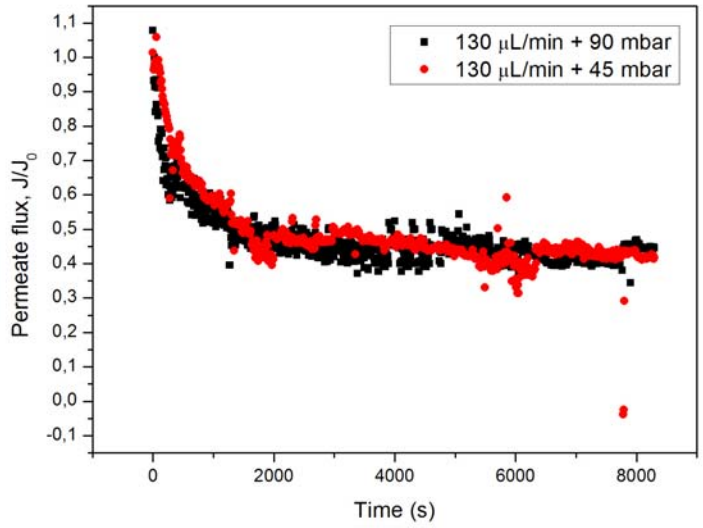

Figure 4.20: The permeate flux reduction profile depending on the transmembrane pressure.

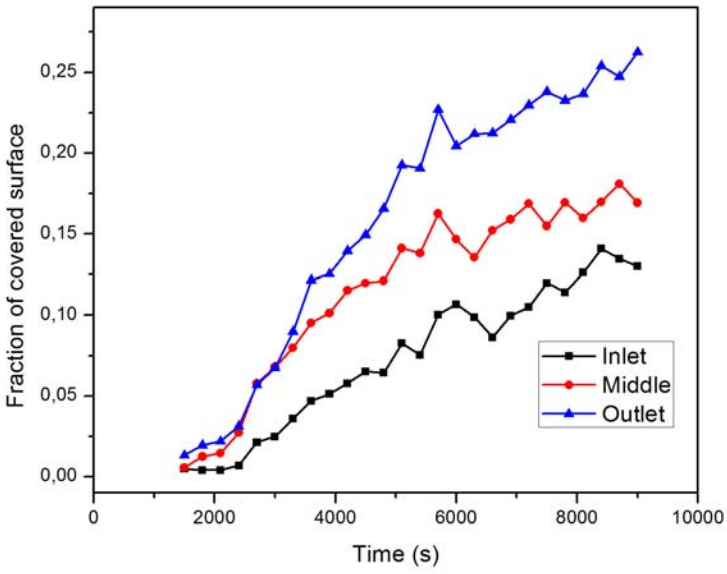

Figure 4.21: Evolution of surface coverage with ACQ zones at feed flow rate of 130 µL min^{-1} and TMP=45 mbar.

Figure 4.21 shows that for the first time in the present research the difference in surface coverage with ACQ zones between the inlet, the middle, and the outlet of

the channel may be observed. It demonstrates that the total quantity of aggregates at the inlet is minimal, while at the outlet is maximal. Obtained result corroborates the afore-discussed hypothesis on the aggregates growth (need of local supersaturation). While high feed flow rate carries the protein solution further along the membrane, the small filtrate flux is not sufficient to induce rapid supersaturation. In such case, longer period of time is required to achieve such condition. Therefore, the observed gradual increase of ACQ zones from the entrance towards the outlet of the system is not surprising.

In addition, the obtained results are in the agreement with the film theory, which states that the boundary layer thickness increases from the inlet towards the outlet of the system. As so, the boundary layer thickness is expected to be maximal at the outlet of the microchannel, which leads to the maximal surface coverage with ACQ zones. Moreover, Peclet number estimated for this process is almost twice lower compared to "130 µL min^{-1}+90 mbar" case: 1.58 vs 2.88.

It could be noticed that at the early stages of the filtration, the surface coverage at the middle and the outlet are almost identical. This may suggest that until this moment the permeate flow is sufficient enough to induce the supersaturation at the middle zone of the MMD. However, with the course of filtration and progressive deposit build-up, it takes more and more time to supersaturate the protein solution. Hence, the rate of surface coverage at the middle starts to deviate from the outlet one after 3000 s. This principle is in agreement with the permeate flow reduction profile (Figure 4.20), where the zone of slow fouling also starts after 3000 s from the beginning of filtration. Moreover, Figure 4.22 depicts the correlation between the permeate flux and the surface coverage at different parts of the microchannel.

According to Figure 4.22, one can see that the minor quantity of aggregates may be detected in all parts of the microchannel only after reaching the flux reduction of 50%. At this point there is no clear difference between surface coverages at the inlet, the middle and the outlet. However, from here on it is possible to notice that the subsequent reduction of membrane permeance is accompanied by uneven rates of aggregates formation along the length of the MMD. Particularly, the minimal coverage of 14% is observed at the inlet, the intermediate – of 18% at the middle, and the maximal one of 27% at the outlet part. This numerical comparison supports the concept, proposed in the paragraph before Figure 4.22.

In view of this concept, the ratio between the axial convection (dependent on feed flow rate) and the transmembrane drag (defined by applied TMP) is an important

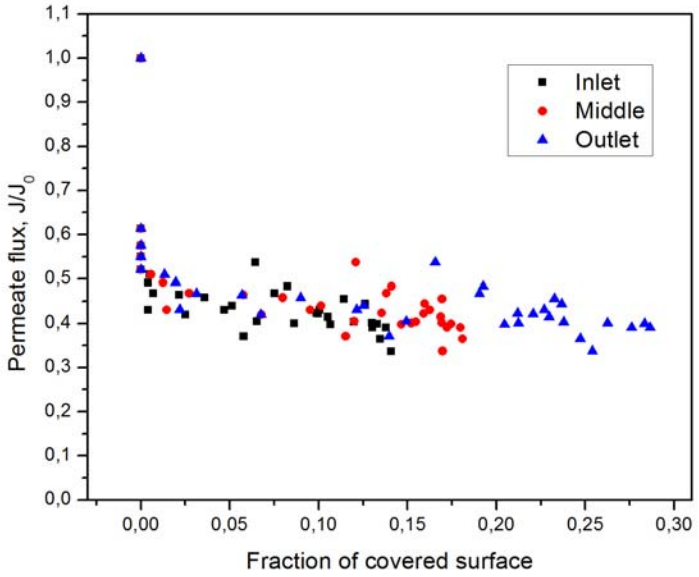

Figure 4.22: Correlation between the permeate flow reduction and the surface coverage with aggregates at different parts of microchannel during the filtration at 130 µL min^{-1} and 45 mbar.

factor, which influences the appearance of the protein deposit on the membrane surface. Considering that we observe the difference in the uniformity of the surface coverage along the length of the microchannel between the experiments 130 µL min^{-1} + 45 mbar" (Figure 4.21) and "130 µL min^{-1} + 90 mbar" (Figure 4.13), we may assume the existence of the critical ratio between two aforementioned convections. Taking into account the initial filtrate fluxes of 25.24±0.48 L m^{-2} h^{-1} bar^{-1} (5.3±0.1 µL min^{-1}) at TMP=45 mbar and of 49.84±1.19 L m^{-2} h^{-1} bar^{-1} (10.5±0.3 µL min^{-1}) at TMP=90 mbar, the critical ratio is between 12.4 and 25 (more precise estimation requires a set of additional experiments). Below this critical value the supersaturation is rapid and it is hard to distinguish the inequality between different parts of the microchannel. However, above this critical value, the attainment of supersaturation requires more time, leading to progressive augmentation of surface coverage with aggregates towards the outlet.

The increase of mean gray values during the filtration process is presented in Figure 4.23.

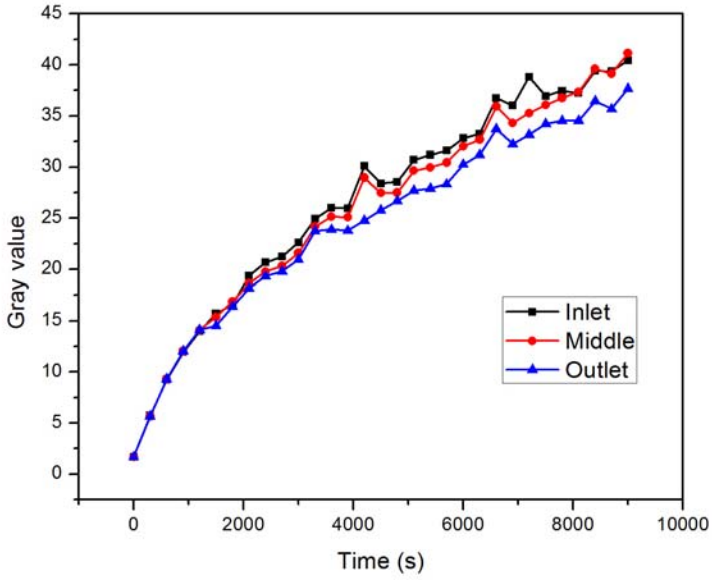

Figure 4.23: Evolution of mean gray value of non-ACQ zone during the experiment conducted at 130 µL min^{-1} and 45 mbar.

The trend in gray value augmentation seems to be transitional between two other extreme cases ("130 µL min^{-1} + 0 mbar" (Figure 4.3) and "130 µL min^{-1} + 90 mbar" (Figure 4.13)). In order to provide a direct comparison Figure 4.24 is plotted and demonstrates the fluorescent signals from the middle part of the microchannel during the experiments performed at feed flow rate of 130 µL min^{-1} and different TMPs.

The "130 µL min^{-1} + 45 mbar" curve is less linear compared to no convection regime, while the approaching of plateau is still not visible, unlike "130 µL min^{-1} + 90 mbar" case. Moreover, the gray values in the end of the process are also intermediate in "130 µL min^{-1} + 45 mbar" case: 41.1 vs 48.4 and 37.7. Considering the previously discussed effect of deposit compressibility on the gray value, the observed dependence suggests the intermediate state of deposit compaction at transitional transmembrane pressure regime.

The variation of controlled parameters during the whole filtration process is presented in Figure 4.25 and Figure 4.26. Since the period from 9000 s until the end did not lead to significant changes in permeate flow rate, the extended graph is not presented.

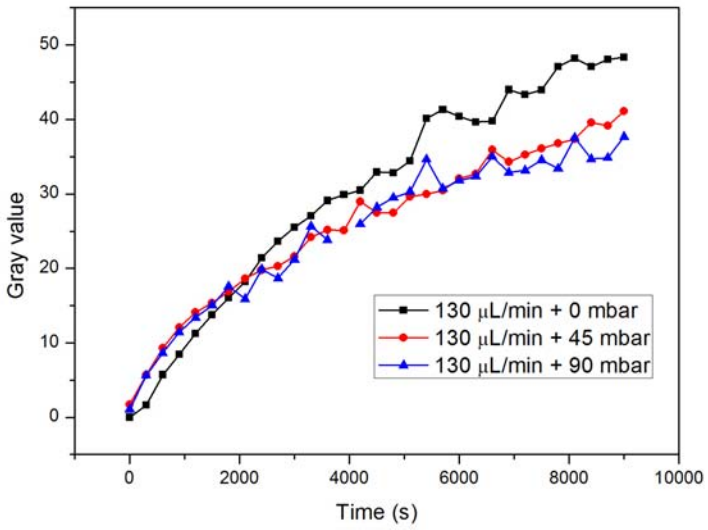

Figure 4.24: Comparison of gray values at the middle of the microchannel during the experiments performed at feed flow rate of 130 µL min^{-1} and different TMPs.

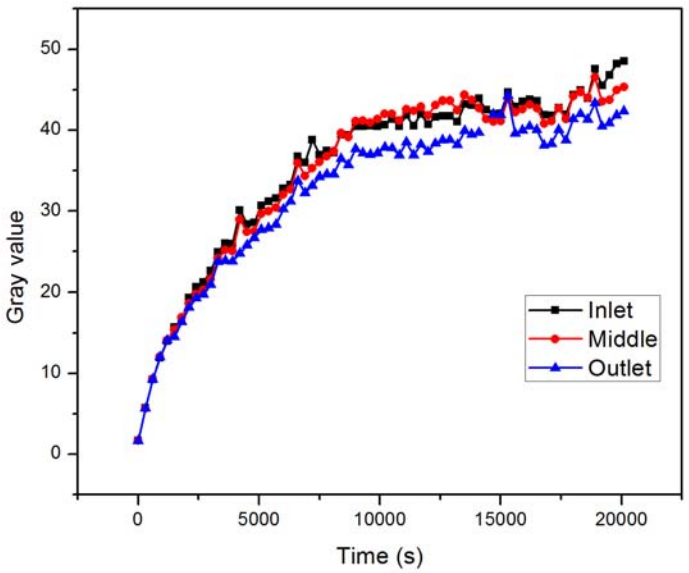

Figure 4.25: Evolution of mean gray value of non-ACQ zone during the experiment conducted at 130 µL min^{-1} and 45 mbar (prolonged experiment).

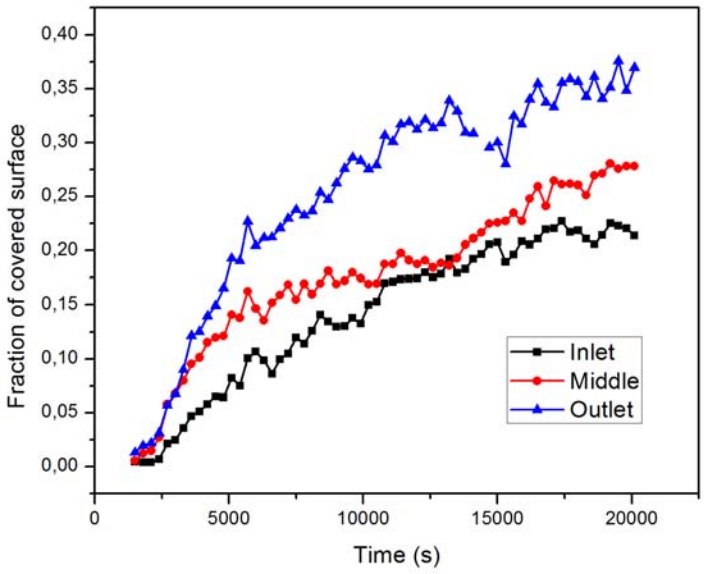

Figure 4.26: Evolution of surface coverage with ACQ zones at feed flow rate of 130 µL min^{-1} and TMP=45 mbar (prolonged experiment).

From Figure 4.25, one can see that the profile of mean gray value is leveling with time. The linear augmentation observed at early stages of the filtration process is progressively shifted to the steady values. This implies that maximal fluorescent signal (41.4 ± 2.3) is reached after 12 500 s of the experiment and its further growth is negligible. In contrary, the surface coverage with ACQ zones is increasing throughout the entire experiment. However, even after the prolonged filtration, the cumulative surface coverage at the inlet, the middle, and the outlet (Figure 4.26) is still lower than the one obtained during "130 µL min^{-1} + 90 mbar" process: 0.29 ± 0.07 vs 0.36 ± 0.02. This serves as an additional confirmation of high importance of ratio between the axial convection and the transmembrane drag force.

5 Do the feed flow rate decrease and the TMP increase act similarly?

Having in mind the conclusion about the importance of ratio between the axial convection and the transmembrane drag force, it is important to compare the influence of two-fold reduction of former force with the two-fold increase of the

latter one. For this, an additional filtration at 75 µL min^{-1} and transmembrane pressure of 180 mbar was performed, and its outcome was compared to the result of "35 µL min^{-1} + 90 mbar" process. The filtration experiment "75 µL min^{-1} + 90 mbar" was taken as a reference.

Figure 4.27 demonstrates the profiles of membrane fouling at different conditions.

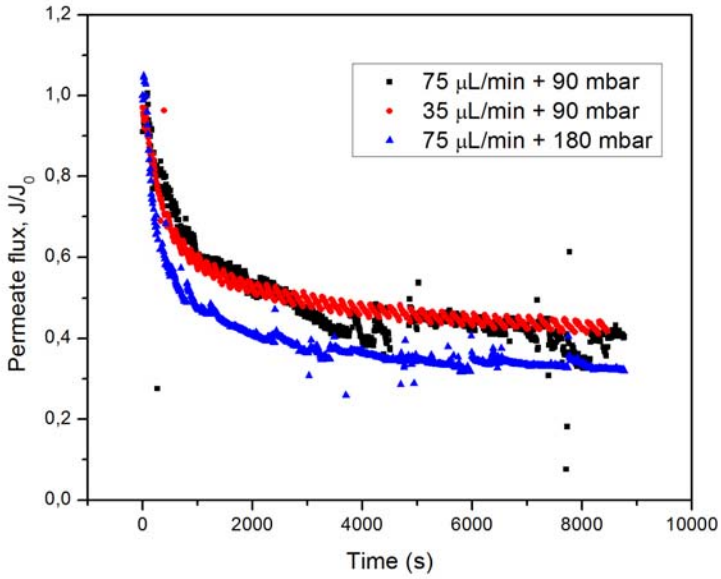

Figure 4.27: The comparison of permeate flow reduction profile at different hydrodynamic and pressure conditions.

As it was discussed previously, the fouling pattern of both experiments performed at 90 mbar is very similar. Both of them start with initial fast linear fouling zone, in the end of which the membrane tested at "35 µL min^{-1} + 90 mbar" lost around 30% of its performance. While the slope of flux decline for "75 µL min^{-1} + 90 mbar" membrane is less steep, but in the end results in 40% drop of permeability. Then, the short intermediate region is observed, which is followed by the slow fouling zone. In the end of these experiments both membranes exhibit only around 42% of their initial permeability. In contrast, the profile recorded at 180 mbar is notably different. The initial fast fouling starts with the steepest decline and is terminated by the permeability drop of 40%. The subsequent protein deposit build up results in the ultimate permeate flow reduction of 68%, which is larger than in two other cases. Hence, it may be postulated that the two-fold increase of transmembrane pressure

has a greater impact on membrane fouling than the two-fold reduction of cross flow velocity. In the view of large difference in applied TMP, the compressibility of protein deposit seems to be a primary reason for this finding.

Besides, the comparison of Peclet numbers reveals that the two-fold increase of transmembrane pressure has a greater impact than the two-fold reduction of cross flow velocity. Particularly, estimated Pe for "75 µL min^{-1} + 180 mbar" case is equal to 7.25, while for "35 µL min^{-1} + 90 mbar" process it is only 4.43. Which means that the increase of Pe leads to greater fouling. Consequently, it can be stated that not only the ratio between axial convection and transmembrane drag force defines the extent of membrane fouling, but also Peclet number which combines the influence of these convections through the film theory.

The evolution of surface coverage with aggregated zones at the highest TMP (Figure 4.29) also demonstrates the highest abundance. In fact, the observed fouling on the membrane surface more resembles continuous scaling layer (Figure 4.28) rather than separated clusters of aggregates, which may also be related to higher compactness of the cake.

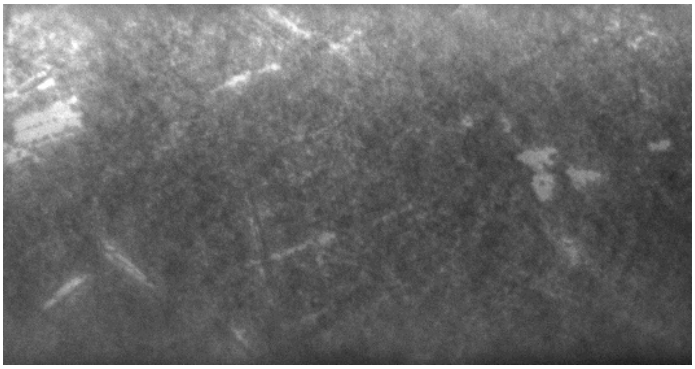

Figure 4.28: Fluorescent image of the membrane surface fouled at 75 µL min^{-1} and TMP=180 mbar. Magnification: x50.

As it can be seen from Figure 4.29, the first aggregates are formed after 300 s from the beginning of the filtration process. After 2000 s 80% surface coverage is achieved, and is already greater than the maximal coverages in other experiments. From here on, the further expansion of quenched zones is taking place, but at much slower rate, and reaches the 90-95% spreading after 4800 s. The last part of experiment is characterized by almost constant state of the fouling layer and at the end of the process demonstrates the 95% coverage everywhere along the microchannel.

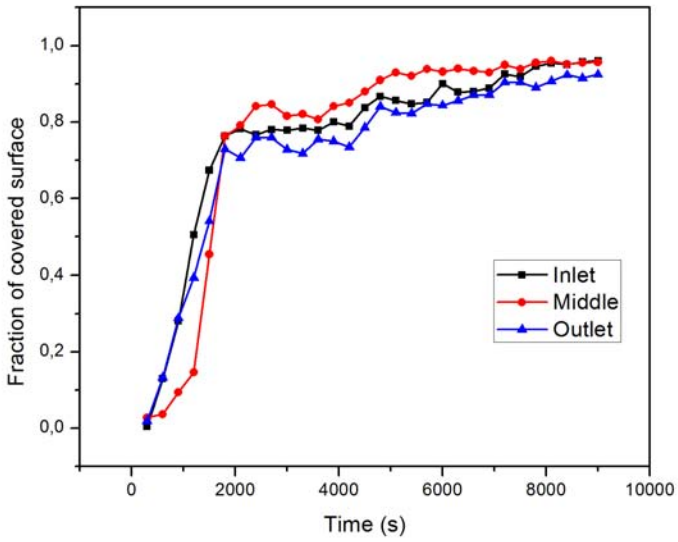

Figure 4.29: Evolution of surface coverage by ACQ zones at feed flow rate of 75 µL min^{-1} and TMP=180 mbar.

To finalize the analysis of this experiment, the evolution of mean gray value is presented in Figure 4.30.

Similarly to the expansion of quenched zones, the mean gray value increases from zero to almost maximal value within first 2000 s. After this time point, the plateau is observed, meaning that the fluorescent signal remains constant until the end of the process. However, it is worth noting that the analysis of fluorescent signal intensity is done only for non-quenched regions. And, considering the high surface coverage with ACQ zones, the remaining part occupies a small part of the surface, which appears as "defects" of scaling layer. Therefore, the conclusions built based on these measurements could be misleading. Hence, it is difficult to compare the fluorescent patterns obtained during this process with gray value profiles recorded during other experiments.

Finally, in order to illustrate the dependence of surface coverage with ACQ zones and the gray values on the Pe number, which was mentioned in the end of Section 3 of this chapter, Figure 4.31 is plotted based on the surface coverages and gray values recorded at the middle part of the microchannel at the moment when the total filtrate volume reached 0.5 mL.

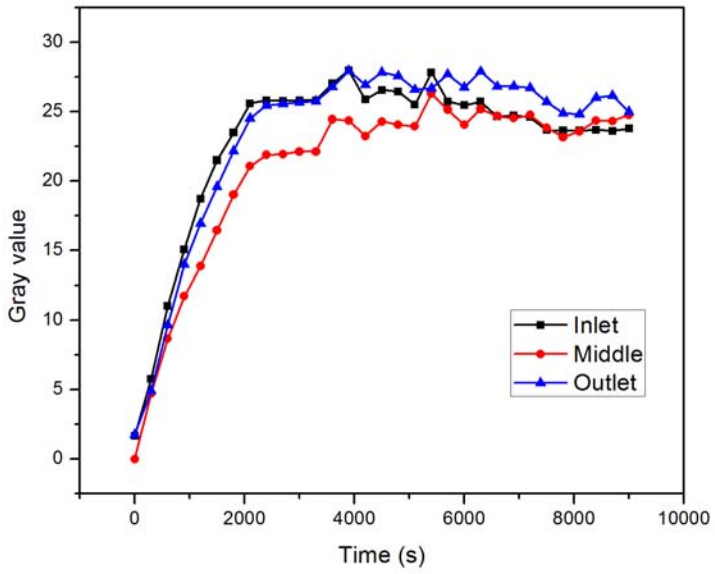

Figure 4.30: Evolution of mean gray value of non-ACQ zone during the experiment conducted at 75 µL min^{-1} and TMP=180 mbar.

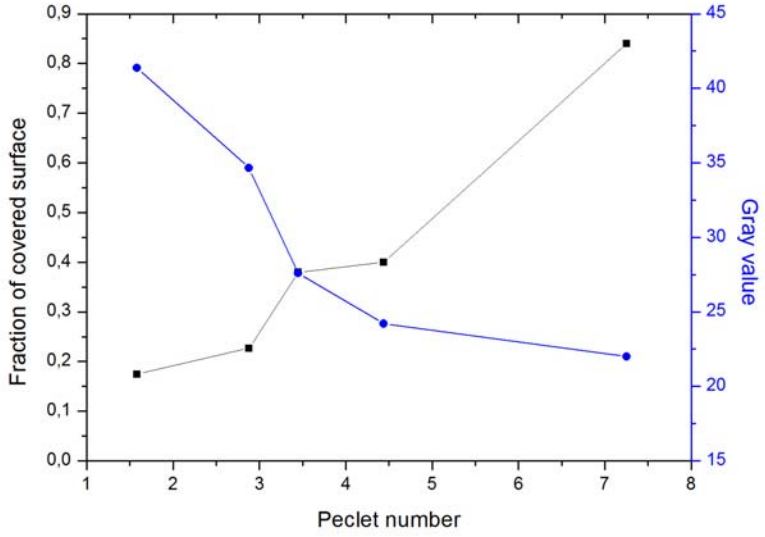

Figure 4.31: The dependence of surface coverage with ACQ zones and gray values at the same filtrate volume on the Pe number.

6 Effect of pressure stepping on the membrane fouling

Aiming to verify the stability of fouling layer depending on the applied transmembrane pressure, the three-step filtration process was performed at constant feed flow rate of $75\ \mu\mathrm{L\,min^{-1}}$. The permeate flow profile is shown in Figure 4.32.

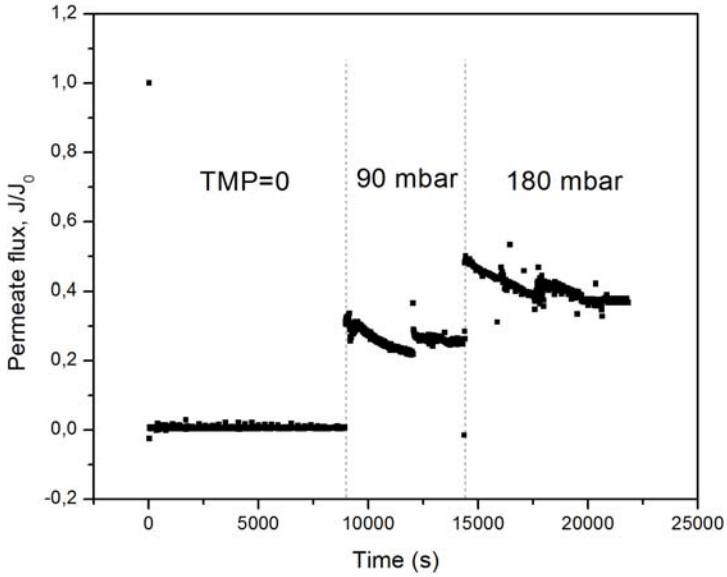

Figure 4.32: The permeate flow profile during the three pressure step experiment at fee flow rate of $75\ \mu\mathrm{L\,min^{-1}}$.

The first part of the experiment was run at no convection regime. The membrane permeability reduction at these conditions is mainly related to the interactions between protein and membrane material. Here, the impact of transmembrane drag force is negligible. This step is then followed by application of TMP of $90\ \mathrm{mbar}$. Since the permeability of clean membrane was measured at maximal TMP of $180\ \mathrm{mbar}$, in order to evaluate the percentage of the permeate flow reduction after the first step the division of the virgin permeability by the factor of 2 is required. Therefore, the no convection regime led to the PRI of 0.37. Immediately after the commencement of the second step the permeate flow profile starts to go down indicating the increase of resistance, which is provided by the layer of accumulated protein. Since, the first stage of this experiment was performed at TMP$\approx$0, we may assume that the thickness of the protein deposit before the increase of TMP is not

large enough to be considered compressible. Thus, it seems that the main phenomena contributing to the flux decline is addition of new protein molecules, which are steadily dragged towards the membrane. The quantitative evaluation of this stage demonstrates that it results in additional permeate flow reduction of 14%. The last part of the filtration process at $90\ \mathrm{mbar}$ appears to be horizontal, suggesting that the steady state was achieved. This stability is disrupted by the increase of TMP from $90\ \mathrm{mbar}$ to $180\ \mathrm{mbar}$. Immediately after the new filtration conditions are established, the membrane permeability continues to decrease, due to the increase of the resistance of the protein deposit. At this stage, two parallel phenomena may take place: further thickening of the deposit layer and the compression of already existing accumulated layers of protein. The plateau of filtrate flow rate is observed in the end of the experiment, which suggests that the maximal state of fouling for these particular conditions is achieved. The terminal value of permeate flow reduction is 63% and is slightly lower compared to the simple one-step "75 µL min^{-1} and TMP=$180\ \mathrm{mbar}$" filtration process, where the ultimate drop was equal to 68%. Such counterintuitive observation can be related to the discovery of van Reis *et al.* [17], who showed that the more gentle beginning of filtration process results in lower extent of fouling. Thus, stepwise increase of TMP allowed to reduce the resulting resistance of protein deposit despite the increased duration of the filtration process.

The fluorescent microscopy provided information on influence of each stage of the pressure stepping experiment on the appearance of fouling layer. Figure 4.33 summarizes the state of the membrane surface in the end of no convection regime and its changes during the filtration at $90\ \mathrm{mbar}$ and $180\ \mathrm{mbar}$.

Image 1 in Figure 4.33 shows the state of the membrane surface in the end of first no convection step. As this point, membrane is uniformly covered by fluorescent species without any apparent ACQ zones. However, $5\ \mathrm{min}$ after the transmembrane pressure is increased up to $90\ \mathrm{mbar}$ the first small grains can be observed (image 2). This finding once again demonstrates that the presence of filtration, which causes local supersaturation, is a key parameter in the formation of ACQ zones. Moreover, preliminary equilibration of system at no convection regime cuts down the time between the beginning of filtration and the detection of first aggregates, as it was seen at similar hydrodynamic conditions (Figure 4.16). The continuation of the filtration process (images 3-5) leads to more significant surface coverage with ACQ zones. Nevertheless, in the end of this stage (image 5) one can see that dark zones are still dispersed and look like small individual islands (do not create a large

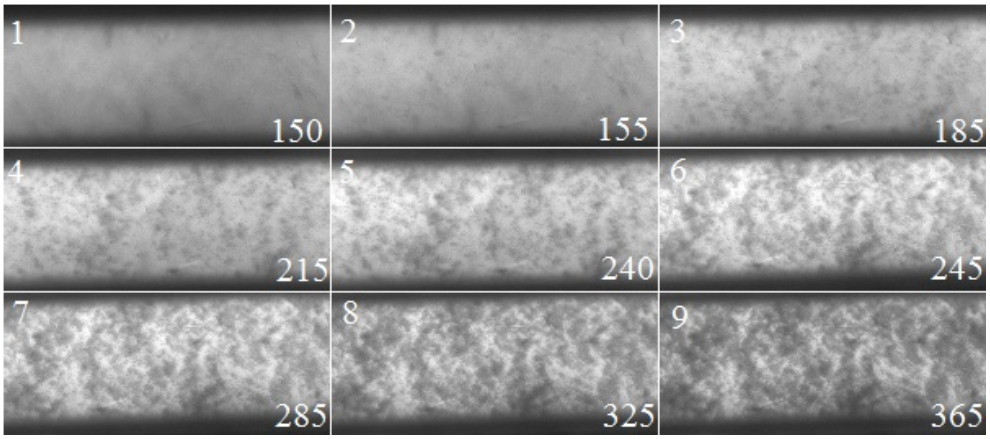

Figure 4.33: Fluorescent images of membrane surface during the three step filtration process and feed flow rate of 75 $\mu L\,min^{-1}$. (Magnification: x50). The number in the bottom right corner indicates the time point in minutes from the beginning of the process at which the image was acquired.

network). However, the shift to the highest TMP (images 6-9) accelerates the formation of new ACQ zones and the growth of already existing ones. As a result, the continuous network of ACQ zones, which covers the great majority of surface, is developed. The final state of fouling layer (image 9), similarly to Figure 4.28, resembles the scaling layer with some "defects" (non-quenched zones) in it. On the other hand, the number of such "defects" in Figure 4.33 is notably greater, which is reflected by smaller permeate flow reduction in Figure 4.29 compared to the respective curve in Figure 4.27. As so, it can be stated that there is a correlation between the number of "defects" in the network of ACQ zones and the membrane permeability reduction.

7 Preliminary study of anti-fouling properties of SlipSkin^{TM} material

Recently, our colleagues in University of Twente developed a novel membrane from a specific hydrophilic SlipSkin^{TM} material. The improved biocompatibility of this material compared to benchmark flat membranes has been already demonstrated [18].

In the present preliminary study, we are aiming at analyzing of antifouling properties of novel SlipSkin^{TM} membranes at the microscale and their comparison

with results obtained for PES membranes. Since these membranes possess significantly different clean water permeabilities: 56 ± 12 $\mathrm{L\,m^{-2}\,h^{-1}\,bar^{-1}}$ (SlipSkin^{TM}) vs 562 ± 53 $\mathrm{L\,m^{-2}\,h^{-1}\,bar^{-1}}$ (PES), the preliminary comparison is done based on the no convection experiments. At these conditions the main parameters influencing the membrane fouling are protein/membrane interaction and the hydrodynamic regime inside the microchannel. The following figures represent the variation of gray value in time at different feed flow rates.

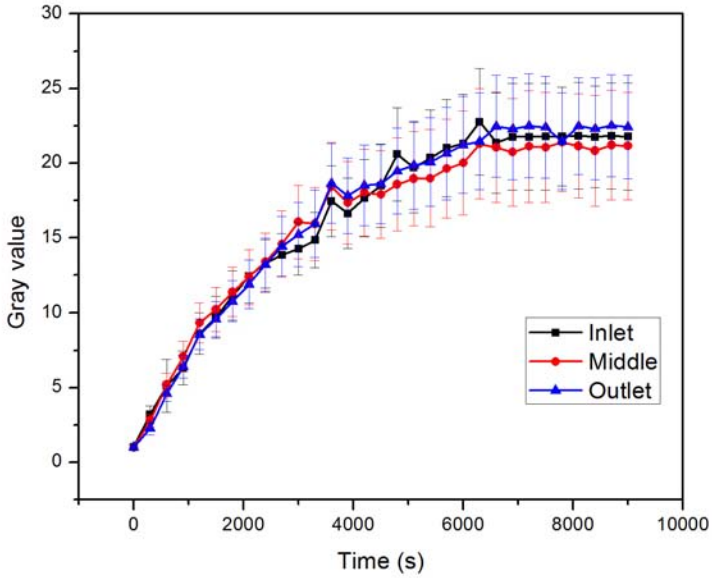

Figure 4.34: The variation of gray value at the different parts of microchannel with SlipSkin^{TM} membrane at feed flow rate of 130 µL $\mathrm{min^{-1}}$ and TMP=0.

The close analysis of Figure 4.34, Figure 4.35 and Figure 4.36 reveals that similarly to PES membrane, the fouling of SlipSkin^{TM} one is dependent on the applied hydrodynamic conditions. As so, in "130 µL $\mathrm{min^{-1}}$" case, the maximal gray value of 21.5 ± 0.5 at the inlet, the middle, and the outlet of the microchannel was detected. The shift for lower cross flow velocity led to lower extent of fouling, which is reflected by the reduction of fluorescent signal. The process conducted at 75 µL $\mathrm{min^{-1}}$ resulted in intermediate membrane fouling with the end gray value of 16.5 ± 0.5, while at the lowest Re the fluorescent signal was minimal: 9.4 ± 0.5. This finding is not surprising in the view of two previously discussed concepts. Firstly, the higher feed flow rate (higher shear stress) may induce greater protein unfolding. Since the protein unfolding influences mainly the intermolecular interaction, the

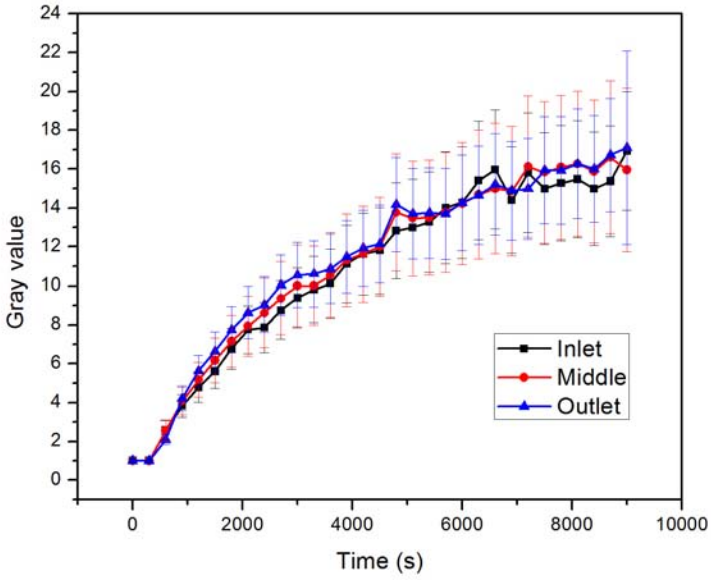

Figure 4.35: The variation of gray value at the different parts of microchannel with SlipSkin™ membrane at feed flow rate of 75 µL min^{-1} and TMP=0.

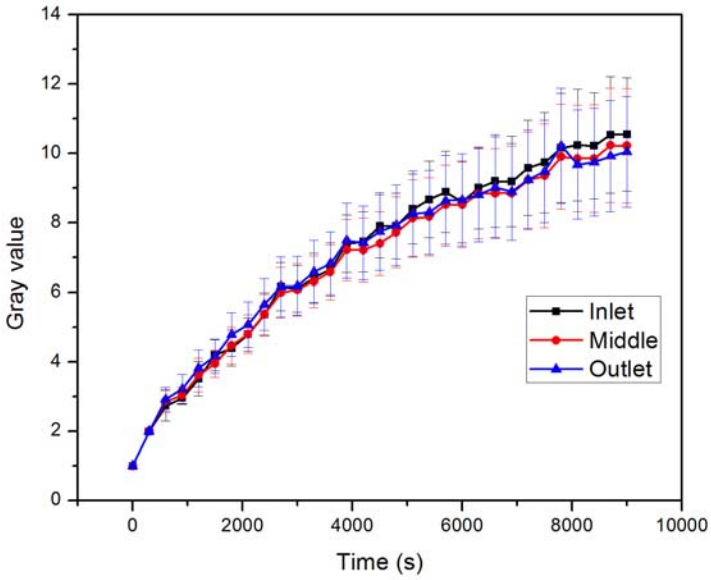

Figure 4.36: The variation of gray value at the different parts of microchannel with SlipSkin™ membrane at feed flow rate of 35 µL min^{-1} and TMP=0.

Figure 4.37: The macroscopic view of microchip with PES and SlipSkin membranes after the no convection experiments at 35 µL min^{-1}. (left image – virgin PES membrane, central – fouled SlipSkin$^{\mathrm{TM}}$ membrane, right – fouled PES membrane).

variation of membrane fouling depending on the hydrodynamic conditions is visible disregarding the membrane material. Secondly, it can be assumed that the adsorption of α-lactalbumin on SlipSkin$^{\mathrm{TM}}$ membrane alike on PES membrane is diffusion-controlled. If this assumption is correct, the obtained result obey the film theory, which suggests thinner boundary layer at higher feed flow rate leads to greater protein adsorption.

One of interesting features of gray value profiles recorded for SlipSkin$^{\mathrm{TM}}$ membrane (Figure 4.34 and Figure 4.35) is that there is almost no difference between fluorescent signals at the inlet, the middle, and the outlet of the MMD. In contrast, the respective graphs for PES membranes (Figure 4.3 and Figure 4.4) exhibit the notable distinction between the parts of the membrane. The mismatch between analyzed membranes is ascribed to the difference in permeability. As SlipSkin$^{\mathrm{TM}}$ membrane is less permeable, the local variation of transmembrane pressure induced by pressure drop along the channel has lower impact on the local filtrate flux. Consequently, the transmembrane drag force (at the inlet) and the backflushing lift force (at the outlet) are lower compared to PES membrane with higher permeability. Therefore, the effect of flow distribution inside the MMD diminishes when the less permeable membrane is used.

The pairwise comparison of gray value profiles recorded at similar experiments, but for different membrane materials, suggests lower accumulation of protein on the surface of SlipSkin$^{\mathrm{TM}}$ material. In particular, during the "130 µL min^{-1}" and

"35 µL min^{-1}" processes, the fluorescence acquired by PES membrane is almost 2.5 times higher: 48.4 ± 6.4 vs 21.5 ± 0.5 and 23.3 ± 0.4 vs 9.4 ± 0.5. The discrepancy found at 75 µL min^{-1} is smaller, but still visible and is around 30% in the favor of SlipSkin™. Thus, all performed experiments clearly demonstrated the lower adsorption of protein by SlipSkin™ membrane compared to PES membrane. This effect may be related either to the lower propensity to adsorb proteins by SlipSkin™ material or to a lower permeability of the developed membrane, which influences the extent of the transmembrane drag force, responsible for transferring the protein from the bulk to a membrane/solution interface. Finally, even the visual examination of both fouled membranes (Figure 4.37) with the unaided eye makes it possible to see that significantly lower quantity of protein (less intense blue color) has been attached to the surface of SlipSkin™ membrane.

8 Conclusion

The objectives of this Chapter were to analyze the membrane fouling at the microscale at different hydrodynamic and pressure conditions and to perform the microscale comparison of commercial polyethersulfone (PES) membrane with the membrane fabricated from novel SlipSkin™ material. The following conclusion could be made based on the obtained experimental results.

The extent of adsorption of α-lactalbumin-Atto647N was found to be dependent on the feed flow rate: the greater gray values were observed at the higher feed flow rates. Probably, this outcome is related to the higher shear stress at greater cross flow velocity, which may lead to greater unfolding of protein chains. If this assumption is correct, the greater shear stress results in facilitation of interaction between hydrophobic parts of the protein molecule adsorbed on the membrane surface with the one flowing in the solution. Besides, considering the film theory and the reduction of the boundary layer thickness with increase in feed flow rate (shear stress), it was assumed that adsorption of α-lactalbumin-Atto647N is limited by diffusion towards the membrane surface.

The difference in the fluorescent signal recorded from the inlet, the middle and the outlet during the experiments at TMP$\approx$0, suggest that the internal filtration induced by pressure drop along the microchannel also influences the adsorption of α-lactalbumin-Atto647N. However, at smallest feed flow rate applied, this

difference vanishes indicating that the pressure drop is too small to have a noticeable impact on the distribution of accumulated protein.

The application of transmembrane pressure (shifting to the filtration conditions) was associated with the formation of dark zones, which were not detected neither during experiment with BSA-FITC (at all studied conditions) nor during no convective fouling experiments with α-lactalbumin-Atto647N. Their formation was ascribed to the phenomena called aggregation-caused fluorescence quenching (ACQ). This phenomena is related to a specific intermolecular π–π electron interactions in tightly packed state the fluorescent tags of the neighboring molecules, which leads to the annihilation of their light emission. Moreover, the highlighted dark zones were not observed during scanning electron microscopy analysis, indicating that these zones are detectable only when the surrounding molecules emit the fluorescent light.

Analysis of correlation between the surface coverage with ACQ zones and the filtrate flux decline demonstrated that there is no visible dependence in the beginning of the filtration process where the primary contact between membrane and protein occurs. However, this outcome is related to the small magnification applied for the real-time observation of surface. Probably, the size of formed ACQ zones is too small to be detected under selected magnification. Besides, at the latter stages of filtration it seems that the surface coverage with ACQ zones has a linear dependence with a negative slope on the permeate flux decline.

The comparison of results obtained during the experiment conducted in filtration mode (at TMP=$90\ \mathrm{mbar}$) revealed that the reduction of feed flow rate leads to a greater surface coverage with ACQ zones and to a reduced gray values of non-ACQ regions. This outcome was related to the ratio between axial convection (directed towards the outlet of the microchannel) and the transmembrane drag force (acting perpendicularly to the membrane). Particularly, the greater this ratio is, the shorter is the residence time of protein solution inside the microchannel. As so, it has less time to achieve a state of supersaturation, the condition which is believed to be prerequisite for the formation of ACQ zones. From another point of view, the increase of aggregates formation is related to increase in Pe number, which is in agreement with film theory. Finally, despite the differences in gray values and surface coverages with ACQ zones, the ultimate permeate flux reduction was practically the same at TMP=$90\ \mathrm{mbar}$. This observation suggested that the compactness of the protein deposit has the determining effect on the filtrate flux

decline.

Based on the obtained results the critical value of ratio between the axial convection and the transmembrane drag force was estimated to be between 12.4 and 25. Below this critical value the supersaturation of solution is achieved rapidly which leads to a uniform coverage of membrane surface with ACQ zones. However, above this critical value, the attainment of supersaturation requires more time, which results in progressive increase of surface coverage with ACQ zones from the inlet towards the outlet. Moreover, the evaluation of influence of two-fold reduction of the axial convection and the two-fold increase of transmembrane drag force on the formation of ACQ zones demonstrated that these two changes are not equivalent. The two-fold increase of transmembrane drag force led to significantly greater fouling, reflected by greater surface coverage with ACQ zones and more significant permeate flux reduction. Analysis of this outcome through the film theory showed that the two-fold changes of convection led to a different changes in Pe number. Particularly, the increase of transmembrane convection leads to a higher Pe number and greater fouling. Therefore, it may be concluded that alike experiments with BSA-FITC, the fouling induced by α-lactalbumin-Atto647N is more severe at processes with higher Pe numbers.

The experiment with stepwise increase of transmembrane pressure demonstrated that each increase of transmembrane convection lead to a progression in the protein accumulation that was reflected by the decline of permeate flux. It was also observed that the gentle beginning of experiment can compensate the increased duration.

The preliminary comparison of α-lactalbumin-Atto647N on the surface of the membrane prepared from the novel SlipSkin^{TM} material and the commercially available PES membrane demonstrated the improved anti-fouling property of SlipSkin^{TM}membrane. It was also demonstrated the extent of protein adsorption on SlipSkin^{TM} membrane is dependent on cross flow velocity: the higher cross flow velocity the greater protein accumulation. However, due to small permeability of this membrane, the difference in fluorescence at the inlet, the middle and the outlet was not observed.

9 References

1. Rosenthal, T.B., The effect of temperature on the pH of blood and plasma in vitro. *J Biol Chem*, 1948. 173(1): p. 25-30.

2. Kamau, S.M., S.C. Cheison, W. Chen, X.-M. Liu, and R.-R. Lu, *Alpha-Lactalbumin: Its Production Technologies and Bioactive Peptides*. Comprehensive Reviews in Food Science and Food Safety, 2010. 9(2): p. 197-212.

3. Argiles, A., M. Garcia-Garcia, J. Derancourt, G. Mourad, and J.G. Demaille, Beta 2 microglobulin isoforms in healthy individuals and in amyloid deposits. *Kidney Int*, 1995. 48(5): p. 1397-405.

4. Vanholder, R., R. De Smet, G. Glorieux, A. Argiles, U. Baurmeister, P. Brunet, W. Clark, G. Cohen, P.P. De Deyn, R. Deppisch, B. Descamps-Latscha, T. Henle, A. Jorres, H.D. Lemke, Z.A. Massy, J. Passlick-Deetjen, M. Rodriguez, B. Stegmayr, P. Stenvinkel, C. Tetta, C. Wanner, and W. Zidek, Review on uremic toxins: Classification, concentration, and interindividual variability. *Kidney Int*, 2003. 63(5): p. 1934-1943.

5. Bingaman, S., V.H. Huxley, and R.E. Rumbaut, Fluorescent dyes modify properties of proteins used in microvascular research. *Microcirculation*, 2003. 10(2): p. 221-31.

6. Bäumle, M. Protein Characterization & Detection. *BioFiles* 2011; Available from: `http://www.sigmaaldrich.com/life-science/learning-center/biofiles/biofiles-5-2/protein-labeling.html#atto_dyes`.

7. Meireles, M., P. Aimar, and V. Sanchez, Albumin denaturation during ultrafiltration: effects of operating conditions and consequences on membrane fouling. *Biotechnol Bioeng*, 1991. 38(5): p. 528-34.

8. Chan, R. and V. Chen, Protein Transport, Aggregation, and Deposition in Membrane Pores, in Supramolecular Structure in Confined Geometries. 1999, *American Chemical Society*. p. 231-246.

9. Greene, L.H., J.A. Grobler, V.A. Malinovskii, J. Tian, K.R. Acharya, and K. Brew, Stability, activity and flexibility in α-lactalbumin. *Protein Engineering*,

1999. 12(7): p. 581-587.

10. Franken, A.C.M., J.T.M. Sluys, V. Chen, Fane,, and F. A.G., A.G. *Role of protein conformation on membrane characteristics*. in Fifth World Filtration Congress. 1990. Nice. France.

11. Prádanos, P., A. Hernández, J.I. Calvo, and F. Tejerina, Mechanisms of protein fouling in cross-flow UF through an asymmetric inorganic membrane. *Journal of Membrane Science*, 1996. 114(1): p. 115-126.

12. Bergström, F., I. Mikhalyov, P. Hägglöf, R. Wortmann, T. Ny, and L.B.Å. Johansson, Dimers of Dipyrromethene boron Difluoride (BODIPY) with Light Spectroscopic Applications in Chemistry and Biology. *Journal of the American Chemical Society*, 2002. 124(2): p. 196-204.

13. Marmé, N., G. Habl, and J.-P. Knemeyer, Aggregation behavior of the red-absorbing oxazine derivative MR 121: A new method for determination of pure dimer spectra. *Chemical Physics Letters*, 2005. 408(4–6): p. 221-225.

14. Ma, X., R. Sun, J. Cheng, J. Liu, F. Gou, H. Xiang, and X. Zhou, Fluorescence Aggregation-Caused Quenching versus Aggregation-Induced Emission: A Visual Teaching Technology for Undergraduate Chemistry Students. *Journal of Chemical Education*, 2016. 93(2): p. 345-350.

15. Kim, K.J., A.G. Fane, C.J.D. Fell, and D.C. Joy, Fouling mechanisms of membranes during protein ultrafiltration. Journal of Membrane Science, 1992. 68(1-2): p. 79-91.

16. Ho, C.C. and A.L. Zydney, Protein fouling of asymmetric and composite microfiltration membranes.*Industrial & Engineering Chemistry Research*, 2001. 40(5): p. 1412-1421.

17. van Reis, R., S. Gadam, L.N. Frautschy, S. Orlando, E.M. Goodrich, S. Saksena, R. Kuriyel, C.M. Simpson, S. Pearl, and A.L. Zydney, High performance tangential flow filtration. *Biotechnology and Bioengineering*, 1997. 56(1): p. 71-82.

18. Tijink, M., J. Janssen, M. Timmer, J. Austen, Y. Aldenhoff, J. Kooman, L. Koole, J. Damoiseaux, R. van Oerle, Y. Henskens, and D. Stamatialis, Development of novel membranes for blood purification therapies based on copolymers of N-vinylpyrrolidone and n-butylmethacrylate. *Journal of Materials Chemistry B*, 2013. 1(44): p. 6066-6077.

Convection-diffusion-adsorption model of solute removal in dialysis by membrane with double functionality

5

Introduction

In this chapter, we develop the model which highlights the benefits of combining the diffusion, convection and adsorption in one double-layer membrane proposed recently by our partners in University of Twente [1, 2]. This membrane consist of two layers: 1) a mixed matrix layer, where activated carbon particles are incorporated inside the membrane material; 2) a particle-free selective layer providing hemocompatibility and selectivity. This functionalized membrane showed an excellent removal of small and protein-bound toxins from human plasma and therefore gave a high promise for its further development for dialytic applications. However, the contribution of the mixed matrix layer to the removal of the uremic toxins as well as the influence of the membrane characteristics and process conditions remains uncertain. We therefore aim at developing the model, which is able to encapsulate the various parameters and their physical relationships, in order to describe the overall performance of the membrane towards removal of small and middle sized uremic toxins. As a result, the model gives an opportunity to optimize the membrane properties and process conditions.

The upcoming sections are organized in the following manner: first, the selected assumptions along with mathematical derivation of required equations are described in order to formulate the model. Secondly, the fabrication and characterization of functionalized double-layer membranes is presented. Then, the prediction of solute concentration profiles across the membrane with use of the model is demonstrated. Finally, the developed model is evaluated by the comparison with the experimental results.

This work was submitted to the Chemical Engineering Science Journal in the form of article. D. Snisarenko, D. Pavlenko, D. Stamatialis, P. Aimar, C. Causserand, P. Bacchin, “Convection-diffusion-adsorption model of solute removal in dialysis by membrane with double functionality”.

Nomenclature

a	Specific surface area of the adsorbent	m^2 per m^3 of mixed matrix membrane
c	concentration	$(\mathrm{mol\,m^{-3}})$
d	diameter	(m)
D	diffusion coefficient	$(\mathrm{m^2\,s^{-1}})$
div	divergence	(-)
j	molar flux density	$(\mathrm{mol\,m^{-2}\,s^{-1}})$
J	convective flow through the membrane	$(\mathrm{m\,s^{-1}})$
k	heterogenic adsorption constant	$(\mathrm{m\,s^{-1}})$
K	pseudo mass transfer conductance	$(\mathrm{m\,s^{-1}})$
l	Length of the fiber	(m)
m	mass	(mg)
M	molecular weight	$(\mathrm{g\,mol^{-1}})$
N	number of fibers	(-)
Pe	Peclet number	(-)
q	quantity of adsorbed specie	µg per mg of membrane
r	rate of adsorption	$(\mathrm{mol\,m^{-3}\,s^{-1}})$
Re	Reynolds number	(-)
s	sink term	$(\mathrm{mol\,m^{-3}\,s^{-1}})$
S	membrane surface area	$(\mathrm{m^2})$
Sc	Schmidt number	(-)
Sh	Sherwood number	(-)
t	time	(s)
V	volume of fluid	$(\mathrm{m^3})$

Greek letters:

δ	Thickness of the domain	(m)
Δ	Determinant defined in Equation 5.5	(-)
ϕ	Thiele modulus	(-)

Subscripts:

0	Initial time point
a	After the adsorptive layer
ads	Adsorption
b	Before the adsorptive layer
$conv$	Convection
d	Dialysate
$diff$	Diffusion
e	external
f	Feed
h	Hydraulic
in	At the inlet of particular domain
l	Lumen of the membrane
max	maximal
out	At the outlet of particular domain
s	Shell side of the module
t	Time different from 0

1 Model development

1.1 System formulation

The geometry of the system was dictated by the novel concept of blood filtration, which employs the functionalized membranes with incorporated adsorptive particles [1]. In its way through the membrane, a toxin present in the blood (feed stream) first passes through the particle-free layer (PFL) and then through the mixed matrix membrane (MMM), where it can adsorb on the dispersed adsorptive particles as depicted in Figure 5.1. The driving force of the solute transport is not the same along the length of the membrane, because solute concentrations in the blood and dialysate compartments change. Aiming to overcome this effect, as the base element of the system, we took the region of the membrane where the solute concentration may be assumed constant. Because boundary layers are present on both sides of the membrane, we have to consider a four-layers system (Figure 5.1).

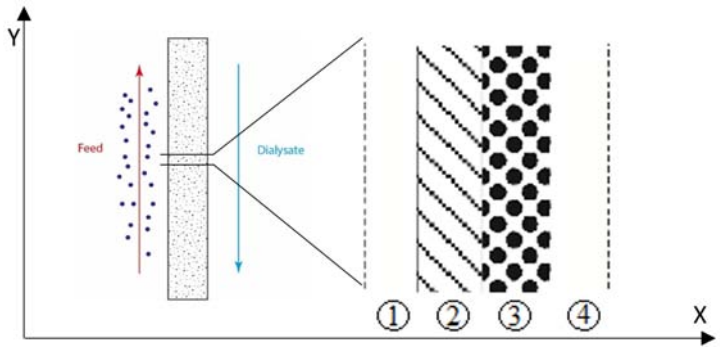

Figure 5.1: The schematic representation of the system geometry (dots in the feed represent the toxin molecules present in the blood stream). 1 – feed side boundary layer, 2 – particle-free membrane, 3 – mixed matrix membrane, 4 - dialysate boundary layer.

The model of solute transport through this system was developed within the frame of following assumptions:

1. Molar flux through the membrane is considered to be at steady state.
2. Fluids in the blood and dialysate compartments are Newtonian.
3. The molar flux at any point is considered as diffusive or as a combination of diffusive and convective contributions.
4. The transport of solute through the membrane occurs through the pores present in both the particle-free and the mixed matrix layers.

5. Adsorptive particles are considered to be uniformly dispersed inside the polymeric matrix;.
6. Absence of concentration gradient along the membrane (along Y axis in Figure 5.1).
7. Adsorption is considered as first order heterogeneous reaction. Dealing with the adsorption mechanism, such a kinetic condition can correspond to the system where the adsorptive capacity is large compared to the amount to be adsorbed.

The mass transport of solute across the membrane is conventionally described by the continuity equation in the form of Equation 5.1:

$$\frac{\partial c}{\partial t} + div(j) = \pm s \tag{5.1}$$

where s is the sink term which represents the adsorption of the permeating solute.

Analyzing the geometry of the model one may distinguish two types of regions depending on the possible toxin removal mechanisms: ones with convection and diffusion only, and one layer where, in addition to these two mechanisms, adsorption also takes place. Therefore, these regions can be studied separately. At steady state, the total molar flux in the region without adsorbent is constant and has the following form (Equation 5.2):

$$j = -D\frac{dc}{dx} + Jc \tag{5.2}$$

where $\frac{dc}{dx}$ is the local solute concentration gradient, D is diffusion coefficient, and J is convective flow through the membrane.

Equation 5.2 can be integrated across each layer assuming a given concentration in the inlet and the outlet. As so, the solution of Equation 5.2 results in a generic formula (Equation 5.3) applicable for the regions of the system without adsorptive particles by setting s = 0.

$$j = J\frac{\left(c_{out} - c_{in}e^{\frac{J\delta}{D}}\right)}{1 - e^{\frac{J\delta}{D}}} \tag{5.3}$$

The application of Equation 5.1 to the MMM layer results in a differential equation (Equation 5.4), which apart from diffusive and convective terms, also accounts for the presence of solute adsorption:

$$D\frac{d^2c}{dx^2} - J\frac{dc}{dx} - akc = 0 \tag{5.4}$$

Where a stands for specific surface area of adsorbent in m^2 per $\mathrm{m}^3$of mixed matrix membrane and k is heterogenic adsorption constant.

The solution of Equation 5.4 (presented in Appendix B) results in Equation 5.5, which describes the solute concentration at any depth (x) inside the MMM layer:

$$c = c_3\frac{e^{\frac{Pe_3}{2}\left(\frac{x}{\delta_3}-1\right)}\sinh\left(\frac{x\Delta}{\delta_3}\right)}{\sinh\left(\Delta\right)} - c_2\frac{e^{\frac{Pe_3}{2}\frac{x}{\delta_3}}\sinh\left(\Delta\left(\frac{x}{\delta_3}-1\right)\right)}{\sinh\left(\Delta\right)} \tag{5.5}$$

where $\Delta = \dfrac{\sqrt{Pe_3^2+4\phi^2}}{2}$; $Pe_3 = \dfrac{J\delta_3}{D_3}$; $\phi = \sqrt{\dfrac{ak}{D_3}}\delta_3$

From the concentration profile, it is possible to determine the molar flux before the MMM layer (j_b), and the molar flux after (j_a) by writing the molar flux Equation 5.2 at the inlet boundary x=0 and the outlet x=δ_3:

$$j_b = c_2\left(\frac{D_3\Delta\cosh(\Delta)}{\delta_3\sinh(\Delta)} + \frac{D_3Pe_3}{2\delta_3}\right) - c_3\frac{D_3e^{\frac{-Pe_3}{2}}\Delta}{\delta_3\sinh(\Delta)} \tag{5.6}$$

$$j_a = c_2\frac{D_3e^{\frac{Pe_3}{2}}\Delta}{\delta_3\sinh(\Delta)} - c_3\left(\frac{D_3\Delta\cosh(\Delta)}{\delta_3\sinh(\Delta)} - \frac{D_3Pe_3}{2\delta_3}\right) \tag{5.7}$$

Finally, since some part of the permeating specie is getting adsorbed inside the MMM, the solute molar flux density before this layer is greater than the one after, $j_b > j_a$. Summarizing the aforementioned model formulation, the schematic depiction of the entire system with key parameters (interface concentrations and fluxed) involved is presented on Figure 5.2.

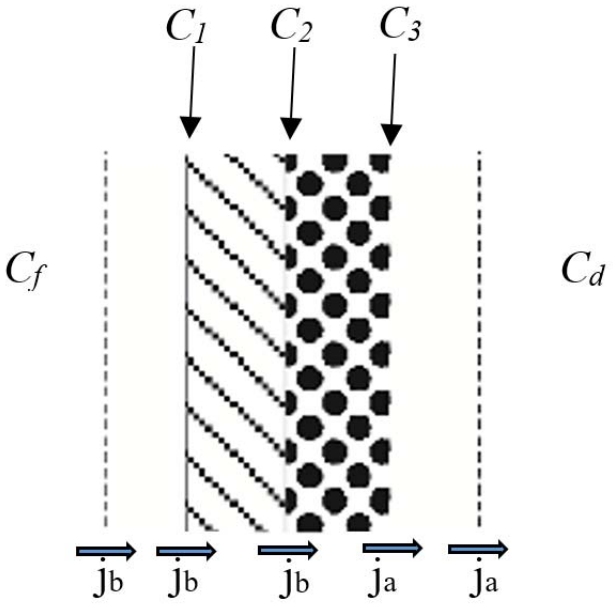

Figure 5.2: Schematic representation of formulated system with the key parameters.

1.2 Application of local mass balance

The model is established by considering the continuity of the molar flux before and after the MMM layer. The following system of five equations with two unknown molar flux densities j_b and j_a, and three unknown concentrations at the interfaces of domains c_1, c_2 and c_3 has to be solved

$$\begin{cases} j_b = c_f K_{1a} - c_1 K_{1b} & ; \\ j_b = c_1 K_{2a} - c_2 K_{2b} & ; \\ j_b = c_2 K_{3a} - c_3 K_{3b} & ; \\ j_a = c_2 K_{3c} - c_3 K_{3d} & ; \\ j_a = c_3 K_{4a} - c_d K_{4b} & ; \end{cases}$$

The expressions for each pseudo mass transfer conductance ($K_{i,j}$,) are determined from the writing of the differential molar balances presented in the previous section. The expressions for these conductances are given in the Appendix A.

An analytical solution can be found for this system when the bulk concentrations in the feed and the dialysate sides are known. The solution for the concentration of

the permeating specie on the interfaces adjacent to the adsorptive layer c_2 and c_3 are given below:

$$c_2 = \\ = \frac{K_{1a}K_{2a}\Big(K_{4a}+K_{3d}\Big)c_f + K_{3b}K_{4d}\Big(K_{2a}+K_{1b}\Big)c_d}{\Big(K_{3a}\big(K_{2a}+K_{1b}\big)+K_{1b}K_{2b}\Big)\Big(K_{4a}+K_{3d}\Big) - K_{3b}\Big(K_{2a}+K_{1b}\Big)K_{3c}} \tag{5.8}$$

$$c_3 = \\ = \frac{K_{1a}K_{2a}K_{3c}c_f + \Big(K_{3a}\big(K_{2a}+K_{1b}\big)+K_{1b}K_{2b}\Big)K_{4d}c_d}{\Big(K_{3a}\big(K_{2a}+K_{1b}\big)+K_{1b}K_{2b}\Big)\Big(K_{4a}+K_{3d}\Big) - K_{3c}K_{3b}\Big(K_{2a}+K_{1b}\Big)} \tag{5.9}$$

Combining these last two expressions with Equation 5.6 and Equation 5.7, enables determining the molar flux before and after the MMM layer. Knowing the input parameters listed in left hand side of Figure 5.3 one can perform the modelling of the instantaneous condition ("snapshot") of the system. In other words, the insertion of such input parameters as thicknesses of boundary layers, sieving and solute diffusion coefficients, rate of convective flow, adsorption constant and solute concentration on both sides of membrane, provides the possibility to analyze the state of the system at a particular moment of time.

The primary outcome of the model is the determination of the solute concentration profile across the membrane and the calculation of the solute mass transfer density across the membrane. Furthermore, the model enables analyzing the impact of the adsorptive particles on the local solute concentration inside the MMM and comparing the transfer efficiency with other scenarios such as: a) absence of convection (solute removal occurs only by diffusion and adsorption); b) absence of adsorption (presence of diffusion and convection), and c) absence of both convection and adsorption. The benefit of the functionalized membrane compared to a conventional single layer membrane of same thickness can be defined through a solute transport enhancement factor (STEF) index:

$$STEF = \frac{j_b}{j_{diff}} \tag{5.10}$$

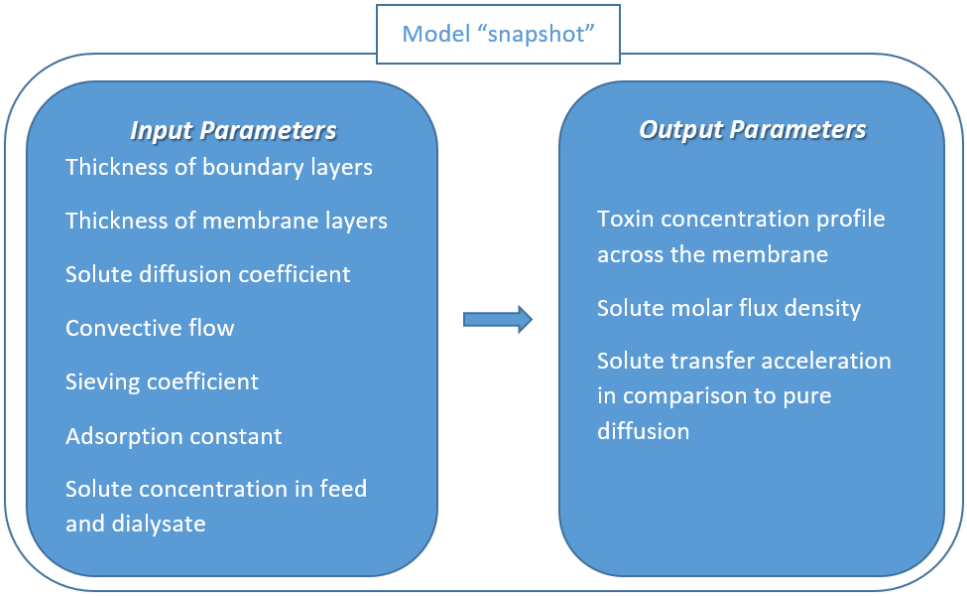

Figure 5.3: Required input and obtained output parameters from the model "snapshot" analysis.

In practice, STEF is defined as a ratio of molar flux density (j_b) obtained in one of the aforementioned scenarios to the molar flux density obtained when only diffusive transport is involved (j_{diff}). The solely diffusive case is used as a reference and STEF demonstrates the intensification of the solute removal due to the contribution of convection or/and adsorption.

1.3 Global mass balance

In order to depict the effect of the mass transfer on the solute removal, equations describing molar fluxes at a local scale presented in the previous section need then to be integrated over the full membrane module and along time. The differential equation to be integrated relies on mass balance on the feed and dialysate streams:

$$\frac{dc_f}{dt} = -\frac{j_b S}{V_f} \tag{5.11}$$

$$\frac{dc_d}{dt} = \frac{j_a S}{V_d} \tag{5.12}$$

Where c_f and c_d stand for the solute concentration in the feed and dialysate, S is the filtration surface area, V_f and V_d are volumes of feed and dialysate.

Since, the model accounts for the presence of the convective transfer, volumes of the feed and dialysate are also changing with time, with respect to Equation 5.13 and Equation 5.14:

$$\frac{dV_f}{dt} = -JS \tag{5.13}$$

$$\frac{dV_d}{dt} = JS \tag{5.14}$$

The integration of these equations combined with the mass flux given in the previous section enables the determination of the variation of the solute in the blood and then the clearance kinetics.

2 Validation experiments

2.1 Membrane fabrication and characterization

Double layer mixed matrix membranes were prepared according to a multistep procedure. For the selective layer, a polymer solution was prepared by dissolving 15% polyethersulfone (PES, Ultrason E 6020, BASF, Germany) and polyvinylpyrrolidone (PVP, K90, Fluka, Germany) of different quantity (details in Table 5.1) in ultra-pure N-methylpyrrolidone (NMP, Acros Organics, Belgium). Adsorptive layer was based on a solution containing 14% PES and 1.4% PVP dissolved in NMP. Activated carbon (AC) with average particle diameter of 27 μm was added gradually to the polymer solution to obtain a final concentration of 60% by weight. Both solutions were degassed for 48 hours before the spinning.

Two different spinning conditions were utilized aiming to obtain membranes of different transport properties. The first batch of membranes (further denoted as Membrane 1) was formed via immersion precipitation method at the conditions summarized in Table 5.1. The second batch of membranes (hereon denoted as Membrane 2) was fabricated according to the procedure described by Tijink *et al.* [2] with the conditions, which are also presented in Table 5.1. Table 5.2 describes the specification of used spinnerets.

Table 5.1: Spinning conditions of the fiber preparation.

	Membrane 1	**Membrane 2**
Inner layer pumping speed, $[\mathrm{mL\,min^{-1}}]$	0.4	0.9
Outer layer pumping speed, $[\mathrm{mL\,min^{-1}}]$	1.6	3.2
Bore pumping speed, $[\mathrm{mL\,min^{-1}}]$	2.8	2.7
Bore composition	Demi water	5 wt% PVP in ultra pure water
Air gap, $[\mathrm{cm}]$	10	-
Pulling speed, $[\mathrm{m\,min^{-1}}]$	3.5	7
Content of PVP in the dope solution for selective layer, [wt%]	7	10

Table 5.2: Spinneret specifications.

	Membrane 1	**Membrane 2**
Inner diameter needle, $[\mathrm{mm}]$	0.16	0.26
Outer diameter needle, $[\mathrm{mm}]$	0.26	0.46
Inner diameter first orifice, $[\mathrm{mm}]$	0.46	0.66
Outer diameter first orifice, $[\mathrm{mm}]$	0.66	0.96
Inner diameter second orifice, $[\mathrm{mm}]$	0.86	1.66

The membranes were cleaned by ultra-pure water to remove the remaining solvent. The fibers were then dried at $37°\mathrm{C}$ for 2 hours and subsequently were fractured in liquid nitrogen. The samples were dried under vacuum at $30°\mathrm{C}$ and gold sputtered using a BalzersUnion SCD $0\ 40$ sputter coater (Oerlikon Balzers, Balzers, Liechtenstein). Finally, samples were imaged using a JEOL JSM-560 0LV Scanning Electron Microscope (JEOL, Tokyo, Japan).

Dry fibers were cut into pieces of 15 cm each and then glued into modules (inner diameter of $4\ \mathrm{mm}$) of 3 fibers each, and $10\ \mathrm{cm}$ in length. Clean-water flux was then measured for each module with use of the set-up (Figure 5.4) described in detail in the following section. For this, modules were initially prepressurized at $2\ \mathrm{bar}$ for $1\ \mathrm{h}$ and then tested at transmembrane pressures of 0.5, 1.0, 1.5 and $2.0\ \mathrm{bar}$, with ultrapure water. The mass of collected permeate was monitored continuously.

2.2 Adsorption kinetics in static mode

At this stage, the knowledge of the adsorptive capacity of the carbon particles is an important issue. Experiments were conducted to determine the kinetics of adsorption of creatinine and α-lactalbumin (as a model compound for middle sized molecules) onto the membrane. For this purpose five pieces of hollow-fiber membranes of $5\ \mathrm{cm}$ each were placed in $25\ \mathrm{mL}$ of $0.1\ \mathrm{g\,L^{-1}}$ solution of creatinine or α-lactalbumin in phosphate buffer solution (PBS). The solution was stirred to avoid transport limitations between solute and surface of adsorptive layer of the membrane. The decay of solute concentration with time was monitored by sampling of $0.5\ \mathrm{mL}$/sample every 3 minutes for further analysis by UV-spectroscopy. The timing of sample collection was adjusted so as to limit the total withdrawal of initial volume at 10%. A linear decrease of the solute concentration in the initial stage of the process was observed. The initial slope of the concentration decrease provides an information on the rate of adsorption which may be used in the calculation of the product of the adsorption constant and specific surface area of adsorbent (ak).

2.3 Experimental study of the clearance of small and middle sized solutes

The experimental analysis of the clearance of solutes with the dual-layer membranes was conducted with use of the set-up (Convergence B.V., Enschede, The Netherlands) presented on Figure 5.4.

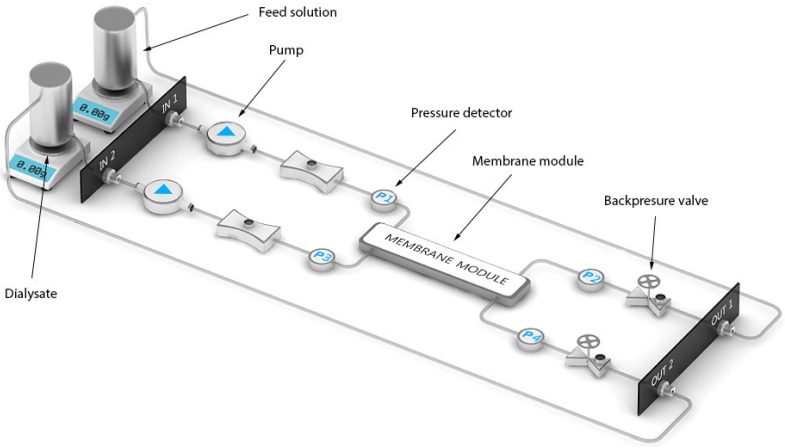

Figure 5.4: Schematic representation of the applied set-up.

Briefly, experimental set-up consists of 2 peristaltic pumps, 4 pressure detectors, 2 back-pressure valves and 2 reservoirs for the model solutions. All the parts of the set-up are connected via PTFE tubings to membrane module which has inlets and outlets for the feed and dialysate solutions that are pumped in counter-current configuration. The flow rates of the feed and dialysate solutions are controled by the peristalitic pumps, while constant TMP is generated by the back-pressure valves. Pressure in the system is monitored by 4 pressure detectors which are installed near the membrane module s inlets and outlets. Compartments for the module solutions are positioned on the balances to control the mass of the system in time.

For the validation experiment, PBS-based $0.1\ \mathrm{g\,L^{-1}}$ solutions of creatinine (Sigma-Aldrich, France) as a model molecule for the small uremic toxin; and α-lactalbumin (Sigma-Aldrich, France) as a model compound for the middle sized molecule were prepared, and were further used as the feed solutions. The pure solution of PBS was used as the dialysate.

Validation experiments were conducted using $50\ \mathrm{mL}$ of the feed and dialysate solutions. Moreover, we followed the convention that the flow rate of the dialysate has to be twice as high as the flow rate of the feed stream [3]. As so, the feed flow rate was set as $5\ \mathrm{mL\,min^{-1}}$, while the dialysate flow was equal to $10\ \mathrm{mL\,min^{-1}}$. In addition, the feed solution was flown inside the hollow fiber membrane lumen, while the dialysate was pumped through the shell side of the module. For experiments in diffusive mode (conventional dialysis), the transmembrane pressure (TMP) was kept around $0\ \mathrm{bar}$, meaning that the toxin removal driving force was generated only by the difference of its concentration across the membrane. In contrary, another set of experiments was conducted with utilization of both diffusion and convection (hemodiafiltration mode). There the TMP was set at $0.17\ \mathrm{bar}$ or $0.5\ \mathrm{bar}$ in different experiments in order to induce the convective transport through the membrane. These pressure regimes were chosen in order to, in one hand, avoid the necessity to add new portion of the feed solution in the system during the experiment, and, on the other hand, to generate convective flow with noticeable impact on overall solute removal. Throughout the experiment, the weight of the feed and dialysate solutions was continuously monitored. Decrease of the feed (increase of the dialysate) mass was considered to be due to the presence of convection. Samples of $1\ \mathrm{mL}$ were taken from both compartments in time and the concentration of creatinine and α-lactalbumin there was measured by UV-spectroscopy (Varian, Cary 300 Scan UV-Visible Spectrophotometer) at $25°\mathrm{C}$ in a $10\ \mathrm{mm}$ quartz cuvette at $230\ \mathrm{nm}$ and $280\ \mathrm{nm}$, respectively. The increase of the solute concentration in the dialysate was

attributed to the diffusive transport, in case of the experiment conducted in diffusive mode (conventional dialysis) or to combination of diffusive and convective removals, in case of the experiment performed in the hemodiafiltration mode. In parallel, based on mismatch between the amount of solute disappeared from the feed side and found in the dialysate the quantity of solute adsorbed inside the membrane was defined. Finally, the total solute removal was considered to be the sum of diffusive/convective and adsorptive removals. Each validation experiment was conducted three times. After the experiments, the modules were dried in air and the effective surface area of membrane inside the module was measured.

3 Results and discussion

3.1 Membrane fabrication and characterization

Figure 5.5 demonstrates the structure and the morphology of the membranes:

Membrane 1 **Membrane 2**

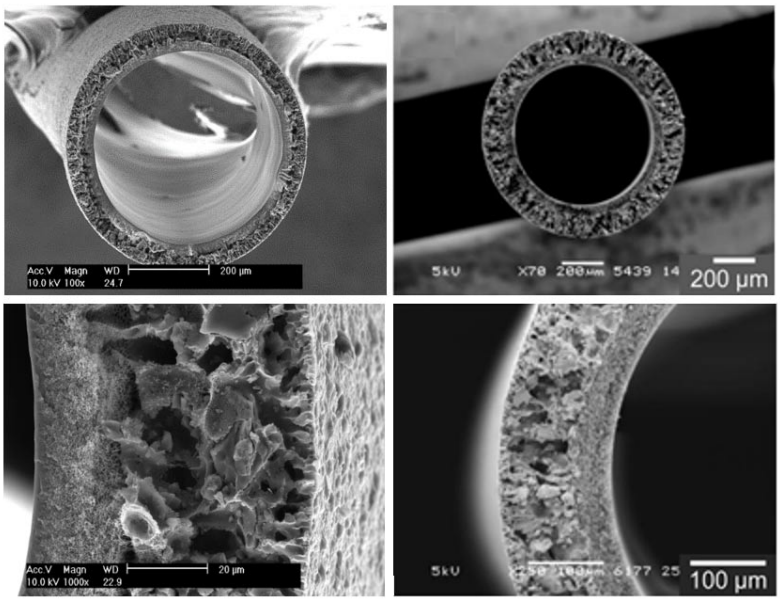

Figure 5.5: SEM images of fabricated dual-layer membranes (right-hand side images are adapted from [2]).

On the images of Membrane 1 and Membrane 2 one can distinguish the inner particle-free region with a denser skin layer on the lumen side and the outer particle-loaded

(MMM) layer. In both cases, the two layers are well attached without apparent gaps between. In both membranes, the MMM layer is more porous than the particle-free layer, suggesting that the main contribution to mass transport resistance of the entire membrane should be the inner layer. In addition, activated carbon particles are uniformly distributed inside the polymeric matrix of MMM. The dimensions of the fibers are summarized in Table 5.3. These values were further used for simulations based on the mass transfer model which has been described here above.

Table 5.3: Geometrical dimensions of the fabricated fibers.

	Membrane 1	**Membrane 2**
Thickness of the inner layer, [μm]	21	49
Thickness of MMM, [μm]	47	111
Lumen diameter, [μm]	450	669
External diameter of the fiber, [μm]	586	984

The clean water flux tests revealed that the Membrane 1 is significantly less permeable than M2: 2.5 ± 1.1 $\mathrm{L\,m^{-2}\,h^{-1}\,bar^{-1}}$ vs 58.4 ± 9.3 $\mathrm{L\,m^{-2}\,h^{-1}\,bar^{-1}}$ [2] respectively. The integrity of the membranes was not affected during the water permeance testing, meaning that fabricated membranes possess sufficient mechanical strength for the dialysis and hemodiafiltration experiments.

The product of heterogeneous adsorption constant and specific surface area of activated carbon (ak) for both membrane types were determined with respect to creatinine and α-lactalbumin Table 5.4.

Table 5.4: Values of "ak" parameter for various pairs "Membrane-solute".

	Membrane 1	**Membrane 2**
Creatinine	$0.152\ \mathrm{s^{-1}}$	$0.082\ \mathrm{s^{-1}}$
α-lactalbumin	-*	$0.011\ \mathrm{s^{-1}}$

* - was not determined, because Membrane 1 was impermeable for α-lactalbumin.

According to Table 5.4, the "ak" parameter for the adsorption of creatinine is almost twice higher for Membrane 1 than for Membrane 2. Since the membrane material and the adsorptive particles are the same for both membranes, the difference in adsorptive properties between these membranes may be attributed to the different accessibility of activated carbon particles embedded in the polymer matrix. In

parallel, the comparison of adsorptive properties of Membrane 2 with respect to creatinine and α-lactalbumin demonstrates that adsorption of the protein is significantly lower, only $0.011\ \mathrm{s}^{-1}$. This may be attributed to either a difference in steric hindrance for small sized creatinine and much larger protein or it can be connected to the different affinity of activate carbon particles to creatinine and α-lactalbumin. Finally, various permeation trials with use of Membrane 1 revealed that it is completely impermeable for α-lactalbumin; therefore, the experimental estimation of "ak" for this case was not performed.

3.2 Double layer membrane transfer modelling

To perform the modelling of the transfer through the MMM the thicknesses of boundary layers (δ) have to be estimated. Since the validation of the model was performed with use of the hollow-fiber membranes placed in the module, two sets of hydrodynamic correlation, for lumen and shell sides, were used. The flow rates of feed and dialysate streams were taken from the filtration the set-up utilized during the validation experiments. The estimation of the conditions in the lumen side were done using two following correlations: $Sh_l = 2.66 Re_l^{0.25} Sc_l^{0.33} \left(\frac{d_{h_l}}{l}\right)^{0.33}$; $\delta_l = \frac{d_{h_l}}{Sh_l}$ [4], while the quantification of the hydrodynamic conditions in the shell side was done by applying another set of equations: $Sh_s = 1.25 Re_s^{0.93} Sc_s^{0.33} \left(\frac{d_{h_s}}{l}\right)^{0.93}$; $d_{h_s} = \frac{\left(d_s^2 - N d_e^2\right)}{\left(d_s + N d_e\right)}$; $\delta_s = \frac{d_{h_s}}{Sh_s}$ [4]. Where d_h stands for the hydraulic diameter, N is number of fibers, d_e and d_s are external diameter of the membrane and the diameter of the module (shell). The selected correlations are assumed to be applicable, as they were developed for hollow fiber modules operated at laminar conditions (Re<2000), while in our experiments Re in the shell and the lumen side was below 100.

Validation experiments were conducted at feed and dialysate flow rates of $5\ \mathrm{mL\,min^{-1}}$ and $10\ \mathrm{mL\,min^{-1}}$, respectively. Since, a low concentration of solute was used for the preparation of all feed solutions and since the pure phosphate buffer was used as the dialysate, the viscosity and density of both solutions were assumed to be equal to the ones of water: $10^{-3}\ \mathrm{Pa\,s}$ and $1000\ \mathrm{kg\,m^{-3}}$ respectively for the calculation of the boundary layer thicknesses. Based on the aforementioned hydrodynamic correlations, the thicknesses of the boundary layers in the lumen and shell sides were determined (Table 5.5).

Table 5.5: Boundary layer thicknesses in the validation experiments.

		Membrane 1	**Membrane 2**
Experiment with creatinine	Lumen boundary layer, [μm]	30.7	45.3
	Shell side boundary layer, [μm]	197	245
Experiment with α-lactalbumin	Lumen boundary layer, [μm]	17.9	23.8
	Shell side boundary layer, [μm]	87.1	124

As it can be seen from Table 5.5, the boundary layer thickness in the creatinine removal experiments differs in case of Membrane 1 and Membrane 2. This difference is ascribed to the difference in geometry (see Section 3.1) of the said membranes. Similarly, due to the difference between the outer diameters of both membranes, the boundary layer thickness on the shell side was found smaller for Membrane 1. Similar results were obtained from calculations of hydrodynamic conditions during the α-lactalbumin removal experiments. The lumen boundary layers were found to be 17.9 μm and 23.8 μm, while the shell side boundary layers are 87.1 μm and 124 μm for Membrane 1 and Membrane 2, respectively.

According to data presented by Shaw *et al.* [5] the diffusion coefficient of creatinine in water at room temperature is 9×10^{-10} $\mathrm{m^2\,s^{-1}}$, while Kim *et al.* [6] used the value of 5.31×10^{-10} $\mathrm{m^2\,s^{-1}}$. Therefore, here we used the average value of 7×10^{-10} $\mathrm{m^2\,s^{-1}}$. To the best of our knowledge, the diffusion coefficient of α-lactalbumin was not reported in the literature. Thus with use of Einstein equation and molecule effective radius reported by Fu *et al.* [7] it was calculated to be equal to 1.07×10^{-10} $\mathrm{m^2\,s^{-1}}$. Finally, for the sake of simplicity we assumed that the solute diffusion coefficient is the same in the all regions of the system.

The parameters used for our simulations have been gathered in Table 5.6. In principle, these parameters represent the filtration of creatinine through the Membrane 2.

The predicted solute concentration profiles across the membrane with and without adsorption have been plotted in Figure 5.6, in the absence of solute in the dialysate stream.

Table 5.6: Input parameters applied to produce creatinine concentration profile across Membrane 2.

Name of input parameter	Value
Blood boundary layer thickness	5×10^{-5} m
Particle-free layer thickness	4.9×10^{-5} m
MMM thickness	1.11×10^{-4} m
"ak" parameter	$0.082\ \mathrm{s}^{-1}$
Solute diffusion coefficient	$7 \times 10^{-10}\ \mathrm{m}^2\,\mathrm{s}^{-1}$
Thickness of dialysate boundary layer	2.3×10^{-4} m
Convective flow rate through the membrane	$1.1 \times 10^{-6}\ \mathrm{m\,s}^{-1}$
Solute concentration in the blood side	$0.885\ \mathrm{mol\,m}^{-3}$

According to Figure 5.6 the presence of adsorptive particles favors the reduction of solute concentration inside the membrane. The molar flux of solute through the membrane is then more important: one can note a steeper decline of the concentration profile in the blood boundary layer (BBL). This effect is attributed to the adsorption of a fraction of the permeating species by the particles present in the MMM that is accelerating the mass transfer. Quantitative expression of such phenomena is given by the solute transfer enhancement factor (STEF) parameter provided by the model (Table 5.7).

Table 5.7: Solute transfer acceleration for various system conditions.

Solute removal mechanisms involved	Molar ux density, j_a	Solute transfer enhancement factor
Diffusion	$1.41 \times 10^{-6}\ \mathrm{mol\,m}^{-2}\,\mathrm{s}^{-1}$	1*
Diffusion and Adsorption	$3.12 \times 10^{-6}\ \mathrm{mol\,m}^{-2}\,\mathrm{s}^{-1}$	2.21
Diffusion and Convection	$1.95 \times 10^{-6}\ \mathrm{mol\,m}^{-2}\,\mathrm{s}^{-1}$	1.39
Diffusion, Convection, and Adsorption	$3.63 \times 10^{-6}\ \mathrm{mol\,m}^{-2}\,\mathrm{s}^{-1}$	2.58

* - taken as reference.

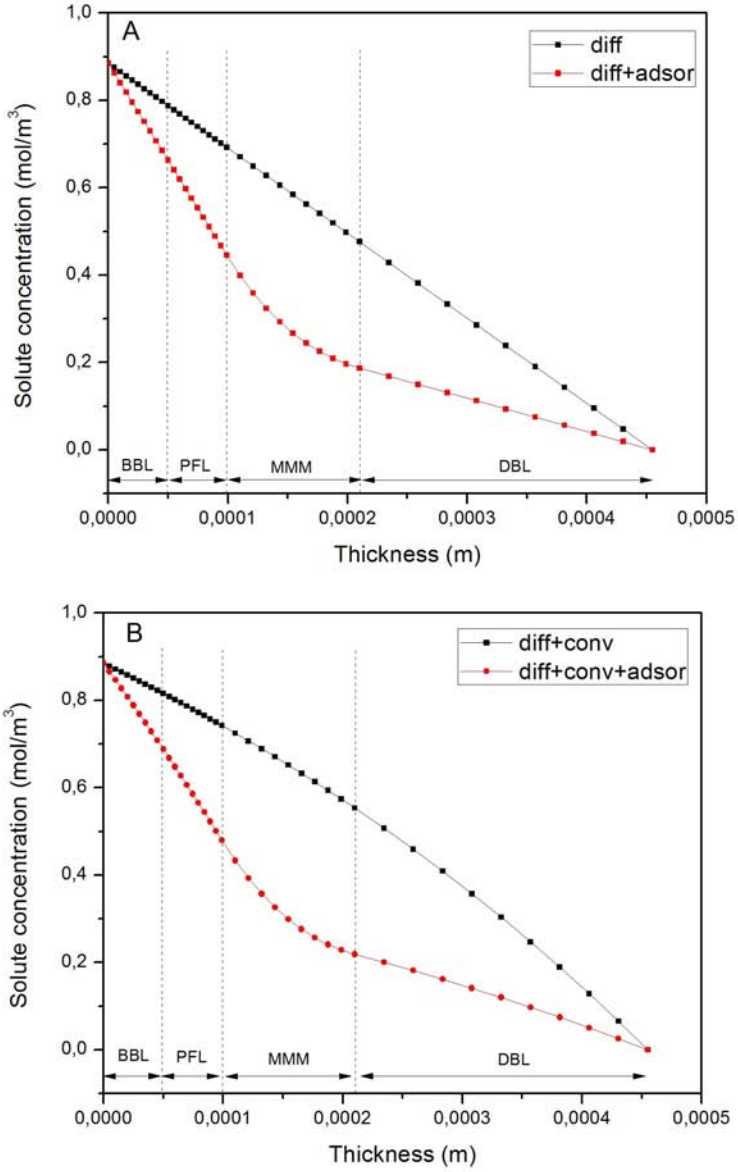

Figure 5.6: Solute concentration profiles across the membrane depending on the removal mechanisms involved. (BBL stands for blood boundary layer, PFL – particle free layer, MMM – mixed matrix membrane) (image A - diffusion vs diffusion+adsorpsion; image B - diffusion+convection vs diffusion+convection+adsorption).

From Table 5.7 one may conclude that for the selected set of input parameters, the addition of convective flow to solely diffusion-driven solute removal results in 1.39 times greater elimination rate, while adsorption provides a STEF of 2.21. Moreover,

the combination of all three removal mechanisms is characterized by a STEF of 2.58, meaning that compared to a pure diffusive transfer, the complete system allows to gain more than 2.5 times a flow of solute out of the feed (blood).

In parallel, the concentration inside the membrane as well as the molar flux across the membrane depend on hydrodynamics on the feed side. Figure 5.7 shows the influence of convection flow rate (Peclet number) on the system, where diffusion, convection and adsorption are employed in the solute elimination from the feed stream.

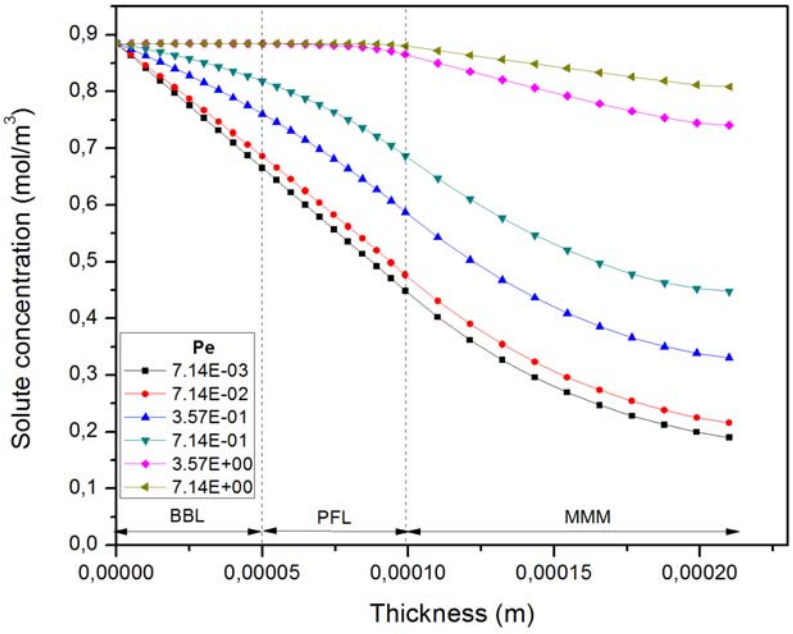

Figure 5.7: Solute concentration profile across the membrane and feed boundary layer at various rates of convective flows.

As it can be seen from Figure 5.7, at lower values of Pe the solute concentration in the MMM is significantly different from the one in the bulk. However, at Pe>1, when convection becomes dominant over diffusion, the solute is more efficiently transferred towards the adsorptive layer, so that the bulk and membrane concentration are balanced. In order to keep a Pe larger than 1, the convective flow of $1.4 \times 10^{-5}\ \mathrm{m\,s^{-1}}$ or greater has to be generated. On the other hand, an excessive convection rate leads to the reduced impact of adsorption on the solute removal. Therefore, at high Pe one does not take advantage of the presence of the adsorptive capacity of the membrane.

3.3 Experimental results vs modelling

A first experiment was conducted in the diffusive mode with use of creatinine solution and Membrane 1. The experimental results are compared to the model in Figure 5.8.

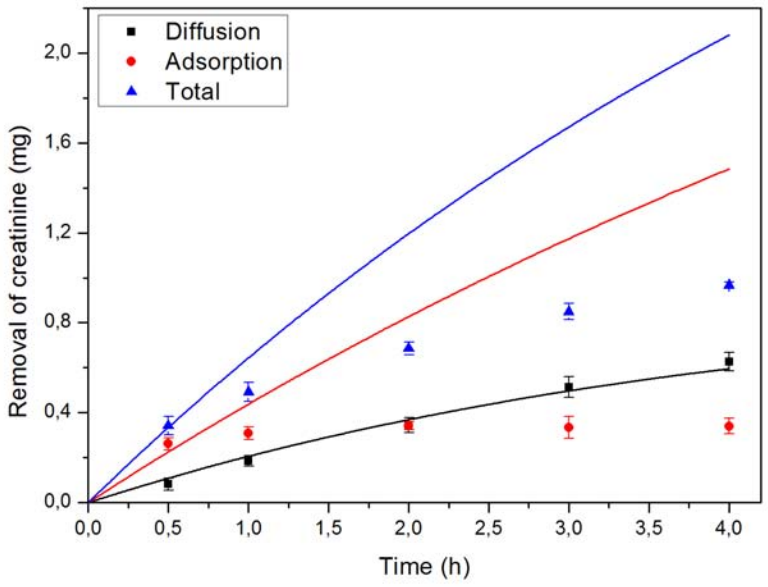

Figure 5.8: Results of validation experiment 1 vs theoretical prediction (continuous lines are predicted evolution of solute removal, while dots represent the experimental results).

According to the Figure 5.8 it can be seen that the diffusive curve is ideally predicting the removal of creatinine by diffusion. Both experimental and theoretical results demonstrated that during a four-hour experiment at given conditions, one may achieve diffusive removal of 0.6 mg of creatinine. The slight deviation of diffusive curve from linearity is a result of decrease of solute concentration in the feed and increase in the dialysate, which led to the reduction of solute removal driving force across the membrane. In contrary, the adsorption curve fits the experimental data only in the early stage of the process. This observation may be explained by saturation of adsorptive particles, which starts to be noticeable after half an hour of the experiment, and ultimately reaching a membrane adsorptive capacity of 0.34 mg or, more precisely, 26.27 µg of creatinine per 1 mg of membrane. Therefore, the modification of model with the new fitted input parameter "Membrane limiting adsorption capacity" (MLAC) was done aiming to account the

activated carbon particles saturation (Figure 5.9). In order to introduce this parameter in the model, the following conditions were applied:

$$\begin{cases} q < q_{max}; & r = akc \\ q \geq q_{max}; & r = 0 \end{cases}$$

As so, until the amount of adsorbed specie (q) is inferior to the maximal capacity (q_{max}), the adsorption mechanism is in force and is happening according to the previously discussed assumptions. However, once the maximal membrane capacity is reached, the adsorption is no longer possible, and, therefore, the adsorptive removal mechanism is switched off by the model.

The result of MLAC application for the experiment 1 is presented in Figure 5.9.

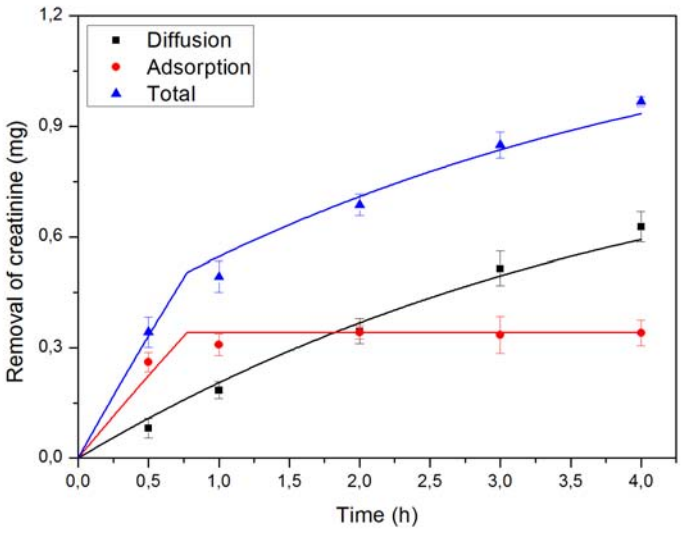

Figure 5.9: Results of validation experiment 1 vs theoretical prediction accounting saturation of the adsorbent.

According to Figure 5.9, the saturation of particles embedded in the polymer matrix of the membrane is reached after 45 min of experiment, meaning that starting from this time point the creatinine removal is governed solely by diffusion. As it can be seen from the total removal curve, insertion of membrane limiting adsorption capacity parameter enables rather precise prediction of the outcome of the experimental creatinine removal. Finally, the "snapshot" analysis of analyzed

system at the initial time point showed that due to the presence of adsorptive particles in the membrane the creatinine transfer acceleration of 93% was gained, meaning that at the early stages of the process, while the adsorbent is not yet saturated the solute removal rate is almost twice higher thanks to the presence of the adsorbent. Such observation provides the numerical justification of the beneficial use of dual-layer membranes with incorporated particles of activated carbon.

Validation experiment with use of creatinine solution and Membrane 1 was also conducted in hemodiafiltration mode (applying TMP). However, due to tight structure of the skin-layer in the particle free membrane the convection was limited even at high pressures, therefore, the convective term had a negligible contribution to over mass transfer during the experiment. Consequently, the result of this experiment were almost identical to the one with diffusive transport only; thus, these results are not presented here.

As it was aforementioned, Membrane 1 was found to be impermeable for α-lactalbumin, therefore this membrane was not suitable for model validation experiments with use of middle sized solutes.

The first validation experiment with use of α-lactalbumin solution and Membrane 2 was performed in diffusive regime. Due to poor diffusivity of the protein, during the four-hour experiment no noticeable concentration reduction in the feed side was observed. This outcome was theoretically predicted by model, which demonstrated that at chosen conditions the removal of α-lactalbumin is negligible both by diffusion and adsorption. Therefore, the results of this trial are also not presented here.

In order to evaluate the validity of developed model with respect to middle sized solutes, a second experiment was conducted with use of Membrane 2 and α-lactalbumin at TMP of $0.5\ \mathrm{bar}$. Applied pressure difference across the membrane resulted in the convective flow of $3.38 \times 10^{-6}\ \mathrm{m\,s^{-1}}$. The results of the second experiment and their comparison with model are presented in Figure 5.10.

According to Figure 5.10, the diffusive+convective removal of α-lactalbumin as in previous validation experiments is in perfect agreement with theoretical prediction. Thanks to significant convection rate, the removal of $2\ \mathrm{mg}$ of α-lactalbumin was achieved within four hours of experiment. In addition, the adsorptive removal of $0.47\ \mathrm{mg}$ was observed after half an hour from the process start, and was not changing throughout the remaining time. This observation indicates that alike the first experiment, the saturation of adsorptive particles was achieved at early stage of

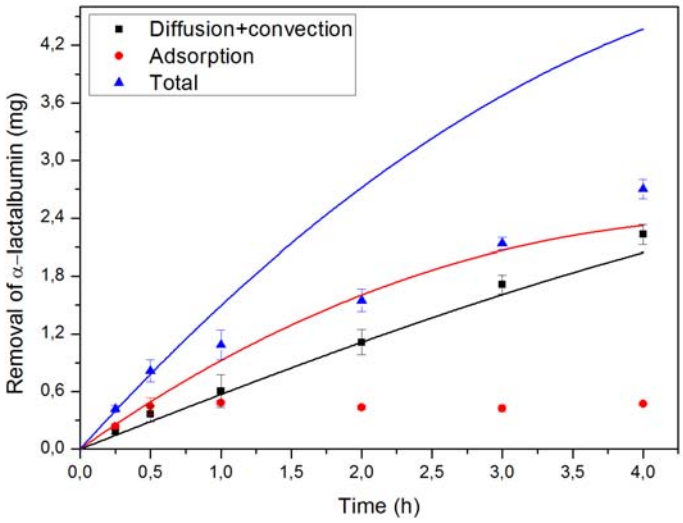

Figure 5.10: Results of validation experiment 2 vs theoretical prediction.

the process. Fast saturation may be attributed to the presence of convection, which enabled facilitated transport of protein towards the surface of activated carbon. This hypothesis was supported by "snapshot" analysis, which demonstrated that convection provided 837% solute transport acceleration in the beginning of the process, while presence of the adsorptive layer resulted in 71% of protein removal facilitation. Finally, the cumulative effect of MMM and convection enabled 9.4 times greater solute removal rate than one may expect from solely diffusion-based process.

Since during the experiment 2 the saturation MMM was achieved, it was possible to modify the model with use of "Membrane limiting adsorption capacity" parameter. Based on the experimental result the input value of 8.1 µg of α-lactalbumin per 1 mg of membrane was taken. The comparison between validation experiment 2 and modified model is presented in Figure 5.11.

According to Figure 5.11 the modified model more precisely describes adsorptive removal of α-lactalbumin, and, consequently, the total elimination of protein is more accurately predicted. In particular, the saturation of adsorbent was reached after 30 min of experiment, and the remaining time α-lactalbumin was happening mainly due to convection and partially due to diffusion.

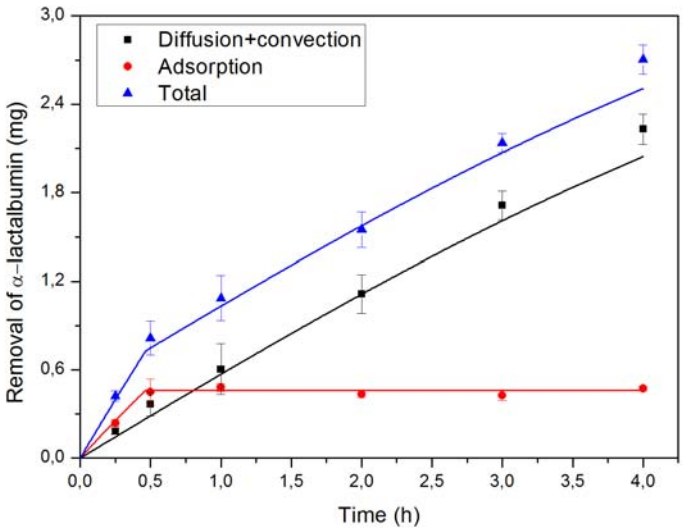

Figure 5.11: Results of validation experiment 2 vs theoretical prediction accounting saturation of the adsorbent.

Based on conducted validation experiments, the developed model demonstrates precise prediction of solute removal at the early stage of the process (less than one hour), which is in the agreement with the assumption that the adsorption is the first-order reaction. However, the modification of model with "Membrane limiting adsorption capacity" parameter was required in order to account the possibility of adsorbent saturation, which was observed in both validation experiments. Finally, the MLAC parameter differs from the limiting adsorbent capacity, because inside the membrane the accessibility of the adsorbent is lower than in the free state, therefore, it can be evaluated only experimentally for each membrane type.

4 Conclusion

The concept of double layer membranes aiming the improvement of removal of blood toxins is a promising advancement of dialysis treatment. In the present study we presented the model which allows more in-depth analysis of interplay of three solute removal mechanisms: diffusion, convection, and adsorption. The model was validated via comparison of model predictions with outcome of experimental testing of home-made double layer mixed matrix membranes. The developed model provides an accurate agreement with diffusive and convective removals obtained

experimentally for both small and middle sized uremic toxins. Moreover, even a rather simplistic approach in the modelling of adsorptive removal of toxins (first-order reaction) provides a possibility to evaluate the amount of adsorbed species at the early stages of treatment process. While after the occurrence of adsorbent saturation the insertion of Membrane limiting adsorption capacity term enables to adjust model for new circumstances. The developed model may be further applied in the optimization of double layer membrane properties and the process conditions.

5 References

1. Tijink, M.S., M. Wester, J. Sun, A. Saris, L.A. Bolhuis-Versteeg, S. Saiful, J.A. Joles, Z. Borneman, M. Wessling, and D.F. Stamatialis, A novel approach for blood purification: mixed-matrix membranes combining diffusion and adsorption in one step. *Acta Biomater*, 2012. 8(6): p. 2279-87.

2. Tijink, M.S., M. Wester, G. Glorieux, K.G. Gerritsen, J. Sun, P.C. Swart, Z. Borneman, M. Wessling, R. Vanholder, J.A. Joles, and D. Stamatialis, Mixed matrix hollow fiber membranes for removal of protein-bound toxins from human plasma. *Biomaterials*, 2013. 34(32): p. 7819-28.

3. Henrich, W.L., *Principles and Practice of Dialysis*. Fourth ed. 2009: Lippincott Williams & Wilkins.

4. Yang, X., R. Wang, A.G. Fane, C.Y. Tang, and I.G. Wenten, Membrane module design and dynamic shear-induced techniques to enhance liquid separation by hollow fiber modules: a review. *Desalination and Water Treatment*, 2013. 51(16-18): p. 3604-3627.

5. Shaw, R.A., C. Rigatto, M. Reslerova, S.L. Ying, A. Man, B. Schattka, C.F. Battrell, J. Matthewson, and C. Mansfield, Toward point-of-care diagnostic metabolic fingerprinting: quantification of plasma creatinine by infrared spectroscopy of microfluidic-preprocessed samples. *Analyst*, 2009. 134(6): p. 1224-31.

6. Kim, J.C., D. Cruz, F. Garzotto, M. Kaushik, C. Teixeria, M. Baldwin, I. Baldwin, F. Nalesso, J.H. Kim, E. Kang, H.C. Kim, and C. Ronco, Effects of Dialysate Flow Configurations in Continuous Renal Replacement Therapy on Solute Removal: Computational Modeling. *Blood Puri cation*, 2013. 35(1-3): p. 106-111.

7. Fu, B.M., R.H. Adamson, and F.R. Curry, Determination of microvessel permeability and tissue diffusion coefficient of solutes by laser scanning confocal microscopy. *J Biomech Eng*, 2005. 127(2): p. 270-8.

6 Conclusions and perspectives

The present work was realized in the frame of international project BioArt, which was focused on the development of new approaches in kidney and liver failure treatments. One of applied strategies was to develop and to optimize the novel membranes with improved properties, such as biocompatibility (lower protein adsorption on the membrane surface), better removal of toxins etc. This particular thesis was focused on the development of methods to control the removal and adsorption of the middle sized uremic toxins in artificial kidney. The primary motivation for this study emerges from the fact that these compounds are poorly removed in modern clinically accepted blood purification techniques. While the accumulation of middle sized uremic toxins in the patients with the lapse of time leads to the new diseases, which negatively influence the quality of their lives. Secondly, the clinical blood purification (hemodialysis) is associated with frequent contact between the blood and the synthetic filters (membranes). This contact normally results in the adsorption of blood components on the surface of the membrane, which may lead to adverse side effects related to the membrane biocompatibility such as blood coagulation, complement activation, blood cells adhesion etc. Therefore, both highlighted problems needed to be addressed and new solutions are required to make the lifesaving hemodialysis technique one step closer to the adequate replacement of the functions of native kidney.

Firstly, the conventional methods of investigation of adsorption on the membrane surface (membrane fouling) include macro approaches, such as the permeate flux measurements or/and control of the transmembrane pressure. However, these methods provide information about the macro scale, while no data is obtained concerning the scale of an isolated fiber inside the hemodialysis module. Therefore, the first part of the present work was focused on the characterization of the novel transparent membrane-based microfluidics device (MMD), which was developed in order to transfer the investigation of membrane fouling to the micro scale. Firstly, the membrane permeability inside the developed MMD was compared to the macroscale set-up and almost identical values were obtained: $562 \pm 53\ \mathrm{L\,m^{-2}\,h^{-1}\,bar^{-1}}$ and $541 \pm 37\ \mathrm{L\,m^{-2}\,h^{-1}\,bar^{-1}}$, respectively. This result demonstrated that the membrane-based filtration can be downscaled in the MMD without loss of membrane productivity per unit of filtration surface. Then, to benefit from the MMD s transparency, it was coupled with fluorescent microscopy, which allows the real-time monitoring of the membrane surface during the contact with fluorescent species. During the coupling optimization, the influence of various microscopy-related parameters on the fluorescence measurements were investigated.

As an outcome of this analysis, it was demonstrated that even $250\ \mu\mathrm{m}$ displacement of focus from the membrane surface in both directions along the Z-axis (normal to the membrane surface) does not have a significant influence on the recorded intensity of the fluorescent signal. Moreover, it was discovered that neither the signal coming from the solution of labelled protein nor one from the adsorbed protein on the internal glass surface of the MMD affect the precision of the acquisition of signal from the membrane surface. As so, the only parameter deserving the careful control is the exposure time, which has to be adjusted depending on the fluorescent tag and the concentration of dissolved species. Then, the MMD was applied for the preliminary real-time study of adsorption of fluorescently labelled Bovine Serum Albumin (BSA) on the surface of membrane, fabricated from polyethersulfone, which is common material of hemodialysis membranes. The BSA was chosen for this test in order to be sure to have the protein deposition on the membrane surface; the protein (Molecular weight = $66\ \mathrm{kDa}$) is totally retained by the membrane with molecular weight cut off $50\ \mathrm{kDa}$. Moreover, albumin is one of the most abundant proteins in blood, and, therefore, it is important to know how this protein interacts with the material of artificial kidney. The application of MMD allowed to discover that adsorption of BSA is a reaction-limited process, meaning that diffusion towards the surface is significantly faster than the reaction on the surface. Moreover, it was demonstrated that depending on applied transmembrane pressure, there is a possibility to observe different extent of fouling (intensity of fluorescence) along the membrane. Particularly, if transmembrane pressure (TMP) is close to zero, it seems that the pressure drop inside the retentate compartment plays a noticeable role in distribution of fluxes inside MMD, which leads to higher accumulation of protein at the inlet part and to lower accumulation at the outlet. In addition, during the filtration experiments (TMP > 0) it was found that the evolution of gray values (the unit of fluorescent intensity) correlates with the permeate flux decline in the beginning of the experiment, where the primary contact between membrane and protein occurs. However, once the minimal value of filtrate flux is reached, it remains unchanged, while the gray value continue to increase a bit. The nature of this disagreement was not clearly understood and requires additional study. Finally, the analysis of obtained results through the generally accepted film theory revealed that the most favoring conditions for the protein accumulation are the ones with highest Pe number.

The developed MMD was then used for the analysis of membrane fouling at

different hydrodynamic and pressure conditions applied for the filtration of solution of fluorescently labelled small size protein (α-lactalbumin). The choice of protein was dictated by its similarity in size and isoelectric point to the main marker (β_2-microglobulin) of middle sized molecules removal during hemodialysis (artificial kidney) and availability of α-lactalbumin. The obtained results suggested that unlike the adsorption of BSA the adsorption of α-lactalbumin at TMP$\approx$0 is dependent on the feed flow rate. Particularly, the greater feed flow rate is, the more noticeable accumulation of α-lactalbumin is observed. This observation is related either to the higher extent of protein unfolding at higher shear stress or to the thinning of the boundary layer at greater feed flow rates, which in turn would imply the diffusion-limited adsorption. In addition, the observed difference in the fluorescent signal recorded from different parts of the MMD during the experiments at TMP$\approx$0, suggest that the pressure drop along the microchannel also influences the adsorption of α-lactalbumin-Atto647N. However, this difference vanishes at low feed flow rates, because the pressure drop becomes too small to have a noticeable impact on the distribution of accumulated protein. Moreover, the surprising observation was done during the application of transmembrane pressure (shifting to filtration conditions). A lot of strange unexpected dark zones were formed, which were not detected neither during experiment with BSA-FITC (at all studied conditions) nor during fouling experiments with α-lactalbumin-Atto647N at TMP$\approx$0. It was hypothesized that their formation is governed by the phenomena called aggregation-caused fluorescence quenching (ACQ), which takes place when π-electrons of neighboring fluorescent tags start to interact leading to the annihilation of the fluorescent light emission. In addition, two factors were found to be determining in the membrane fouling during the filtration experiments. Firstly, it is the ratio between axial convection (directed tangentially to the membrane surface) and the transmembrane drag force. It was estimated that there is a critical value of this ratio (between 12.4 and 25), below which the supersaturation of solution is achieved rapidly which leads to a uniform coverage of membrane surface with ACQ zones. While above this critical value, the attainment of supersaturation requires more time, which results in progressive increase of surface coverage with ACQ zones from the inlet towards the outlet. Secondly, analysis of obtained results through the film theory demonstrated that the fouling induced by α-lactalbumin-Atto647N is more severe at processes with higher Pe numbers. Finally, the comparative study of α-lactalbumin adsorption on polyethersulfone and novel SlipSkin^{TM} membranes demonstrated the lower propensity of latter material

to interact with protein, suggest it as a promising candidate for fabrication of membranes for biomedical application. The obtained results shed the light on the membrane fouling induced by middle sized molecules at the microscale during the use of artificial kidney. Therefore, this knowledge may be used for the optimization of operating conditions and membrane materials for currently used artificial kidney.

The development of a mathematical model, which describes the toxin removal from the blood stream using functionalized double-layer membrane, was then investigated. The model combines three solute removal mechanisms: diffusion, convection and adsorption. Therefore, it allows more in-depth analysis of interplay of three solute removal mechanisms happening simultaneously. The model was then validated by comparison of model predictions with outcome of experimental testing of home-made double-layer mixed matrix membranes. The comparison revealed that even a rather simplistic approach in the modelling of adsorptive removal of toxins (first-order reaction) provides a possibility to evaluate the amount of adsorbed species at the early stages of treatment process. However, since the possibility of adsorbent saturation was not initially considered, the insertion on a new parameter "Membrane limiting adsorption capacity" is required in order to adjust model for new circumstances. As so, the developed model illustrates how the proposed double-layer membrane concept offers significant benefits in terms of toxin removal in comparison to conventional dialysis. Finally, the main achievement of the developed model is that it may serve as tool for the further improvement of functionalized membrane in terms of toxin removal and optimization of process conditions.

As further developments of this thesis, several directions may be proposed.

Firstly, the developed microfluidics device may be further optimized. At the current form, it resembles the micro cross flow filtration unit, where permeate compartment has only one exit. From the blood purification point of view, this design is a miniaturized version of hemofiltration, which as it was discussed in Chapter 1 is not the most optimal technique. In contrast, addition of one outlet in the permeate side of the MMD would allow to perform the filtration process at counter-current mode, which would bring research closer to micro hemodialysis and hemodiafiltration.

Concerning the application of fluorescent microscopy in the investigation of protein accumulation on the membrane surface, several points are still to be clarified. Firstly,

it is important to evaluate whether the recorded fluorescent signal comes from the top layer of the deposit or from its entire thickness or maybe there is a specific depth of the deposit which can be analyzed. This knowledge would provide an opportunity to understand the correlation between the reduction of membrane permeability and the recorded gray values.

Secondly, there is an interest in developing a method to correlate the fluorescent signal with the quantity of adsorbed protein. Aiming to progress in this direction, one of additional tasks would be to investigate the influence of fluorescence quenching phenomena on this quantification. This need emerges from our observation that over the course of filtration α-lactalbumin tends to form specific dark zones, which are believed to be related to its aggregation. In addition, if this assumption is correct, and considering the premise that aggregates are highly concentrated it would be an intriguing advancement to determine at which critical local concentration these aggregates are formed.

Lastly, in this project it was found that conventional film theory could not explain the outcome of BSA filtration at relatively slow feed flow rate and intensive transmembrane flux (Figure 3.20). More significant protein accumulation was located at the inlet of the system and less significant at the outlet, while the film theory suggests absolutely the opposite scenario. Therefore, the additional study is required to obtain a better understanding of mechanisms, which are governing such distribution of fouling along the membrane.

Some additional modifications could also be made in order to improve the developed mathematical model. Firstly, our model demonstrated its potential for the evaluation of removal of small and middle sized uremic toxin. However, it is not able to model the removal of protein-bound toxins. In fact, the toxins belonging to this group are present in the blood of patients both in the protein-bound and the free forms and the ratio between these forms is described by the association constant. Taking into account that only non-bound molecule may be transferred through the membrane, the model can be “equipped” with a term, which would calculate the free fraction of protein-bound toxin at a given time. In such case, the model would be able to simulate the dissociation of protein-molecule complex in response for the continuous removal of the free fraction of the toxin.

Besides, the blood is multicomponent solution, while our model was developed and validated only for mono component solutions. Therefore, aiming to make the model closer to real biological system, it could be expanded in the way that the removal of

several toxins can be predicted simultaneously. Finally, based on conducted validation experiments, the adsorptive particles are getting saturated over the course filtration. Therefore, the assumption that the adsorption is a first order reaction is applicable only at the beginning of the process. As so, the sink term (adsorptive removal) in the model could be changed from the first-order to Langmuir-like form, so that the progressive saturation will be accounted.

At the end of this manuscript, it could be stated that the developments done during this project may be applied in other membrane-based applications. For example, the developed mathematical model may be applied to study other systems where diffusion, convection and adsorption (reaction) are taking place in the same time. Talking about the novel membrane-based microfluidics device, it can be pointed out that its application may go beyond protein filtration. It may be used to downscale any other kind of liquid separation. Hence, its development can be considered as a benchmark for transferring the studies of membrane-based processes to the micro scale with an opportunity to monitor its progress in the real time.

Appendix

APPENDIX A

The complete expressions for pseudo mass transfer conductances ($K_{i,j}$), which are used in Section 1.2, have the following form:

$$K_{1a} = \frac{Je^{Pe_1}}{e^{Pe_1} - 1} \tag{A.1}$$

$$K_{1b} = \frac{J}{e^{Pe_1} - 1} \tag{A.2}$$

$$K_{2a} = \frac{Je^{Pe_2}}{e^{Pe_2} - 1} \tag{A.3}$$

$$K_{2b} = \frac{J}{e^{Pe_2} - 1} \tag{A.4}$$

$$K_{3a} = \frac{D_3\sqrt{Pe_3^2 + 4\phi^2}\cosh\left(\frac{\sqrt{Pe_3^2 + 4\phi^2}}{2}\right)}{2\delta_3 \sinh\left(\frac{\sqrt{Pe_3^2 + 4\phi^2}}{2}\right)} + \frac{D_3 Pe_3}{2\delta_3} \tag{A.5}$$

$$K_{3b} = \frac{D_3 e^{-\frac{Pe_3}{2}}\sqrt{Pe_3^2 + 4\phi^2}}{2\delta_3 \sinh\left(\frac{\sqrt{Pe_3^2 + 4\phi^2}}{2}\right)} \tag{A.6}$$

$$K_{3c} = \frac{D_3 e^{\frac{Pe_3}{2}}\sqrt{Pe_3^2 + 4\phi^2}}{2\delta_3 \sinh\left(\frac{\sqrt{Pe_3^2 + 4\phi^2}}{2}\right)} \tag{A.7}$$

$$K_{3d} = \frac{D_3\sqrt{Pe_3^2 + 4\phi^2}\cosh\left(\frac{\sqrt{Pe_3^2 + 4\phi^2}}{2}\right)}{2\delta_3 \sinh\left(\frac{\sqrt{Pe_3^2 + 4\phi^2}}{2}\right)} - \frac{D_3 Pe_3}{2\delta_3} \tag{A.8}$$

$$K_{4a} = \frac{Je^{Pe_4}}{e^{Pe_4} - 1} \tag{A.9}$$

$$K_{4b} = \frac{J}{e^{Pe_4} - 1} \tag{A.10}$$

APPENDIX B

Detailed solution of the differential equation Equation 5.4, which describes the combined diffusive, convective, and adsorptive solute removal mechanisms. The initial equation to solve:

$$D\frac{d^2c}{dx^2} - J\frac{dc}{dx} - akc = 0$$

Solution:

$$c = K_1 e^{\frac{J+\sqrt{J^2+4akD_3}}{2D_3}x} + K_2 e^{\frac{J-\sqrt{J^2+4akD_3}}{2D_3}x} =$$

$$= \left\{ \begin{matrix} BC.1 & x = 0, c = c_2 \\ BC.2 & x = \delta, c = c_3 \end{matrix} \right\} =$$

$$= \begin{cases} c_2 = K_1 + K_2 \\ c_3 = K_1 e^{\frac{J+\sqrt{J^2+4akD_3}}{2D_3}\delta} + K_2 e^{\frac{J-\sqrt{J^2+4akD_3}}{2D_3}\delta} \end{cases} =$$

$$\begin{cases} K_1 = \dfrac{c_3 - c_2 e^{\frac{J-\sqrt{J^2+4akD_3}}{2D_3}\delta}}{2e^{\frac{J\delta}{2D_3}} \sinh\left(\dfrac{\sqrt{J^2+4akD_3}}{2D_3}\delta\right)} \\ K_2 = \dfrac{c_2 e^{\frac{J\delta}{2D_3}} e^{\frac{\sqrt{J^2+4akD_3}}{2D_3}\delta} - c_3}{2e^{\frac{J\delta}{2D_3}} \sinh\left(\dfrac{\sqrt{J^2+4akD_3}}{2D_3}\delta\right)} \end{cases} \Rightarrow$$

$$\Rightarrow c = \frac{c_3 - c_2 e^{\frac{J-\sqrt{J^2+4akD_3}}{2D_3}\delta}}{2e^{\frac{J\delta}{2D_3}} \sinh\left(\frac{\sqrt{J^2+4akD_3}}{2D_3}\delta\right)} e^{\frac{J+\sqrt{J^2+4akD_3}}{2D_3}x} +$$

$$+ \frac{c_2 e^{\frac{J\delta}{2D_3}} e^{\frac{\sqrt{J^2+4akD_3}}{2D_3}\delta} - c_3}{2e^{\frac{J\delta}{2D_3}} \sinh\left(\frac{\sqrt{J^2+4akD_3}}{2D_3}\delta\right)} e^{\frac{j-\sqrt{J^2+4akD_3}}{2D_3}x} \quad \text{(B.1)}$$

Medium sized molecules clearance through artificial kidneys

Despite a long history of development, the hemodialysis procedure (artificial kidney) still possesses some limitations, such as loss of the initial properties of the membrane due to fouling and poor removal of the middle sized uremic toxins.

The present study is part of an European project named BioArt the aim of which was to overcome these limitations. In that objective, one of the partners of BioArt project reported on the development of the novel promising concept of double layer membrane with embedded adsorptive particles. A thorough characterization of the new membrane was then necessary, more precisely the extent to which mixed matrix layer can improve the removal of the uremic toxins from various groups needed to be evaluated, as well as the propensity of the membrane material to become fouled.

The studies of the fouling phenomena are conventionally performed at the macro scale (bundle of hollow fibers) without insights of what is happening at the scale of an isolated fiber. Therefore, the primary aim of the present Thesis was to transfer the research of the protein-induced membrane fouling from the macro to the micro scale. A novel transparent microfluidics device with the polymeric membrane inside has been developed and applied for the filtration of model proteins: bovine serum albumin (BSA) and α-lactalbumin. Thanks to the coupling of the microchip with the fluorescent microscopy, different patterns of protein deposition on the membrane surface were observed and related to the variations in the hydrodynamic conditions inside the microchip. It was found that at certain conditions one may observe the difference in protein accumulation in the inlet, the middle, and the outlet of the channel while at other conditions this effect vanishes. Additionally, the unexpected phenomena of α-lactalbumin aggregation was observed over the course of filtration. The location and shape of the aggregates were also dependent on the hydrodynamic conditions and the applied transmembrane pressure.

Aiming to address the problem of membrane design optimization for the enhancement of the middle molecules elimination from the bloodstream, a mathematical model, which accounts for the presence of adsorptive particles inside the complex double-layer membrane, has been proposed. The objective of the model was to understand the interplay of three solute removal mechanisms: convection, diffusion, and adsorption. The model allows predicting the influence of various parameters such as molecule diffusivity, membrane thickness, the presence of convection, content of adsorptive particles on the flux intensification across the membrane. The developed model seems to be a useful tool, which may be applied to design optimized membranes for the removal of toxins.

Keywords: Hemodialysis, Microfluidics Device, Membrane Fouling, Protein Adsorption, Mass Transfer Model

---

Clairance de molécules de taille moyenne à travers un rein artificiel

Malgré une longue histoire de développement, l'hémodialyse (rein artificiel) possède encore quelques limitations, telles que la perte des propriétés initiales de la membrane en cours de traitement à cause du colmatage et la mauvaise élimination des toxines urémiques de taille moyenne.

La présente étude fait partie d'un projet européen nommé BioArt dont le but est d'apporter des solutions à ces limites. Dans cet objectif, l'un des partenaires du projet a proposé le développement d'un nouveau concept de membrane double couche au sein de laquelle sont incorporées des particules adsorbantes. Une caractérisation complète de cette nouvelle membrane était alors nécessaire, plus précisément l'impact de la matrice mixte sur l'élimination des toxines urémiques de divers groupes devait être évalué, ainsi que la propension du matériau membranaire à se colmater.

Les études des phénomènes de colmatage sont classiquement menées à l'échelle macroscopique (faisceau de fibres creuses) sans analyse à l'échelle d'une fibre isolée. Le but premier de la présente thèse a alors été de proposer un dispositif permettant une étude du colmatage membranaire induit par la protéine à l'échelle microscopique. Un dispositif microfluidique transparent dans lequel la membrane polymère est insérée a été élaboré et mis en œuvre pour la filtration des protéines modèles : l'albumine de sérum bovin (BSA) et l'α-lactalbumine. Grâce au couplage avec la microscopie de fluorescence, différents modes d'adsorption des protéines sur la surface de la membrane ont été observés et liés aux variations des conditions hydrodynamiques à l'intérieur de la puce. Il a été constaté, sous certaines conditions, une différence dans l'accumulation de protéines entre l'entrée, le centre et la sortie du canal tandis que dans d'autres conditions cet effet s'annule. En outre, un phénomène inattendu, l'agrégation de l'α-lactalbumine, a été observé au cours de la filtration. La localisation dans le canal et la forme des agrégats dépendent également des conditions hydrodynamiques et de la pression transmembranaire appliquée.

Dans le but d'optimiser la conception de la membrane vis à vis de son aptitude à éliminer des molécules de taille moyenne de la circulation sanguine, un modèle mathématique a été proposé. L'objectif du modèle était, en prenant en compte la présence de particules adsorbantes à l'intérieur de la membrane double couche, de rendre compte de la combinaison des trois mécanismes d'élimination du soluté : la convection, la diffusion et l'adsorption. Le modèle permet de prédire l'influence de divers paramètres tels que la diffusivité de la molécule, l'épaisseur de la membrane, la présence de la convection, la charge en particules adsorbantes, sur l'intensification des flux à travers la membrane. Le modèle semble être un outil utile pouvant être appliqué à l'optimisation de membranes pour l'élimination des toxines.

Mots clés: Hémodialyse, Dispositif Microfluidique, Colmatage de la Membrane, L'adsorption de la protéine, Modèle de transfert de la masse.